

# **Mineralisation-Related Flow Heterogeneity within the Zubair Formation in the Rumaila Oilfield, Southern Iraq**

A thesis submitted to the University of Manchester  
for the degree of

Doctor of Philosophy

Faculty of Science and Engineering

**2018**

**Haitham Ghazi Faisal Al-Ziayyir**

School of Earth and Environmental Sciences



# Table of Contents

Table of Contents	3
List of Figures	7
List of Tables	11
Abstract	12
Declaration	13
Copyright Statement	14
Acknowledgements	15
<b>Chapter 1</b>	<b>16</b>
Introduction, Study Aim and Objectives	16
1.1. Scientific Rationale	18
1.2. Study Aims and Objectives	19
1.3. Database, Data Quality and Constraints	20
1.4. Study Area	25
<b>Chapter 2</b>	<b>27</b>
Geologic Setting and Background Literature	27
2.1. Geologic Setting	28
2.2. Tectonic and Structural Setting	29
2.3. Previous Work and Background Literature	39
2.3.1. Previous Work	39
2.3.1.1. Lithology of the Zubair Formation	39
2.3.1.2. Depositional Environment	40
2.3.1.3. Clay Mineralogy	41
2.3.1.4. Reservoir and petroleum geochemistry	42
2.4. Petroleum System of the Zubair Formation	42
2.5. Basin and Reservoir Seal and Compartmentalization	44
2.5.1. Definition of Seals	46
<b>Chapter 3</b>	<b>48</b>
Methodology and Analytical Techniques	48
3. Methodology	50
3.1. Core-Log Sampling	50
3.2. Systematic Core Description	50
3.3. Core Photography	52
3.4. Analytical methods	52
3.4.1. Scanning Electron Microscope (SEM)	52
3.4.2. X-ray Diffraction XRD Samples Preparation	55
3.4.2.1 XRD specimen's preparation and treatment	55
3.4.2.1.1 Procedure for the Removal of Carbonates by Acetic Acid Treatment	56
3.4.2.1.2. Procedure for Organic Matter Removal with Hydrogen Peroxide	58
3.4.2.1.3. Separation of Silt and Clay by Decantation	58
3.4.2.1.4. Preparation of Clay Fraction for XRD Analysis	61

3.4.2.1.5. Procedure of Preparation of Oriented Mounts	61
3.4.2.1.6. Treatment with Ethylene Glycol	62
3.4.2.1.7. Heated-Treated Samples	63
3.5. Wireline Logs Digitizing	63
3.6. Petrophysical Analysis from Well Logs	64
3.7. X-ray CT and Pore-Scale Network Models	64
3.7.1 Analysis of X-ray CT data	64
3.7. 2. Permeability Test	65
<b>Chapter 4</b>	67
Lithofacies and Electrofacies Analysis	67
Introduction	69
4.1. Lithofacies	70
4.1.1. Facies Association H	74
Interpretation	74
4.1.2. Facies Association E	74
Interpretation	75
4.1.3. Facies Association D	75
Interpretation	75
4.1.4. Facies Association C	75
Interpretation	76
4.1.5. Facies Association N	76
Interpretation	77
4.1.6. Facies J	77
Interpretation	77
4.2. Electrofacies Analysis	77
4.3. Basic Log Curve Types	79
4.3.1. Cylindrical shape	79
4.3.2. Bell Shape	79
4.3.3 Funnel Shape	79
4.3.4. Oval Shape	80
4.3.5. Irregular Shape	80
4.4. Electrofacies Results and Interpretation	81
4.4.1. Thin funnel shaped	81
4.4.1.1. Description	81
4.4.1.2. Interpretation	81
4.4.2. Cylindrical Shaped	81
4.4.2.1. Description	81
4.4.2.2. Interpretation	82
4.4.3. Bell shaped	82
4.4.3.1. Description	82
4.4.3.2. Interpretation	82
4.5. Well Correlation	86
4.5.1. Stratigraphic and Structural Well Correlations	86
4.6. Discussion and Conclusion	87

<b>Chapter 5</b>	90
Mineralogical Characterisation Using XRD and SEM Studies	90
Introduction	92
5.1. Preface	92
5.2. Distinguishing Petrographic Characteristics	94
5.2.1. Light minerals	94
5.2.2. Feldspar and Rock Fragments	94
5.3. Clay minerals studies	95
5.4. Interpretation of X-ray diffraction data	95
5.4.1. Qualitative analysis of XRD data	95
5.4.1.1. Chlorite and kaolinite	99
5.4.1.2. Smectite	99
5.4.1.3. Illite and Glauconite	100
5.4.1.4. Chlorite	100
5.4.1.5. Quartz	100
5.5. Results of XRD qualitative analysis	100
5.5.1. Quantitative Analysis of XRD Data	106
5.5.2 Results of First Batch of XRD Scans	106
5.5.3. Results of Second Batch of XRD Scans	109
5.5.4. Results of Third Batch of XRD Scans	112
5.6. Results of Scanning Electron Microscopy	118
5.7. Discussion and Conclusion	126
<b>Chapter 6</b>	128
Pore Scale Characterisation of Mineralisation within the Zubair Formation Using X-ray Computed Tomography and Well log Analysis.	128
Introduction	130
6.1. Background	131
6.2. The rationale behind using X-ray micro CT for this research	133
6.3. Micro- CT scanning configuration	134
6.4. Methods and Imaging Techniques	134
6.4.1. Sample Preparation	135
6.4.2. X-ray micro CT Data acquisition	135
6.5. Data quality check	140
6.6. Mineral, Rock and Pore Characterization	140
6.7. Image Segmentation	142
6.7.1. Micro-CT image segmentation results	143
6.8. X-ray CT Data of the Zubair Formation's Sandstones	148
6.9. Results of Core Material Characterisation	149
6.10. Pore Network Extraction	151
6.11. Permeability Test	152
6.11.1. Permeability Estimate for Mineralised Mesh	153
6.11.2. Permeability estimate for unmineralised mesh	155
6.12. Discussion of Permeability Estimates	156
6.13. Well Log Analysis	158

6.13.1. Results of Well log analysis	158
6.14. Discussion and Conclusions	161
<b>Chapter 7</b>	162
Synthesis and Conclusions	162
Introduction	164
7.1. Synopsis of key findings and suggestions	164
7.1.1. Problem statement	165
7.1.2. Facies associations of the Zubair Formation	166
7.1.3. Depositional Setting	166
7.1.4. Depositional Textures and Fabrics	167
7.1.5. Mineral Characterisation	167
7.1.6. Reservoir Quality	168
7.2. Recommendations for Future Work	169
<b>References</b>	170
<b>Appendices</b>	184
<b>Appendix 1</b>	185
<b>Appendix 2</b>	219
<b>Appendix 3</b>	221

## List of Figures

Figure name	Caption	Page Number
Figure 1.1	Structure contour map of Unit AB of Main Pay of the Zubair Formation.	26
Figure 2.1	Mesopotamian Zone of Iraq, after (Buday and Jassim 1984 and 1987; Al-Kadhimi et al., 1996 and Jassim and Goff 2006).	28
Figure 2.2	A map shows the distribution of fault and fault system in Iraq after (Jassim and Goff, 2006)	31
Figure 2.3	A map shows transversal blocks in Iraq modified after (Jassim and Goff, 2006).	32
Figure 2.4	Tectonic map of Iraq modified from Buday and Jassim. Published by GEOSURV.	33
Figure 2.5	Isopach map of the Zubair Formation.	35
Figure 2.6	Type locality of the Zubair Formation	36
Figure 2.7	Stratigraphic column of Iraq	38
Figure 3.1	Systematic core descriptions in Core workshop at S.O.C, Iraq	51
Figure 3.2	Photograph of representative lithofacies about 3.3 meters	51
Figure 3.3	Mobile microscope work flow.	53
Figure 3.4	Environmental Scanning Electron Microscope FEI XL30 ESEM – FEG	54
Figure 3.5	SEM image from Well D	54
Figure 3.6	Energy Dispersive X-Ray spectrum (EDX) for the same sample taken from well D.	54
Figure 3.7	XRD Bruker D8Advance diffractometer	56
Figure 3.8	Photo shows materials required for carbonates removal with acetic acid.	57
Figure 3.9	Photo shows disposal method for acid waste(Poppe et al., 2001).	57
Figure 3.10	Materials required to perform decantation on the sediments	60
Figure 3.11	Screenshot shows the interface of Digder V4.0	63
Figure 3.12	Screenshot of Techlog 2014	64
Figure 3.13	X-ray CT imaging workflow diagram	66
Figure 4.1	Facies associations	73

Figure 4.2	Magnified photos of sample collected from Facies C	76
Figure 4.3	Classification of electrofacies by motifs of log response after (Serra and Abbott, 1980).	78
Figure 4.4	Generalised gamma- ray or self-spontaneous SP logs motifs	78
Figure 4.5	Irregular trend of gamma-ray log motif (Nazeer et al., 2016)	80
Figure 4.6	Electrofacies classification of the Zubair Formation – Upper Sandstone Member in Well B.	83
Figure 4.7	Electrofacies classification of the Zubair Formation – Upper Sandstone Member in Well C.	84
Figure 4.8	Electrofacies classification of the Zubair Formation – Upper Sandstone Member in Well D.	85
Figure 4.9	Stratigraphic correlation of wells B, D and C.	88
Figure .4.10	Structural correlation of wells B, D and C.	89
Figure 5.1	Oriented mount of the clay fraction from well D	98
Figure 5.2	XRD spectra of untreated clay fraction collected from well C	104
Figure 5.3	XRD spectra of treated-hated sample from well C.	105
Figure 5.4	Distribution of clay minerals, which were identified in well A	105
Figure 5.5	Distribution of clay minerals, which were identified in well D	105
Figure 5.6	Quantitative analysis of untreated clay fraction samples of well A	107
Figure 5.7	Quantitative analysis of ethylene glycol treated-heated clay fraction samples of well A	107
Figure 5.8	Non-clay minerals quantified in Well A.	108
Figure 5.9	Distribution of minerals quantified from XRD scans of bulk powder samples.	109
Figure 5.10	Quantitative analysis of clay minerals found in untreated samples of clay fraction.	111
Figure 5.11	Quantitative analysis of clay minerals of the second batch of ethylene glycol treated – heated to 550C <sup>o</sup> samples.	111
Figure 5.12	Graphical data of quantitative analysis of the bulk powder samples- second batch.	112
Figure 5.13	Graphical representation of quantitative analysis results of the untreated clay fraction samples.	113
Figure 5.14	Graphical representation of ethylene treated -heated clay fraction samples of the third batch of XRD scans.	114



Figure 5.15	Graphical distribution of minerals data found in the third batch of bulk powder samples.	115
Figure 5.16	SEM images of kaolinite and dickite.	120
Figure 5.17	SEM photos of polytype kaolinite.	121
Figure 5.18	SEM image of well-developed authigenic kaolinite.	121
Figure 5.19	SEM image of well-developed anhydrite.	122
Figure 5.20	Anhydrite crystals	122
Figure 5.21	SEM images of illite	123
Figure 5.22	SEM images of detrital illite and kaolinite	124
Figure 5.23	SEM microgram of sheet-like kaolinite	124
Figure 5.24	SEM images of framboidal pyrite.	125
Figure 6.1	<i>Diagram shows typical set up for a lab based micro-CT</i>	134
Figure 6.2	Core sample taken from larger sample. This sample was cut using rotary cutting tool. The core diameter is 6mm.	135
Figure 6.3	Nikon Metris XTH 225 X-ray CT scanner	136
Figure 6.4	Reconstructed computed tomographic image using CT Pro3D.	137
Figure 6.5	Bulk volume render of cropped sample taken from the Zubair sandstone.	138
Figure 6.6	Big core sample 80mm collected from the Zubair	139
Figure 6.7	Grey level values of components studied by (Long et al., 2009)	141
Figure 6.8	An orthoslice of micro-CT image Orthoslice shows segmented phases within Micro-CT dataset.	143
Figure 6.9	Skeletonised volume images of a cropped cubic volume of the sample	144
Figure 6.10	Ortho slice from Tiff stack collected from the big core sample.	145
Figure 6.11	Pyrite mesh volume segregated from the big core. This dendritic distribution of pyrite looks very clear in this image.	146
Figure 6.12	Orthoslice shows medium size quartz grains, with well-defined pores.	147
Figure 6.13	Massive sandstone sample from well D	148
Figure 6.14	SEM photos show pyrite framboid	149
Figure 6.15	Phase segmentation results of well B	150
Figure 6.16	Pore network	152

Figure 6.17 a.b.	inverted two channel binary image	154
Figure 6.18 a.b	Three channel binary image of pore and inverted binary image.	155
Figure 6.19 a	Streamlines of the mineralised pore mesh	157
Figure 6.19 b	Streamlines of the unmineralised pore mesh	158
Figure 6.20	Petrophysical analysis by using well log data of well B	159
Figure 6.21	Petrophysical analysis by using well log data of well A	160
Figure 7.1	Schematic of the scales of analysis performed throughout this project.	165

## List of Tables

<b>Table number</b>	<b>Title</b>	<b>Page Number</b>
Table(1.1)	Core data collected from the Rumaila field, Zubair Formation.	22
Table(1.2)	Well aliases, well coordinates and available wireline log data.	23
Table(1.3)	Number and depth of XRD and SEM samples collected from the study wells.	24
Table(1.4)	X-ray Micro CT representative core samples collected from the study wells.	25
Table (2.1)	Compartmentation types according to (Ortoleva, 1994a)	45
Table (2.2)	Seal types according to their spatial relationship to the compartment	46
Table (3.1)	Withdrawal time and temperature	61
Table (4.1)	Core based lithotypes, their names and description.	71
Table (5.1)	Classification of Phyllosilicates related to clay minerals	97
Table (5.2)	after (Brindley and Brown, 1980) d spacing in Å, and intensities for preliminary identification of clay minerals.	101
Table (5.3)	Summary of quantitative analysis of minerals identified in clay fraction samples of the Zubair Formation weight percentage	102
Table (5.4)	Summary of quantitative analysis of minerals identified in clay fraction samples of the Zubair Formation weight percentage	103
Table (5.5)	Minerals identified in the first batch of samples	115
Table (5.6)	Minerals identified in the second batch of samples	116
Table (5.7)	Mineralogical content identified in the third batch of the X-ray diffractometry scanned samples.	117

# The University of Manchester

Haitham Ghazi Faisal Al-Ziayyir

*Doctor of Philosophy*

Mineralisation-Related Flow Heterogeneity within the Zubair Formation in the Rumaila Oilfield, Southern Iraq

1<sup>st</sup> August 2017

## **Abstract**

Modelling subsurface deposits is extremely challenging with limited subsurface datasets such as cores, wireline logs and seismic data. However, integrated studies, which rely on extensive subsurface datasets can lead to improve the quality of spatial and temporal distributions of subsurface reservoirs. Nevertheless, a significant source of uncertainty within subsurface reservoirs is the controls upon hydrodynamic pressure distributions is not well understood. The depositional system is responsible for the style of heterogeneity, which is connected to chemical and physical diagenetic processes. These diagenetic controls may have very local or broad impact on reservoir properties related to pressure distribution. The uncertainty in pressure distribution can be reduced by providing a more detailed knowledge of mineralisation related to flow heterogeneity using Scanning Electron Microscopy (SEM), Energy Dispersive Spectrum (EDX) and X-ray Computed Tomography (X-ray CT). In this study, volume images of representative samples of the mineralised Zubair sandstones obtained using X-ray tomography are to be used as the basis for Computational Fluid Dynamical (CFD) modelling. Three phase segmentation will enable pore space, quartz matrix and in-situ pyrite mineralisation to be isolated from the volume images, enabling mineralised and unmineralised mesh based representations of the samples to be generated. Mineralogical characterisation on a small scale may open new paths for improving understanding of the impact of mineralisation upon fluid flow. As well as reducing uncertainty related to flow heterogeneity on a larger scale. The most obvious finding to emerge from mineralogical characterisation performed in this study is that dendritic pyrite mineralisation comprises potentially significant control upon pressure distribution. As well as using non-destructive technique such as X-ray computed tomography would be valuable to improve the understanding about the influence of mineralisation upon the trapping and transfer mobile geofluids by applying further studies, which are based on finite volume based flow solver to the collected images.

## **Declaration**

I hereby declare that only some information on petrographical study presented in Chapter 3 was done on the Upper Shale Member - Zubair Formation and has been submitted in partial fulfilment of the requirements for the degree of Masters of Science in Reservoir Geology at the University of Basrah.

Haitham Ghazi Faisal Al-Ziayyir

## Copyright Statement

- i. The author of this thesis (including any appendices and/or schedules to this thesis) owns certain copyright or related rights in it (the “Copyright”) and s/he has given The University of Manchester certain rights to use such Copyright, including for administrative purposes.
- ii. Copies of this thesis, either in full or in extracts and whether in hard or electronic copy, may be made only in accordance with the Copyright, Designs and Patents Act 1988 (as amended) and regulations issued under it or, where appropriate, in accordance with licensing agreements which the University has from time to time. This page must form part of any such copies made.
- iii. The ownership of certain Copyright, patents, designs, trademarks and other intellectual property (the “Intellectual Property”) and any reproductions of copyright works in the thesis, for example graphs and tables (“Reproductions”) which may be described in this thesis, may not be owned by the author and may be owned by third parties. Such Intellectual Property and Reproductions cannot and must not be made available for use without the prior written permission of the owner(s) of the relevant Intellectual Property and/or Reproductions.
- iv. Further information on the conditions under which disclosure, publication and commercialisation of this thesis, the Copyright and any Intellectual Property and/or Reproductions described in it may take place is available in the University IP Policy (see <http://www.campus.manchester.ac.uk/medialibrary/policies/intellectual-property.pdf>), in any relevant Thesis restriction declarations deposited in the University Library, The University
- v. Library’s regulations (see <http://www.manchester.ac.uk/library/aboutus/regulations>) and in The University’s policy on presentation of Theses.

## **Acknowledgments**

I would first of all like to express my sincere gratitude to my supervisor, Dr. David Hodgetts, for the continuous support over the course of my PhD studies, for his patience, motivation and encouragement. I could not have imagined completing this work without his guidance and mentoring for my PhD.

I would also like to thank a number of staff and colleagues within the School of Earth and Environmental Sciences at the University of Manchester. I feel myself privileged to engage with over the past years I spent with them. Special thanks are given to Dr. John Waters for assisting me in XRD analyses, Dr. Kofi Owusu for his continuous help and support, Dr. Thomas Seers with whom I have had many interesting discussions about X-ray computed tomography applications in petroleum geosciences. I thank my fellow office and lab mates: Mohammed Salim and Saad Saadi, I would also like to thank my friend in Basrah University: Rafed Abdulhasan. Special thanks go to my sponsor, the Higher Committee for Education Development in Iraq HCED, the Iraqi Government.

Most of all, my greatest thank to my wife Hiba, without whom I would never complete my thesis. Hiba has never hesitated in her support of my PhD career. I must also rise thanks to my three beautiful daughters: Shahad, Rund, and Wurd. Last but not the least; I thank my parents for supporting me and loving me unconditionally.

# Chapter 1

---

## Introduction, Study Aim and Objectives





# **Chapter 1**

## **Introduction**

### **1.1. Scientific Rationale**

A greater understating of the reservoir anatomy and its deep-seated control on fluid flow network helps to increase the level of assessment of the so called reservoir architecture. It is basically dependent upon sophisticated knowledge of the depositional systems within the reservoir, which is represented by genetic relationships between facies and compartmentalisation. The knowledge of reservoir architecture will dynamically enhance recoverable hydrocarbons that are hindered by intra-reservoir seals or surrounding subsurface from flowing to the borehole.

The construction of reservoir architecture is one of the most challenging and complicated works that relies on the reservoir model. The geological model represents a static model because it utilizes all known data such as sedimentological, clay mineralogy and petrophysical interpretations. Reservoir architecture uses the dynamic reservoir model which integrates reservoir fluids flow across the reservoir (Pápay, 2003).

The depositional system is responsible for the style of the heterogeneity which is connected to chemical and physical diagenetic processes. Hence diagenesis, intra-formational seals, barriers and compartmentalisation may significantly influence reservoir performance and behaviour. In addition, the pressure distribution framework within the reservoir rocks can be related to one or more of these factors.

The present study deals with the siliciclastic Zubair Formation, which is one of the most important and prolific reservoirs in the southern Iraq region (Buday, 1980). A significant source of uncertainty within the Zubair is the controls upon hydrodynamic pressure distributions (Liu et al., 2013). As the directional change of reservoir pressure (Hydrodynamic Feature) arises in most of the well-known giant oilfields in the Middle East region such as Mishrif reservoir in Iraq. In such reservoirs, the aquifer pressure has a directional trend which consequently leads to tilted oil water contact. While in the Zubair Formation in the Rumaila oilfield, the directional trend exists with no titled oil water contact. The scientific explanation of this phenomena is still under discussion (Liu et al., 2013). Therefore, the main aim of this study is to improve the understanding about the nature of pressure distribution within the Zubair Formation. Once a comprehensive analysis of the flow regime, flow direction and other related components have been mapped, the outcome can be a more detailed subsurface visualization to understand the orientation of the area to which hydrocarbons have been drained (Dahlberg, 1982).

Despite a lot of research on the Zubair Formation, no published or documented study has reported the effects of intgura-reservoir mineralization upon hydrocarbon production.

## **1.2. Study Aims and Objectives**

Previous studies done on the lower Cretaceous Zubair Formation were mainly focused on petrographic, stratigraphic and sedimentological relationships on a large scale. What is not yet understood is the influence of mineralisation-related flow heterogeneity within the Zubair in both large and small scales. The aim of this study is to reduce the uncertainty in our understanding of pressure distribution by providing a more detailed

knowledge of mineralisation-related flow heterogeneity using X-ray computed tomography, Scanning Electron Microscopy (SEM) and Energy Dispersive Spectrometry (EDS) analysis .

In order to achieve this PhD aim, a set of objectives were made as follows:

1. To examine the impact of clay mineralogy on the Zubair Formation, by providing a more detailed knowledge of type and distribution and diagenetic evolution of the clay minerals.
2. To characterise the reservoir units, investigating permeability and porosity relationships within each depositional facies.
3. To characterise mineralisation within the Zubair Formation by using X-ray CT imaging. In this study, volume images of representative samples of the mineralized Zubair sandstones obtained using X-ray computed tomography are to be used as the basis for computational fluid dynamical (CFD) modelling. Three phase segmentation will enable the pore space, quartz matrix and in-situ pyrite to be isolated from the volume images, enabling mineralized and unmineralized mesh based representations of the samples to be generated.

### **1.3. Database, Data Quality and Constraints**

This PhD study is largely based on the available core data collected from Iraqi South Oil Company with inadequate coverage for each of the six study wells. It is worth mentioning that pure core curation has limited the amount of core data. Other data included some internal technical reports and unpublished studies. The work is based on the following data:

- a total of 448.89 m of core across the available intervals of the Zubair in the study wells (Table 1.1).
- final geolical reports
- available well logs of variable format i.e. LAS, TIF, ASCII, and PDF for the well listed in table (1.2).
- location map of the Rumaila Oilfield (Figure 1.1).
- Formation tops within the studied wells and surrounding wells.
- Technical reports (laboratory core analyses).
- Unpublished geological studies and reports.
- Digital photography of core data of each of the six wells.
- XRD and SEM samples collected from the study wells (Table 1.3).
- X-ray miro CT iamges of 8 samples collected from 6 wells (Table 1.4).

Table 1.1: Core data collected from the Rumaila field, Zubair Formation.

Well alias	Core No.	Core top	Core base	Net thick. ( m )	Formation
A	C.1	3160	3167.9	7.9	ZUBAIR
	C.2	3178.88	3192.3	13.42	ZUBAIR
	C.3	3196	3210.6	14.6	ZUBAIR
	C.4	3212	3224.4	12.4	ZUBAIR
	C.5	3230	3242.1	12.1	ZUBAIR
	C.6	3243	3267	24	ZUBAIR
	C.7	3261.3	3279	17.7	ZUBAIR
	C.8	3279	3285	6	ZUBAIR
B	C.1	3202	3219.4	17.4	ZUBAIR
	C.2	3221.5	3239.5	18	ZUBAIR
	C.3	3239.5	3256.5	17	ZUBAIR
C	C.1	3162.18	3171	8.82	ZUBAIR
	C.2	3174.35	3186.17	11.82	ZUBAIR
	C.3	3189.5	3207.75	18.25	ZUBAIR
	C.4	3208.5	3208.65	0.15	ZUBAIR
	C.5	3209	3214.5	5.5	ZUBAIR
	C.6	3216.6	3230.56	13.96	ZUBAIR
	C.7	3233.6	3251.3	17.7	ZUBAIR
	C.8	3251.56	3265.32	13.76	ZUBAIR
	C.9	3269.5	3286.53	17.03	ZUBAIR
D	C.9	3084	3099.63	15.63	ZUBAIR
	C.10	3100	3116	16	ZUBAIR
	C.11	3116	3120	4	ZUBAIR
	C.12	3120.12	3135.33	15.21	ZUBAIR
	C.13	3137.33	3146.26	8.93	ZUBAIR
F	C.1	3270	3282	12	ZUBAIR
	C.2	3283	3286.38	3.38	ZUBAIR
	C.3	3286.5	3298.9	12.4	ZUBAIR
	C.4	3298.9	3316.9	18	ZUBAIR
G	C.1	3145	3160	15	ZUBAIR
	C.2	3160	3175.7	15.7	ZUBAIR
	C.3	3178	3188.2	10.2	ZUBAIR
	C.4	3190.5	3207.5	17	ZUBAIR
	C.5	3208.5	3226.43	17.93	ZUBAIR

Table 1.2: Well aliases, well coordinates and available wireline log data.

Well alias	WGS84/UTM Zone38North		Depth (m)TVDSS	Depth RT (m)	Formation Top	Well logs
	Easting	Northing				
A	720558.09	3383386.44	-3145.77	3161.07	AB-Zubair	None
B	719552.77	3388636.32	-3109.13	3116.53	Upper Shale Member-Zubair	MLL, RHOB, Calliper, Neutron, GR,S, SP.
C	725560.138	3392095.332999	-3058.770595	3065.969971	Upper Shale Member-Zubair	IND, SN,SP, GR, RHOB, Calliper, Neutron, DT, MLL
D	723558.848	3392098.619999	-2978.40	2986	Upper Shale Member-Zubair	DT, MLL, SN, SP,IND, RHOB, GR, Neutron, Calliper
F	719520.61	3399043.01	-3118.04	3125.19	Upper Shale Member-Zubair	None
G	729359.139054	3338853.893998	-3064.069611	3126.77002	Upper Shale Member-Zubair	None

Table 1.3: Number and depth of XRD and SEM samples collected from the study wells.

Well A		Well B		Well C		Well name D		Well name G	
No.	Depth	No.	Depth (m)	No.	Depth (m)	No.	Depth (m)	No.	Depth (m)
1	3161.5	1	3287.5	1	3193	1	3090	1	3226.35
2	3200	2	3286	2	3199.75	2	3167	2	3225
3	3163.5	3	3285.5	3	3182.51	3	3131.7	3	3222.5
4	3201	4	3284.5	4	3279	4	3178	4	3218.5
5	3162.5	5	3283.5	5	3226	5	3169.5	5	3216.5
6	3188	6	3282.5	6	3219	6	3159	6	3208
7	3195.5	7	3281	7	3179	7	3187.5	7	3206.5
8	3164.5	8	3279.5	8	3231.75	8	3173	8	3205
9	3276.5	9	3277	9	3245.55	9	3188.5	9	3203
10	3232.95 sand contact	10	3274.5	10	3241.56	10	3140.8	10	3201.5
10`	3232.95 shale contact	11	3273	11	3213.73	11	3184.5	11	3195
11	3238	12	3271.5	12	3194.75	12	3166 sand contact	12	3185
12	3239.9	13	3270.5	13	3260	13	3119.4	13	3170.8
13	3240.88 sand contact	14	3269	14	3220.39	14	3160.75	14	3161.5
13`	3240.88 shale contact	15	3268.5	15	3200.48	15	3175	15	3156.9
14	3164.5	16	3266	<b>Well Name F</b>		16	3177		
15	3245.27	17	3263.5	<b>No.</b>	<b>Depth (m)</b>	17	3091.3		
16	3246.23 sand contact	18	3260.5	1	3293.5	18	3166 shale contact		
16`	3246.23 shale contact	19	3255.5	2	3294	19	3115.5		
17	3249	20	3251	3	3298.5	20	3168		
18	3256.1	21	3246.5	4	3298.9	21	3143		
19	3254.2	22	3238	5	3300.9	22	3189.5		
20	3269.19 snad contact	23	3233.5	6	3303	23	3170.5		
20`	3269.19 shale contact	24	3230.5	7	3306	24	3106.5		
		25	3226.5	8	3307	25	3113.3		
		26	3222.5	9	3311.9	26	3127.1		
		27	3218.5	10	3313	27	3154		
		28	3207	11	3313.9	28	3089.5		
		29	3205	12	3315	29	3134.53		
		30	3201.98	13	3316	30	3188.5		



Table 1.4: X-ray Micro CT representative core samples collected from the study wells.

Well alias	Diameter (cm)	Depth(m)	Resolution (micron)	Facies Description
A	6mm	3269.19-3270.19	5 micron	Massive sandstone, beige, medium – fine grains, wavy lamination, with some amber fragments.
B	5mm	3205	5 micron	Shaly sandstone, fine–fine grain size with intercalation of very thin lamination of shale and sandstone, flaser bedding and burrows.
C	6mm	3210-3211	5 micron	
D1	8 cm	3160	10 micron	Massive sandstone with burrows +oil shows+ parallel lamination + medium grain size.
D1*	5 mm	3160	5 micron	Massive sandstone with burrows +oil shows+ parallel lamination + medium grain size.
F	6mm	3273-3274	5 micron	Rippled laminated sandstone, fine grains, oil impregnation, and carbonaceous material.
F*	6mm	3289.5-3290.50	5 micron	Massive sandstone with parallel lamination and burrows, oil impregnation and carbonaceous material.
G	6mm	3198.5	5 micron	Massive sandstone, medium –fine grains, with some coal deposits, wavy lamination.

## 1.4. Study Area

Rumiala field is situated in South East of Iraq, about 50 kilometer to the West of Basrah. This oilfield is one of the super giant fields in the world. The estimated reserve in the Rumiala is about 17 billion barrels of oil. Mohammed (2017, November 29) in his news article cited that the Rumaila field produces about 1.452 million barrels per day. The Rumaila encompasses one main fold, which comprises three domes, that extend from Kuwaiti border at the southern region, to Alhammar marsh land towards north.

These three domes are; South Rumaila, North Rumaila and West Qurna respectively. All together, they comprise an oil structure, which extends over 100 kilometer in length and 15 kilometer wide (Alsakiny, 1992). (Figure 1.1) shows structure contour map of the Zubair Formation in the Rumaila field and the location of this oilfield on Iraq map. This map is based on Top AB (First sub unit of the Upper Sandstone Member), or so called the Main Pay.

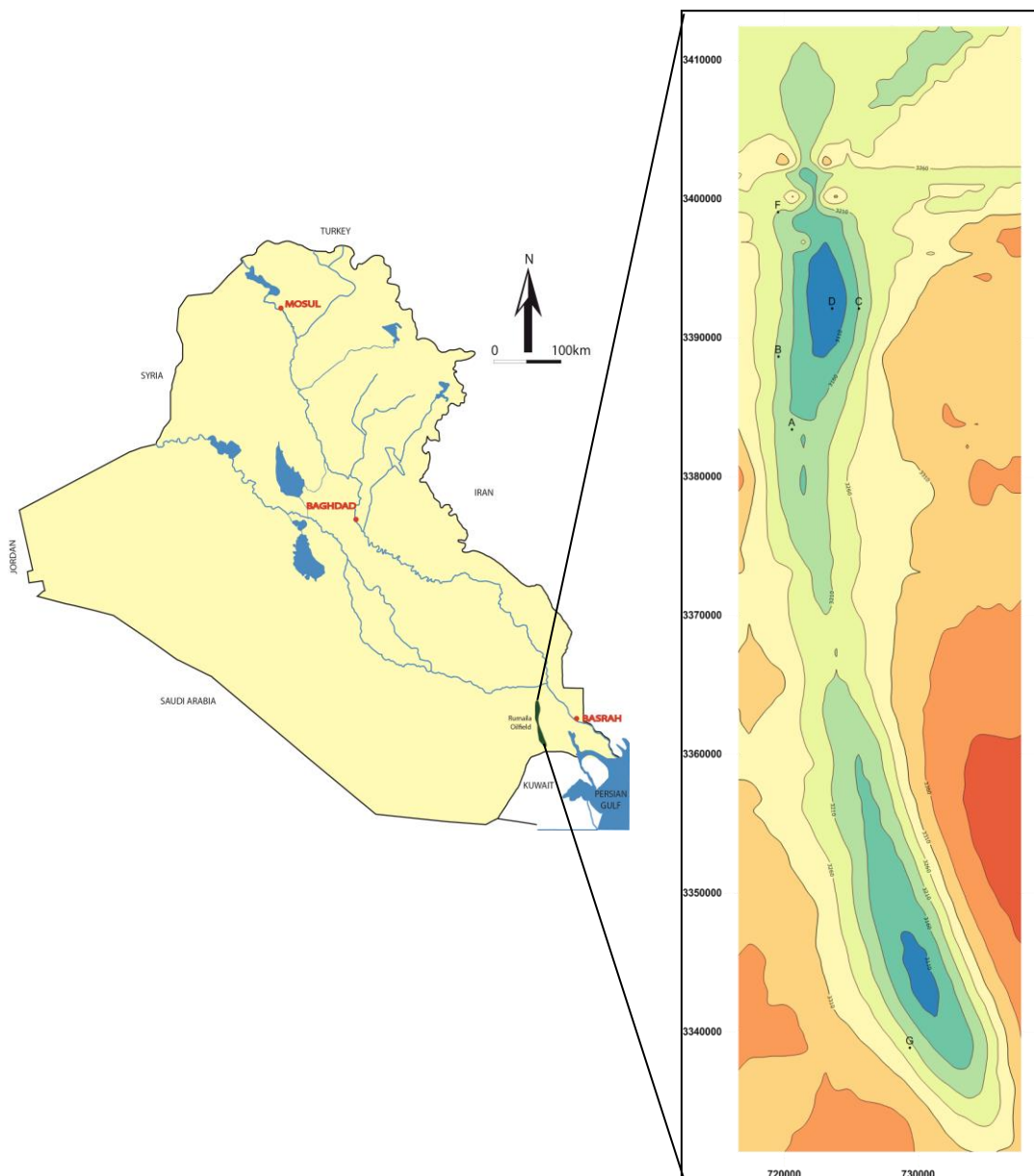


Figure 1.1: Structure contour map of Unit AB of Main Pay of the Zubair Formation. The study wells were given aliases in accordance with anonymity instruction required by Iraqi South Oil Company. Both of Iraq and Rumaila maps were drawn by Haitham AL-Ziayyir.

# Chapter 2

---

## Geologic Setting and Background Literature

## 2.1. Geologic Setting

Iraq is situated in the north east corner of the Arabian Plate. A significant disparity can be clearly observed in the geography of Iraq whereas in the west, arid land (Western desert) and the rough mountains of Zagros and Taurus in the North East (Jassim and Goff, 2006). The study area is located within the Mesopotamian Zone which is part of the Stable Shelf. The Tigris and Euphrates rivers are encompassed in this zone. Quaternary sediments cover a great portion of the Mesopotamian Zone except its northern and eastern parts (Fouad, 2010). The recent Mesopotamia Zone disseminates from Syria to the Hormuz salts (Figure 2.1). The Mesopotamia Zone comprises of terrestrial and marine ambits. Terrestrial ambit covers parts of NE Syria, Iraq, parts of Kuwait and coastal plain of Iran. While marine ambit covers the Arabian Gulf basin (Berberian, 1995; Alsharhan and Nairn, 1997; Brew, 2001; Sharland et al., 2001; Alavi, 2004 and Fouad and Nasir, 2009 cited in (Fouad, 2010).

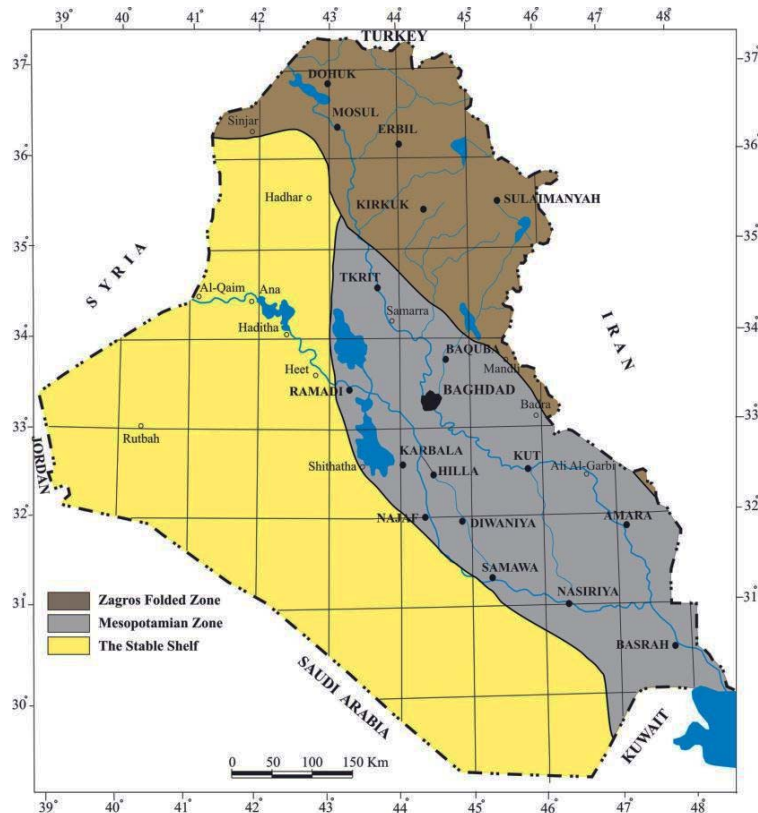


Figure 2.1: Mesopotamian Zone of Iraq, after (Buday and Jassim 1984 and 1987; Al-Kadhimi et al., 1996 and Jassim and Goff 2006).

## **2.2. Tectonic and Structural Setting**

Paleostructural elements and current tectonic subdivisions are linked to petroleum geology as they have influenced on distribution of petroleum system elements; source rock, reservoir, and seals. Additionally, they have affected both of structural patterns and oil trap evolution (Aqrawi et al., 2010). The boundary between Iraq's two basic tectonic units which are the Arabian Shelf and Zagros Suture Zone was set by Henson (1951). He elucidated that the boundary extends along the eastern border of the Stable Shelf. There are two major units within the Arabian Shelf namely; the Stable shelf and the Unstable Shelf and the boundary between them are lied at the western boundary of the Mesopotamian Zone (Jassim and Goff, 2006). Structural elements of North–South trend are dominating the Stable Shelf units thoroughly. The Mesopotamian Zone in divided into three subzones; Zubair, Euphrates and Tigris subzone respectively. The study area is located within the Zubair Subzone. The tectonic division of Iraq has been a of a great interest for many researchers e.g.(Buday, 1980); (Buday and Jassim, 1987); (Jassim and Goff, 2006). Iraq can be categorized into three main tectonic areas: the Stable Shelf which contains large buried arches and antiforms. However no surface anticlines are found within it, the Unstable Shelf that contains surface anticlines, and the Zagros Suture area which encompass thrust sheets of radiolarian chert, and metamorphic and igneous rocks (Jassim and Goff, 2006). Each one of these main tectonic areas is tectonically subdivided into smaller areas. Tectonic movements of Paleozoic were led to the N-S trend in the Stable Shelf, whilst the trends of NW-SE or E-W in the Unstable Shelf and the Zagros Suture are related to Cretaceous-Recent Alpine orogenesis (Jassim and Goff, 2006). A group of indistinctive subsurface paleostructural elements are found in Iraq which characterizes by its fault systems which consist of five major transversal blocks bounded by major transverse faults

(Figure 2.2). The Nabitah System of N-S trend, the Najd System of NW-SE trend, and the NE-SW or E-W Transversal System; (Aqrabi et al., 2010). Jassim and Buday, 2006a as cited in Jassim and Goff; 2006) interpreted three major fault systems which trend NW-SW and the transversal fault systems. Buday (1987) identified five tectono-physiographic zones: three zones within the Unstable Shelf, and two zones within the Stable Shelf. These zones are bounded by major faults (Figure 2.3). Four zones comprise the Unstable Shelf divisions: The Foothill Zone, the high folded Zone, and the overlapped (Ora) Zone and Balambo-Tanjero Zone.

The five tectono-physiographic zones are follows:

- 1- Thrust Zone: this zone extends over North and NE border with Turkey and Iran.
- 2- The Folded Zone: mountain area in North and NE Iraq underlies within this zone.
- 3- The Mesopotamia Zone: where both Euphrates and Tigris rivers are encompassed in this zone.
- 4- The Salman Zone: this zone comprises paleohigh with shallow basement. It is located at the east of the Stable Shelf.
- 5- The Rutba –Jezira Zone: this zone lies within the Western Desert and belongs to Paleozoic.

Cretaceous plays encompass the largest and most prolific oil province within the Mesopotamian Zone (Aqrabi, Goff et al., 2010). Mesopotamian Zone is subdivided into three subzones: Zubair, Euphrates and Tigris as illustrated on tectonic map of Iraq (Buday and Jassim, 1987) (Figure 2.4).

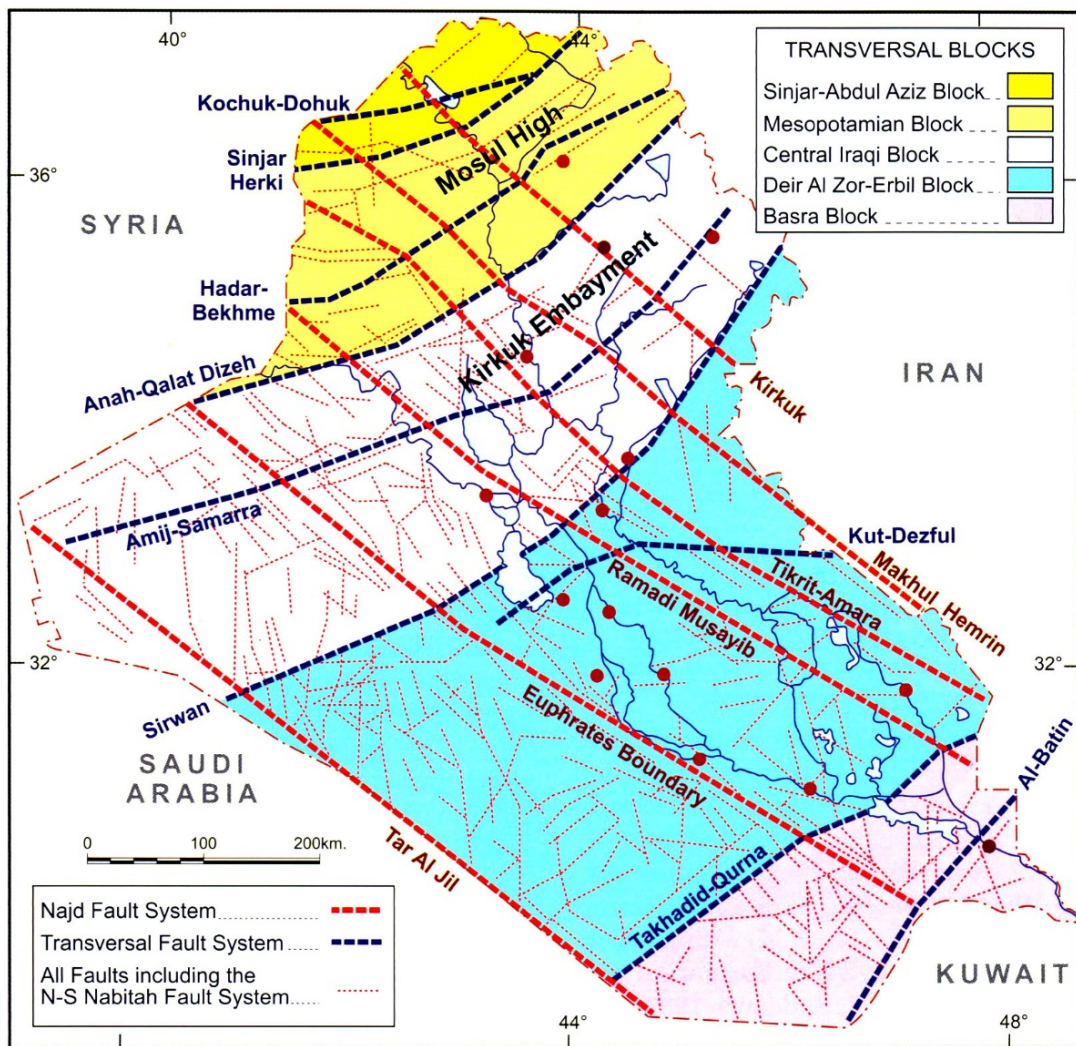


Figure 2.2: A map shows the distribution of fault and fault system in Iraq after (Jassim and Goff, 2006)

The Tigris and Euphrates Quaternary fluvio-eolian deposits and southern Mesopotamian lacustrine sediments cover the surface of the Mesopotamian Zone (Fox and Ahlbrandt, 2002 cited in (Almutury and Al-Asadi 2008).

Episodic sedimentation and structural development occurred during Mesozoic and Middle Tertiary have led to forming of the Mesopotamian Passive Margin (Almutury and Al-Asadi 2008).

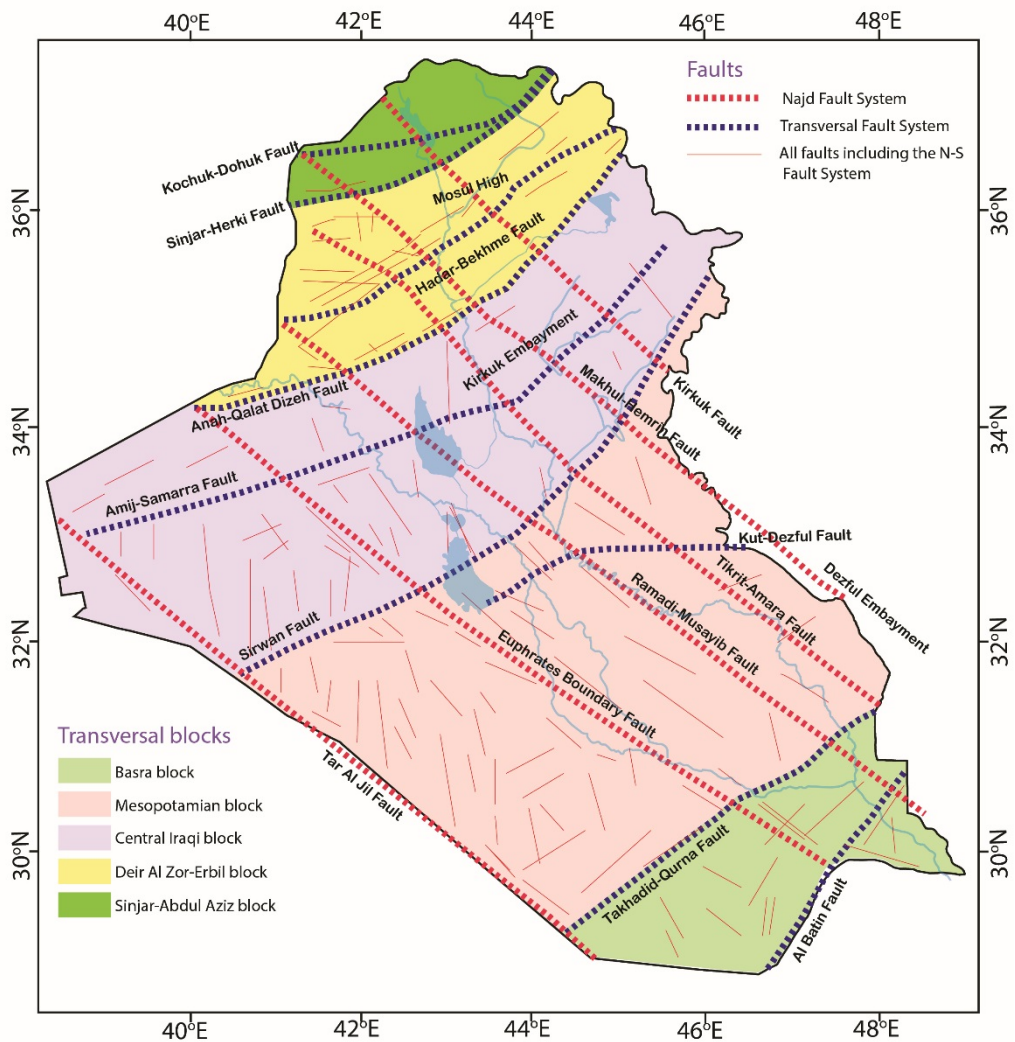


Figure 2.3: A map shows transversal blocks in Iraq modified after (Jassim and Goff, 2006).

The Tigris and Euphrates Quaternary fluvio-eolian deposits and southern Mesopotamian lacustrine sediments cover the surface of the Mesopotamian Zone (Fox and Ahlbrandt, 2002 cited in Almutury and Al-Asadi 2008).

Episodic sedimentation and structural development occurred during Mesozoic and Middle Tertiary have led to the formation of the Mesopotamian Passive Margin (Almutury and Al-Asadi 2008).

According to Jassim and Goff (2006) the Mesopotamia Zone can be subdivided into three subzones: the Zubair Subzone in the southern Iraq region of N-S trending structure



in the south, Euphrates Subzone in the west, and Tigris Subzone at the northeast most with NW-SE direction structures.

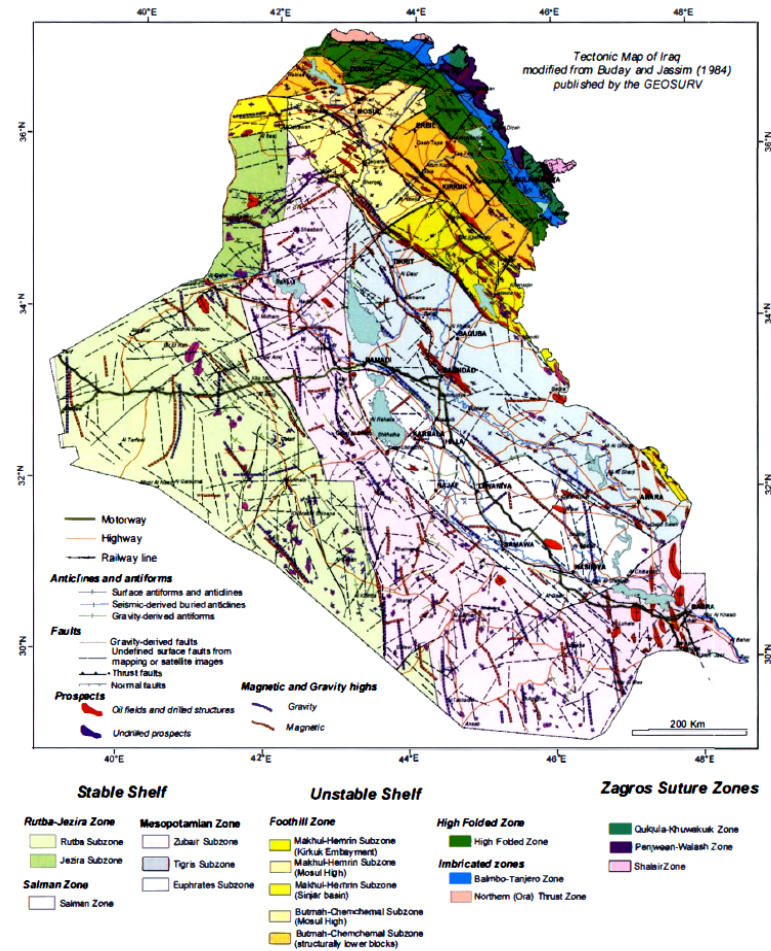


Figure 2.4: Tectonic map of Iraq modified from Buday and Jassim. Published by GEOSURV.

The study wells of the Rumaila field are located in the Zubair Subzone which is lined by a transversal fault called Takhadid-Qurna, whilst its southern boundary can either be found within the Albatin Fault or extending across transversal fault in Kuwait. The abundance of the N-S orientation structures of the Zubair subzone intensify with depth and reach 300 m depth at Lower Cretaceous level (Jassim and Goff, 2006). Southernmost unit of the Mesopotamian Zone is represented by the Zubair Subzone which is characterized by its constant structural pattern controlled by the lying beneath basement. Moreover, the N-S trending structures of this subzone were formed

during the Nabita Orogeny and reactivated during Permo- Carboniferous, Mesozoic and Tertiary time. Furthermore these structures extend a few hundreds of kilometres southward into Kuwait and E Saudi Arabia (Jassim and Goff, 2006).

It is worth mentioning that the Zubair and Rumaila comprise the most distinguished tight (narrow) elongated structures within Zubair Subzone (Jassim and Goff, 2006).

During ocean floor spreading in the Neo-Tethys, a large intra-shelf basin has witnessed the deposition of the Late Tithonian-Early Turonian megasequence (AP8). The Upper Tithonian–Aptian Thamama Group and the Albian-Lower Turonian Wasi’a Group are encompassed in this megasequence (Jassim and Goff, 2006). Two sequences are included within the Thamama Group: Late Tithonian-Hautervian Sequence and Barremian-Aptian Sequence. The onset of Barremian–Aptian sequence is marked by Zubair Formation (Salman and Mesopotamian zones) which was formed during the time of low stand followed by the high stand Shuaiba Formation (Jassim and Goff, 2006). Barremian-Aptian sequence includes set of facies as follows:

- 1) Clastic Inner Shelf facies (Zubair)
- 2) Carbonate Ramp facies (Shu’aiba) which extend along the Tikrit–Amara paleo-ridge in southern Iraq and the Qamchuqa Ridge in NE Iraq.
- 3) Outer Shelf Basin facies (Sarmord and Lower Balambo) within the high folded and Balambo-Tanjero zones, and the Kirkuk Emabayment of the Foothill zone of the Unstable Shelf.

The Barremian sediments include the Zubair Formation clastics and shales of Upper Ratwai Formation of the Stable Shelf which corresponds to the characteristics of delta/prodelta facies. The Zubair deltaic facies are engaged by the Ratawi shale in both upwards and westwards directions.

The lower Cretaceous Zubair Formation is one of the most important and prolific oil reservoirs in the southern Iraq region. The Zubair sandstones are originated from fluvio-deltaic, deltaic and marine environments (Aqrawi, Goff et al., 2010). The thickness of the formation ranges from 200-500m in the southern Iraq region (Figure 2.5).

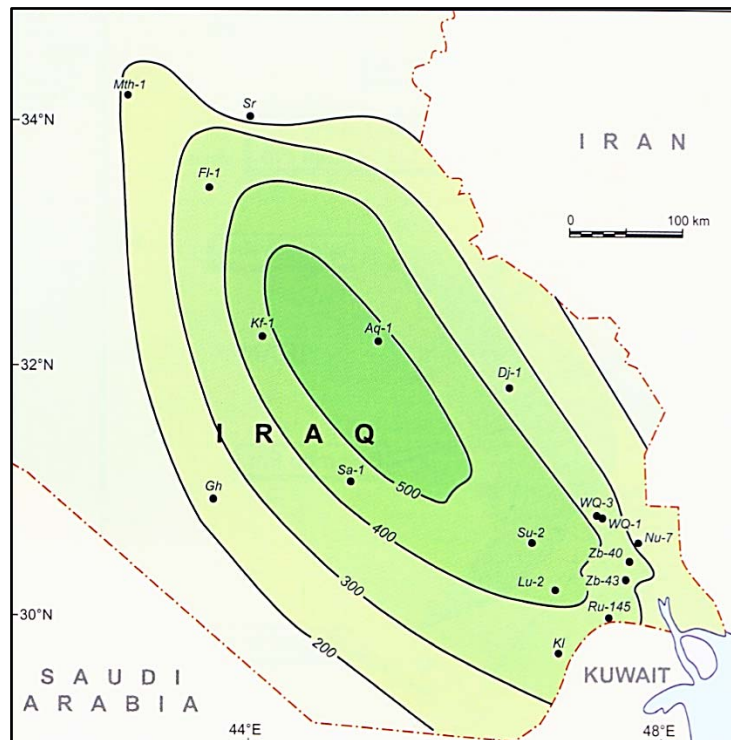


Figure 2.5: Isopach map of the Zubair Formation. After (Ali and Nasser, 1989). The minimum thickness of the Zubair Formation is 200m near Saudi Arabia at the SW of Iraq map. Whilst at the depocentre it becomes 500m thick (Aqrawi, et al., 2010)

The type locality of Zubair Formation is in the Zubair Field in the well Zb-24 (Figure 2.6). Within the Zubair Zone, the formation is divided into five members (Owen and Nasr, 1958, Van Bellen et al., 1959, Abbo and Safar, 1967). These five members are from top to bottom: the Upper Shale Member (Up.Sh.br), of 100m thick, the Upper Sandstone member (Up.S.St.br or Main Pay), the Middle Shale Member (Mid.Sh.br), the Lower Sandstone Member (L.SSt.br), and the Lower Shale Member (L.Sh.br).

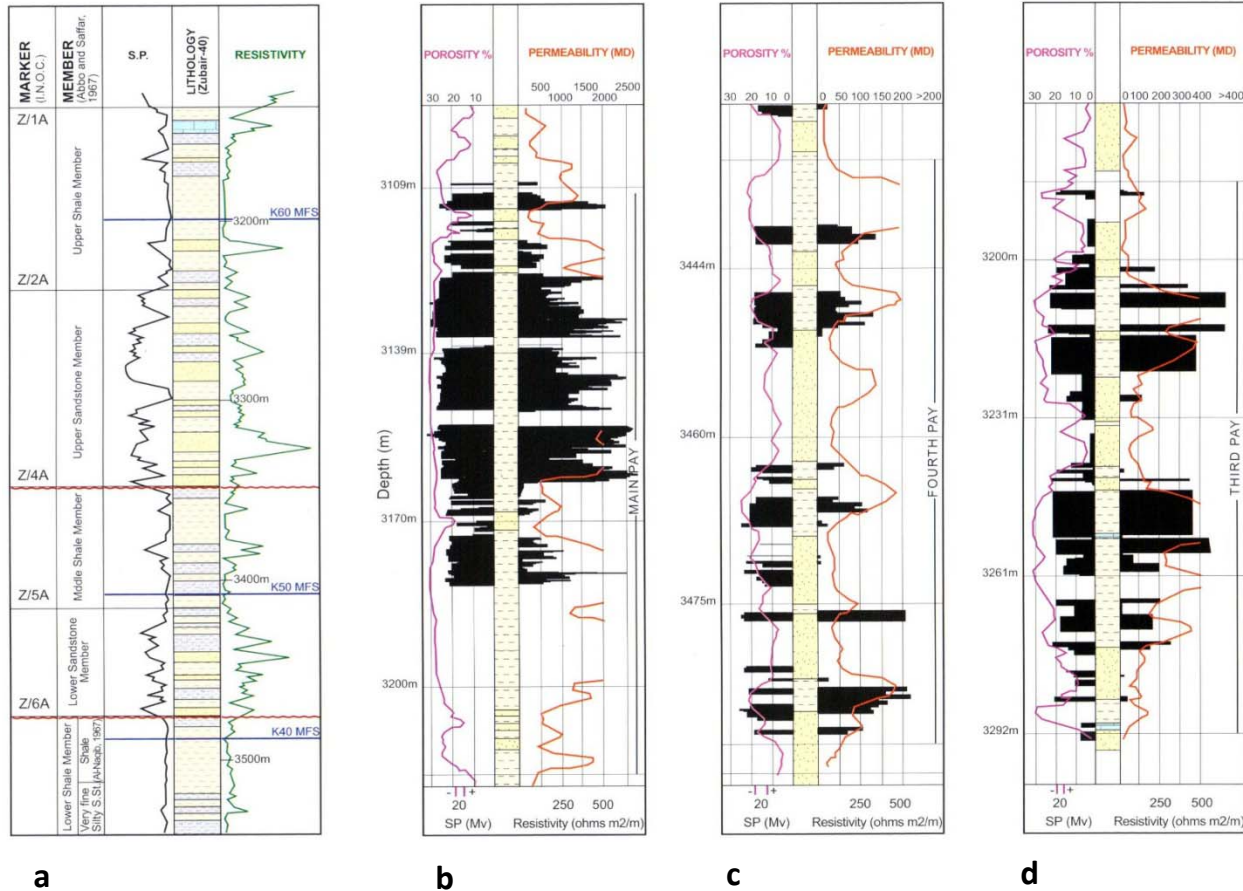


Figure 2.6: (a) Type locality of the Zubair Formation at well Zb-40. After (Van Bellen et al., 1959); (Abbo and Safar, 1967) and (Ali and Nasser, 1989) (b-d) a comparison of logs characters through the Zubair Formation in Rumaila and Zubair fields (b) logs patterns across the Zubair's Main Pay in the Rumaila Field (c) Logs characters through Fourth Pay of the Zubair Formation in Zubair Field (d) Third Pay logs patterns at the Zubair Field. From (Jassim and Al-Gailani, 2006) cited in (Aqrabi et al., 2010).

The Zubair Formation sand/shale ratio decreases towards the basin centre and nearly becomes pure shaly formation at the vicinity of Dujaila area. Whereas towards northeast and north in Makhul and Buzurgan areas the formation passes laterally into the limestone marl of Sarmord or Qamchuqa formations (Buday, 1980). Thickness of the Zubair Formation at the Rumaila field is between 380-390m (Jamil, 1978 cited in Aqrawi et al., 2010) The Zubair Formation sand/shale ratio decreases towards the basin centre and nearly becomes pure shaly formation at the vicinity of Dujaila area. Whereas towards northeast and north in Makhul and Buzurgan areas the formation passes laterally into the limestone marl of Sarmord or Qamchuqa formations (Buday, 1980). Thickness of the Zubair Formation at the Rumaila field is between 380-390m (Jamil, 1978 cited in Aqrawi, Goff et al., 2010). The upper contact of the Zubair is marked by shales. Carbonates of Shuaiba Formation bound the upper of contact of the Zubair, whilst the lower contact is marked by Ratawai Formation limestone (Buday, 1980). It is worth mentioning that many authors have agreed that both contacts of the Zubair are stratigraphically conformable (Figure2.7). Both age and lithological characteristics of the Zubair Formation are analogous to the Biyadh Formation of Saudi Arabia (Powers et al., 1966).

GEOLOGIC AGE		STRATIGRAPHIC UNIT	LITHOLOGY	MEGA-SEQUENCES
TERTIARY	PLIOCENE	Bakhtiari		AP 11
	MIOCENE	Lower Fars		
	OLIGOCENE	Palani / Kirkuk Group		
	EOCENE	Jaddala		AP 10
	PALEOCENE	Aaliji		
			Hiatus	
CRETACEOUS	LATE	Shiranish		AP 9
		Hartha		
	MIDDLE	Sa'di / Kometan		
		Tanuma		
		Khasib		
		Mishrif		
		Rumaila		
		Ahmadi		
	EARLY	Mauddud		
		Nahr Umr		
Shu'aiba				
Zubair				
Ratawi	AP 8			
Yamama				
LATE		Sulaiy	AP 7	
		Chia Gara		
		Gotnia		
MIDDLE		Najmah		
		Naokelekan		
EARLY		Sargelu	AP 6	
		Alan		
		Mus		
TRIASSIC	Adaiyah			
	Butmah			
	Kurra Chine			
MIDDLE	Geli Khana			
	Beduh			
EARLY	Mirga Mir			
	Hiatus			
PERMIAN	LATE	Chia Zairi	AP 5	
		Satina Evaporite		
	Chia Zairi			
	EARLY	Ga'ara		
CARBONIFEROUS		Harur / Ora	AP 4	
DEVONIAN		Pirispiki / Kaista	AP 3	
		Jauf Group		
EARLY SILURIAN		Akkas	AP 2	
CAMBRIAN-ORDOVICIAN		Khabour		
'INFRA-CAMBRIAN'			AP 1	
PRECAMBRIAN		Basement	Pre AP 1	

Figure 2.7: Stratigraphic column of Iraq, illustrating formations identified in each categorised mega sequence, their age and lithological character. Modified after (Aqrabi et al., 2010) modified after (Verma et al., 2004), after getting official permission of GeoArabia to publish megasequences after (Sharland et al., 2001).

## **2.3. Previous Work and Background Literature.**

This section covers two parts; the first part provides details on previous work done on the Zubair. And the second part explains concepts, theories, and background knowledge.

### **2.3.1. Previous Work**

A number of research and unpublished reports dealt with the Stratigraphy, reservoir properties, geochemistry, diagenesis and environmental tectonic setting of the studied formation as mentioned below:

#### **2.3.1.1. Lithology of the Zubair Formation**

-Lithologically, the lower cretaceous Zubair Formation which belongs to the Berriasian-Aptian sub-cycle. The Zubair formation consists of detrital clastics in the form of sand /shale succession (Buday, 1980).

-The first to describe the Zubair formation was Jones (1948), later both Naser and Hudson (1953) presented a modal definition of Zubair Formation represented by a type section of the well Zb-24 according to Bellen et al., (1959) cited in Buday (1980). Bellen et al., (1959) also estimated the total thickness of Zubair as ranging between 380 to 400 m.

-Bellen et al ., (1959) stated that the formation mainly consisted of a succession of sandstones and shale beds with a some silt deposits distributed in the form of five main subdivisions (members). Bellen et al., (1959) also mentioned that the total thickness of Zubair in the type section ranges between 380-400 m.

- Al-Fadel and Al-Ansari (1992) itemized the Stratigraphy of the Upper Sandstone member of the Zubair formation in which they subdivided it into nine strata of sandstone interbedded with three strata of shale.

-Petrography of the Upper Sandstone Member was studied by Ali and Nasser, (1989 ) cited in Al-Fadel and Al-Ansari (1992) who revealed that its framework mainly composed of : 95-99 % weakly cemented quartz grains, 0.2 % silica cement, 0.3 % carbonate cement and 0.1% iron oxides.

- Hasan (1988) concluded that the Upper shale member of Zubair Formation in South Rumaila field has an average thickness of 100 m and fundamentally consists of shale /sandstone alterations, silt and limestone. On one hand, she identified three main oil prolific units which namely are: 1F, 1L and 1MT and noticed that their petrophysical characteristics enhance significantly from north to south. She proposed that the depositional environment of 1F and 1L could be related to channel source, while 1MT is likely to be attributed to transgression and regression.

### **2.3.1.2. Depositional Environment**

Much of the greater part of the literature on the Zubair Formation depositional Environment comes from theses written in Arabic and unpublished internal reports and studies done by the South Oil Company S.O.C-Iraq.

Rohan (1975) identified the Zubair Formation environment as deltaic, which has comprises of cyclic depositional packages. He reveals that the deltaic environment of the Zubair Formation encompasses marine and fluvial sediments. Hence it is marine dominated delta.

The Zubair Formation was deposited in relatively shallow continental shelf, which is extended broadly as can be inferred from Ostracod faunas (Al-Fares et al., 1998).

-Abbo & Safer (1967 cited in Hmood, 2002) points out that the Zubair formation has the characteristics of deltaic depositional environment.



- Al-Siddiki 1978 cited in Hmood, 2002 and Al-Azzawi, 2012) suggests neritic to deltaic environment for the Zubair Formation. He is also estimated the assigned Aptian-Hautervian as of the Zubair Formation.

- Hakim and Hasan (1980) conclude that the Upper Shale Member of the Zubair Formation is a multi-layer reservoir. This conclusion is based on previous work on the same member which led to subdivide into seven sub units termed as: 1A, 1BD, 1E, 1F, 1GK, 1L & 1MT .They also suggest that the sandstones of both unit 1F and 1MT are primarily of a channel origin.

-In their study on the Zubair Formation Al-Fadhel and Al-Ansari (1992) an assessment of the depositional environment of the Upper sand stone member was made, holds the view that it is a result of the deposit pulling up within meandering distributary channels of a fluvial dominated delta.

-Along the same line, Al-Ameri and Batten,1997) in their palynological study on the Zubair Formation see that it was deposited in a subsiding deltaic environment which comprises favourable conditions to boost the preservation of the accumulated organic matter.

### **2.3.1.3. Clay Mineralogy**

-Ashoor (1990) used XRD technique to diagnose the clay mineralogy of the Upper Shale member of Zubair and to assess the effect and occurrence of clays on its petrophysical properties. He revealed that the dominant clay mineral which found in 1L, 1F, 1GK and 1MT is Kaolinite and ranges between (45%-100%) of the total clay content followed by a percentage ranges between (35%-45 %) of Chlorite and a small amount of smectite which is found in a percentage do not exceed 19% of the total clay content predominantly in 1L and 1MT.

#### **2.3.1.4. Reservoir and Petroleum Geochemistry**

In his analysis for bitumen accumulations within the Upper Sandstone Member of the Zubair Formation, Ali (1989) points out that reservoir bitumen found in North Rumaila and West Qurna fields is either solid or semi-solid. It can be either found dispersed finely throughout the pore system or centralised in a depth interval in the form of tar mat, likely creating fluid flow barrier. Similarly, well logs interpretation done by (Al-Fadel and Al-Ansari, 1992) asserts that tar mat (reservoir bitumen) is found within the Upper Sandstone Member. A low oil gravity of 29API has also been also identified in unit LN, and this low API may potentially hinder the aquifer support within some of its beds. Moreover, their study demonstrated that reservoir bitumen found in this member does not act like a complete barrier (i.e. impeding baffle). The may cause a small damage in reservoir properties of the Main Pay (Ali, 1989). Oil generated from the lower Cretaceous Zubair Formation and the Upper Jurassic oil is mixed up together. Hence stratigraphic and fold structural traps of the Zubair Formation have also prompted by these oils (Al-Ameri et al., 2011). Sulphur content in crude oils of the Lower Cretaceous reservoir in the southern Iraq region is high according to (Abeed et al., 2012).

#### **2.4. Petroleum System of the Zubair Formation**

A key study on the petroleum system of the Zuabir Formation was conducted by the Zubair Formation (Al-Ameri et al., 2011) in which a 1D petroleum system modelling was applied to the Zubair Formation. The Zubair Formation was deposited in subsiding deltaic sediment accumulations, which comprise convenient conditions that can preserve organic matter accumulations (Al-Ameri and Batten, 1997). Notably, an enrichment of the amorphous organic matter AOM was found in the Zubair, which could be related to oil prone source rock (Al-Azzawi, 2012; Idan, Faisal et al., 2015). Four palenofacies types were identified in a study on the Zubair Formation done by

(Al-Ameri and Batten, 1997). An abundance of the Amorphous Organic Matter AOM in two of these palenofacies is related to the thermal changes and biodegradation of the organic matter (Al-Ameri and Batten, 1997).

Idan, Faisal et al., (2015) point out that the Zubair Formation comprises a source rock of kerogen type II and III. The authors have also concluded that the Zubair Formation within the Zubair sub-zone is at the early peak oil window. Thus the sandstone members of the Zubair Formation encompass the high prospective, which is clued by the organic richness found within thin beds of the pro-deltaic shales (Idan et al., 2015). The Zubair Formation has poor-fair prospective source rock, since some oil could have been generated from these rocks (Al-Ameri et al., 2009). Porosity and permeability of the reservoir rocks are encompassed in the multi-story sand bodies. The porosity ranges between 18%-30 %, and permeability ranges between 100-1000md (Al-Azzawi, 2012).

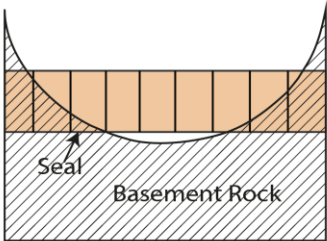
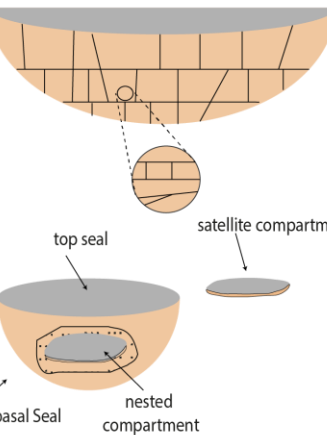
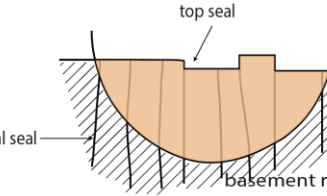
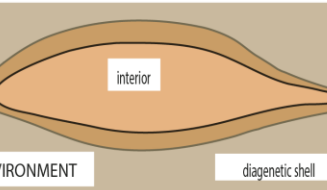

There is very little research on the seal efficiency of the Zubair Formation.

Previous studies on the Zubair Formation have not dealt with sealing efficiency of it. The only research on the sealing capacity has been carried out by (Al-Azzawi, 2102) in which he stated that both of the Zubair's Formation seal rocks at the upper and lower parts are efficient, as these seals comprise high mud content with low-extremely low permeability. However, this seal may not be extended continuously across the basin. The Zubair Formation's oil is innate since it was indicated by TOC and S1 relationship. This finding was confirmed by (Al-Azzawi, 2012, Idan et al., 2015).

## **2.5. Basin and Reservoir Seal and Compartmentalization**

In recent years there has been an increasing amount of research on the origin of seals and compartments at each of basin and reservoir scales (e.g. Smalley et al., 1995; Jolley et al., 2010; Smalley and Muggeridge, 2010; Dolson, 2016). A greater understanding of the reservoir anatomy and its deep-seated control on fluid flow network helps to increase the level of assessment of the so called reservoir architecture (e.g. Ramon and Cross, 1997, Pápay, 2003). It is basically dependent upon sophisticated knowledge of the depositional systems within the reservoir represented by genetic relations between facies and compartmentalisation. Thus knowledge of reservoir architecture will dynamically enhance recoverable hydrocarbons that are hindered by intra-reservoir seals or surrounding surfaces from flowing to the borehole. The depositional system is responsible for the style of the heterogeneity which is connected to chemical and physical diagenetic processes. Hence diagenesis, intra-formational seals, barriers and compartmentalisation may significantly influence reservoir performance and behaviour. In addition, the pressure distribution framework within the reservoir rocks can be related to one or more of these factors. The disequilibrium in rock compaction can lead to trapping fluid in compartments for a period of time. (Ortoleva, 1994a) defined compartment as a domain of rock which has a relatively good petrophysical properties (permeability and porosity) surrounded by a shell-like domain of rock of low permeability that the fluids within the compartment do not exchange perfectly with the environment for a period of geologic time (long period) and the surrounding shell-like domain represents the seal. In their unpublished manuscript (Powley and Bradly cited in Ortoleva, 1994b) showed that the sedimentary basin can be divided into box-work areas and each one of them is hydraulically isolated from its ambient by seals. These box-work compartments are as illustrated in (Table 2.1).

Table 2.1: Compartmentation types according to (Ortoleva, 1994a).

Compartment Type	Description	Illustration
Compartment boxwork	according to (Ortoleva, 1994)" the basin can be divided into a boxwork of compartments separated by seals". this boxwork can be extended into basement rock.	
Nested compartments	compartments can be occupied in compartments and the spatial scale of this nesting ranges from supra-kilometer to the sub-meter.	
Mega-compartment and its complex interior and satellites	A basin- scale compartment, which encompasses top seal and basal seal. Hierarchy of compartmentation can be existed within compartmentation. compartmentation may have inner compartments in the form of mega-compartment complex and may have satellite compartments.	
Columnar compartment	A domain which is relatively elongate that is similar to a compartment with no distinguishable bottom.	
Intra-stratum compartment	A compartment may dwell entirely within an individual sedimentary stratum. This type of compartmentation may exist when the stratum is bounded by low permeability strata or when a diagenetic process tend to bring about cementation growth or compaction near the surrounding of the stratum.	
Micro-compartment	Hydraulically isolated very thin layer which is entirely sitted within a individual stratum. This type of compartmentation may exist as a layered sequence.	

### 2.5.1. Definition of Seals

Based on (Hunt, 1990), the term seals “refers to a zone of rock capable of hydraulic sealing, that is preventing the flow of oil, gas, and water “

A pressure drop “depletion” with compartments fluids breakout is the result of seal fracturing and this fracturing can be attributed to both hydrocarbon generation within compartment, and pore fluid caused by thermal expansion which ultimately lead to an upward hydrocarbon vertical movement and eventually accumulate in a trap. Seals can be classified on the basis of spatial relationship to compartmentalization and they could bind compartments from top and basal or bounding the compartment sides laterally or vertically (Ortoleva, 1994b). Seals can categorised as shown in table (2.2)

Table 2.2: the table below summarises seal types according to their spatial relationship to the compartment (Ortoleva, 1994b).

Seal Type	Description	Example
Stratigraphic seals	An individual lithologic unit that has been cemented or compacted due to its indigenous texture and chemistry.	Shale and anhydrite beds
Diagenetically banded seals	Internally layered structure seals. That has evolved through diagenesis. This type of seal occurs horizontally. Additionally can be found as vertical seal (diagenetically banded).	Horizontal seal which lies entirely within a single stratum
Repetitive banded seals	A group of alternations which are involved in seal banding. These alternations are of the same textural repetition unit.	-Roughly regular spaced arrays of stylolite, dissolution seams. -Alternation of augmented compaction and porosity band with bands of highly cemented rocks.
Precipitated seals	This type of seal resulted from the precipitation of cements. As this cementing material may have filled occupied pores or fracture or could have replaced the indigenous structure.	Carbonate bands in sandstones

Gradational seals	Seals of gradual textural changes resulting in very low- permeability domains.	Chalk lithology
Fault s associated seals	The fault may comprise or encompass the seal.	Seals in faults
Free vertical seals	This type of seal has formed with the absence of faults.	

# Chapter 3

---

## Methodology and Analytical Techniques





## **Chapter 3**

This chapter describes methods used to reduce the uncertainty within the Zubair Formation related to the controls upon hydrodynamic pressure distributions. Methods used in this study are aimed to identify clay minerals, grain size measurement, petrophysical properties, and detailed knowledge about mineralisation related flow heterogeneity using X-ray micro imaging.

### **3. Methodology**

In order to achieve the study aim, integrated studies were done using a combination of traditional core data collection, portable microscopy, Scanning Electron Microscope (SEM), Energy Dispersive Spectrum (EDS), and X-ray Computed Tomography. The analytical techniques have been applied to core samples collected from selected wells of the Rumaila field, southern Iraq. The poor curation of historical core data of the Zubair and limited core recovery were big challenges associated with this work. Figure 3.1 illustrates the different levels of analysis applied core studies done to the Zubair Formation.

#### **3.1. Core–Log Sampling**

Core samples were collected from the available core data at Iraqi South Oil Company. It is worth mentioning that log-core depth correction has been applied to the study wells prior to start sampling and routine core description. Collected core data was taken from sandstone/shale contacts and sandstones.

#### **3.2. Systematic Core Description**

A routine standardised approach of core's physical description was performed on the available cored interval of the Zubair Formation as follows:

- Written documentation: this part of work included making notes on a number of lithological observations such as colour, mineral content, oil shows, sedimentary structures, thickness of cored intervals and biological activity and fossil content.
- Visual estimation of grain size in the field, and sedimentary structures to be used in the identification of depositional environments.

Systematic core description was performed in South Oil Company’s Core Workshop located in Nahran Omar near the city of Basra about 340 miles (550km) southeast of the Iraqi capital, Baghdad (Figure 3.1),(Figure 3.2).



Figure 3.1: Systematic core descriptions in Core workshop at S.O.C, Iraq. Log-core depth calibration were applied to the cored intervals prior to start sampling and core visual core description



Figure 3.2: Photograph of representative lithofacies about 3.3 meters. Each one of these core trays contains 1 meter of the cored samples taken from the Zubair. The red arrow refers to the direction of drilling.

### **3.3. Core Photography**

Core photography was produced to the study wells in order to capture some important features like sedimentary structures, colour, oil shows, lithological features, bioturbation, and bio-organism activity. As these features comprise part of the routine used in facies classification. Furthermore, a detailed examination and photography were performed on the cores samples by using a mobile microscope to acquire more details about these samples such as grain size, and visual description related to mineralization bands, clays, and grain morphology. The mobile microscope used in this study comes with 5 mega pixel of resolution and 200X (500 X by digital) magnification. The acquired photos were measured using specialized software comes with the microscope (Figure 3.3).

### **3.4. Analytical Methods**

Reservoir performance and its characteristics are related to the level of heterogeneity and distribution of these heterogeneities. Analytical methods used in this study were aimed to improve the understating of hydrodynamic pressure distribution within the Zubair. These methods include the following:

#### **3.4.1. Scanning Electron Microscope (SEM)**

Polished carbon coated chips were collected from Rumaila South and North fields. These samples were examined under FEI XL30 ESEM-FEG Environmental Scanning Electron Microscope (Figure 3.4). The SEM examination is suited for a number of observations that enable the identification of clay minerals and these observations include studying distribution, texture and morphology of particle arrangements, and fabric of clay minerals (Figure 3.5). Furthermore, qualitative and partly-quantitative analyses were done by using Energy Dispersive X-ray (EDX) spectra (Figure 3.6).

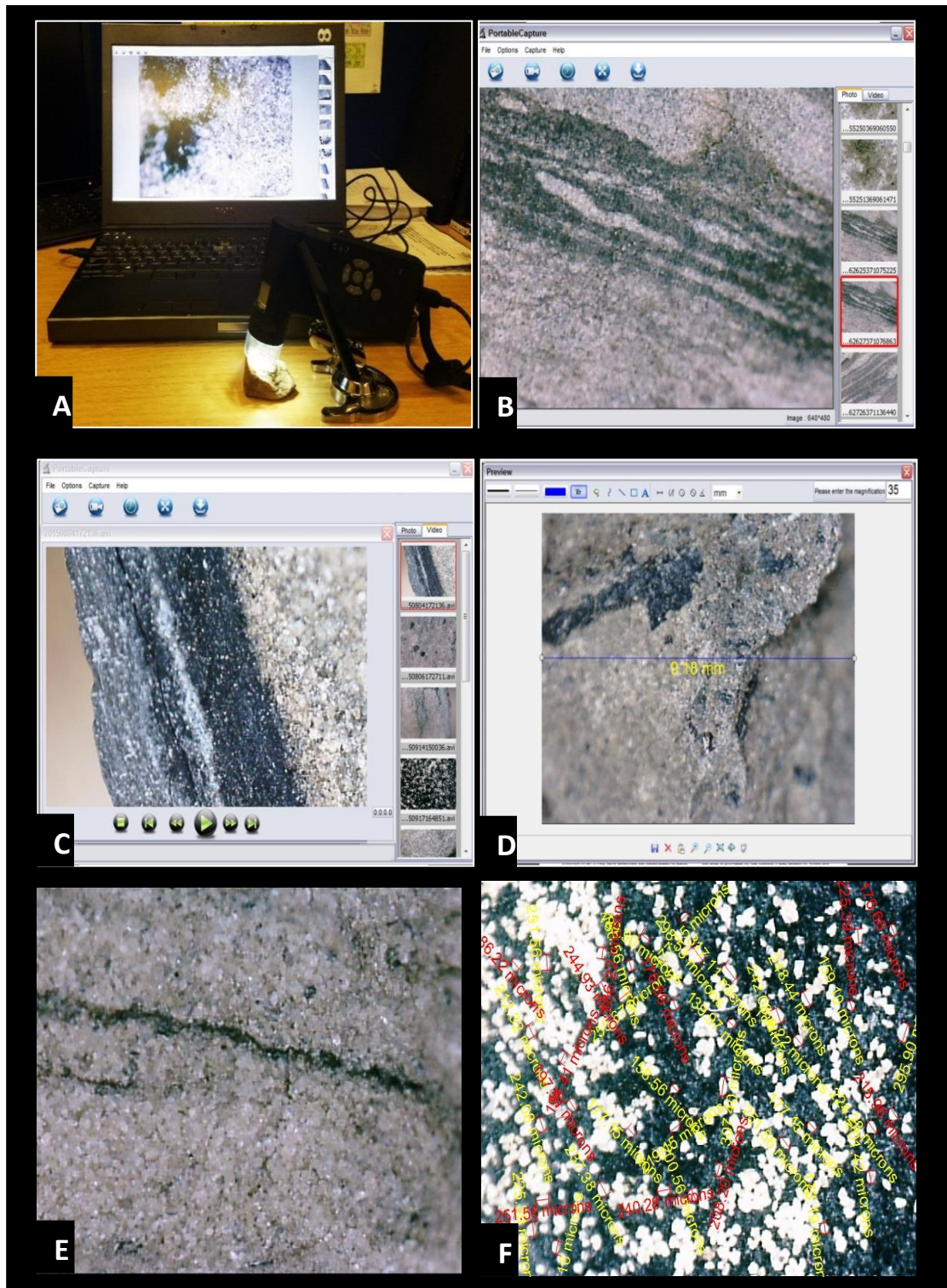


Figure 3.3: (A) a mobile microscope connected to the computer the microscope magnification is up to 500X with 5 MP resolution (B) 35X magnified image of sandstone chip sample taken from the Zubair core (C) picture shows a capture of video recording of sandstone sample (D) measuring tool used for measuring dimensions, like grain diameter, distance between two points (E) An image of a core sample shows magnified details (F) grain size analysis, the diameter of each grain is measured by using the ruler tool in this software.



Figure 3.4: Environmental Scanning Electron Microscope FEI XL30 ESEM -FEG located in School of Earth and Environmental Sciences, The University of Manchester. This microscope is designed to work on Hi and Low VAC.

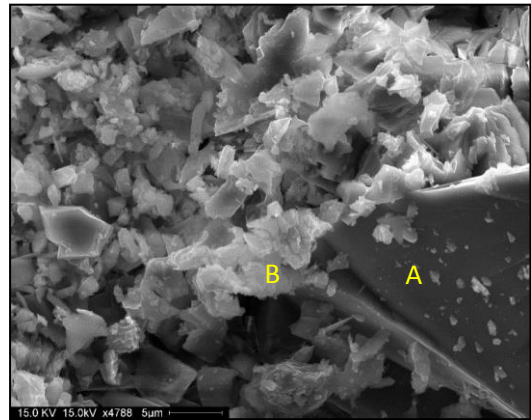


Figure 3.5: SEM image from Well D. shows morphological and textural observations A) quartz grain with silica overgrowth B) pore lining kaolinite. This image was taken under HI VAC, intensity 15.0KV, magnification: X4788, and the scale is 5micron.

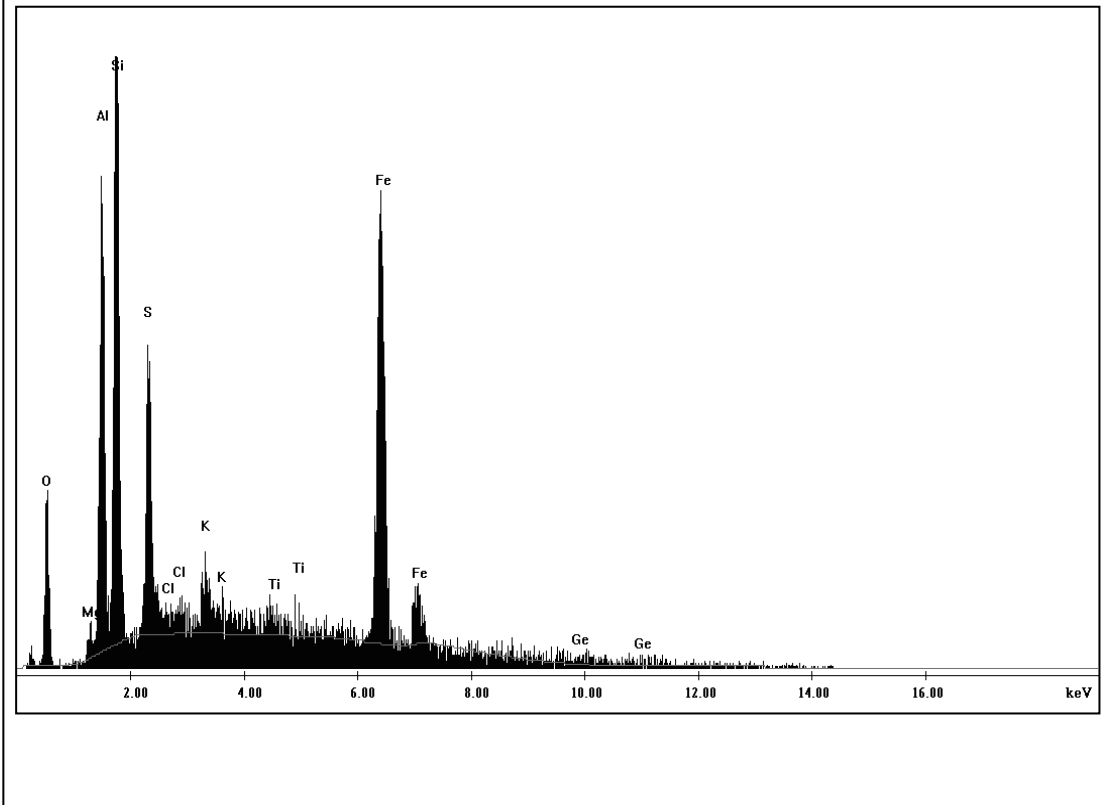


Figure 3.6: Energy Dispersive X-Ray spectrum (EDX) for the same sample taken from well D.

### **3.4.2. X-ray diffraction XRD Samples Preparation**

In order to identify clay mineralogy, the clay fraction which is  $< 2\mu$  needs to be separated from the samples. Clay fraction separation technique used by the United States Geological Survey USGS was applied to the collected samples from the Zubair Formation (Poppe et al., 2001). The method used in this study for clay fraction separation is reliable and accurate. Hence many researchers used it for the same purpose (e.g. Ashmawy et al., 2002; Jin et al., 2010). Further analysis was carried out by using X-ray diffraction that aimed to collect XRD spectra for the clay fraction separated from these samples. This analysis encompasses a series of preparation and treatment procedural work applied to the clay fraction of the samples collected from the Zubair sandstones and from Sand/shale contacts. The clay fraction samples were subjected to three phase analysis according to (Moore and Reynolds, 1989, Moore and Reynolds, 1997). Before starting the clay fraction separation procedure, grinding of rock samples was carried out using an agate mortar and pestle; additional sample grinding was performed using ball mills on a very low percussion speed and short time in order not to destroy the clay minerals content within the sample. The milled samples were put through sieve of 250 micron mesh size to get rid of any lumps and unwanted particle sizes.

#### **3.4.2.1 XRD Specimen's Preparation and Treatment**

This paragraph explains pre-analysis treatments are required to remove the organic materials, carbonates from the sediment samples, and the gravity settling of particle in a suspension (decantation) (Poppe et al., 2001). The resulted clay fraction samples were subjected to further treatments followed by analysing them by using XRD Bruker D8 Advance diffractometer located in the School of Earth and Environmental Sciences at the University of Manchester (Figure 3.7).

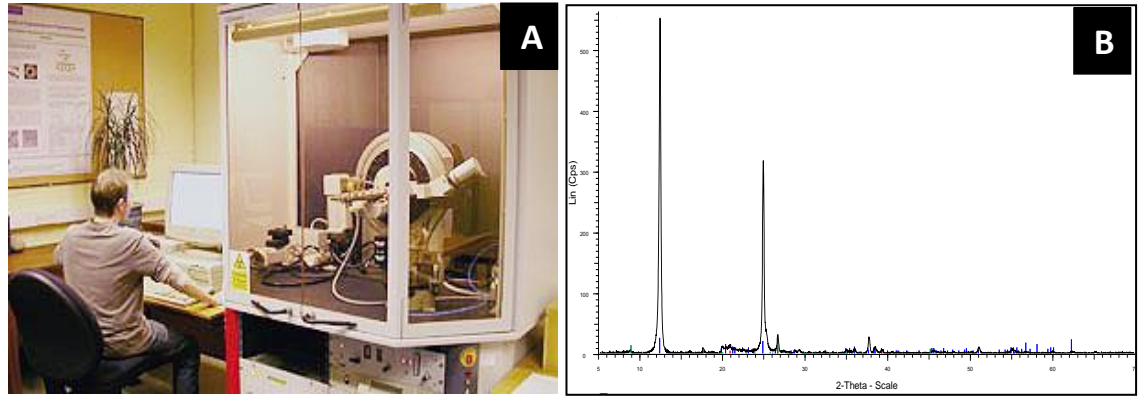


Figure 3.7: (A) XRD Bruker D8Advance diffractometer located in the School of Earth and Environmental Sciences at the University Of Manchester. (B) XRD spectra generated by X-ray diffractometer.

### 3.4.2.1.1 Procedure for the removal of carbonates by acetic acid treatment

In some sediment, carbonates can affect the clay minerals identification. Removal of these carbonates from them sediment specimens is an important step, done by treating samples with acetic acid to dissolve carbonates. Using dilute acetic acid is less likely to destroy clay Crystallinity. Prior to the start of the digestion of carbonates with acetic acid, a diluted solution was prepared by pouring 1 part of acetic acid into a graduated cylinder, then adding 4 parts of deionized water and mixed carefully (Figure 3.8). The molarity of the concentrated glacial acetic acid is 17.5 Molar.

In order to perform this procedure the following apparatus are required:

- 50-75 ml glass beakers.
- Glass rod to stir samples.
- Acetic acid solution
- Graduated cylinder to measure solutions
- Deionized water
- Marker pen



- Pipette

The acetic acid treatment was carried out as follows:

1. In a glass beaker 50-75 ml of dilute acetic acid solution was added to 25 g of the powdered sample. Acetic acid was added slowly and carefully in order to avoid overflowing of the beaker.
2. Another 50-75 ml of dilute acetic acid was added gradually until ebullition was subsided.
3. A glass rod was used to stir the contents of the beaker (attention is required to make sure that the glass rod is clean and washed with deionized water)
4. The beaker was left to stand for overnight (acid digestion).
5. The acid digestion was repeated until no further ebullition occurred.
6. The supernatant liquid was poured off by siphon then the samples were washed by centrifuging.
7. The collected supernatant liquid was disposed in accordance with safety regulations (Figure 3.9).



Figure 3.8: Photo shows materials required for carbonates removal with acetic acid. And these materials include: glacial acetic acid, distilled water, glass graduated cylinder, glass rod, 250-500 ml glass beakers, pipette, and siphon (Poppe et al., 2001).



Figure 3.9: Photo shows disposal method for acid waste (Poppe et al., 2001).

#### **3.4.2.1.2. Procedure for Organic Matter Removal with Hydrogen Peroxide**

In spectrometry analysis, organic matter can cause a broad hump on the X-ray diffraction patterns; hence the treatment of sediments with hydrogen peroxide ( $H_2O_2$ ) is required to remove unwanted organic matter. Degradation of organic matter by hydrogen peroxide, however, may work as an oxidizing agent leading to the partial leaching of metals from the sample.

The treatment was applied using the following steps

1. A diluted solution of 3% from  $H_2O_2$  was prepared with a grade 30%.
2. 50-100 ml of 3% dilute solution of hydrogen peroxide was added to each one of the beaker contained samples.
3. The bubbling was started after  $H_2O_2$  was added.
4. The particles of the solution were suspended by stirring with a glass rod.
5. After the froth was subsided, another 50-100 ml of dilute hydrogen peroxide was added.
6. Degradation of organic matter was completed after the bubbling stopped after the addition of hydrogen peroxide. In practice, digestion of organic matter with hydrogen peroxide from sediments may take several days (Mikutta et al., 2005).
7. The supernatant liquid was siphoned then disposed properly.

#### **3.4.2.1.3. Separation of Silt and Clay by Decantation**

Although this procedure is time consuming, it is crucial for the separation of silt and clay fractions. This part of the laboratory work was carried out on sediments after getting both carbonate and organic matter removed. In

order to perform this procedure the following apparatus are required (Figure 3.10a):

- Wide-mouth glass jars with lids.
- Measuring tape.
- Permanent marking pen.
- Sodium hexametaphosphate (dispersant).
- Distilled water.
- Thermometer.
- Water bath.
- Syringe
- Timer.

The procedure used for decantation was as follows:

1. Before worked was started, the glass jars were labelled with a 0-5 cm depth scale (Figure 3.10B).
2. Into each jar, the suspension to be separated was added.
3. The glass jars were filled to 5cm level with de-ionised water.
4. 2.5 g of sodium hexametaphosphate ( $\text{Na}_6\text{O}_{18}\text{P}_6$ ) was weighed and added to each sample (Figure 3.10C).
5. Suspension was homogenized by shaking sealed jars vigorously. Then was dispersed with a sonic probe (if available) for 15-20 seconds (Figure3.10D).
6. The temperature of the water bath was checked before jars submerged in it. The temperature was set to 20°C.

7. The glass jars were submerged one by one onto the water bath.
8. Starting time for each jar was recorded, and the timer was set according to the values in Table 3.1 (Figure 3.10E).

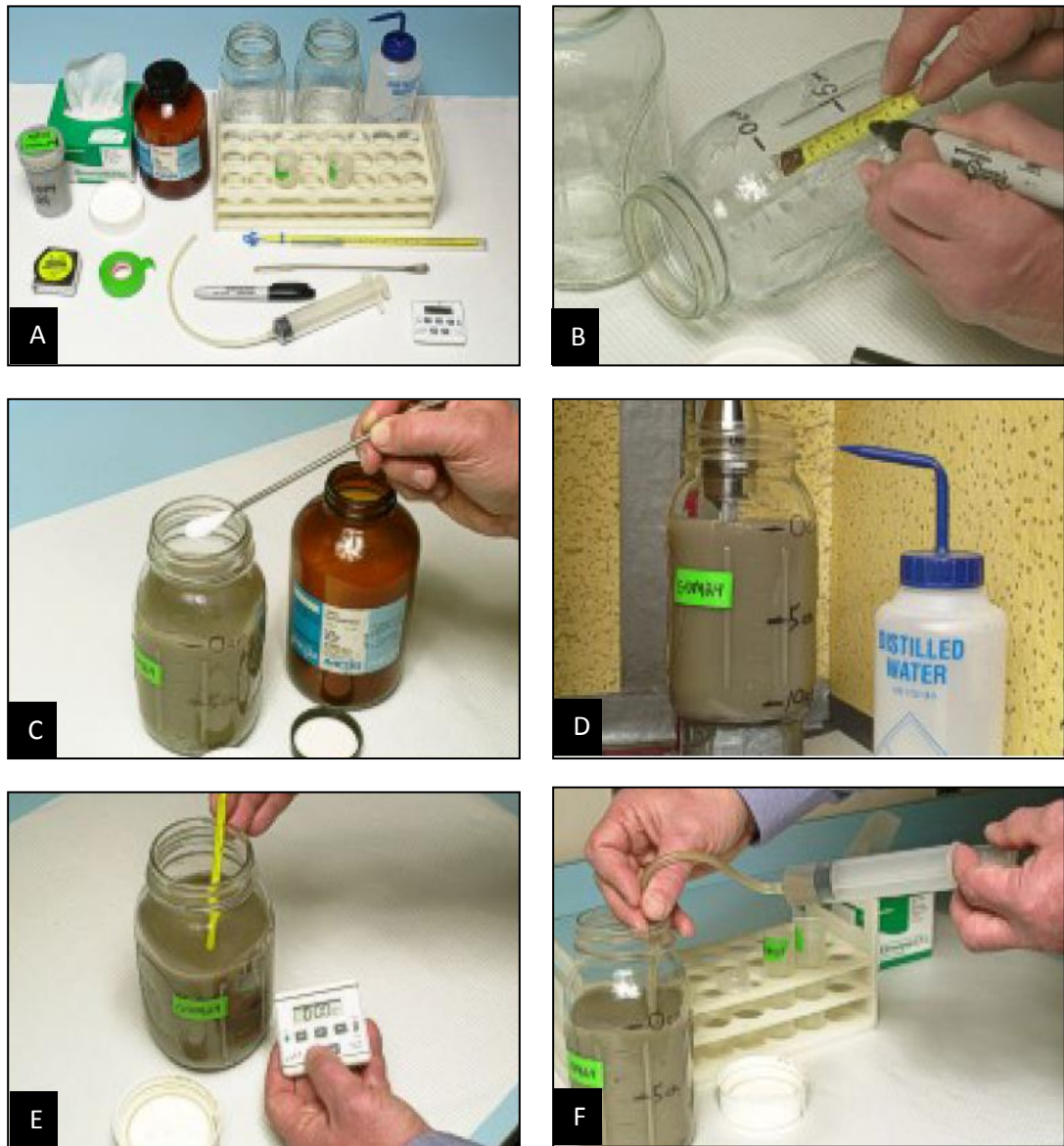


Figure 3.10: (A) Materials required to perform decantation on the sediments (B) labelling glass jars with 5-0 cm depth (C) addition of  $\approx 2.5$  g of sodium hexametaphosphate (D) stirring using sonic probe (E) Setting time for each withdrawal of the clay fraction (F) Sample withdraw at depth between 0-5 cm (Poppe et al., 2001).

9. After each time elapse, the solution contained in each one of the glass jar was withdrawn using a syringe. Three withdrawals were taken per each sample, based on three times; 4h06m, 3h54m and 2h 58m.

10. After each time lapse the following procedure was followed: the clay suspension was withdrawn from depth above the 5 cm mark on the glass jar (Figure 2.10F). Each one of the withdrawn samples was injected in a test tube and labelled according a proper naming convention for the XRD analysis.

Table 3.1 Withdrawal time and temperature which was applied to the silt and clay suspension <2 micrometres fractions by decantation (FOLK, 1974); (Poppe et al., 2000).

Temperature C°	Time
20	4h6m
24	3h54m
32	2h58m

#### **3.4.2.1.4. Preparation of Clay Fraction for XRD Analysis**

Three phases of data acquisition were encompassed in the XRD analyses, in which the separated clay fraction samples were subjected to a series of procedures before analysing them with the XRD facility located in the Williamson Research Centre at the University of Manchester. These procedures are based on (Moore and Reynolds, 1989, Moore and Reynolds, 1997).

#### **3.4.2.1.5. Procedure of Preparation of Oriented Mounts**

The following apparatus list is essential to perform work

- Glass slides cut to fit diffractometer
- Carbide or diamond glass scribe
- Lab tissues
- Vacuum pump

- Millipore filtration apparatus vacuum tubing
- Millipore HA, 47-mm, 0.45-micron  
nominal pore opening cellulose filters
- pipette or 20-25 cc syringe
- single-edge razor or metal spatula
- cylinder with a 2.5 - 5 cm outside diameter

This analysis is aimed to orient the clays flat, it was done according to the following methodology:

- 1- Place the separated clay fraction into 10ml measuring cylinder.
- 2-Complete the volume to 5 ml by adding deionized water.
- 3- Stir thoroughly using a glass rod.
- 4-Using an eye dropper, withdraw the upper part of the solution after about 20 minutes have passed already.
- 5- Release eyedropper slowly on a clean glass slide.
- 6- Make sure that the glass slide is completely covered with the released liquid.
- 7- Leave the slides to dry out at room temperature as high temperatures can be destructive to poorly crystalline clay minerals.

#### **3.4.2.1.6. Treatment with Ethylene Glycol**

Ethylene glycol (CH<sub>2</sub>OH)<sub>2</sub> is an odourless, colourless organic compound. Water within the sample is replaced by ethylene glycol (the solvating agent), which is aimed to give a constant interlayer spacing. The treatments were applied as follows:

- 1- Samples were subjected to the vapour of ethylene glycol.

2- Dry the samples in an oven at 60 C<sup>0</sup>.

3- Analyse the samples using XRD to identify the presence of montmorillonite by comparing the XRD data of air dried samples with Ethylene Glycolated samples.

According to (Moore and Reynolds, 1989), a very distinctive 001 basal reflection at  $2\theta = 5.2^\circ$  of wavelength 16.9 Å can be identified in glycolated samples. Whilst, in air dried samples, 001 basal reflection shifts to  $2\theta = 6^\circ$  (15 Å).

### 3.4.2.1.7. Heated-Treated Samples

The next level of XRD analysis encompasses heating of the treated samples in the furnace at 550C<sup>0</sup> for about 30-40 minutes. The reason behind heating samples slides is to differentiate between kaolinite and chlorite peaks. Kaolinite becomes shapeless (amorphous) at higher temperatures. Hence, kaolinite peaks will disappear. The analysis of heated –treated samples is crucial for confirming that the identified clay mineral is chlorite (Moore and Reynolds, 1989).

## 3.5. Wireline logs digitizing

An automated well log digitizing was performed on some of the scanned well logs of the Zubair Formation using Digder 4. Well logs were calibrated then digitized and saved as LAS files (Figure 3.11).

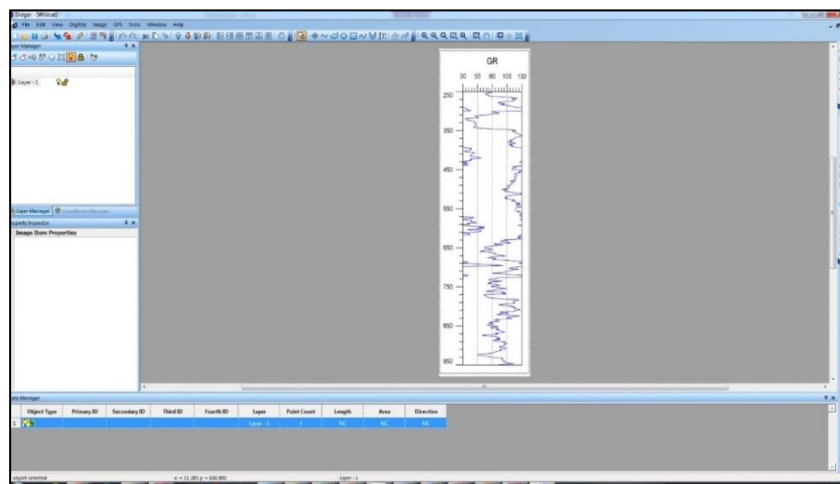


Figure 3.11: Screenshot shows the interface of Digder V4.0, which was used to digitize missing well logs of the study area.

### 3.6. Petrophysical Analysis from Well Logs

Well log analysis was performed using Techlog 2014 by Schlumberger. As this software platform is designed to perform both easy and more advanced petrophysical interpretation tasks (Figure 3.12).

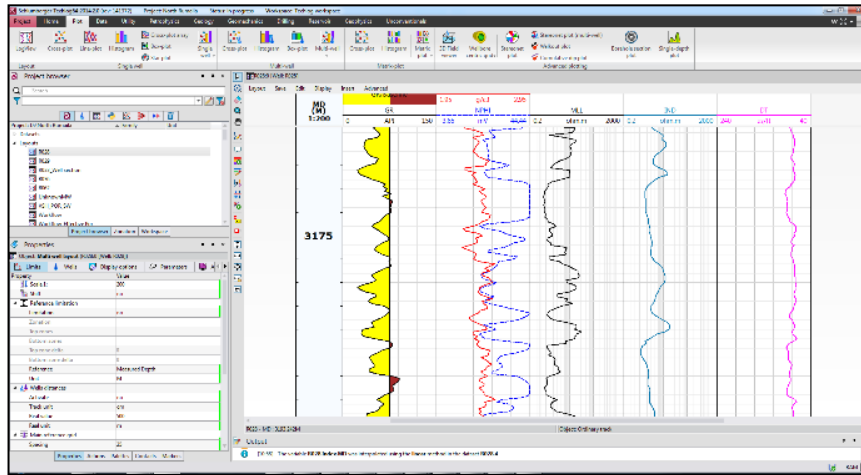


Figure 3.12: Screenshot of Techlog 64 2014.2.0.

### 3.7. X-ray CT and Pore-Scale Network Models

Pore scale X-ray CT imaging was performed on the Zubair sandstones aiming to improve the understanding of porous media by 3D visualization at a micro – scale. X-ray micro imaging was conducted on 7 representative core samples from the Zubair sandstones. Cylindrical core plugs with a diameter of 5 mm, 6 mm were cut from big a bigger core samples using mini diamond cutter blade (Figure 3.13). An additional scan of core material (80 mm diameter) was obtained to assess the macroscopic distribution of the mineral assemblage. X-ray CT scan was performed in MXIF facility-Manchester University using Nikon Metris custom bay.

#### 3.7.1 Analysis of X-ray CT Data

Digital rock analysis of the Zubair scanned cores was carried out using advanced 3D analysis software called Avizo Fire 9.0. and PerGeos. The original volume images were converted into TIF stack of 8 bit resolution by using Avizo Fire 9.0. These TIFs were



subjected to thresholding algorithms to segment pores and mineralisation. The segmentation was performed on a cropped size from the bulk volume render obtained from each one of representative core samples. Further processing aimed to extract the pore network skeleton was performed on these cropped cubes.

### **3.7. 2. Permeability Test**

To examine the impact of mineralisation on fluid flow through pore space, comparative permeability studies were applied on segmented images collected by X-ray computed tomography. Set of algorithms were applied to X-ray micro CT images in order to segment mineralisation, pore space, quartz matrix. Two types of binary images were used in permeability estimates; three channel binary images, which encompass pore space, quartz matrix and mineralisation(mineralised mesh), and another set of binary of binary images which consist of two channel, one for pore space + added volume of mineralisation and quartz matrix. These binaries were subjected to permeability estimates using HydroXLab extension in PerGeos software. Hence, comparison between mineralised and un-mineralised meshes was made.

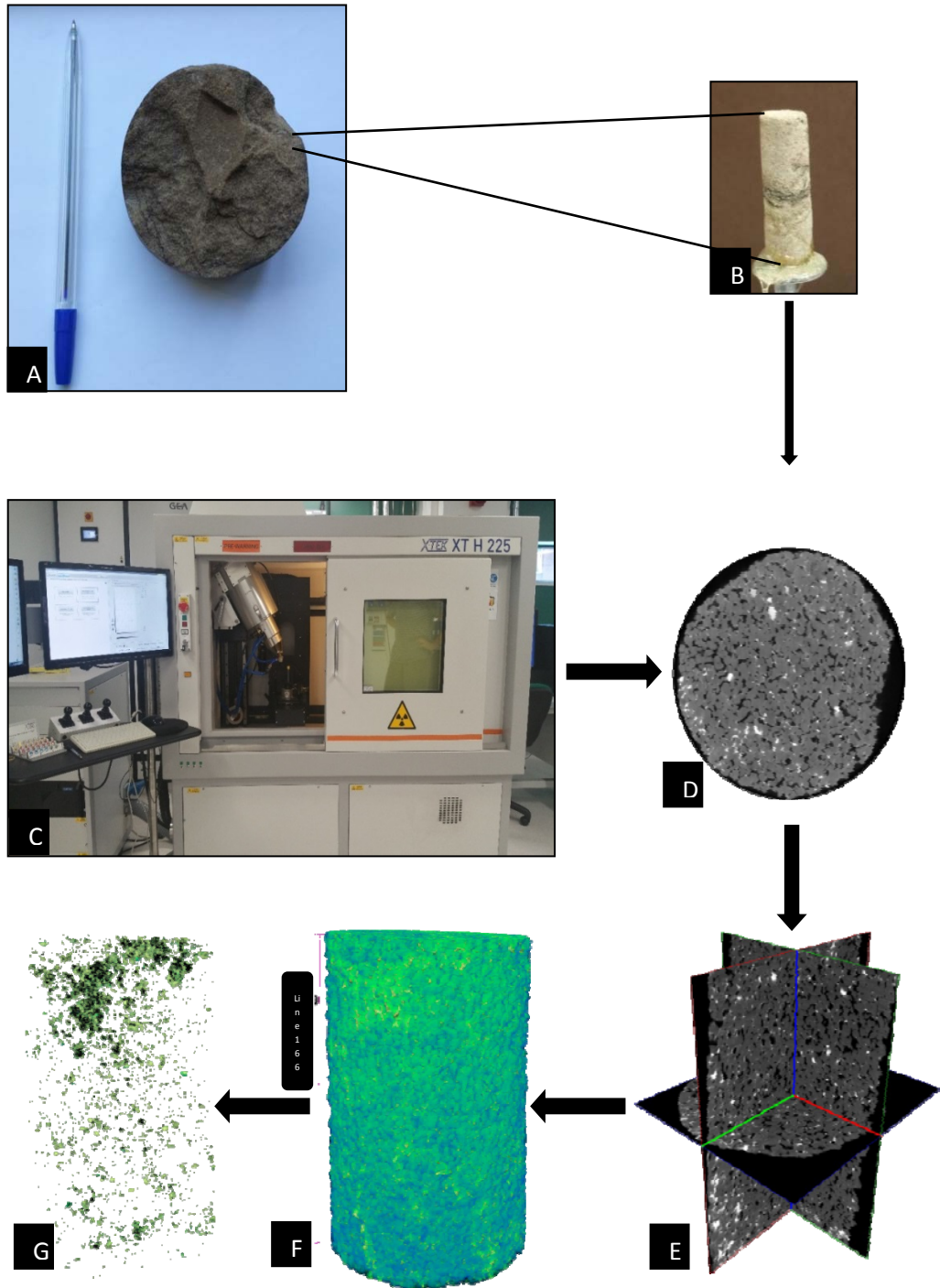


Figure 3.13: (A) Big core sample 80 mm in diameter taken from the Zubair Formation, which was scanned to assess the macroscopic distribution of the minerals assemblage (B) small core sample of 6 mm taken from representative core interval, was scanned to obtain images, these image were converted into a stack of Tagged Image Format (TIF) in order to be displayed into 3D volume render (C) Nikon Metris XT H 255 X CT scanner, which was used to obtain scans of the study samples (D) TIF slice from one of the scanned small cores, in which pores are in black, grains in grey and mineralisation in light colour (E) 3D orthoview of the scanned core shows the distribution of mineralisation, pores within the core sample (F) 3D bulk volume render of sandstone core sample contains significant amount of mineralisation, thresholding algorithms were applied on these volume images to extract pore network volume and pyrite mineralization. These model volumes can be analysed in terms of connectivity, and used for a basis of fluid flow modelling.

# Chapter 4

---

## Lithofacies and Electrofacies Analysis



## Chapter Four

### Introduction

The purpose of classification and simplification of existing patterns in well sections or an outcrop is to make an idiosyncratic ordering of events within a given sequence, leading to understand the lithological variability relationship to the basin architecture. And this can be done by illustrating facies models to depict their spatial relationships within the basin. It worth mentioning that, there is no universal diagram or scheme to be adapted as standard facies model. However, some authors have presented their own universal classifications (e.g. Farrel et al., 2012), who gave a classification of clastic sediments. This chapter is aimed to introduce our classification of sedimentary facies, which was done on the basis of main depositional attributes such as: grain size, sedimentary structures, bedding, colour and hardness. As well as attempting understand relationship between mineralogical distribution and facies. It is important to know that the cored Zubair used in this study was almost from the Main Pay. The lower Cretaceous Zubair Formation comprises the onset of Barremian-Aptian sequence (Salman and Mesopotamian Zones). It was formed during the time of low stand. (Jassim and Goff, 2006). The Zubair Formation consist of an alteration of sandstone and shale with intercalation of siltstone (Alsharhan and Nairn, 1997). The Zubair Formation is one of the most important and prolific oil reservoirs in the southern Iraq region. The Zubair sandstones are originated from fluvio-deltaic, deltaic and marine environments (Aqrawi et al., 2010). The thickness of the formation is ranges from 200-500m in the southern Iraq region. Thickness of the Zubair Formation at the Rumaila field is between 380-390m (Jamil, 1978 cited in Aqrawi et al., 2010). The upper contact of the Zubair is marked by shales. Carbonates of Shuaiba Formation bound the upper of contact of the Zubair, whilst the lower contact is marked by Ratawai Formation

limestone (Buday, 1980). The Zubair Formation was deposited in a fluvial dominated deltaic environment (Al-Fadel and Al-Ansari 1992). Thirteen lithotypes have been identified into the Zubair cored intervals. Depositional attributes such as sedimentary structure, grain size, and bioturbation were observed at subbed-bed scale units. These lithotypes are summarised in (Table 4.1), which are based on their key characteristics as shown in photographs. The identified lithotypes are represented by (1) massive sandstones of stratified nature, which comprise about 68-70 % of the Upper Sandstone Member of the Zubair Formation, (2) massive mudstones which vary from little or no amount of bioturbation (3) bioturbated mudstone associated with siltstone. These mudstones are also characterised by distinctive lamination and carbonaceous material. (4) heterolithic lithotypes were also identified in cored intervals of the Zubair. However, poor core curation has limited detailed distinction between these facies.

#### **4.1. Lithofacies**

Based on cored Zubair interval see (Table 1.1), 8 lithofacies of predominantly sandstone were identified and their lithotypes have been named as follows: massive sandstone / bioturbated sandstone, cross bedded stratified sandstone, rippled laminated sandstones, deformed sandstone, bioturbated sandstone, bioturbated sandstone with susceptible mud, bioturbated sandstone with superabundant mud, an intercalation of very fine sandstone with mud, silt very fine sand of thickness between cm-0.1m. Distinctive Sedimentary structures of this lithology are ripples, thin lamination and cracks due to desiccation and Mostly cm thick. It consists of sandy siltstone, argillaceous sandstone laminae, burrows and other distinctive sedimentary structures such as ripple and parallel lamination (Table 4.1). As mentioned earlier, facies classification was based on a number of observations such as grain size, colour, hardness of core material, sedimentary structures, mineralisation, roots of plants, fossil content and organism's

activity. Representative lithofacies identified in this study are shown in Table 4.1.

Selected photos of core material from the available Zubair cored depths can be seen in

Appendix 3.

Table 4.1: Core based lithotypes, their names and description. These lithotypes were applied to the studied wells-Zubair Formation in the Rumaila Field.

Lithology code	Lithology	Graphic lithology	Mud	Sand	Cgl.	Thickness range in cored intervals (m)	Description of lithotypes
Sm/Bsm	Sandstone					0.5-10	Massive sandstone/Bioturbated sandstone.
SX						0.10-2	Cross bedded stratified sandstone.
Sr/SI						0.5-6	Rippled-laminated sandstone.
Sdf						0.10-2	Deformed sandstone.
Sba						0.10-8	Bioturbated sandstone.
Sbb	Muddy sandstone					0.10-6	Bioturbated sandstone with susceptible mud.
Sbc						0.10-7	Bioturbated sandstone with superabundant mud.
Hs	Heterolithic					0.1-1	An intercalation of very fine sandstone with mud and silt Very fine sand of thickness between cm-0.1m. Distinctive sedimentary structures of this lithology are ripples, thin lamination and cracks due to desiccation.
Hm						0.01-0.10	Mostly cm thick. It consists of sandy siltstone, argillaceous sandstone laminae, burrows and lenses. It has ripple and parallel thin lamination.
Mm	Mudstone					0.1-1	Massive mudstone of thickness varies between cm-m. It has no or very little bioturbation and almost has no lamination.
Ml						0.1-0.90	Laminated mudstone of thickness varies between cm-0.10 m. This type of lithology has indistinctly parallel lamination with the absence of bioturbation. In this type of lithology, lamination can be inferred from fissility/platy character seen in rubbed core intervals.
Mc						0.1-1	Carbonaceous mudstone with organic-filled and coal or lignite material. This lithology thickness varies between cm-0.10 m.
Mb						0.1-1.10	Bioturbated mudstone/silt stone. This lithology varies between cm-0.10 m.





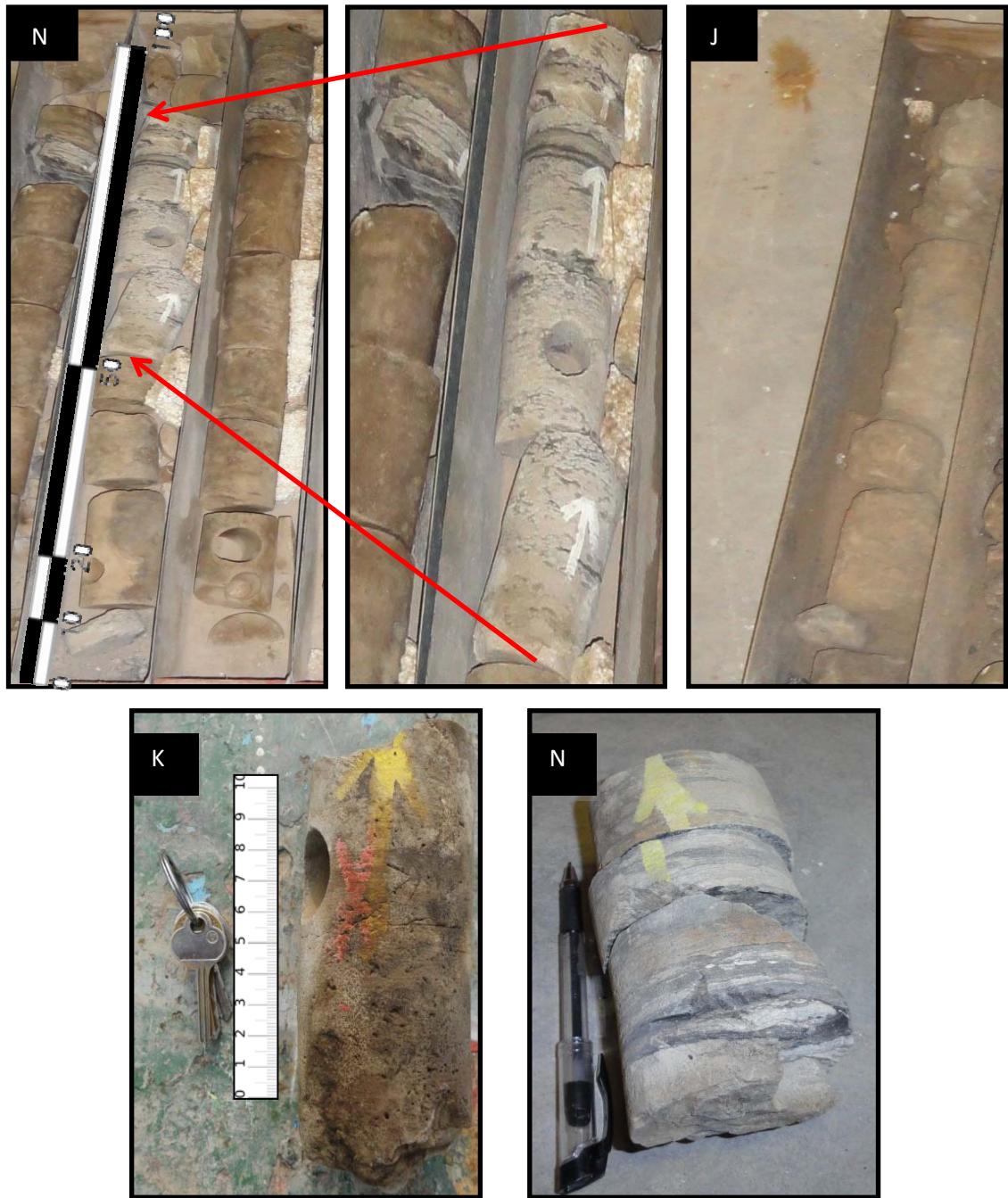


Figure 4.1: Shale K shows shale dark grey fissile with intercalations of bioturbated silty sand stones Sbb in some parts of it. (D) Consists of massive sandstone, with parallel lamination of argillaceous material. Facies associations E-1 and Facies E-2 both comprise one lithology, but with more shale content due to sedimentary influx of clays. (C) Consists of massive sandstone of fine-medium grain. Pyrite mineralisation was identified in quite few samples collected from this facies as well as some other facies. (G) Consists of massive sandstone, of high hardness m medium grain size, ferruginous arenite and bioclasts. (H) Shows silty shale with thin lamination of argillaceous material it shows coarsening upward in grain size. It also has some coal deposits and bioturbation. (J) Shows greenish colour siltstone with some ferrous deposits. Facies (K) consists of massive sandstone, very fine grained, silty, with high clay content, ripple, wave lamination, greenish colour. (M) Massive sandstone sample shows burrows due to organism activity. (N) Heterolithic Massive sandstone with high clay lamination, fine grain size.

#### **4.1.1. Facies Association H**

Silty shale, thin lamination of clay (argillaceous) and slight bioturbation with some coal deposits (HM). Observed sedimentary structures in this facies also encompass lenticular lamination, some wavy bedding, and cross-lamination. Sandstone part in this facies is of light brown colour, very fine- fine grain size. These sandstones are intercalated with clay deposits (HS). In some part of it, sedimentary structures such as planar and trough cross bedding were observed. Thickness of this facies ranges from less than 10 cm- 1 m. This facies comprises clastic deposit of coarsening upward in grain size. It also has coalification in some parts of it (Figure 4.1).

#### **Interpretation**

Observations made by us on this part of the Zubair cored material, suggest that it is located in a depositional setting, which is influenced by both marine and fluvial sedimentary processes. The thinly laminated siltstone part of this facies association belongs to prodelta. The sandstone part represents the distributary mouth bar deposits (delta front), in which sediment accumulation is high due to rapid deposition, associated with limited bioturbation (Tonkin, 2012).

#### **4.1.2. Facies Association E**

This facies consists of massive fine silty sandstone / mud, high shale content, with lamination (ripple and wavy), dark grey shale, coal, and bioturbation can be seen in some parts of it with lamination (ripple and wavy). This facies encompasses two parts; E-1 (Hs) and E-2 (Hm). Thickness of this facies ranges between dm-8 m. This facies shows fining upward trend as can be indicated by electrofacies motif of bell shape or sometimes gamma- ray log shows cylindrical shape. Core porosity if this

facies is about 15-17%., whilst log porosity is about 22-24%. Core material from well A shows some structures resulted by root plants and high coalification.

### **Interpretation**

Visual core description and electrofacies analysis made on this facies, suggest that it represent subaerial part of delta or what is commonly called delta plain. This part of delta deposits encompasses distributary channel fills (Fisher, 1969) (Figure 4.1).

#### **4.1.3. Facies Association D**

This facies consists of silty sandstone (Hm) with high argillaceous material, bioturbation H with some intercalations (about 15 cm thick) of massive sandstone of fine grains (Sx). Lenses of very fine grained sandstone can be seen in this facies. The underlying facies is facies C. This Facies comprises finning upward as the underlying bed forms sandstone medium-fine grain size of Facies C. Facies D contains thin bedded laminations of shales. These thin laminations of very fine grain size sediments give an indication of finning upward as it was confirmed by gamma-ray electro-facies (serrated bell shape), which corresponds to sandstone / shale alternated lithology. Thickness of this facies ranges from dm-3 meters (Figure 4.1).

### **Interpretation**

This lithological alteration suggests condition of quiet water environment, which contributed in depositing very fine grain sizes.

#### **4.1.4. Facies Association C**

Massive sandstone (Sm), thin parallel lamination of sandstone and clay, oil shows, burrows. Fine-medium grain size. This facies contains some carbonaceous deposits. Thickness of this facies ranges from dm-10 meters. It comprises amalgamated

sandstone facies (Figure 4.1). This facies association encompasses some carbonaceous muds with organic filled and coal (Mc).

### **Interpretation**

This facies has a grain size ranges from medium at the bottom of it to fine upward. Electrofacies log pattern shows characteristics of bell shape with some clay intercalations accompanied by burrows of organisms. This facies suggests it was deposited as delta plain deposits.

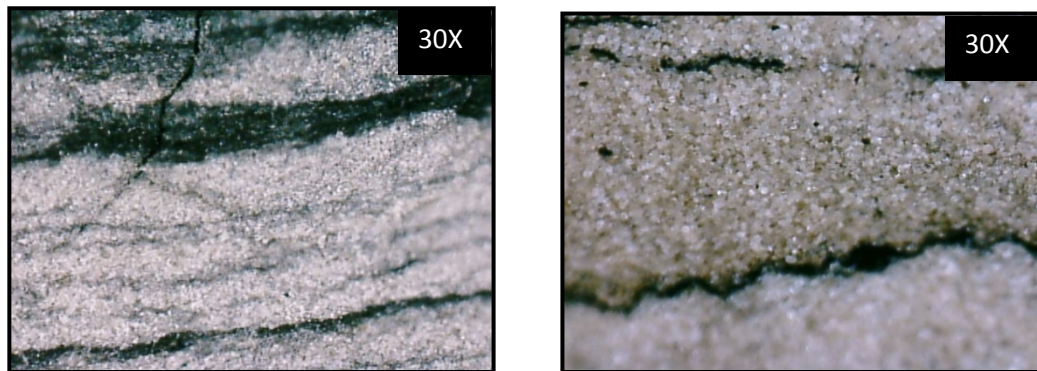


Figure 4.2: Magnified photos of sample collected from Facies C. Thin lamination can be seen in both photos. Average grain size of this facies is about 150 micron.

#### **4.1.5. Facies Association N**

An intercalation of very fine sandstone sandstone, very fine grained, silty, with high clay content, ripple, wave lamination, greenish colour. This facies thickness ranges from 0.05-7 meters. It comprises heterolithic lithologies of sand / shale (Hs). This facies contains some bioturbation and irregular lamination. Field description of the cored intervals reveals sharp abrupt at the lower base of this facies (Figure 4.1).

### **Interpretation**

This facies corresponds to condition of high deposition as can be shown by its heterolithic lithologies.

#### **4.1.6. Facies J**

Siltstone, green colour, with some ferrous content and coalification (Mb). This facies appears like green powder due to finning upward. Siltstone of this facies is of high clay content (Figure 4.1).

#### **Interpretation**

The high clay content within this facies suggests deposition in very quiet environment. As well as high organic content as indicated from the green colour of silt, which suggest it was deposited in tidal and fluvial channel.

#### **4.2. Electrofacies Analysis**

The process of partitioning well log dataset into units or clusters (electrofacies) is called electrofacies analysis. These electrofacies can be then correlated to lithofacies identified from core data e.g. (Serra and Abbott, 1980) as they were the lead on introducing the term electrofacies. A set of wireline log data is required to conduct electrofacies analysis. Whereas, wireline log data corresponds to different attributes of sediments according to well log patterns. In this study I have used conventional well logs Gamma Ray and Resistivity logs for the discrimination of electrofacies (table 1.2). The distinctive patterns identified in this study were based on typical Gamma ray patterns presented by (Serra and Abbott, 1980, Slatt, 2013) (Figure4.3 )and (Figure 4.4).

The interpretation of depositional facies relies on the shape of wireline log curves Selley 1978 as cited in (Nazeer et al., 2016) . The Gamma-ray log reflects vertical profile of grain size.

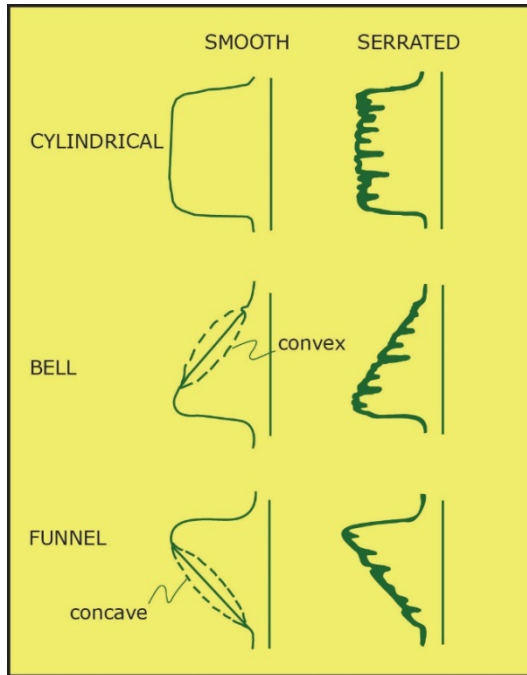


Figure 4.3: Classification of electrofacies by motifs of log response after (Serra and Abbott, 1980).

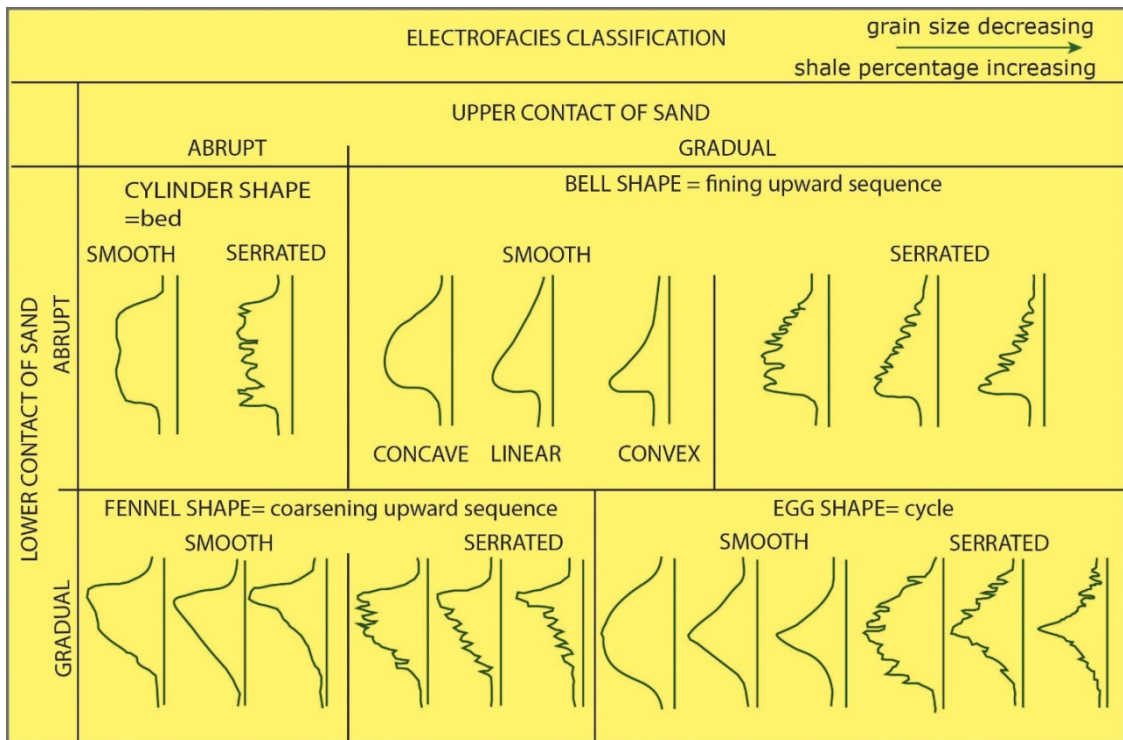


Figure 4.4: Generalised gamma-ray or self-spontaneous SP logs motifs. These curves shapes represent are used to classify electrofacies based on their lithological characteristics and depositional environments. After (Slatt, 2013) who has mentioned that source of this figure is unknown.

### **4.3. Basic Log Curve Types**

Five distinctive gamma-ray log curve types are used in the electrofacies classification:

- 1- Cylindrical shape
- 2- Bell shape
- 3- Funnel shape
- 4- Oval (egg) shape
- 5- According to Nazeer et al. (2016), there is another log curve type which can be classified as irregular shape.

#### **4.3.1. Cylindrical Shape**

The boundaries of this log pattern are sharp at top and base. Gamma-ray reading of this log pattern is consistent which reflects consistent lithology. The consistent overall trend of this log curve indicates relatively consistent lithology (Figure 4.4).

#### **4.3.2. Bell Shape**

In this log motif, gamma-ray log reading increases upward due to increasing shale content. The bell shape indicates fining upward in grain size trend which has abrupt base. Depositional environments which can be indicated by the bell shape motif encompass fluvial or deltaic channel, deep tidal channel, fluvial point bar, braided streams, distributaries, proximal deep sea and sea channel (Nazeer et al., 2016). The bell shaped successions associated with detritus of carbonaceous matter are deposited in fluvial or deltaic channel environments (Selly, 1978 as cited in Nazeer et al. 2016) (Figure 4.4).

#### **4.3.3 Funnel Shape**

Gamma-ray reading of the funnel shape motif decreases upward due to cleaning upward or coarsening upward trend. Funnel shape log curve is characterised by coarsening upward with abrupt at its top. Favourable depositional environments indicated by funnel shape log curve are regressive barrier bar, prograding deltas or

crevasse splay and prograding sub-marine fans (Selly, 1978 as cited in Nazeer et al. 2016) (Figure 4.4).

#### 4.3.4. Oval Shape

This type of gamma-ray log curves is characterised by gradual cleaning upward succession (no sharp abrupt) (Figure 4.4).

#### 4.3.5. Irregular Shape

This type of log motifs comprises a fluctuation of high and low gamma-ray readings that occurs over short interval. The explanation of this fluctuation in gamma-ray values can be attributed to rapid deposition of turbidity (Nazeer et al., 2016). These sharp changes in depth-lithology and deposition related change are related to deposition break which can be indicated by such gamma-ray log motif.

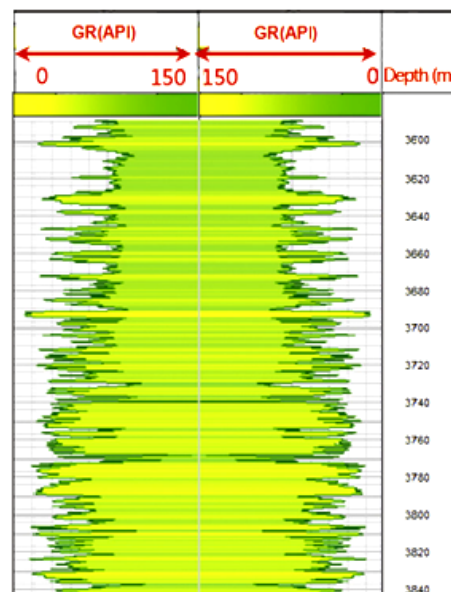


Figure 4.5: Irregular trend of gamma-ray log motif (Nazeer et al., 2016)



## **4.4. Electrofacies Results and Interpretation**

Correlation between typical gamma-ray motifs and has come out with a number of distinctive electrofacies that correspond to grain size and lithology of the study section.

Four electrofacies were identified in this study; which have been given numbers from 1-4. These electrofacies correspond to fluvio–deltaic environment. As shown in (Figure 4.6), (Figure 4.7) and (Figure 4.8). According to Selly (1985), log motifs are not 100 % unique to a specific depositional environment. Therefore combining and comparing data of both gamma-ray log motifs and core data can help in the interpretation of depositional environment. The results of electrofacies analysis indicate that the gamma-ray log motifs belong to thin funnel shaped, oval shaped, bell shaped, and cylindrical shaped log motifs.

### **4.4.1. Thin funnel shaped**

#### **4.4.1.1. Description**

The analysis of gamma-ray log in the study wells shows successions of thin funnel shapes. Log curve of this motif is mostly smooth, and has thickness which is less than 8 meter.

#### **4.4.1.2. Interpretation**

Gamma-ray log motif of thin funnel shaped indicates coarsening upward or cleaning upward (Selley, 1998). The depositional environment seems to be crevasse splay of deltaic channel (prograding delta).

### **4.4.2. Cylindrical shaped**

#### **4.4.2.1. Description**

Cylindrical shaped gamma-ray log motif is formed due to the existence of shales at both of its top base boundaries. The maximum thickness of this log motif in the study

wells is about 16 meters. The identified lithology which corresponds to gamma-ray log reading of this motif is mostly sandstone.

#### **4.4.2.2. Interpretation**

The abrupt at both top and base of the cylindrical shaped gamma-ray indicates rapid termination of deposition (Chow et al., 2005). Selley (1998) presented three depositional environments which are related to this log motif; tidal wave, deltaic distributary channel and grain flow fill. The identified depositional environment from this log motif is more likely to be deltaic distributary channel.

#### **4.4.3. Bell shaped**

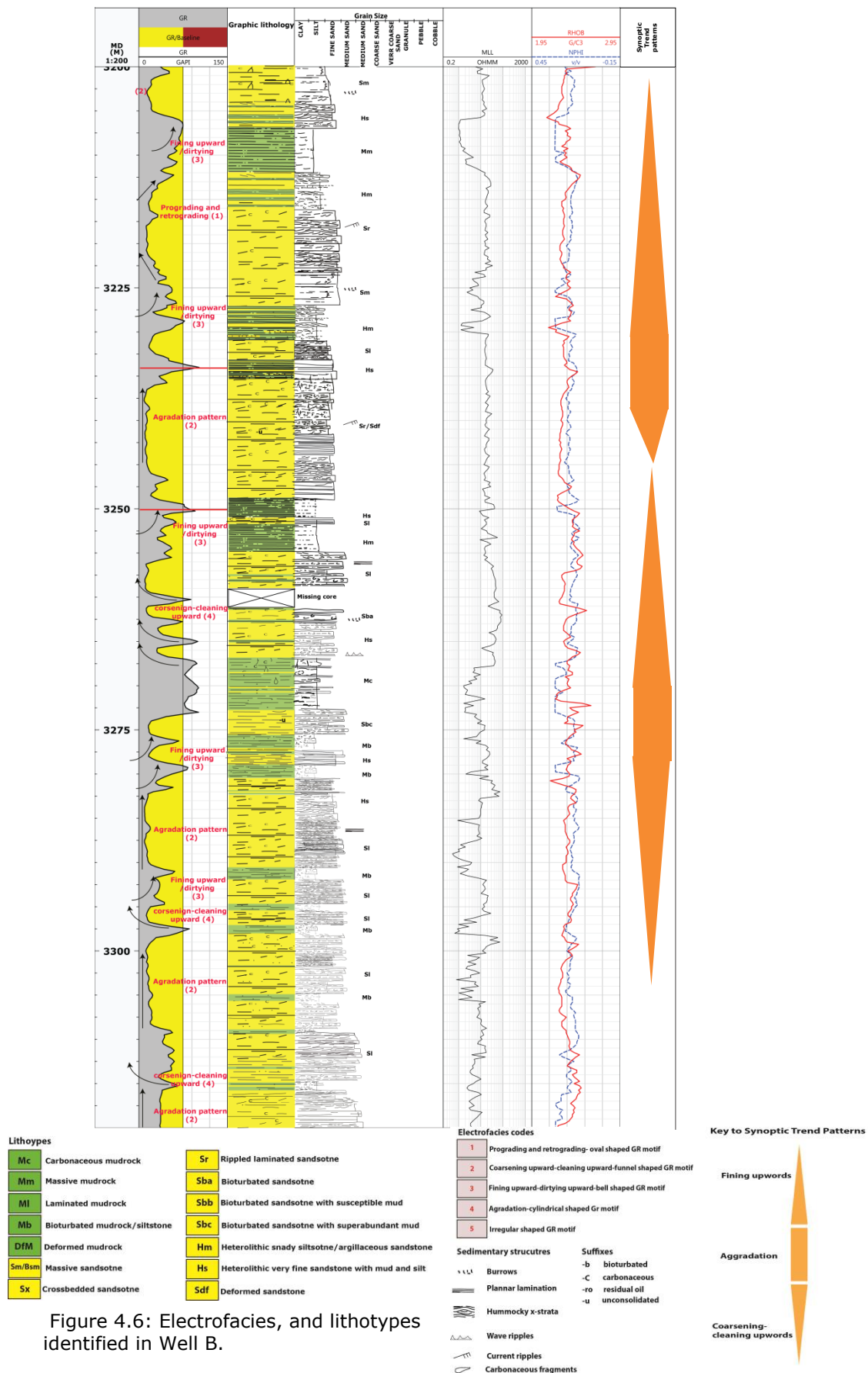
##### **4.4.3.1. Description**

The gamma-ray log motif in the study wells shows bell shaped succession of sandstone and shale with detritus of carbonaceous matter. The bell shape indicates fining upward (Serra and Abbott, 1980).

##### **4.4.3.2. Interpretation**

According to Chow (2005), three types of environments are indicated by the bell shaped succession: tidal channels, turbidite fills and fluvial or deltaic channels. The bell shaped gamma-ray log motif identified in the study well indicates to fluvial or deltaic channel depositional environment (Selley, 1998).

Well B



Lithotypes

Mc	Carbonaceous mudrock	Sr	Rippled laminated sandstone
Mm	Massive mudrock	Sba	Bioturbated sandstone
Ml	Laminated mudrock	Sbb	Bioturbated sandstone with susceptible mud
Mb	Bioturbated mudrock/siltstone	Sbc	Bioturbated sandstone with superabundant mud
DfM	Deformed mudrock	Hm	Heterolithic sandy siltstone/argillaceous sandstone
Sm/Bsm	Massive sandstone	Hs	Heterolithic very fine sandstone with mud and silt
Sx	Crossbedded sandstone	Sdf	Deformed sandstone

Electrofacies codes

- 1 Prograding and retrograding- oval shaped GR motif
- 2 Coarsening upward-cleaning upward-funnel shaped GR motif
- 3 Fining upward-dirtying upward-bell shaped GR motif
- 4 Agradation-cylindrical shaped GR motif
- 5 Irregular shaped GR motif

Sedimentary structures

- ~ ~ ~ Burrows
- Plannar lamination
- ~ ~ ~ Hummocky x-strata
- △△△ Wave ripples
- ~ ~ ~ Current ripples
- Carbonaceous fragments

Suffixes

- b bioturbated
- c carbonaceous
- ro residual oil
- u unconsolidated

Key to Synoptic Trend Patterns

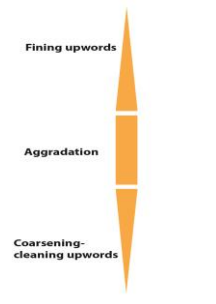
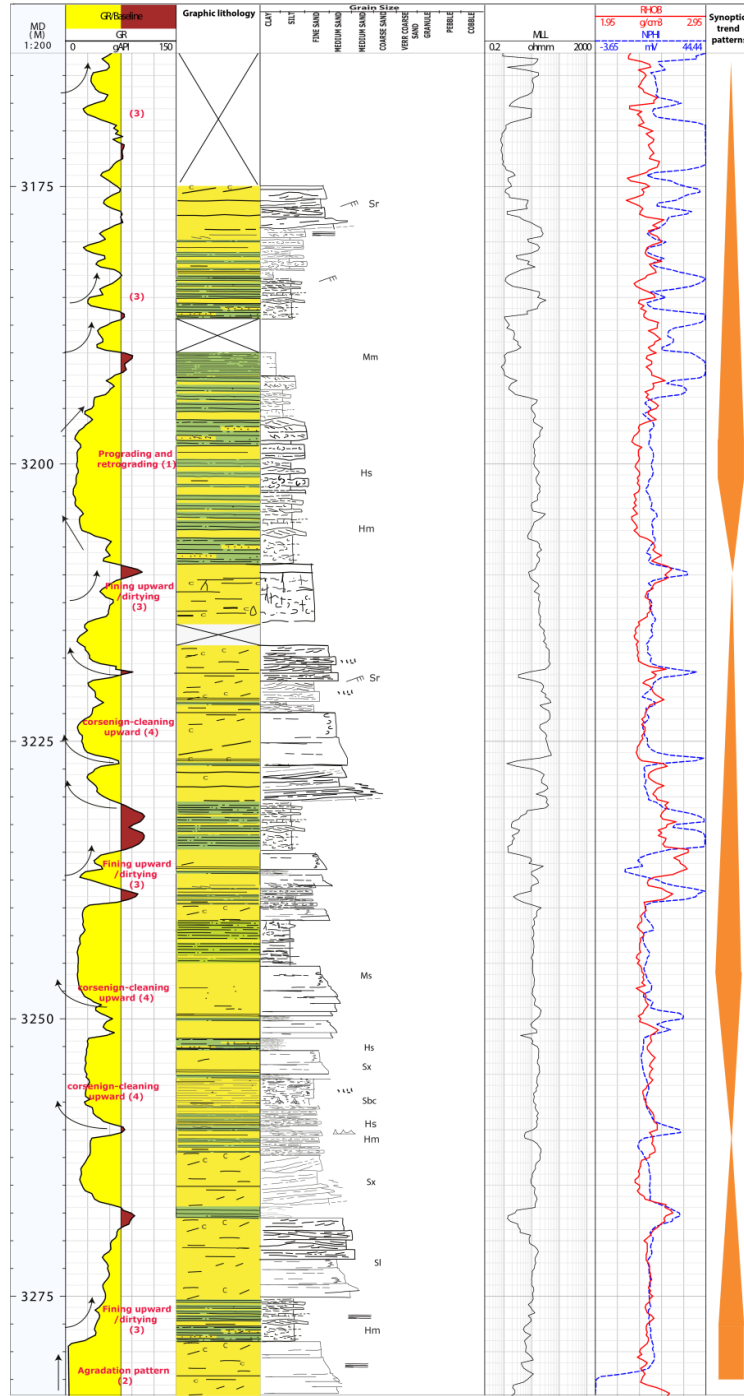


Figure 4.6: Electrofacies, and lithotypes identified in Well B.

Well c



Lithotypes

Mc	Carbonaceous mudrock	Sr	Rippled laminated sandsotne
Mm	Massive mudrock	Sba	Bioturbated sandsotne
Ml	Laminated mudrock	Sbb	Bioturbated sandsotne with susceptible mud
Mb	Bioturbated mudrock/siltstone	Sbc	Bioturbated sandsotne with superabundant mud
DM	Deformed mudrock	Hm	Heterolithic snady siltstone/argillaceous sandstone
Sm/Bsm	Massive sandsotne	Hs	Heterolithic very fine sandstone with mud and silt
Sx	Crossbedded sandsotne	Sdf	Deformed sandstone

Electrofacies codes

1	Prograding and retrograding- oval shaped GR motif
2	Coarsening upward-cleaning upward-funnel shaped GR motif
3	Fining upward-dirtying upward-bell shaped GR motif
4	Agradation-cylindrical shaped Gr motif
5	Irregular shaped GR motif

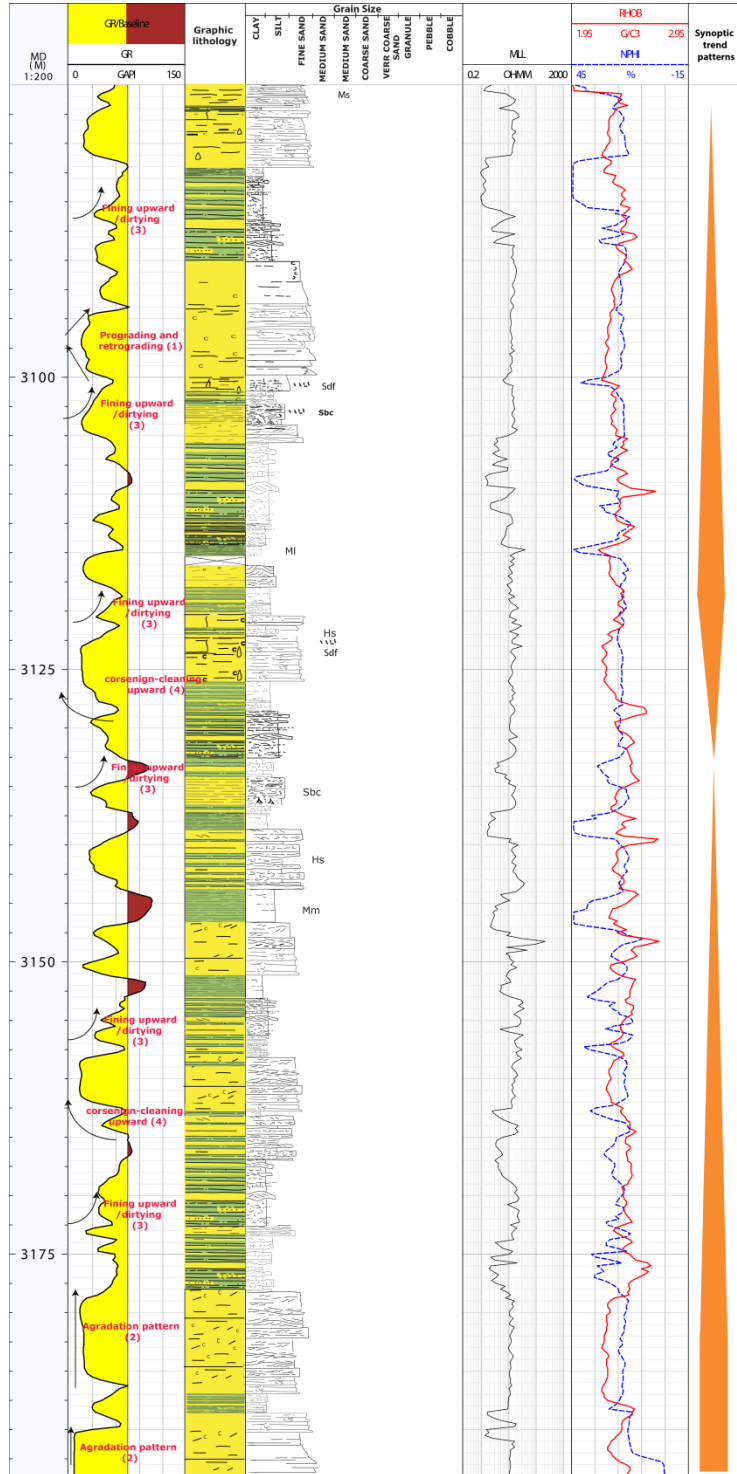
	Burrows	<b>Suffixes</b>	-b	bioturbated
	Planar lamination	-c	carbonaceous	
	Hummocky x-strata	-ro	residual oil	
	Wave ripples	-u	unconsolidated	
	Current ripples			
	Carbonaceous fragments			

Key to Synoptic Trend Patterns



Figure 4.7: Electrofacies, and lithotypes identified in Well c.

# Well D



Lithotypes	
Mc	Carbonaceous mudrock
Mm	Massive mudrock
MI	Laminated mudrock
Mb	Bioturbated mudrock/siltstone
D/M	Deformed mudrock
Sm/Bsm	Massive sandstone
Sx	Crossbedded sandstone
Sr	Rippled laminated sandstone
Sba	Bioturbated sandstone
Sbb	Bioturbated sandstone with susceptible mud
Sbc	Bioturbated sandstone with superabundant mud
Hm	Heterolithic sandy siltstone/argillaceous sandstone
Hs	Heterolithic very fine sandstone with mud and silt
Sdf	Deformed sandstone

Electrofacies codes	
1	Prograding and retrograding- oval shaped GR motif
2	Coarsening upward-cleaning upward-funnel shaped GR motif
3	Fining upward-dirtying upward-bell shaped GR motif
4	Agradation-cylindrical shaped GR motif
5	Irregular shaped GR motif
Sedimentary structures	
~ ~ ~	Burrows
— — —	Planar lamination
~ ~ ~	Hummocky x-strata
~ ~ ~	Wave ripples
~ ~ ~	Current ripples
~ ~ ~	Carbonaceous fragments
Suffixes	
-b	bioturbated
-c	carbonaceous
-ro	residual oil
-u	unconsolidated

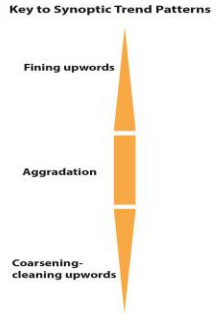


Figure 4.8: Electrofacies, and lithotypes identified in Well D.

## **4.5. Well Correlation**

Two correlation sections were drawn for the study wells: stratigraphic and structural correlation.

### **4.5.1. Stratigraphic and Structural Well Correlation.**

Both stratigraphic and structural well correlations were drawn by using PETREL 2014 software. Upper shale Member was used as marker bed for in stratigraphic correlation (Figure 4.9). While structural well correlation was based on the sea level to give an overall view of the real subsurface structure. Stratigraphic well correlation of wells B, D, and C illustrates a group of lithofacies. Lithologically, these facies comprise of sandstone, shales and shaly sandstone. The Zubair Formation is sub- divided into members and each one of them is sub-divided into units. The Upper Sandstone Member is the Main Pay within the Zubair Formation. Thickness of sandstone facies increases towards N-W of the Rumaila field. It gives an indication that amalgamated sandstone increases towards the North of the Rumaila field. Overlapping shale facies (well D) could potentially influence the reservoir quality of the Zubair Formation in unit F and H. Shale facies can be clearly seen in unit AB. Significant amount of pyrite was observed in this facies. This facies consists of massive sandstone of medium-fine grain size. Shale overlapping could deteriorate the reservoir quality especially in unit AB, C, and L. Unit K is mostly comprised of shale. Observations within a distance of 2 km between well D and C shows that the top units AB, C and D of the Zubair Formation are influenced with shale content. This could lead to deterioration in reservoir quality. However, the unite L; M and N are cleaner than top units of the Upper Sandstone Member. Net / Gross sand increase towards N-W of the Rumaila Field. Overall reservoir quality in units M, N and L improves due to upward grain size increase (cleaning upward). The best reservoir quality is in unit L (channel fill deposits).

#### **4.6. Discussion and Conclusions**

Facies analysis of the Zubair Formation encompassed was performed by using lithofacies and electrofacies analysis. The absence of core data of the Upper Shale Member has limited the analysis and which was only done on the Main Pay of the Zubair Formation. Facies analysis indicates sandbodies of heterolithic nature prograding-deltaic conditions in unit N and L. While units D and H indicate the depositional conditions of distributary channel-fill deposits which overlie deposits of prodelta (mud-prone) / interdistributary channel fill deposits. Depositional environment of the Zubair Formation-Main Pay reflects river-dominated, wave-influenced delta.

Grain size in the Zubair Formation ranges from clean, fine to medium and coarse grained sandstones. Decreasing grain size is associated with higher argillaceous and ductile content and bioturbation. Heterolithic deposits reduce reservoir quality.

From key finding of lithofacies and electrofacies analysis, the depositional system of the Zubair Formation comprises a coherent hierarchy from sub-bed to bed-scale lithotypes. However, to improve the understanding of its hierarchy, larger well logs and core datasets are essential to increase confidence level of the analysis, preferably to be incorporated with seismic dataset.

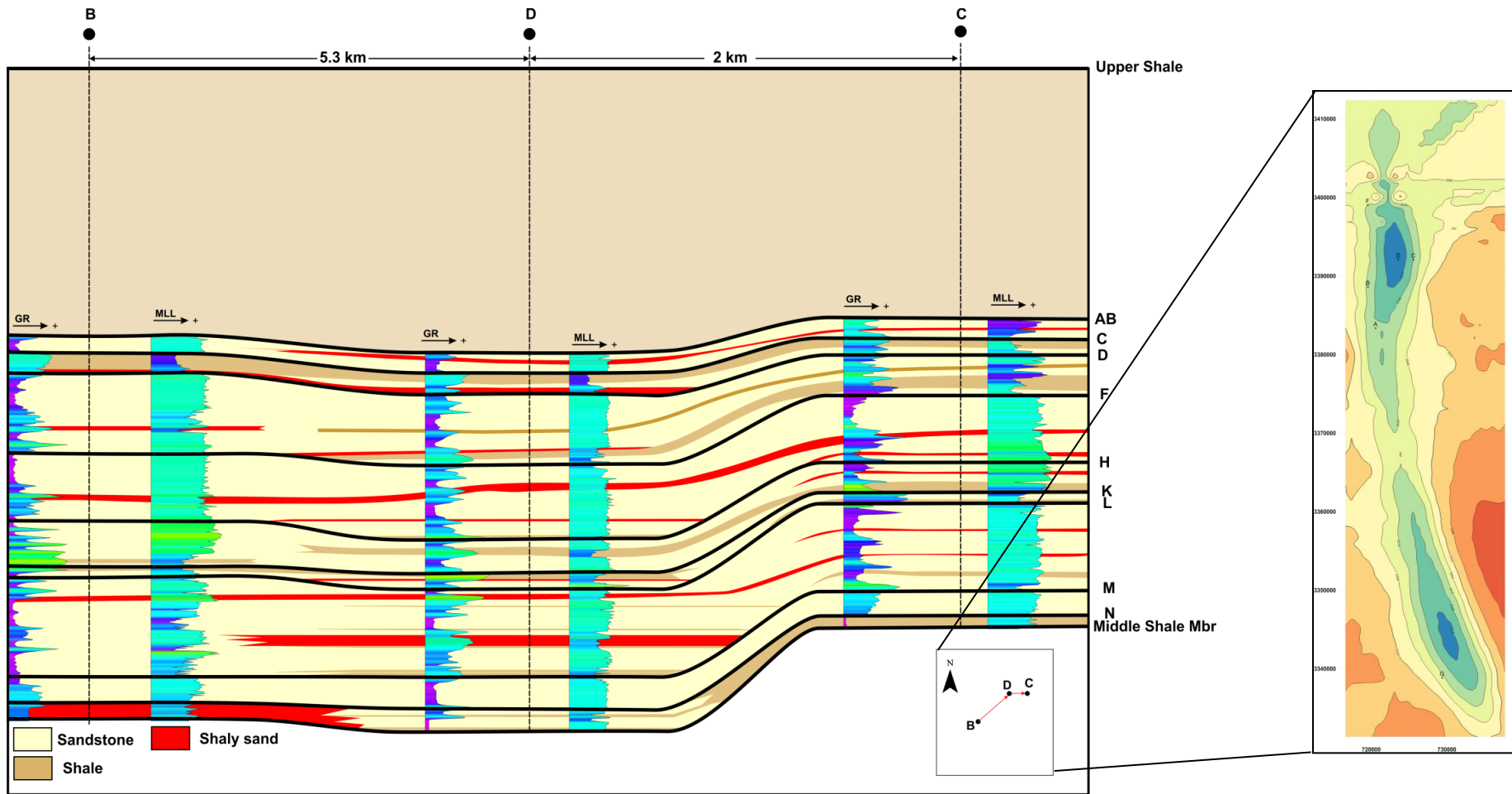


Figure 4.9: Stratigraphic correlation of wells B, D and C. Structure contour map was produced by Haitham Al-Ziayyir.



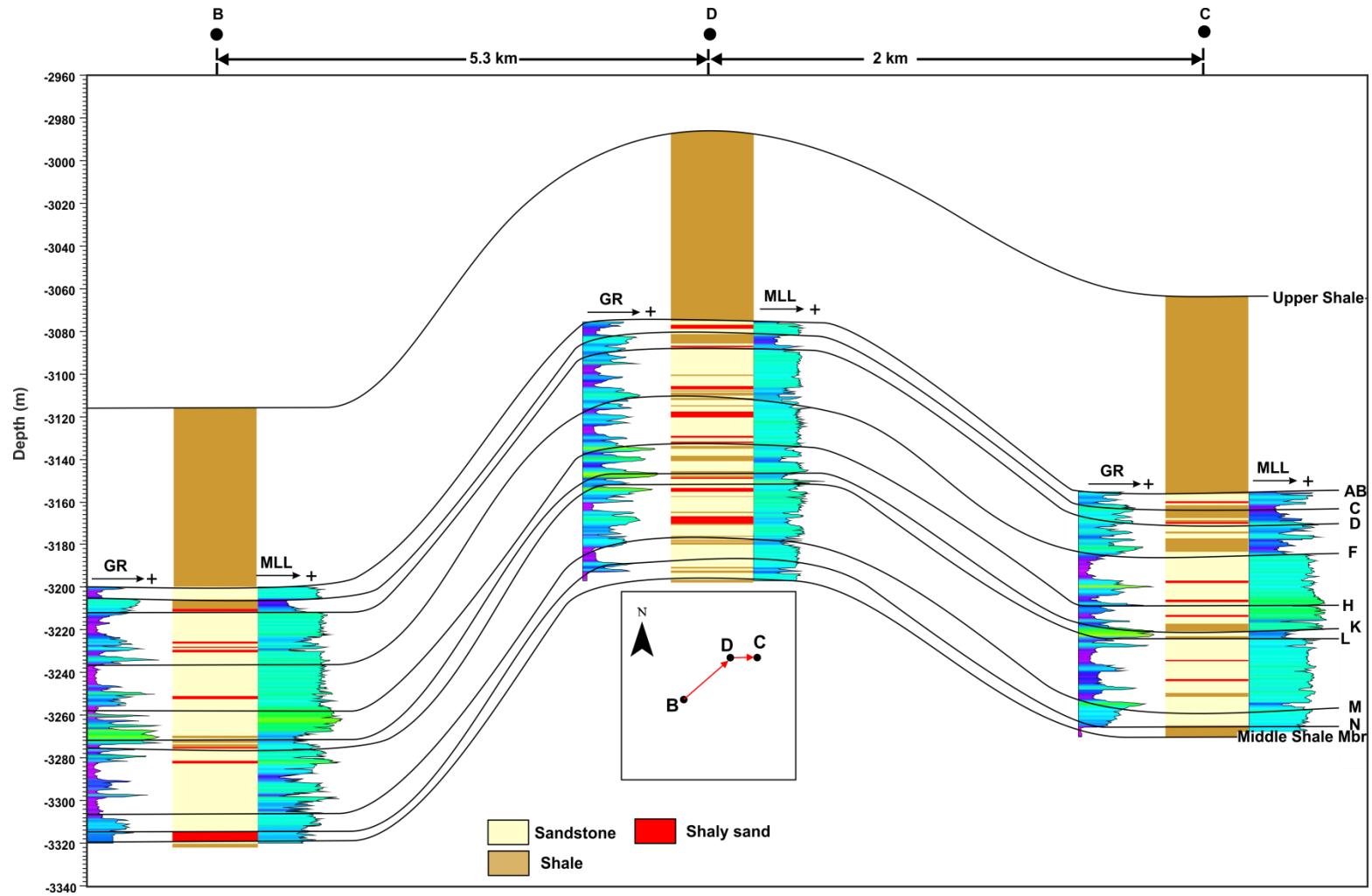


Figure 4.10: Structural correlation of wells B, D and C.

# Chapter 5

---

## Mineralogical Characterisation Using XRD and SEM Studies



## **Chapter Five**

### **Introduction**

This chapter aims to identify, and semi quantify clay minerals at the vicinity of sandstone / shale contacts. It also attempts to improve understanding of the influence of clay minerals on reservoir characteristics. Data used in this chapter are in Table (1.3).

### **5.1. Preface**

A key objective of most sandstone reservoir characterisation studies is to investigate the impact of authigenic or diagenetic clay minerals on reservoir characteristics. The distribution of clay minerals in sandstones varies according to type, morphology and complexity of diagenesis. Physical and chemical properties of sandstones and shales are controlled by clay minerals (Bjølykke, 1998, Dewers and Ortoleva, 1991). Clay minerals comprise assembled aggregate and ordinarily multitudinous source, they can either be found as authigenic or detrital (Worden and Morad, 2003). The distribution of clay minerals in sedimentary rocks varies according to the type, morphology and complexity of diagenesis. Mechanical breakdown occurs in minerals that have been formed previously within the rocks, whilst chemical reactions leading to the formation of clay mineral rely on two mechanisms; the first occurs during the precipitation from flowing solutions, which is termed as neo-formation. The second mechanism comprises a major inherited constituent of skeletal remains of silicate that originated from previously existed minerals (Eslinger and Pevear, 1988). In order to identify textural relationships of clay minerals in a given sedimentary rock, detailed analysis aiming to characterise clay mineral needs to be done by using X-ray diffractometry and Environmental Scanning Electron Microscopy (ESEM). The study of clay mineralogy can either be performed at micro or macro scale. Despite extensive research on clay minerals distribution and texture at micro scale, little research has been done on clay

minerals at macro-scale. Thus, clay minerals study on microscopic scale requires significant care. Hence, upscaling the effect of clay minerals from microscopic scale to larger scale to be applied to reservoir studies, that deal with fluid flow at lateral extension ranges between tens of meters to a few kilometres requires care (Hurst and Archer, 1986). Diagenetic studies aim to improve understanding of depositional and post-depositional operations engagement in sedimentary particles through gradual burial. Accordingly, the study of clay minerals comprises a vital part of diagenetic studies. The assessment of clay minerals comprises important part of improving understanding of diagenetic processes, and their impact on reservoir heterogeneity. Clay minerals studies can be integrated with thermal diagenetic models aiming to depict or estimate timing of migration and production related to porosity evolution (e.g Nadeau, 1998). In this chapter I will attempt to examine impact of clay minerals within the Zubair Formation on diagenetic trends. It is also important to mention that organic maturation analyses will not be incorporated in this study, as different authors have applied organic maturation studies on the Zubair Formation (e.g. Al-Ameri and Battenm1997, Al-Ameri et al., 2009, Al-Ameri et al., 2011, Al-Azzawi, 2012).

Clay minerals are found as abundancy in sedimentary rocks. They comprise the cements within the grain framework. Clay cementation could be a product of reactional exchange between pore fluid and grain framework (Jonas et al., 1977). Complexity of diagenesis is influenced by fluid flow in a given sedimentary basin, as fluids flowing in reservoir rocks comprise transport medium for heat and solids. Hence flowing fluids can anomalously stimulate thermal exchange causing dissolution and precipitation of minerals.

Petrographic analysis of the Zubair sandstones was not undertaken in this study, because part of research on the Zubair Formation has been fairly covered by a number

of researchers (e.g. Hmood, 2002; Al-Muhalhal, 2004). It worth mentioning that data collected from core analyses included laboratory petrophysical analysis and flooding tests, which were collected from technical reports of South Oil Company S.O.C, Iraqi Ministry of Oil. The analyses were performed in Iraqi Oil Exploration Company and Laboratory Section in South Oil Company-Nahran Omar site.

## **5.2. Distinguishing Petrographic Characteristics**

Fabric, textural and detrital component of the Zubair Formation is based on previous work done on petrography. However, grain size measurement and estimation are based on visual core description and digital images taken by mobile microscope. The cored Zubair sandstones exhibit medium–fine sandstones. Grain size measurement was using measurement software, which is based on digital image analysis.

### **5.2.1. Light minerals**

Microscopic examination of the Zubair Formation (e.g. Hmood, 2002; Al-Muhalhal, 2004), and internal reports of Iraqi South Oil Company S.O.C reveal monocrystalline quartz is a predominant component within the Zubair Formation. Polycrystalline quartz was also found in small quantity less than 5%.

### **5.2.2. Feldspar and Rock Fragments**

From other rock framework components, feldspar was identified in small amounts (about 3% of the total rock framework). Feldspar if deeply buried destructs due to dissolution (Wilkinson et al., 2001). The low percentage of feldspar confirms that it is a detrital component. Hence diagenesis prompted detrital feldspar to dissolve (Blatt, 1979). Rock fragments are mainly argillaceous and ranges between (0-20%) (Hmood, 2002)

According to unpublished internal reports in S.O.C, ductile components sparsely exist in the Zubair sandstones. Detrital clays are predominantly distributed as pore-filling, with minor grain-coating component.

### **5.3. Clay minerals studies**

Integrated studies using Environmental Scanning Electron Microscope SEM and X-ray Diffraction analysis were done on selected core samples from the Zubair in order to characterise clay mineralogy aiming to improve understanding of diagenetic influence on reservoir characteristics. The type of clay mineral can be identified by using X-ray diffraction spectra. For an individual X-ray diffractogram a set of peak intensities are proportional to the concentrations of the clay minerals found in the sample (Jozanikohan et al., 2016). Clay minerals in sandstones can either be authigenic or detrital (allogenic). The term authigenic refers to clay minerals which have been locally created within the depositional context of sedimentary basin. There are two modes of origin of authigenic clay minerals; neoformed clay are formed solution as chemical precipitates, and transformed clays that are created due to alteration of phyllosilicate (Eslinger and Pevear, 1988). Detrital Kaolin minerals group include different minerals such as kaolinite, dickite and nacrite. This group of minerals and illite are prevalently found in sandstone reservoirs. Clay minerals can be found as mixed-layer stacking of two component; dioctahedral and trioctahedral. The common form of mixed 1-layer minerals are; illite + smectite, kaolinite + smectite

### **5.4. Interpretation of X-ray diffraction data**

#### **5.4.1. Qualitative analysis of XRD data**

Layer structure and material of the inter-layer are two main characteristics of any clay mineral group. Minerals existed in clay fraction sample can be identified based on their basal reflection (00L). Each clay mineral has its basal spacing and intensity

(Table 5.1). From the table we can see that kaolinite-serpentine sub group are near 7Å (first order basal reflection). First order basal reflection near 10Å represents non swelling minerals 2:1 such as mica and illite. While first order basal reflection near 14Å includes swelling minerals such as smectite and vermiculite, besides a non-swelling mineral, which is chlorite, as well as palygorskite and sepiolite.

These are some challenges engaged in the process of identification clay minerals. For instance, some clay minerals have more than basal spacing e.g. smectite. On the other hand the overlapping of chlorite basal reflection with others basal reflections such as vermiculite may cause confusion in distinguishing between them. As they both have 00L basal reflections (Eslinger and Pevear, 1988). Therefore, further treatment for the designate clay fraction sample is required for the distinction between real peaks of clay minerals which exist in the analysed sample. As discussed in methodology part on sample's preparation for X-ray data analysis, three pre-treatments have been performed for each phase of X-ray diffraction analysis; preferentially oriented mount specimens, heated samples, and 550<sup>0</sup>C heated-treated specimens. These three phase pre-treatments have been done on clay fraction specimens by the experimental officer at the Williamson Research Centre-the University of Manchester. There was another batch of bulk powder samples, which have been analysed to identify mineralogy. The air-dried specimens that contain kaolin minerals correspond to a basal reflection of 7.2 Å (Figure5.1). X-ray diffraction patterns of clay minerals have their own signature character, which includes; position of peak, shape, breadth and intensity



Table 5.1: Classification of Phyllosilicates Related to Clay minerals (Brindley and Brown 1980; S. W. Bailey, Pers. Comm., 1987 cited in Eslinger and Peaver, 1988)

Layer Type	Interlayer material	Group	Subgroup	Species (Examples)
1:1	None or H <sub>2</sub> O only	Serpentine-Kaolin (X=0)	Serpentine Kaolin	
2:1	None	Talc-pyrophyllite (X ~ 0)	Talc Pyrophyllite	Talc, willemseite Pyrophyllite
	Hydrated exchangeable cations	Smectite (X ~ 0.2-0.6)	Saponite Montmorillonite	Saponite, hectorite, saunonite, stevensite, etc. Montmorillonite, beidellite, nontronite
	Hydrated exchangeable cations	Vermiculite (X ~ 0.6 - 0.9)	Trioctahedral vermiculite Diocahedral Vermiculite	Trioctahedral vermiculite Diocahedral vermiculite
	Nonhydrated cations	True mica (X ~ 0.5-1.0)	Trioctahedral true mica Diocahedral true mica	Phlogopite, biotite, lepidolite, annite Muscovite, illite, glauconite, paragonite, celadonite
	Hydrated cations	Brittle mica (X ~ 2.0)	Trioctahedral brittle mica Diocahedral brittle mica	Clintonite Margarite
	Hydrated cations	Chlorite (X Variable)	Trioctahedral chlorite Diocahedral chlorite	Clinochlore, chamosite, nimitte, pennantite Donbassite
2:1 Mixed-layer (regular)	Variable	None	None	Hydrobiotite, rectorite, corrensente, aliettite, tosudite, kulkeite
Modulated 1:1 layer	None	No group name (X ~ 0)	No subgroup name	Antigorite, greenalite
Modulated 2:1	Hydrated exchangeable cations	Sepiolite-palygorskite (X ~ Variable)	Sepiolite Palygorskite	Sepiolite, loughlinitite Palygorskite
	Variable	No group name (X ~ variable)	No subgroup name	Minnesotaite, stilpnomelane, zussmanite

X= Layer charge/<sup>0</sup>10 (OH)<sub>2</sub>

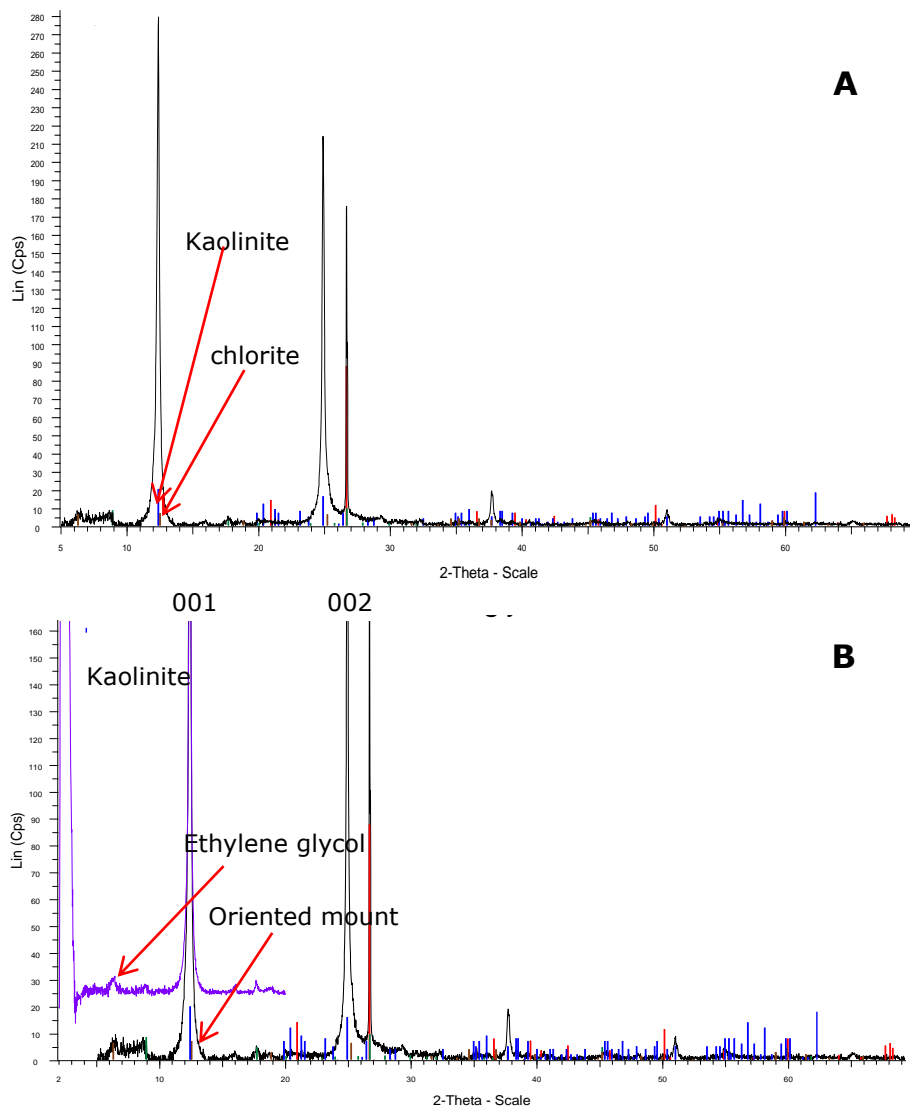


Figure 5.1: (A) oriented mount of the clay fraction from well D, in which we can see that we have two prominent peaks of basal reflections 001, 002, 003 and 004. Kaolinite comprises dominant clay mineral with a small amount of illite and chlinochlore (chlorite). (B) Same sample after treating it with ethylene glycol. We can see that prominent peaks confirm the existence of kaolinite as dominant clay in this sample. This kaolinite is well crystalline as indicated from sharp peaks basal reflection 001 and 002 of the oriented mounts, and 001 basal reflection of ethylene glycol treated sample.

Details about the determination of peak's position are found in Moore and Reynolds (1989). Peak positions and intensities are very important in the identification of clay minerals. However, identification of clay minerals needs some experience to precisely identify each individual clay mineral. Routine procedure followed in the identification

of clay minerals requires distinguishing the presence of clay minerals peaks for each clay type such as illite, vermiculite, kaolinite, chlorite and smectite.

#### **5.4.1.1. Chlorite and kaolinite**

The occurrence of and structure of kaolinite and chlorite are varied. However, their peaks may present together, especially chlorite with high Fe content, which makes the distinction between chlorite and kaolinite challenging. Whereas, d spacing of kaolinite is 001, which is similar to chlorite d spacing 002 at 7 Å. Therefore further treatment with ethylene glycol and thermal treatment to 550°C are required for the distinction between kaolinite and chlorite (Biscaye, 1964, Moore and Reynolds, 1989). 24.9° 2θ, kaolinite basal reflection is 002. Whilst at 25.1°2θ chlorite gives 004 peak of basal reflection. However, there is not 100% accurate method to distinguish between kaolinite and chlorite. Sharp peaks mean that crystallinity of clay mineral is high (well crystalline).

#### **5.4.1.2. Smectite**

This clay mineral group encompasses two sub- groups; saponite and montmorillonite. In order to distinct smectite from X-ray diffraction patterns, a comparison between diffraction patterns of both oriented mount and ethylene glycol treated samples. As basal reflection 001 16.9 Å is prominently strong at 5.2° 2θ (Moore and Reynolds, 1989). Smectite group has low layer charge X=0.2-0.6 as shown in (table 5.1). Smectite capacity of cation exchange is high; similarly vermiculite has high cation exchange capacity. Basal reflection spacing of smectite and vermiculite of oriented mount vary in response to their cation saturation. As well as humidity controls inter-layer swelling. Challenges accompanied interpretation of smectite XRD patterns lie in arbitrating whether clay mineral is smectite or mix-layer clays (illite-smectite). Higher orders of basal reflection 002,

003, etc. are weak. Hence, they are undetectable on XRD patterns due to small amount of smectite. Samples analysed revealed small or very weak peaks of smectite. Treating samples with glycerol causes dissolution of  $K^+$ . Therefore distinction between smectite and vermiculite can be made (Macewan, 1944, Bradley, 1945).

#### **5.4.1.3. Illite and Glauconite**

Diffraction patterns of pure illite and pure glauconite remain unaffected by thermal and/or chemical treatments. Although intensity of glauconite at basal reflections 001 and 003 is higher than it in illite, the distinction between them is based on the absence of 002 basal reflection of glauconite due to effect of octahedral iron (Moore and Reynolds, 1989). A common mistake may happen when identifying clay minerals as illite, whilst it is actually illite/smectite mixed-layer or glauconite (Eslinger and Pevear, 1988).

#### **5.4.1.4. Chlorite**

The analysed samples revealed chlinochlore, which is trioctahedral (tri-tri) chlorite with Mg and Al content. Four basal reflections have been observed in chlorite 001, 002, 003 and 004 of  $2\theta$  between 2 and 35. These basal reflections arise near 14.2 Å, 7.75 Å, and 3.53 Å. Heavy elements control intensities of these peaks, such as high Fe concentration, which causes a decrease in first and third order basal reflection.

#### **5.4.1.5. Quartz**

Distinctive quartz peak arises at 003 basal reflection at 3.34 Å near illite or vermiculite and smectite (Eslinger and Pevear, 1988) (Figure 5.2 a,b)

### **5.5. Results of XRD qualitative analysis**

Clay fraction samples were subjected to three levels of XRD analysis, the first level was performed on air-dried clay fraction samples. A group of minerals/clay minerals were

identified by using XRD scans collected from these untreated clay fraction samples. Distinction level of confidence of some clay minerals / minerals is high e.g. chlorite, kaolinite and illite, and minerals such as calcite, which has also been identified at different depths (Table 5.3.). However, identification of other minerals was challenging (e.g. mixed layered clays). Qualitative analysis of XRD data is based  $2\theta$  and d-spacing for each one of clay minerals / minerals as shown in Table 5.2.

Table 5.2: After(Brindley and Brown, 1980) Spacing in Å, and intensities for preliminary identification of clay minerals.

Minerals	$d(001)$	Intensity of (00/)					$d(060)$
		L=1	2	3	4	5	
Kaolinite group	7.15-7.20	100	90	15	10	4	1.489
Mg-serpentine	7.25-7.35	100	100	-	20	20	1.536-1.540
Fe-Serpentine	7.04	100	100	-	-	5	1.555
Berthierine							
Pyrophyllite	9.20	80	30	100	5	10	1.493
Talc	9.35	vs	w	s	vw	m	1.527
Smectite							
Diocahedral			variable				1.49-1.50
Triocahedral			variable				1.52-15.4
Vermiculite	14.3	100	10	15	30	30	1.541
Muscovite	10.0-10.05	>100	55	>100	20	20	1/499
Phlogopite	10.0-10.05	>100	20	>100	30	30	1.538
Biotite	10.0	100	20	90	10	10	1.530
Celadonite	9.95	50	-	70	-	-	1.510
Glauconite	9.95	100	-	60	-	-	1.511
Paragonite	9.62	30	20	100	-	-	1.481
Chlorites	14.15-14.35	70	100	50	80	80	1.549
(Magnesian)							
Chlorite(iron-rich)	14.10-14.25	20	100	20	50	50	1.560

Sepiolite  $d(110) = 12.1-12.3, I=100; d(131) = 4.30, I=25-40$

Palygorskite  $d(110) = 10.4-20.5, I=100; d(121) = 4.25, I=10-30$

Table 5.3: summary of quantitative analysis of minerals identified in clay fraction samples of the Zubair Formation weight percentage

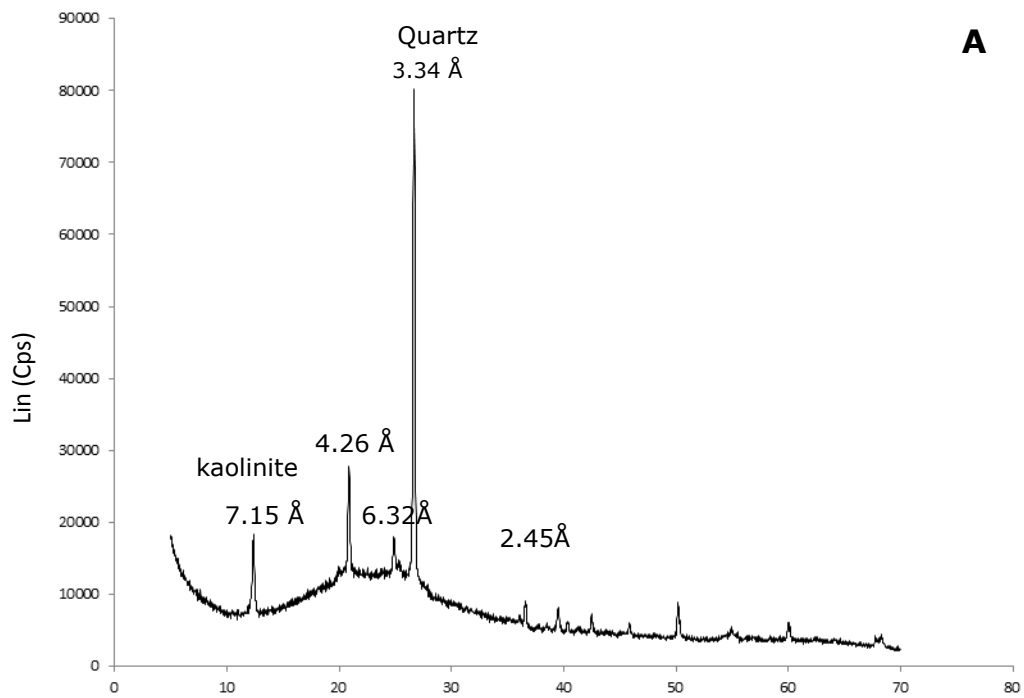
	<b>illite</b>	<b>kaolinite</b>	<b>chlorite</b>	<b>pyrite</b>	<b>Albite</b>	<b>Augite PX</b>	<b>quartz</b>	<b>anatase</b>
<b>Average</b>	9.57	17.45	3.48	1.12	0.14	7.69	71.29	2.6
<b>Max</b>	11.47	36.3	11.66	4.22	8.14		98.84	4.2
<b>Min</b>	8.97	1.159	0.2	0.114	8.14		48.26	1

Kaolinite was identified as predominant clay minerals in most of the untreated XRD scans (Figure 5.2a). Most of the untreated samples revealed mixed-clay minerals; kaolinite, illite and clinochlore in both shallower and greater depths. The second set of analysis was done on samples, which have been treated with ethylene glycol, and the last set of analysis was performed on these treated samples by heating them to 550°C. The last set of analysis showed that some peaks have disappeared. Hence heating treated samples could help in the distinction between two overlapped peaks (e.g. kaolinite and chlorite). It is apparent from results obtained from treated-heated samples that kaolinite was dominant clay at shallower depth. However, illite appears to be predominant in most of samples collected from deeper core intervals (Table 5.3). Whilst, clinochlore (chlorite) and kaolinite were found together at sandstone / shale contacts. Kaolinite identified in these samples exhibits high crystallinity as indicated from sharp peaks at 001 and 002. Quartz has been also identified in some of clay fraction sample. This quartz probably comprises fine crystals of quartz of less than 2 micrometre in size (Figure 5.3). Scans of bulk powder samples (randomly oriented) reveal group of clay minerals such as kaolinite, illite and chlinochlore (chlorite). Quartz was identified as main component in the Zubair sandstone. Also pyrite was almost found in majority of the samples analysed. Table 5.4 summarises minerals quantified in the clay fraction samples collected from the Zubair Formation.

Table 5.4: summary of quantitative analysis of minerals identified in clay fraction samples of the Zubair Formation weight percentage

	<b>illite</b>	<b>kaolinite</b>	<b>Chlorite</b>	<b>Pyrite</b>	<b>Anatase</b>
<b>Average</b>	42.79	30.35	1.63	1.55	2.49
<b>min</b>	2.673	1.9	0.098	0.21	1
<b>Max</b>	83.77	100	4.755	6.66	2.43

These scans were collected from three batches of samples selected from the studied cores. Figure 5.4 and Figure 5.5 show Gamma-ray log records of two representative wells, on which identified clay minerals can be seen.



2-Theta Scale

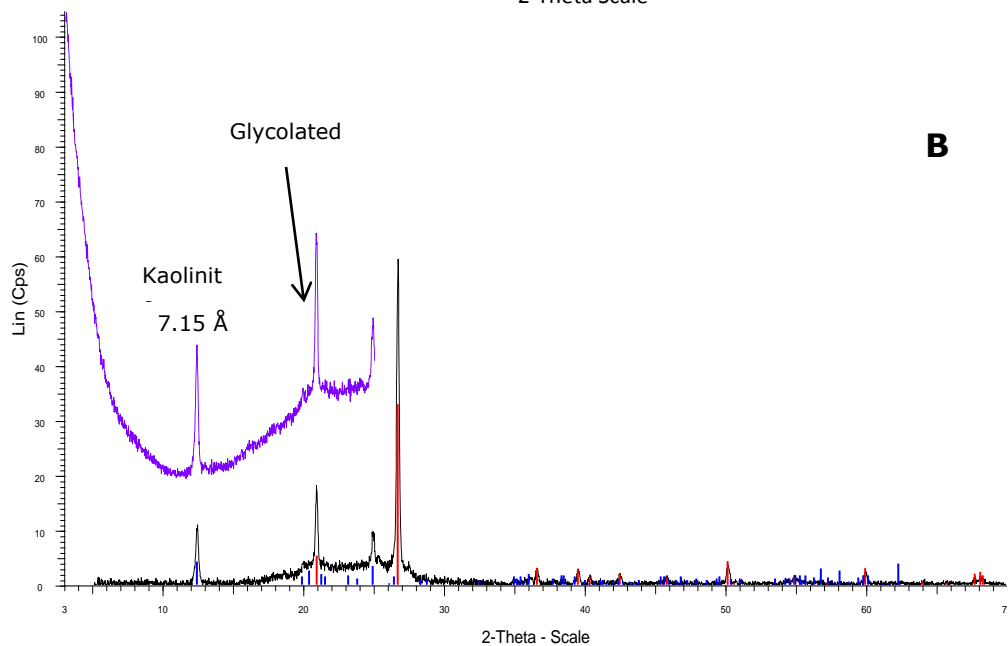


Figure 5.2: (A) XRD spectra of untreated clay fraction collected from well C of depth 3219 m. It shows kaolinite peak is sharp due to high crystallinity. Quartz has also been identified in this sample. (B) XRD spectrum of both glycolated and untreated clay fraction samples. Kaolinite is the only clay mineral identified in this sample.





Figure 5.3: XRD spectra of treated -hated sample from well C. It shows quartz identified within it. Also illite can be seen in this sample.

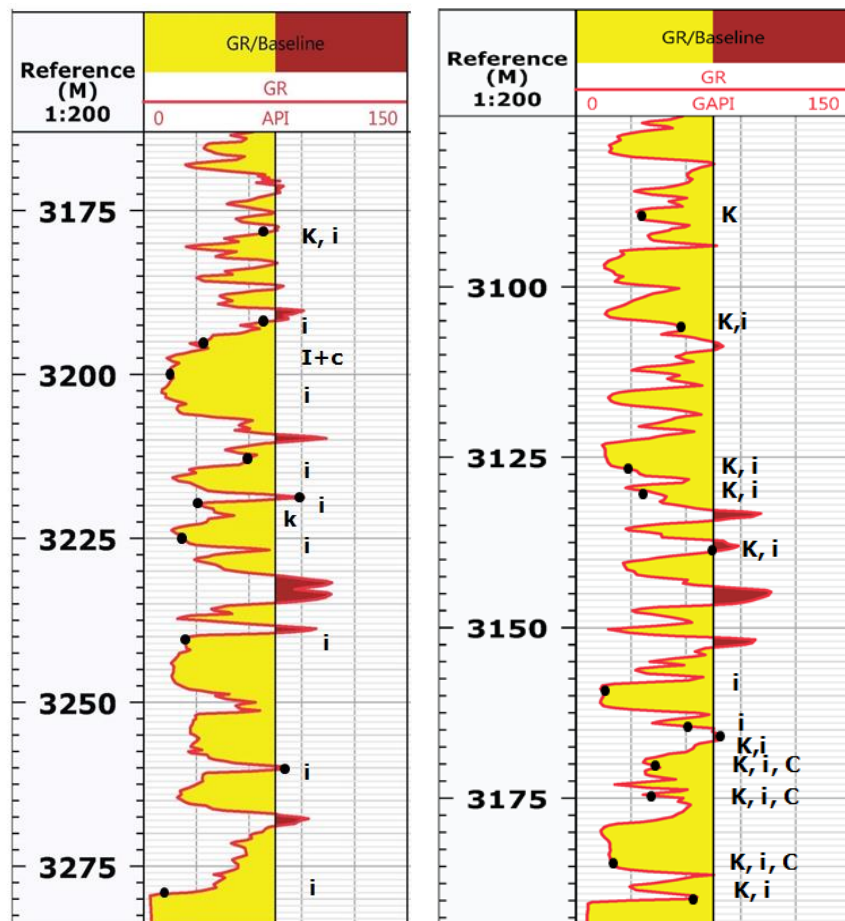


Figure 5.4, Figures 5.5: Distribution of clay minerals, which were identified in two of the studied wells A, D respectively in the Rumaila filed. It can be clearly seen that kaolinite is predominant in shallow depths. While illite increases with burial depth. Chlorite has also been identified at sandstone/shale contacts.

### **5.5.1. Quantitative Analysis of XRD Data**

Complexity of qualitative analysis emerges from precise comparison of XRD scans with standard diffraction patterns of minerals aiming to quantify amounts of the identified phase(s). Minerals' peak positions and their intensities are essential in quantitative analysis. Hence, carefulness in preparation of samples is vital for a successful analysis. Pre-defined peaks (standard) of mineral data are to be used as calibration for effective quantitative analysis of XRD data. Computational modelling of XRD patterns with standard patterns of minerals could be achieved by applying robust analytical software such as the one we have used in this study, which is located at the Williamson Research Centre. It is worth to mention that performing software aided quantitative analysis requires experience in peaks fitting of both experimental and observed (standard) data. Therefore, quantitative analysis in this study was applied on representative XRD patterns, collected from of both clay fraction and randomly oriented powder (bulk samples) by using Diffrac Plus TOPAS 4.2.

### **5.5.2 Results of First Batch of XRD Scans**

Quantitative analysis of the first set of the untreated representative samples reveals that maximum amount of illite is 30.773Wt%, which was found at greater depth at 3276 m. While, minimum amount of illite was at shallower depth (3241m) (Figure 5.6) Highest weight percentage of kaolinite was confirmed to exist at shallow depths of 3241m, 3233m and 3161m respectively(Figure 5.6). Whilst chlorite determined in these samples is sparsely distributed, and only found in three samples. The highest amount was 1.341 wt% at 3161, while minimum amount quantified is 0.59 (Figure 5.6) wt%, which was found at 3421m. Quantitative analysis of ethylene glycol treated-treated samples is based on quantification of clay and non- clay minerals, in which kaolinite was quantified as highest amount at 3233m with wt. % of 50.40, whilst the less amount of it was found at

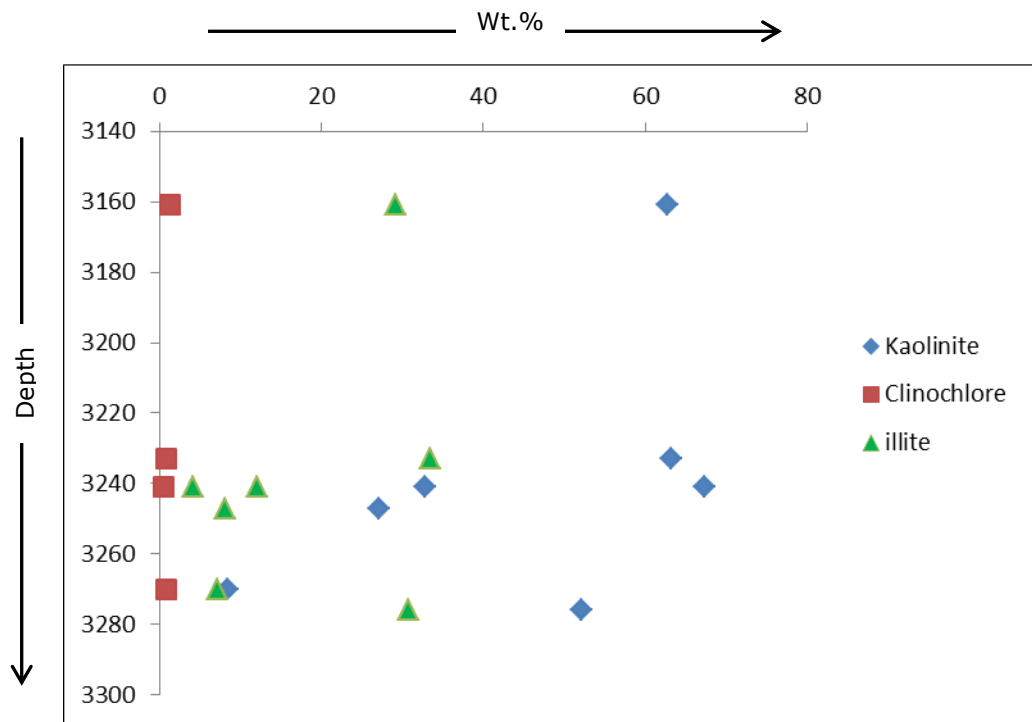


Figure 5.6: Quantitative analysis of untreated clay fraction samples of well A. kaolinite can be clearly seen at as high concentration at shallow depth 3161m. Illite concentration becomes higher with the increasing depth as shown by its wt. percentage of 30.77 at 3276m. However, clinochlore (chlorite) was quantified in two samples only. Minimum concentration was at shallower depth.

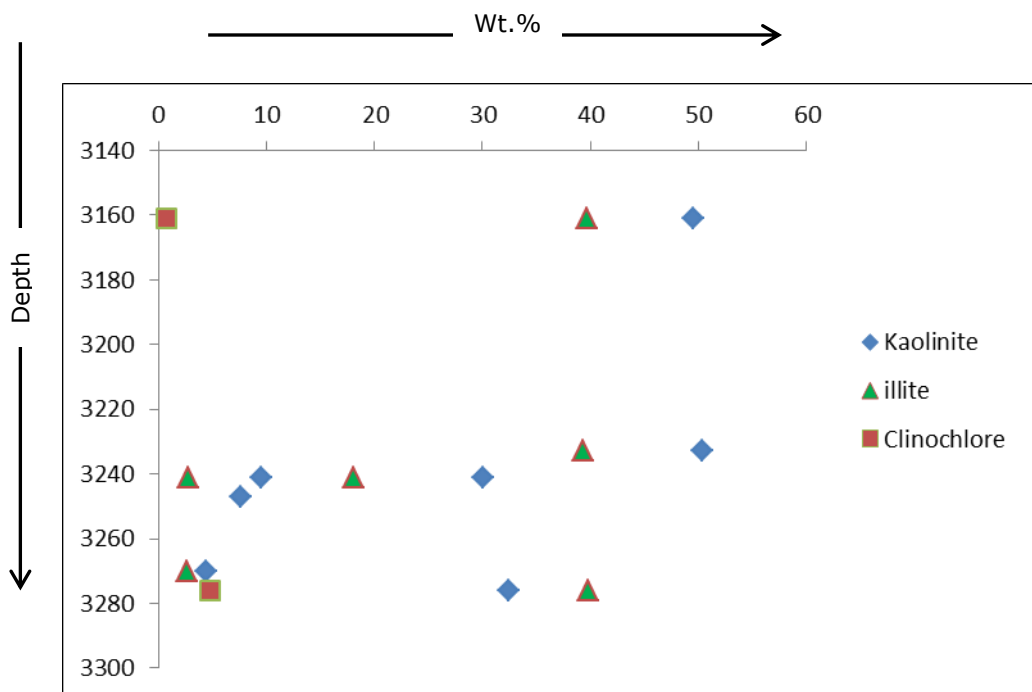


Figure 5.7: Quantitative analysis of ethylene glycol treated-heated clay fraction samples of well A. kaolinite can be clearly seen at as high concentration at shallow depth. While, illite concentration becomes higher with the increasing depth. However, clinochlore (chlorite) was quantified in two samples only. Minimum concentration was at shallower depth.

3270m (4.40 wt. %). Illite wt. % is 39.76 at 3276m. Clinochlore was identified in two of the analysed samples; highest wt. % is 4.755, which was quantified at 3276m. Whereas is was 0.739 wt. % at 3161 m (Fig 5.7). Quantitative analysis of ethylene glycol treated-heated clay fraction samples show the occurrence of pyrite, and anatase. Pyrite ranges between 0.757-6.669 weight percent distributed among four samples. The highest amount of pyrite was determined at greatest depth at 3276m of well A. Anatase was also quantified in two samples 2.437 and 2.211 wt% at 3233m and 3241m respectively (Figure 5.8).

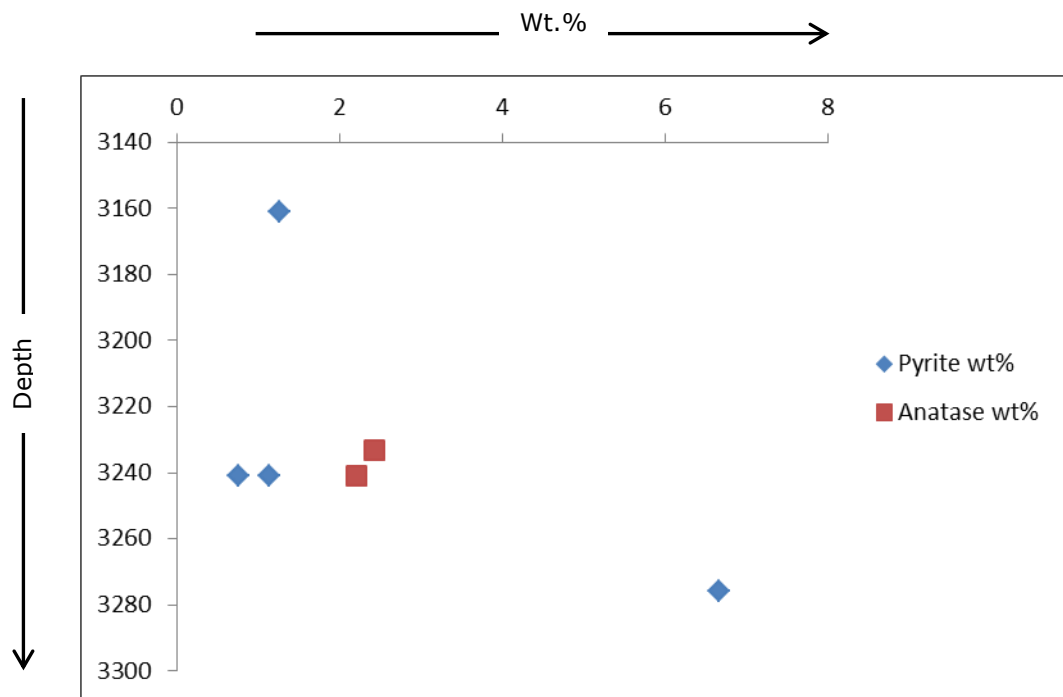


Figure 5.8: Non-clay minerals quantified in Well A. these minerals were identified within clay fraction samples after treating and heating samples to 550°C.

Quantitative analysis of bulk powder samples shows that highest weight percentage minerals is quartz 98.841 at 3247m . Anatase was quantified in three samples 4.278, 1.006 and 2.534 wt% at 3233m, 3270m and 3276m respectively. Pyrite was also identified in four samples in ranges between 0.259-4.221 wt%. Identified illite was quantified in three bulk powder samples. It ranges between 9.079-9.55. Clinochlore

ranges between 0.2- 0.674 wt%, which was identified only in two samples at 3161m and 3233m. While kaolinite is predominant at shallow depth with an average wt% of 17.76. Highest kaolinite weight percentage is 35.362, which was quantified at 3233m (Figure 5.9). Overall trend of clay mineralogy reflects high kaolinite content, followed by illite. On the hand, both pyrite and anatase comprise minerals of medium occurrence.

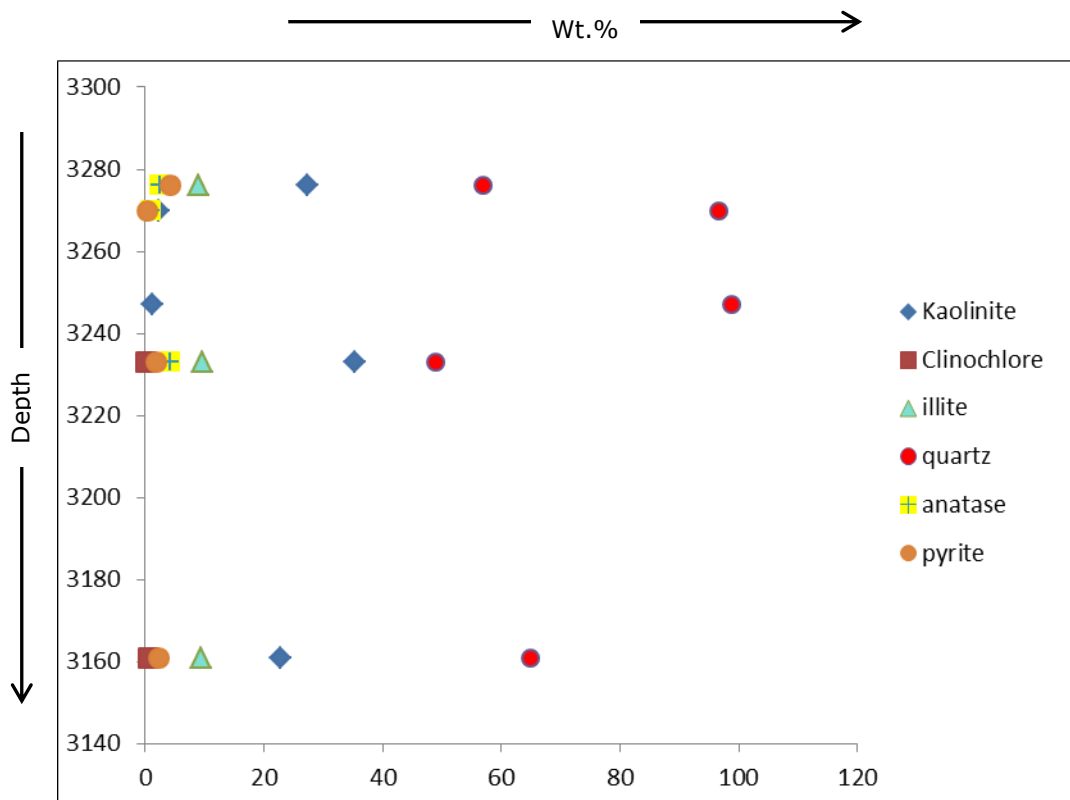


Figure 5.9: Distribution of minerals quantified from XRD scans of bulk powder samples.

### 5.5.3. Results of Second Batch of XRD Scans

The results of second batch of untreated samples reveal three types of clay minerals in these samples. Quantitative analyses of the second batch of untreated samples reveal predominant illite, which increases with depth. It ranges between 56.97-73.34 weight percent. Quantitative assessment of kaolinite displays that minimum amount of it was 12.43 wt% at 3279 m. While highest amount is 33.67 wt% at shallower depth of 3201m. Clinocllore was quantified in three untreated samples. It ranges

between 2.679-5.51. However, it has disappeared from samples after heating them to 550°C (Figure 5.10).

Quantitative analysis of the same samples after treating them with ethylene glycol and heating to 550°C reveals the following weight percentage; Kaolinite wt. % ranges between 1.90-36.10. It decreases at deeper burial depths at 3279m. While illite quantified at same depth (3279m) is 67.583 wt%, which is higher than kaolinite. Chlorite was not found in these samples, except one at 3279m. The quantity of the determined chlorite is 0.09Wt% in this sample (Figure 5.11)

The results of bulk powder XRD scans reveal the occurrence of clay and non-clay minerals. Kaolinite, illite and clinochlore were quantified in these samples. Kaolinite ranges between 2.03-28.10 wt. percent. Kaolinite is quantitatively higher in shallower depth than it in deep burial. Illite remains at nearly same amount, as shown by its quantity determined in three samples out of four. It ranges between 8.97-11.47 wt. %. Clinochlore is the third clay mineral quantified in these bulk powder samples. However, it was found in two samples only with wt. % of 11.66 and 1.41 at 3179m and 3201m respectively. Other minerals quantified in these samples are pyrite, albite, augite pyroxene and quartz. Pyrite ranges between 0.142-1.066 wt. %. The highest amount was determined in deep burial at 3279m (Figure 5.12).

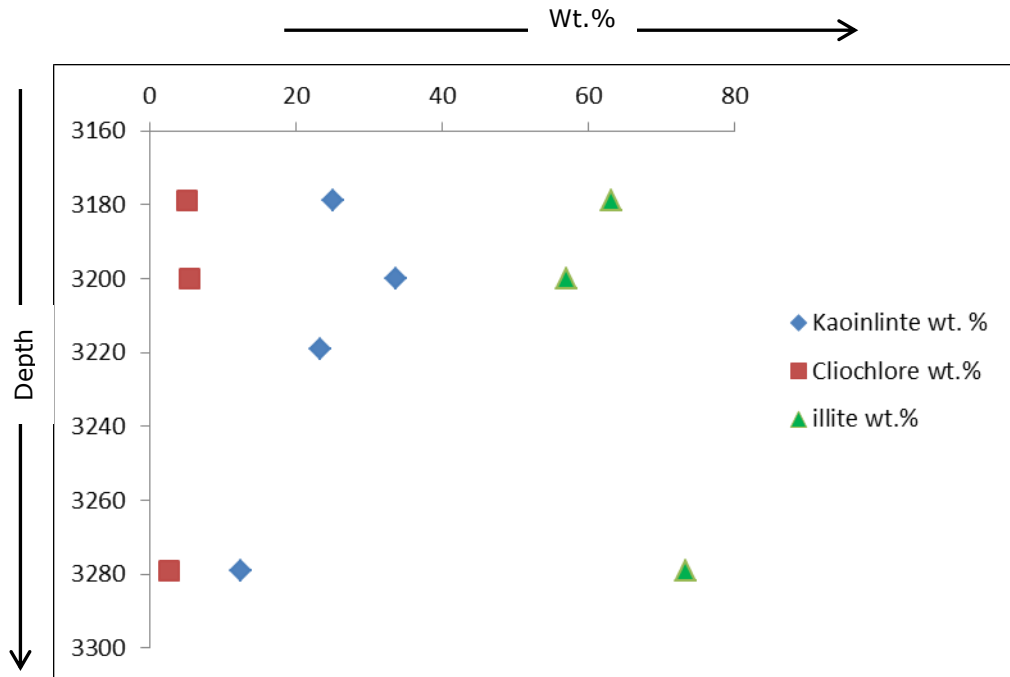


Figure 5.10: Quantitative analysis of clay minerals found in untreated samples of clay fraction. Highest wt % of Kaolinite is quantified at depth of 3201m. Whilst, it declines with continuous burial depth. Illite ranges between 56.97-73.34 wt%. Chlorite wt% ranges between 2.67-5.51.

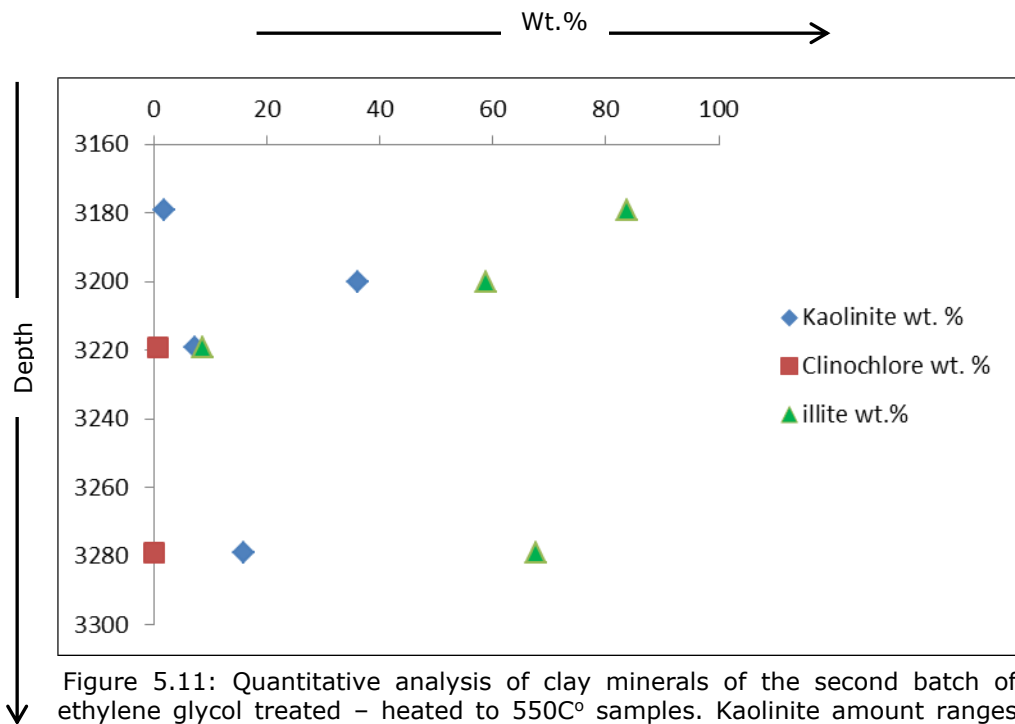


Figure 5.11: Quantitative analysis of clay minerals of the second batch of ethylene glycol treated - heated to 550C samples. Kaolinite amount ranges between 1.92-36.109. It decreases with burial depth. Quantitative analysis of illite exhibits high wt % of illite at greater depth 3279m. Whilst clinochlore is almost not existed in these samples. It was identified in only one of these representative samples at 3279m.

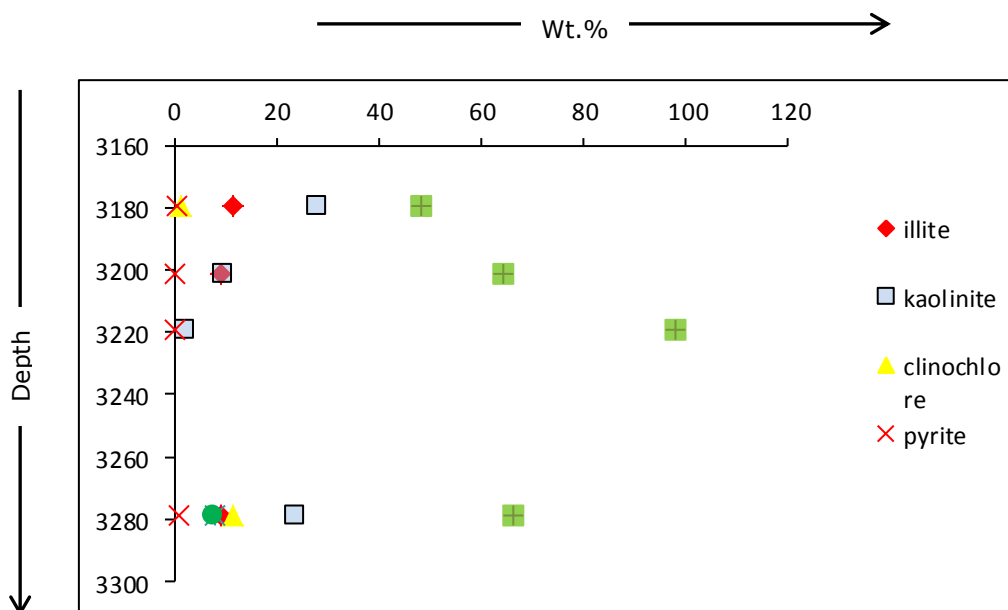


Figure 5.12: Graphical data of quantitative analysis of the bulk powder samples- second batch. Shows that quartz is a main constituent. Followed by kaolinite, which is predominantly found in shallower depths. Pyrite was quantified across depth interval of these samples. In ranges between 0.18-1.06 wt%. Albite was also quantified in one sample at 3200m. Only one sample revealed the occurrence of Augite pyroxene.

#### 5.5.4. Results of Third Batch of XRD Scans

Quantitative analysis of the third batch of untreated samples reveals high content of kaolinite in all of the quantified XRD scans. It ranges between 52.62-70.87 wt. %. Illite has also been quantified in these samples. Highest concentration of illite was at 3188m. Illite weight percent of these untreated samples ranges between 22.34-37.55 (Figure 5.13). Clinochlore in these samples was the less among other clay minerals. Hence, further treatment could confirm whether it is clinochlore or kaolinite. Non-clay minerals were also quantified in the clay fraction samples such as pyrite, which was found in one sample at 3188m. Calcite was in only one sample. The amounts quantified in these two samples are 0.90 and 6.77.



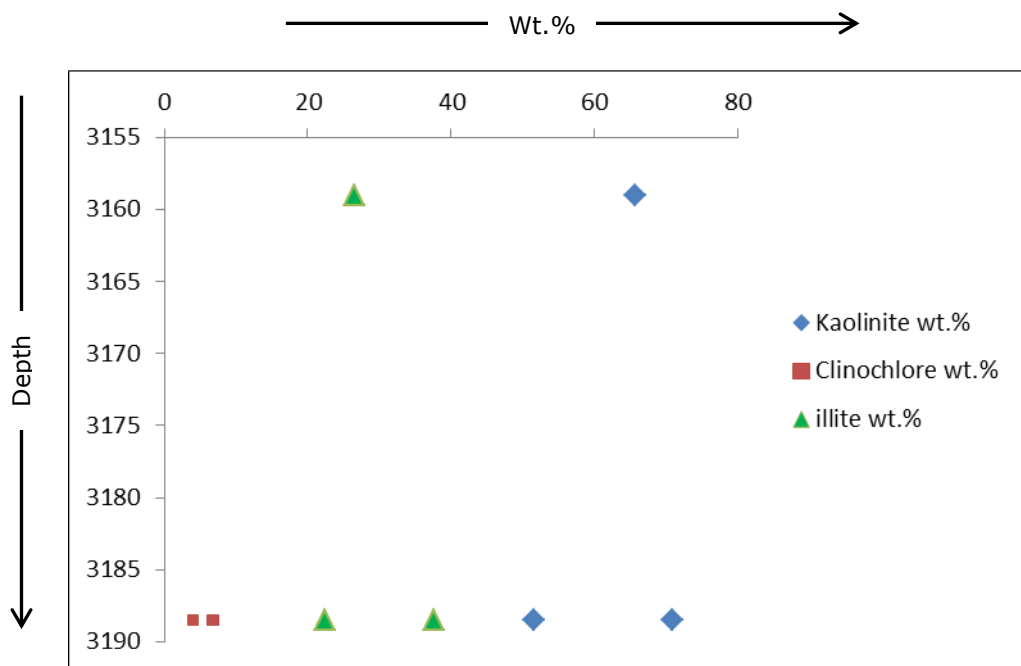


Figure 5.13: Graphical representation of quantitative analysis results of the untreated clay fraction samples. Kaolinite wt. % is nearly the same at 3188 m. Illite wt. % ranges between 22.34-37.55. Graphical representation of Clinochlore wt. % shows that it was found only two samples collected from the same depth 3188m.

Quantitative analysis of the last batch of treated-heated samples reveals high amount of kaolinite at shallower depth at 3159m. Whilst, illite was 36.25 wt.% at the same depth. On the other hand, almost all of Clinochlore identified in the untreated sample has disappeared due to treatment and heating. Hence, Clinochlore was quantified in these treated-heated samples (Figure 5.14)

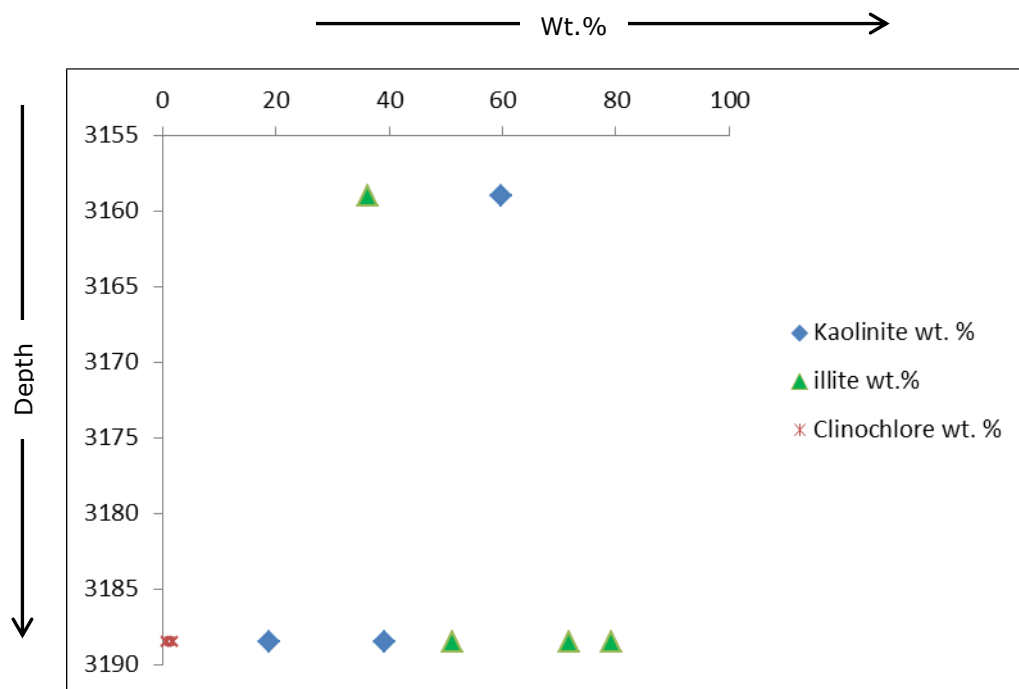


Figure 5.14: Graphical representation of ethylene treated -heated clay fraction samples of the third batch of XRD scans. Kaolinite is 100% at shallower depth of 3169 m. Illite shows high amounts of it at greater depths. At 3188m illite wt% is 71.667 and 51.11 for both samples collected from this depth. Clinochlore shows very small of it 0.66 and 1.92 wt%, as it has disappeared from the first two samples after heating them.

Quantitative analysis of clay fraction samples has also revealed occurrence of some minerals such as quartz, which ranges between 5.042-7.431 wt. %. Pyrite was found in three samples in small amounts ranges between 0.21-0.41 wt. %. Anatase was found in small quantity at sample collected from 3189m. See Appendix 2 for more details of the results of quantitative analysis.

Quantitative analysis of bulk powder of the third batch samples shows a group of clay minerals such as kaolinite and illite. Kaolinite predominantly exists in these samples. Other minerals such pyrite and quartz were quantified in these samples. Quartz comprises a predominant constituent in the quantified XRD scans with a range between 63.583 - 77.97 wt. % (Figure5.15).

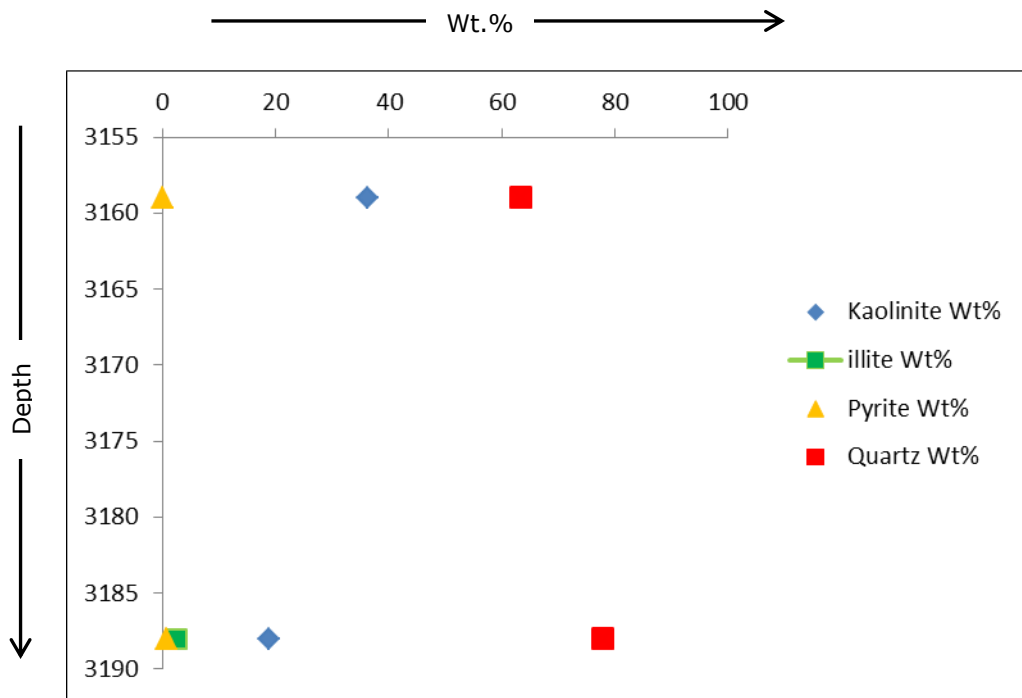


Figure 5.15: Graphical distribution of minerals data found in the third batch of bulk powder samples.

Minerals identified in the analyzed samples are summarized in tables 5.4, 5.5 and 5.6.

Table 5.5: Minerals identified in the first batch of samples, including clay minerals identified in each one of the three levels of the analysis; Air-dried, Ethylene Glycolated and treated – heated.

Depth	Air-dried	Ethylene Glycol Treated	Treated-Heated
	Quartz Kaolinite	Quartz Kaolinite	kaolinite
Depth 3090	Illite clinocllore	Illite clinocllore	
3106.5	Kaolinite Illite	Kaolinite Illite	Kaolinite Illite quartz
3127.1	Kaolinite	Kaolinite	Kaolinite quartz
	Illite	Illite	Illite
3131.33	Kaolinite Illite clinocllore calcite	Kaolinite Illite clinocllore calcite	kaolinite
3140.83	quartz Kaolinite	quartz Kaolinite	kaolinite illite
3143	Quartz Kaolinite Illite clinocllore	Quartz Kaolinite Illite	
3159	kaolinite illite	kaolinite illite	quartz illite
3164.75	Quartz Kaolinite Illite clinocllore	Quartz Kaolinite Illite clinocllore	quartz illite

	calcite	calcite	
3166.5	Quartz Kaolinite illite calcite	quartz Kaolinite illite calcite	quartz kaolinite illite
3169.5	kaolinite illite calcite	kaolinite illite calcite	quartz illite clinocllore
3171	Kaolinite  Illite	Kaolinite Illite clinocllore	Kaolinite Illite clinocllore
3175	Kaolinite Illite clinocllore	Kaolinite Illite clinocllore	Kaolinite Illite clinocllore
3187.5	Quartz Kaolinite Illite clinocllore	Quartz Kaolinite Illite	
3188	Kaolinite Illite clinocllore	Kaolinite Illite clinocllore calcite	Kaolinite Illite clinocllore
3189.5	Kaolinite Illite	Kaolinite Illite	Kaolinite Illite pyrite

Table 5.6: Minerals identified in the second batch of samples, including clay minerals identified in each one of the three levels of the analysis; Air-dried, Ethylene Glycolated and treated – heated.

Depth	Air-dried	Ethylene Glycol Treated	Treated-Heated
3178.31- 3179.31	kaolinite illite quartz clinocllore	kaolinite illite quartz clinocllore	kaolinite illite quartz clinocllore
3192.50- 3193.5	kaolinite illite quartz clinocllore	kaolinite illite quartz clinocllore	illite
3194.50- 3195.50	kaolinite illite clinocllore quartz calcite	kaolinite illite clinocllore quartz calcite	illite
3199.50- 3200.48	kaolinite illite quartz clinocllore	kaolinite illite quartz clinocllore	illite quartz clinocllore
3200.48- 3201.48	kaolinite illite chlorite quartz calcite	kaolinite illite chlorite quartz calcite	illite
3213.75	kaolinite illite clinocllore quartz calcite	kaolinite illite clinocllore quartz calcite	illite  quartz
3218.59-	kaolinite	kaolinite	kaolinite

3219.59	quartz	quartz	
3220.59-3221.59	kaolinite illite	kaolinite illite	illite
3225.5-3226.5	kaolinite illite clinochlore calcite	kaolinite illite clinochlore calcite	illite
3241.56-3242.56	kaolinite illite clinochlore	kaolinite illite clinochlore	illite
3245.55-3246.55	kaolinite illite clinochlore calcite	kaolinite illite clinochlore calcite	quartz illite clinochlore
3259.54-3260.52	kaolinite illite quartz	kaolinite illite quartz	illite
3278.54-3279.54	kaolinite illite quartz calcite	kaolinite illite quartz calcite	illite

Table 5.7: Mineralogical content identified in the third batch of the X-ray diffractometry scanned samples.

Sample no.	Depth	mineralogical content
1	3161-3162	quartz kaolinite illite pyrite
2	3163-3164	quartz kaolinite illite clinochlore pyrite
3	3199-3200.83	quartz kaolinite illite pyrite
5	3162-3163	quartz kaolinite illite pyrite
7	3195.3-3196.97	quartz kaolinite illite clinochlore pyrite
10	3232.95-3233.95	quartz kaolinite illite pyrite
10'	3232.95-3233.95	quartz kaolinite

		illite clinocllore pyrite
11	3237.90- 3238.90	quartz kaolinite pyrite
13	3240.88- 3241.88	quartz kaolinite pyrite
13`	3240.88- 3241.88	quartz kaolinite
16	3246.23- 3247.20	quartz kaolinite illite
16`	3246.23- 3247.20	quartz kaolinite
17	3248.19- 3249.15	quartz kaolinite illite pyrite
18	3256.09-3257	quartz kaolinite
19	3254.10- 3255.10	quartz kaolinite illite pyrite
20	3269.19- 3270.19	quartz kaolinite illite pyrite
20`	3269.19- 3270.19	quartz kaolinite pyrite
21	3278-3279	quartz kaolinite illite pyrite

## 5.6. Results of Scanning Electron Microscopy

In this section I present a number of observations, which were made using the Environmental Scanning Electron Microscope ESEM facility located in the Williamson Research Centre. A number of representative samples were selected from the from the study area. Observation encompassed morphological features, distribution of clay minerals, identification of other minerals, porosity and crystallinity. These observations reveal that kaolinite is predominant in the study samples collected from the Zubair Formation. Polytypes of kaolinite were observed in a few samples (Figure 5.17 and 5.18). Well-developed authigenic kaolinite was

identified as large crystal clay mineral, which coexists with flakes or platelets of kaolinite (Figure 5.19). Anhydrite crystals were identified in some of these samples (for example well developed crystals of Anhydrite at sample collected from well C at 3019.30; Figure 5.20). Prismatic anhydrite identified in Well C was identified by correlating its EDX with typical EDX spectrum after (Welton, 1984) (Figure 5.21 and 5.22). Massive detrital illite was also identified in the study samples. However, it was not easy to distinguish between illite and kaolinite due to this morphology. This illite comprises sets of platelets, which are organised in parallel orientation (Welton, 1984). As this type morphology is not easily identifiable from ESEM images (Figure 5.23), the identification of this massive detrital illite was confirmed with the aid of EDX spectrum (Figure 5.24). Mica of sheet-like morphology was identified in Well D at 3119.40m. SEM observations reveal it is distributed as pore filling (Figure 5.24). Pyrite was identified in few samples. It occurs as framboidal pyrite or rhombic pyrite crystals (Figure 5.25). The mode of occurrence observed in some of the study samples at Well C was pore filling pyrite (Figure 5.25).

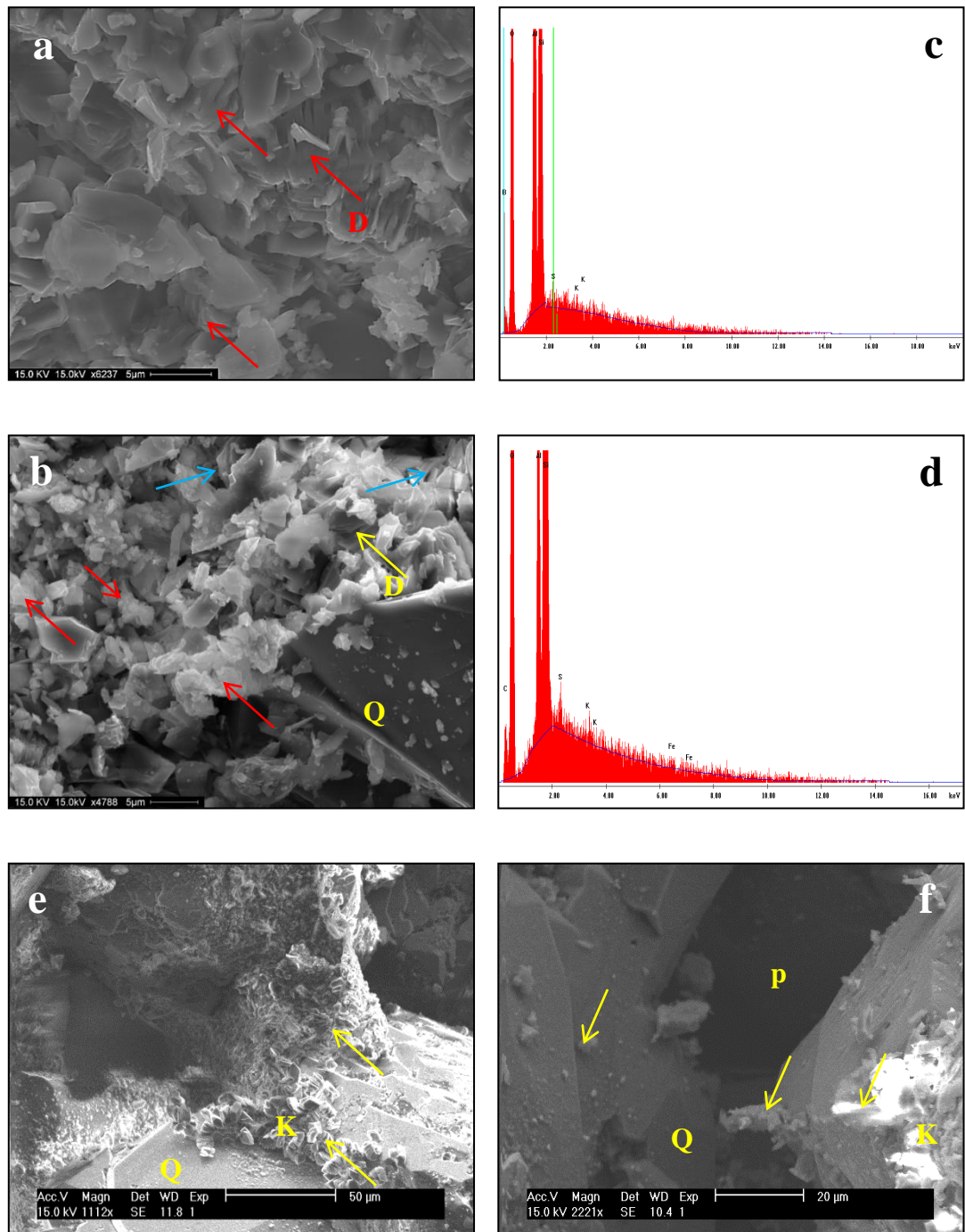


Figure 5.16: (a) Red arrows denote coarse kaolin mineral booklets of dickite (D). (b) SEM of thin kaolinite plates, which appear as small plates (red arrows) found in sample collected from depth of 3178m of the Zubair Formation. These thin plates of kaolinite are coexisting with larger and well developed crystals of kaolinite (yellow arrow). Whilst, blue arrows denote booklet of dickite (D) closing entirely pore spaces within these sandstones. As kaolin minerals are inundated by quartz overgrowth (Q). (c) is a graph of EDS spectra inside dickite, in which the elemental analysis shows: O, Al, Si, S, and K. (d) elemental analysis observations within a larger field of view of this sample reveal these elements: C, O, Al, Si, S, K, and Fe. (e) SEM image of the same sample shows pore lining kaolinite booklets K ( yellow arrows )and quartz grains Q. (f) pore lining kaolinite over quartz grains (yellow arrows) dark space P represents pores.



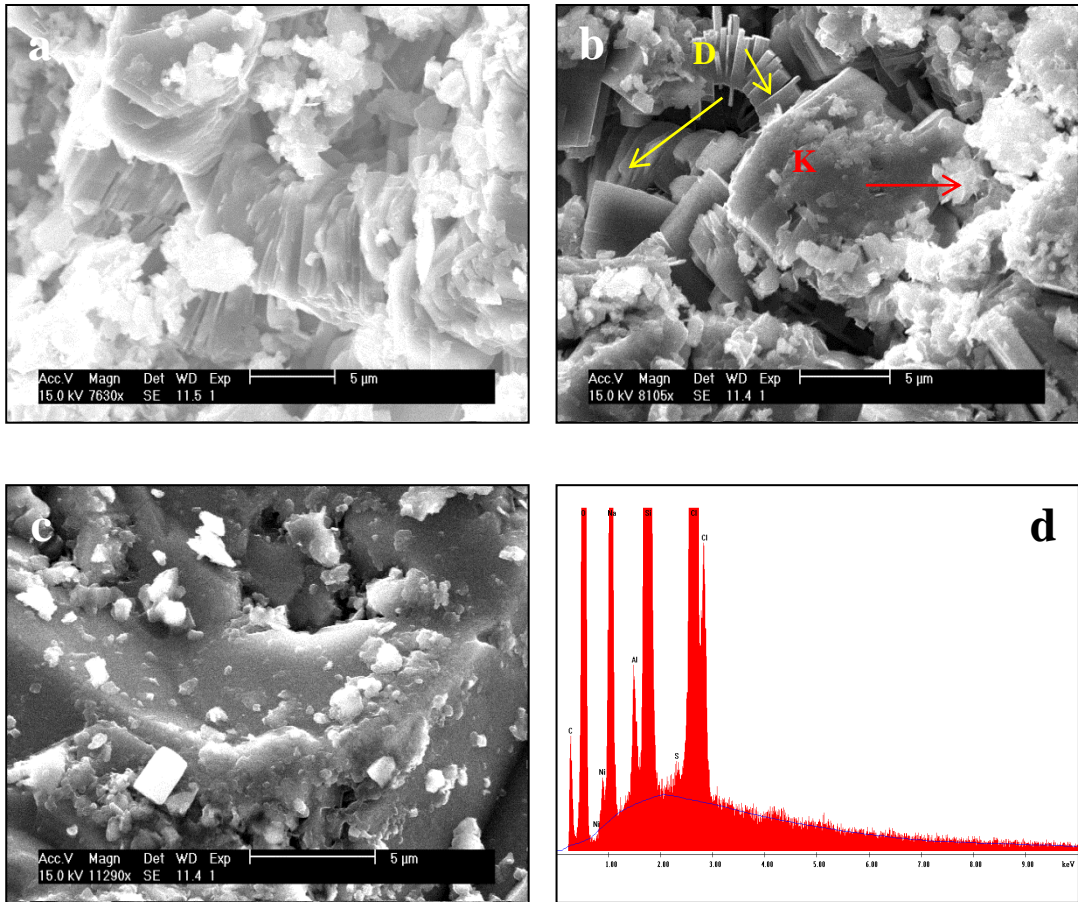


Figure 5.17: Polytype kaolinite identified in deeper samples (a) kaolinite booklets mixed with kaolinite flakes (b) Dickite D as shown in yellow arrows, kaolinite flakes K- red arrow. (c) Kaolinite flakes at 1129X (d) EDX spectra of kaolinite.

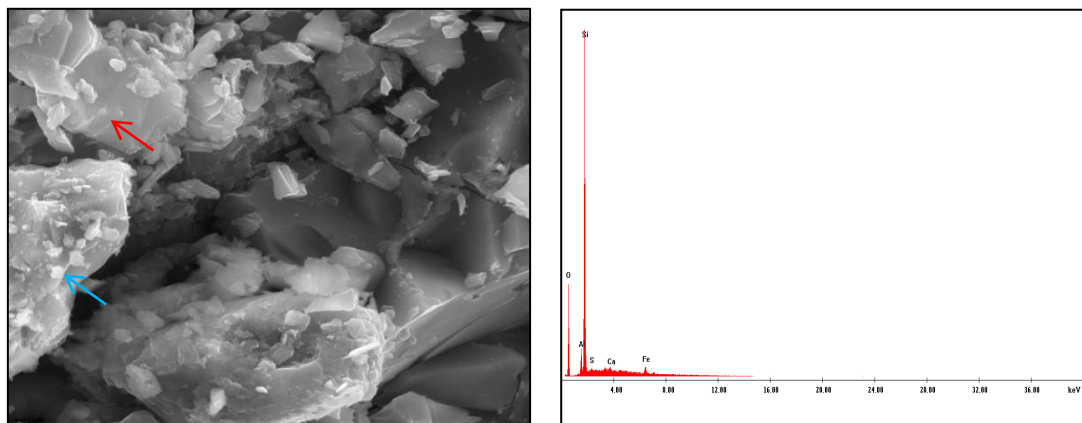


Figure 5.18: SEM image of well-developed authigenic kaolinite (red arrow), which appear big crystal. This kaolinite is coexisting with thin flakes or plates of kaolinite (blue arrow).

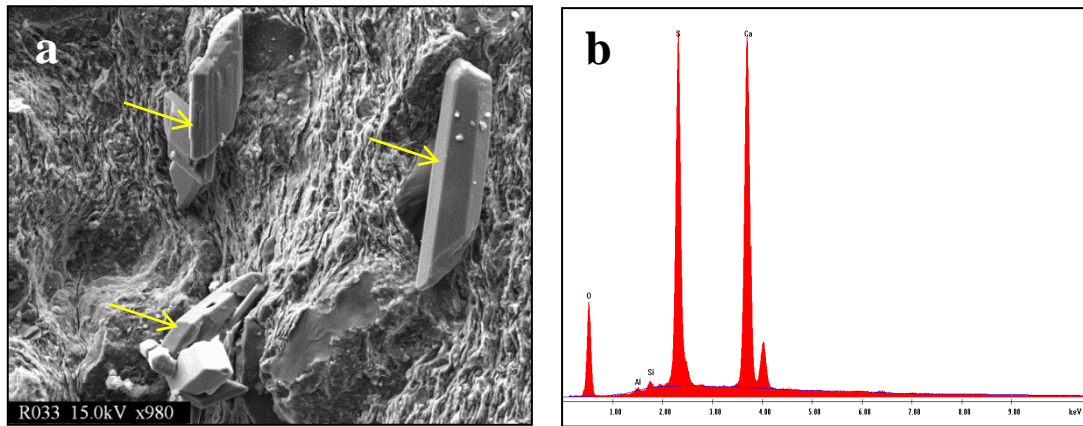


Figure 5.19: (a) SEM image of well-developed anhydrite crystals Well D taken from depth of 3091.30 m (yellow arrows). (b) EDX spectra shows elemental analysis of these crystals, which reveals the occurrence of major element Al, Sand Ca with minor amount of Si and Al.

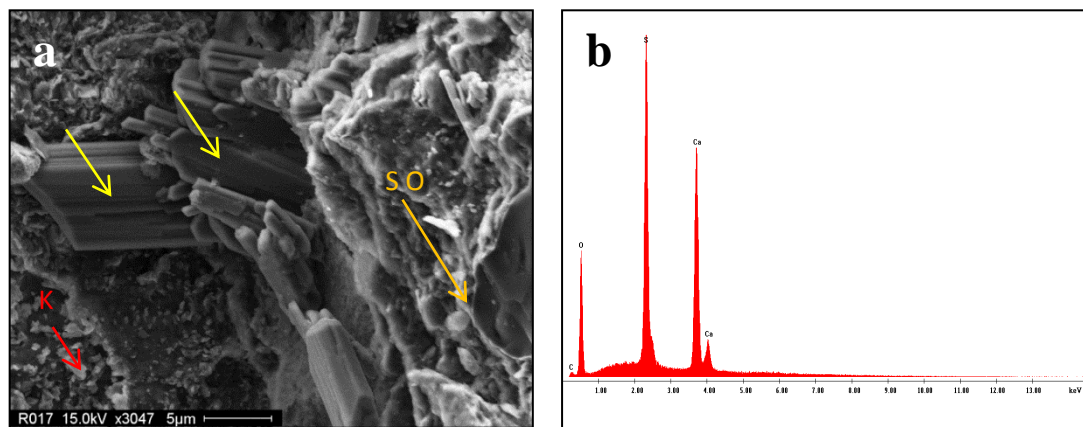


Figure 5.20: (a) Anhydrite crystals (yellow arrows) can be clearly seen in this sample, which is located at 3162.5m of Well C. We can also see pore lining kaolinite particles K (red arrow) and silica overgrowth (SO) (amber arrow). (b) EDX spectrum of prismatic kaolinite identified, the elemental analysis shows that major elements are S and Ca.

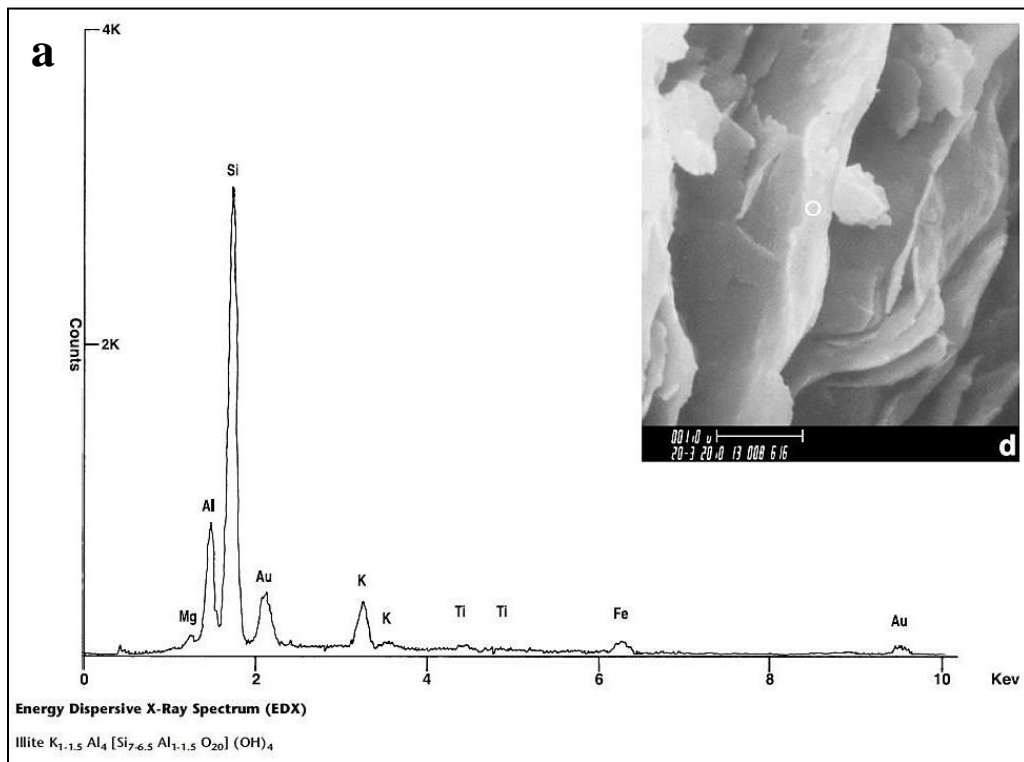


Figure 5.21: (a) Massive detrital illite, which has flaky morphology platelets and its EDX (Welton, 1984)

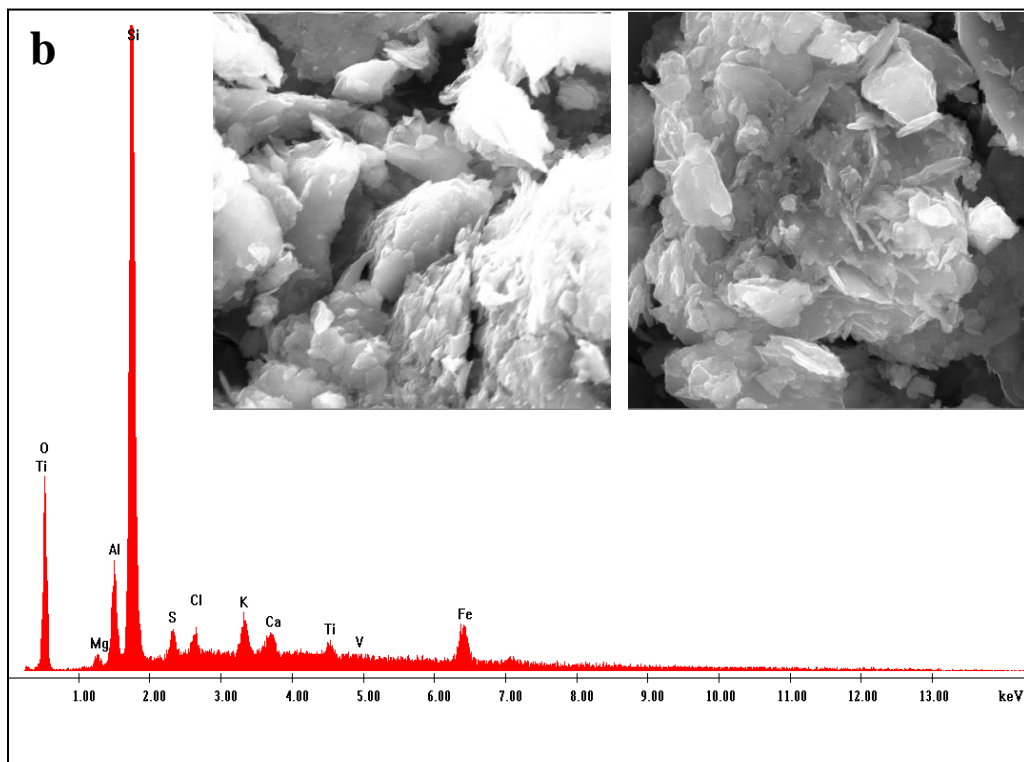


Figure 5.21: (b) illite flake-like morphology identified in Well D. Both images show parallel platelets of illite. The EDX collected of this sample

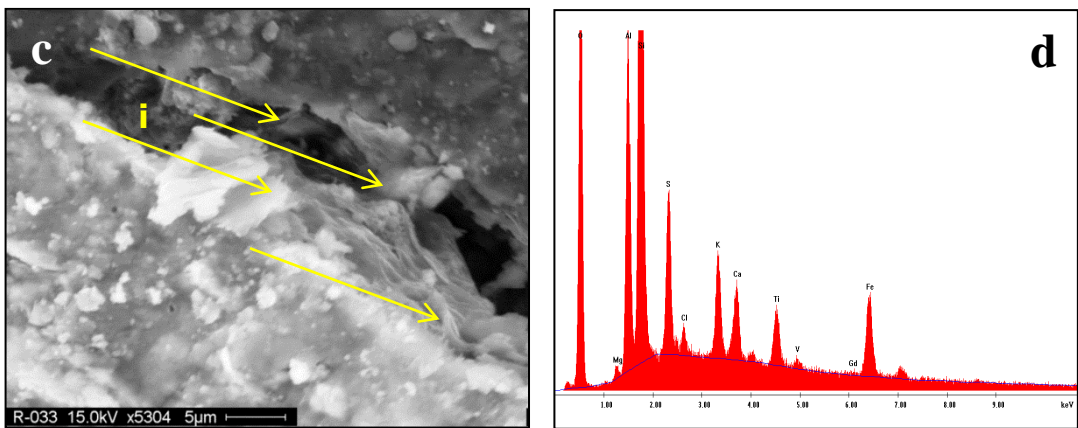
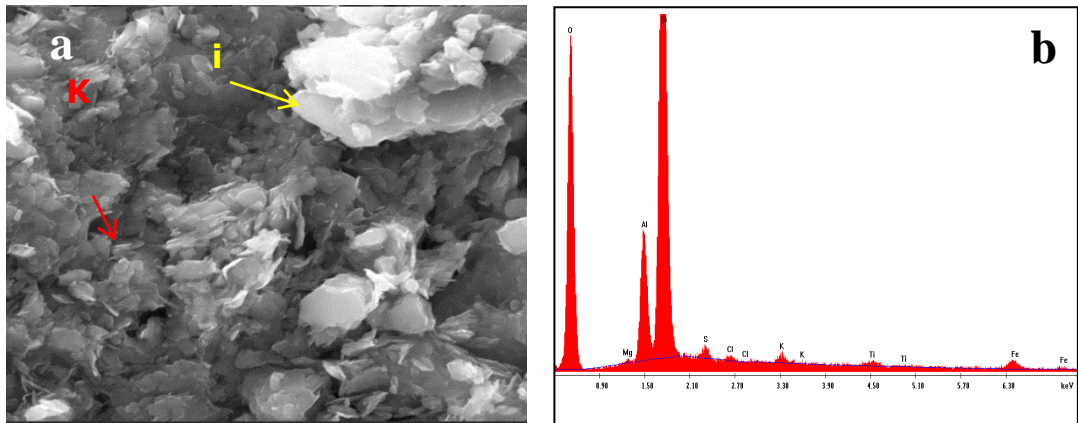


Figure 5.22: (a) detrital illite (yellow arrow) and pore filling kaolinite (red arrows, which were identified at 3166m . (b) EDX spectra of illite produces minor amounts of mg, s, cl, k, Ti and Fe with major elements; Al and Si. c) illite (i) pore bridging fibers can be clearly seen in sample (yellow arrows). (d)EDX spectrum collected from this sample, containing illite of fibrous morphology.

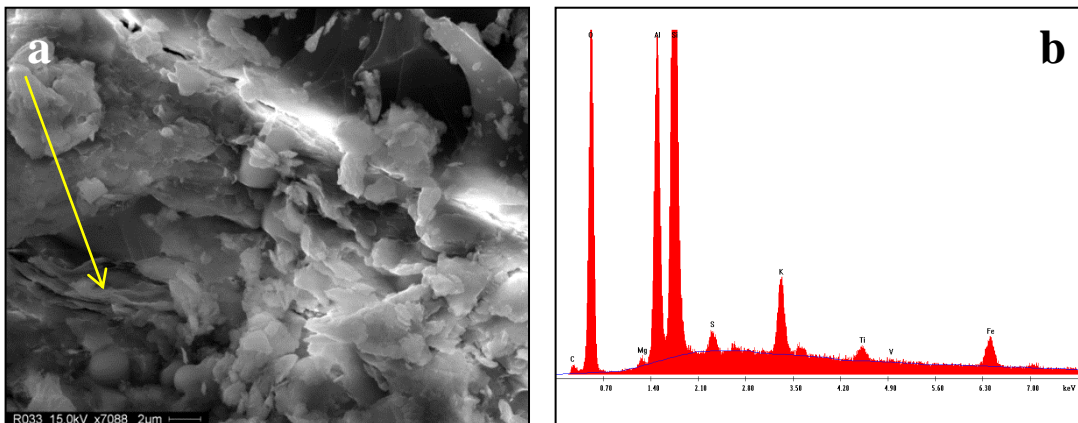


Figure 5.23: (a) SEM microgram shows mica of sheet like morphology identified in Well D at 3119.40 m (yellow arrow). Observation of this mica shows that it distributed as pore filling. (b) EDX spectrum collected from this sample. Elemental analysis of this sample shows major elements are Al and Si and minor elements include Mg, S, K, Ti, and Fe.

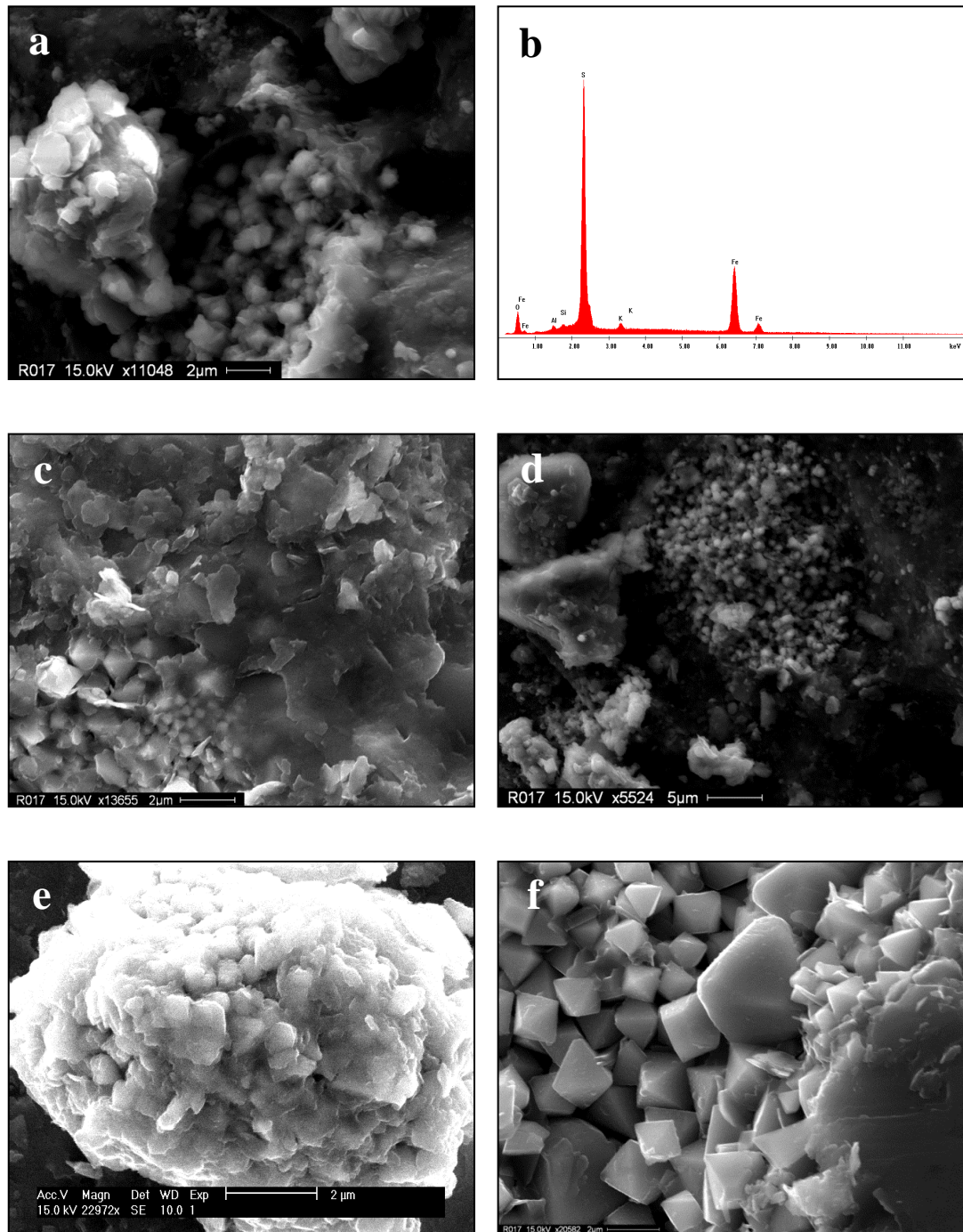


Figure 5.24: (a) Pore filling framboidal pyrite identified in sample collected from well C. (b) EDX micrograph produced for this sample. (c) Pore filling pyrite associated with flakes of pore filling kaolinite. (d) SEM microgram of the same sample with larger field of view. (e) Magnified pyrite framboid. (f) Magnified pore filling pyrite.

## 5.7. Discussion and Conclusions

Although authigenic overprint of the Zubair Formation is subaltern, but it could be effective on a small scale i.e. local scale. As I mentioned earlier, petrographical interpretation of the Zubair Formation is based on previous work, which reported the occurrence of quartz overgrowth, kaolinite, feldspar, rutile in trace amounts, siderite and pyrite, ferric oxides as rock fragments, amber and glauconite (Hmood, 2002, Al-Muhalhal, 2004).

Quartz overgrowth was observed in the Zubair Formation thin sections. It comprises cement material within its sandstone framework. This overgrowth appears as dust ring around quartz grains. Hence it appears in optical continuity with quartz grains. Kaolinite appears as pore filling and pore lining as shown in SEM images. Observation of clay minerals shows polytype kaolinite exists in some the study samples. As both kaolinite and dickite were identified (Figure 5.20). Transformation of kaolinite into dickite is congruent to temperate increase with burial depth. According to Zimmerle and Rösch, 1990 cited in Cuadros et al., 2014) hydrothermal processes control dickite occurrence. They also came into conclusion that dickite is associated with hydrothermal mineralisation, coalification, thermal flow conditions, which most likely to be in porous and preamble lithology. SEM-aided identification of kaolinite shows that it is mainly a pore filling clay mineral, where replacement of feldspar was probably caused by kaolinite. Authigenic kaolinite looks very well crystalized as indicated by its sharp peak on XRD spectra collected for these samples. Based on quantitative analysis, kaolinite wt. % ranges between 1.9%-100 % of the clay fraction samples with an average wt. % of 30.35. Quantitative analysis of bulk powder samples reveals the maximum wt. percent of kaolinite is 36.3%. Average wt. % of kaolinite is 17.45, and it ranges between 1.159-36.3 (Table 5.3). This kaolinite was found as kaolinite of blocky

morphology and also as booklets of dickite were identified together in facies D of silty sandstone with high argillaceous material, bioturbation, with lenticular sand stones (very fine sandstones), which represent prodelta facies. This kaolinite is mostly distributed as pore filling. However, it does not appear to have significant impact on porosity and permeability of these reservoir rocks.

Illite was identified in the clay fraction of the Zubair. Illite weight percentage increases with burial depth, which proves hypothesis of illitization. As well as illitization becomes more with temperature.

Mineralogical characterisation reveals that pyrite wt. % in the analysed sample was not significant. Nevertheless, qualitative and quantitative analysis of XRD datasets and SEM observations of pyrite reveal that it was identified in quite few samples.

# Chapter 6

---

**Pore Scale Characterisation of Mineralisation within the Zubair Formation Using X-ray Computed Tomography and Well log Analysis.**





## **Chapter 6**

### **Introduction**

In Chapter 3 I described and identified facies associations that comprise the Zubair Formation based on cored intervals and well logs collected from the Zubair Formation. We have also mapped petrophysical properties and up-scaled them on each facies identified in the study area within the Rumaila field. 13 lithotype have been identified in the Zubair Formation. In this chapter we present X-ray CT micro imaging performed on 6 samples, which were selected from the studied facies of grain size ranges between very fine-medium. The objective of using X-ray CT analysis to examine the Zubair sandstones at micro-scale is to provide more detailed knowledge of mineralisation related to flow heterogeneity.

This chapter is organized as follows:

Background of X-ray CT micro- imaging

Scientific rationale

Configuration of X-ray CT micro- imaging

Image segmentation

Permeability test

Results of permeability tests using XLab hydro extension.

Well log analysis using Techlog

Discussion

## 6.1. Background

X-ray computed tomography (CT) is an established and rapidly evolving technology of proven value for geological investigations (Ketcham and Carlson, 2001). Wilhelm Röntgen discovered X-ray radiation which has been used in many fields of research. Back to 50 years ago, radiographic imaging has been used in geosciences to examine the internal structure of wide range of geological specimens. The main disadvantage of X-ray CT technique is the lack of capturing 1D information (Cnudde and Boone, 2013). In the 1972, a new technique called Computerized Transverse Axial Tomography CAT was adopted (Ambrose, 1973, Hounsfield, 1973). It was widely used for medical applications, in which computer algorithms are used to construct 3D volume from set of projection images acquired from different directions (Gawler et al., 1974). CAT has also been applied later to geosciences (Wellington and Vinegar, 1987). Beer's law on X-ray is capable of penetrating material at varying degree, as this is mathematically represented by Beer's law as follows:

$$I = I_0 e^{-\int \mu(s) ds} \quad (1)$$

Where

$I_0$  is beam intensity and the local linear attenuation coefficient is  $\mu(s)$  over the ray path  $s$ . It can be inferred from equation (1) that the coefficient of integrated linear attenuation can be derived at each point of the image produced by x-rays (radiograph) as shown below:

$$\int \mu(s) ds = -\ln\left(\frac{I}{I_0}\right) \quad (2)$$

If a 3600 rotational movement applied to the sample mounted adjacent to the X-ray source and detector system, then a number of angular projection images can be made (Cnudde and Boone, 2013).

The use of X-ray computed tomography in geosciences has become one of the most common techniques used to image geologic samples (Ketcham and Carlson, 2001, Rivers et al., 2004).

The study of large core samples involves both outer surface and the internal structure such as fractures, bedding, mineralization, organic matter, cementation, density, and grain size (Orsi et al., 1994, Coles et al., 1998).

The study of large core samples can be performed using medical CT and custom bay industrial CT systems. In terms of high radiation exposure, the industrial CT has no constraints on the amount of radiation dose, The voxel size of 250 micron is often applied to large core samples to achieve better spatial resolutions (Ketcham and Carlson, 2001, Baraka-Lokmane et al., 2009). Data acquisition using medical CT scanners has become better in terms of data acquisition speed, image quality and the amount of absorbed radiation dose. The recent advances have presented new generations of medical CTs. such as dual-energy (Primak et al., 2007). Less 100 milliseconds temporal resolution has been improved in modern medical CT (Flohr et al., 2009). However, the spatial resolution persists limited to a few hundreds of microns due to constraints on the object's dimensions (Cnudde and Boone, 2013).

In the 1980s, micro-CT was introduced as a new research method represented by three main types; X-ray tubes (Sato et al., 1981, Elliott and Dover, 1982), sources of gamma-ray (Gilboy et al., 1982) and synchrotron X-ray source (Grodzins, 1983 , Flannery et al., 1990). The rapid advancement of both X-ray tubes or lab-based and

synchrotron-based micro-CT systems has continued through the years, whilst gamma-ray sources are uncommonly used. The spatial resolution of 200 $\mu$ m can be used to distinguish between CT and micro-CT as this resolution can be achieved by medical CT systems. The ability of micro-CT scan to image much fine detail allows it to be used in geoscience studies. (Rosenberg et al., 1999) discuss the beginnings of using micro-CT applications in digital rock analysis and relevant fields were in 1990s. 3D visualization of pore structures has also been applied to micro-CT data by Carlson et al., (2000). X-ray micro CT technique can be used as 3D petrographic tool, which can also be used to extract quantitative petrophysical data (Van Geet et al., 2001). In geological applications micro-CT based studies, sample size ranges from 1mm-5cm (Cnudde and Boone, 2013). The internal structure of a porous medium and the physical properties of the fluids and solid components within the pore space define its macroscopic properties (Øren and Bakke, 2003). Some core large-scale features within bore cores can be identified at low resolution (60 $\times$ 60 $\times$ 60 $\mu$ m) by scanning it using medical CT (Orsi et al., 1994).

## **6.2. The Rationale behind Using X-ray Micro CT for This Research**

The Zubair Formation is one of the major hydrocarbon reservoirs within southern Iraq. Due to the poor curation of historical core data of the Zubair Formation, a non-destructive technique such as X-ray computed tomography would be valuable to improve the understating of the influence of dendritic pyrite mineralisation upon the trapping and transfer mobile geofluids, by applying finite volume based flow solver to the collected images. Applying comparative studies on segmented images collected by X-ray computed tomography of both mineralised and unmineralised samples, will

greatly improve the understanding about flow physics upon sandstone reservoirs rather than using standard petrophysical core analysis.

### 6.3. Micro-CT Scanning Configuration

The rotational movement of the scan in medical CT differs from it in micro-CT. The system of X-ray source and detector in medical CT rotates around the patient's body, whilst in micro-CT the object under study rotates and X-ray source and detector system remains steady (Cnudde and Boone, 2013) (Figure 6.1). In order to achieve the best resolution, it is important to apply this setup.

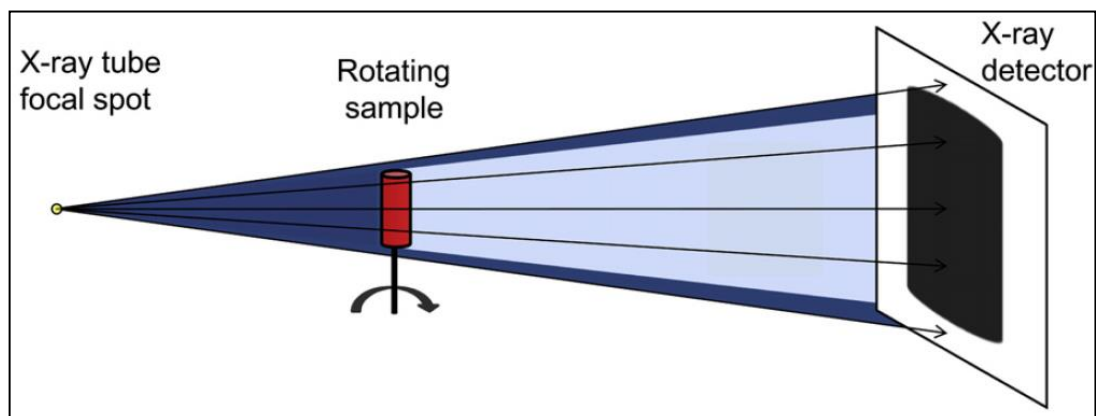


Figure 6.1: Diagram shows typical set up for a lab based micro-CT where conical X-ray beam helps getting geometrical magnification (Cnudde and Boone, 2013).

### 6.4. Methods and Imaging Techniques

A significant source of uncertainty within the Zubair Formation is the controls upon hydrodynamic pressure distributions. By providing a more detailed knowledge of mineralization related to flow heterogeneity using X-ray computed tomography, this uncertainty can be reduced. Micro-CT images provide 3D volume rendering of the samples used in the SM/EDS analysis showing the distribution of the mineralogy in the sample volume. In this section I will cover methods and techniques used to prepare samples, X-ray CT data acquisition, and image reconstruction as follows:

#### 6.4.1. Sample Preparation

Selected core samples were cut by using rotary cutting and grinding tool as shown in the attached video clip (see enclosed DVD). The diameter of the selected samples ranges between 5-7 mm. These samples were mounted on metal stubs by using super glue (Figure 6.2), and then placed on the Nikon Metrics XTH 225 system rotating stage. Samples analysed are listed in (table 1.4).



Figure 6.2: Core sample taken from larger sample. This sample was cut using rotary cutting tool. The core diameter is 6mm.

#### 6.4.2. X-ray Micro CT Data Acquisition

A total of 8 representative core samples were taken from 6 wells. These samples were cut and prepared and placed on the rotation stage of Nikon Metris XTH 225 at Henry Moseley X-ray imaging facility at Manchester University (Fig 6.3a and b). The diameter of core samples ranges between 5-7 mm and the voxel resolution is 5 micron. An additional scan of core material (80mm diameter) was obtained to assess the macroscopic distribution of the mineral assemblage of the dendritic pyrite of the sample imaged (Figure 6.6). Micro-CT scanning can be performed on samples of different size, shape and composition. Therefore there is no standardised protocols for

X-ray CT scanning such as tube voltage, total exposure time and beam filtering (Cnudde and Boone, 2013).

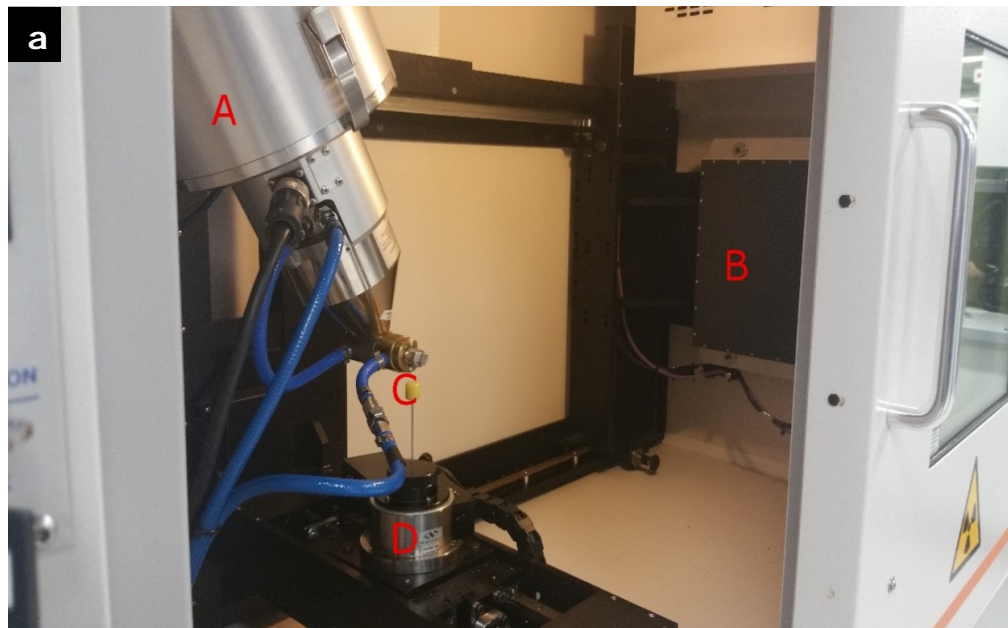


Figure 6.3: (a) Nikon Metris XTH 225 X-ray CT scanner, which was used to image core samples of the study area. Letters in red refer to the following: "A" is the X-ray source, "B" is X-ray detector, "C" is sample to be scanned. "D" is the rotating stage on which sample is placed.



Figure 6.3: (b) Nikon Metris XTH 225 X-ray CT scanner, which was used to image core samples of the study area. The X-ray scanner is connected to the control workstation, which is used to adjust scan setting, data collection, data format and export to a storage hard drive.

The geographical magnification of 25x was selected to achieve the field of view of 16mmx 11.5 mm. For each projection, the acceleration voltage of 90kv, 0.5second per



exposure was used. Specimen scanned using the X-ray CT was rotated over 360° rotation range, collecting 3001 projections per scan. Image acquisition was followed by dataset reconstruction using the CT Pro3D reconstruction software of CT data generated by Nikon Micro CT scanners (Figure 6.4).

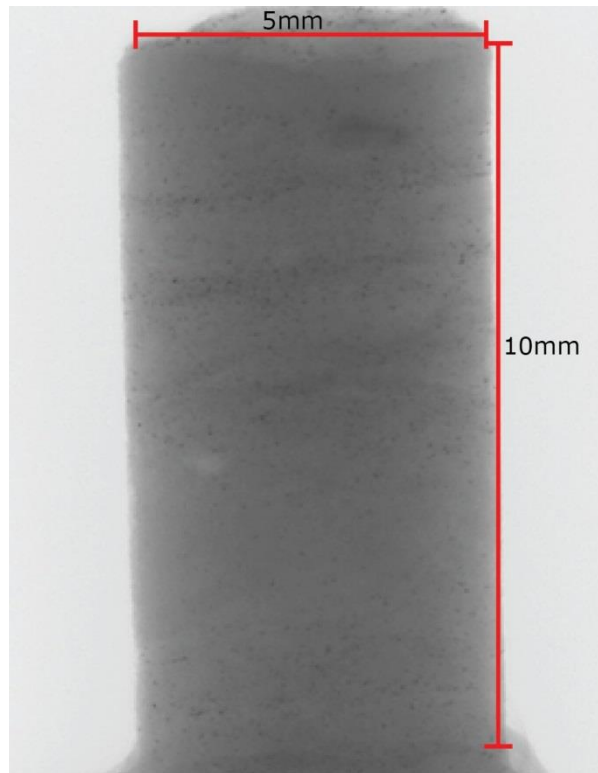


Figure 6.4: Reconstructed computed tomographic image using CT Pro3D.

After reconstruction, the obtained micro-CT data was loaded into digital image analysis software. Two specialised software from FEI Visualisation Sciences Group called Avizo Fire 9.0.1 and PerGeos 1.0.1 alpha-1 (50 days evaluation copy) were used to visualise the slices, 3D volume rendering and image segmentation. PerGeos 1.0.1 is similar to Avizo except from minor built-in changes made for extensions within the original software. The file extension of the reconstructed micro-CT data is vgi. This type of data was converted into a stack of tagged images format slices (tiff). The loaded

images were volume rendered, cropped into cubes selected from region of interest. Three phase segmentation will enable the pore space, quartz matrix and in-situ pyrite to be isolated from the volume images, enabling mineralized and un-mineralised mesh based representations of the samples to be generated. The bulk volume render in Figure (6.5.a) shows the full 3D sample volume. By applying thresholding algorithms to the bulk volume the pore network volume can be extracted. Further processing allows the individual minerals to be classified, resulting in the render of the pyrite mineralization (Figure 6.5.b). These model volumes can be analysed in terms of connectivity, and used for a basis for computational fluid dynamic CFD modelling.

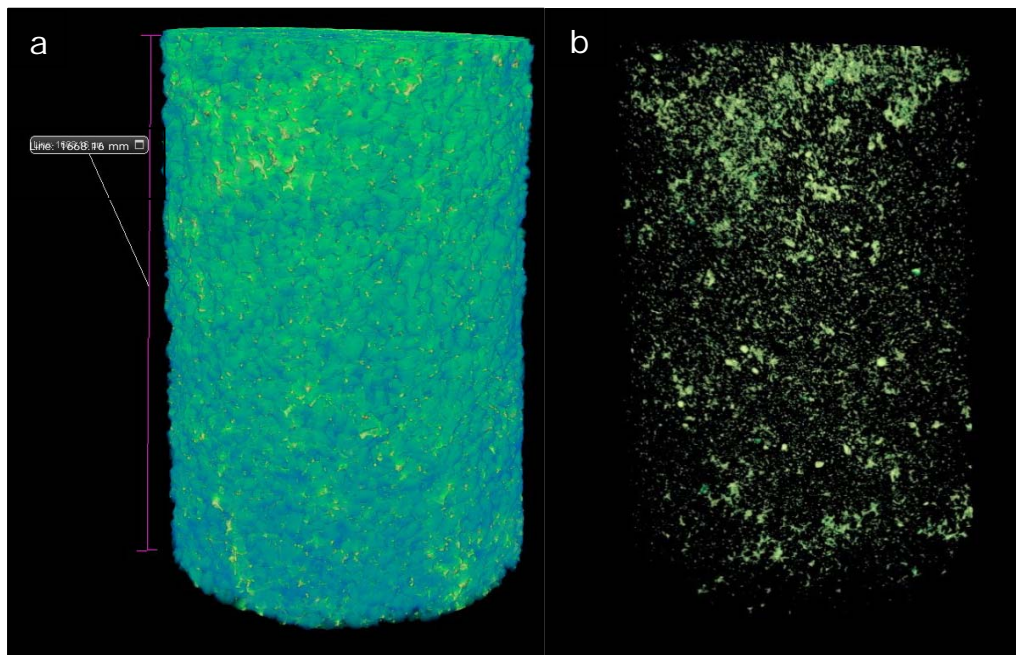


Figure 6.5: (a) Bulk volume render of cropped sample taken from the Zubair sandstone. The original scanned sample is 8 mm, and its diameter is 5 mm. further cropping has been applied to this volume render in order to apply image segmentation and permeability test more smoothly (b) segmented mineralisation found in the same sample, which can be converted into mesh in order to apply flow modelling.

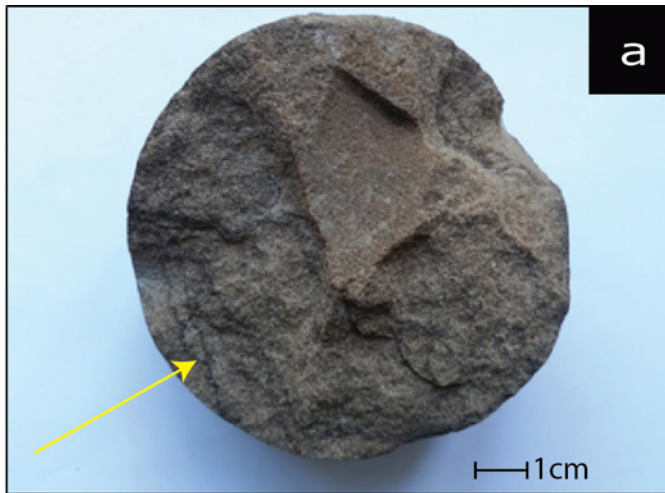
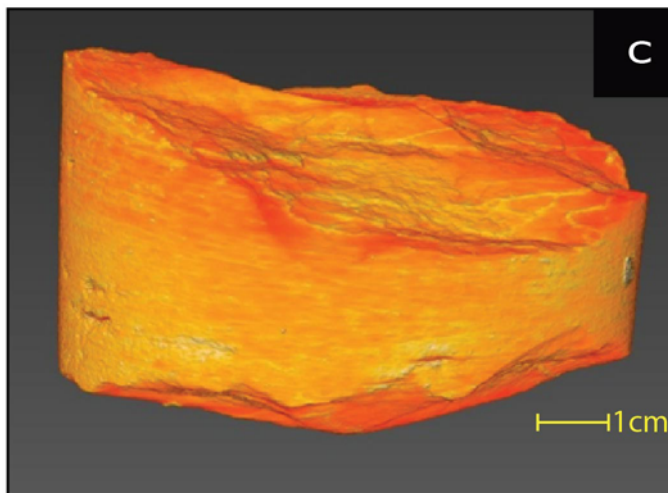
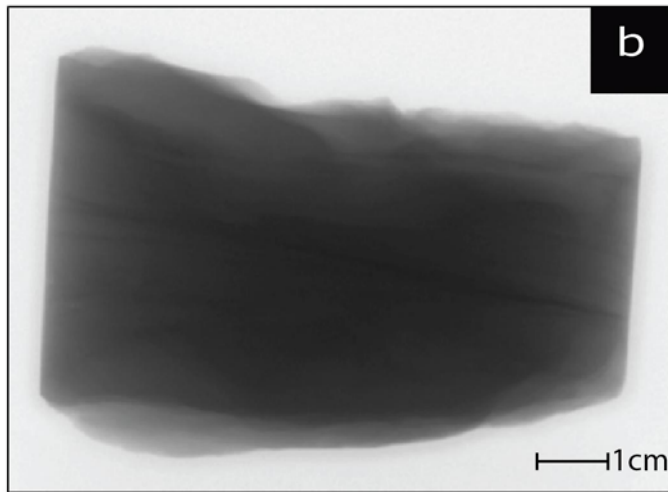


Figure 6.6: (a) Top view of a big core sample of 8 cm diameter collected from the Zubair. Mineralisation can be clearly seen in this sample (yellow arrow). (b) X-ray computed tomography image of 80mm diameter bore core material collected from well D to assess the macroscopic distribution of the mineral assemblage of the dendritic pyrite. (c) Three dimensional volume render of the big core sample, in which mineralisation can be clearly seen.



## **6.5. Data Quality Check**

In this section I will describe some important steps that should be applied to the X-ray CT data set prior to start image segmentation routine. As I mentioned earlier, the extension of the reconstructed data is vgi, which was converted into tiff stack. This type of data needs to be converted into a stack of tagged image format slices (tiff). Working with such type of data can be challenging due its large size, which requires high random access memory RAM speed. Therefore, the tiff stack can be stored as 8-bit or 16-bit. Data matrix class unit 8 is represented by 8-bit image. Three dimensions volume rendering is a crucial step as it helps to visual micro-CT dataset. Hence, each voxel is assigned to colour, which is also a phase representative. Data visualisation is important for defining regions of interest (ROI). However, pre-segmentation processing is essential to improve the quality of the micro-CT data identified phases (Godel, 2013).

## **6.6. Mineral, Rock and Pore Characterization**

In order to identify phases of different constituents, a three dimensional analysis was carried out using Avizo Fire 9.0.1. X-ray CT data as follows

- 1- Data was loaded and opened in Avizo Fire.
- 2- Displaying a proper thresholding by viewing ortho-slice data in order to distinguish different phases of minerals within data under study.
- 3- Mineral phase was identified, and then a proper filtering was applied. Filtering technique involves applying de-noising filters. This step is crucial to recover original X-ray CT imagery from noise prior to process these data. Non-local means filter was applied to X-ray CT data collected from the Zubair samples. This filter was proposed by (Buades et al., 2006), in which the mean value is calculated from encirclement pixels resulting in a smoother image. This process would improve the image clarity leading to a better image segmentation.

A multi-procedural image processing and analysis was applied to micro-CT dataset of the selected samples collected from the Zubair Formation. It is important to differentiate various constituent of the scanned rock materials by knowing their effective atomic number and specific gravity by applying an appropriate thresholding on single component (Long et al., 2009). Characterisation of constituent of rock material was done on the studied samples, which revealed significant pyrite mineralisation. X-ray CT images of the big core sample display high attenuation values which revealed the existence of dendritic pyrite. The grey level in CT images represents Quartz which comprises the greater area captured in X-ray CT images. It is challenging to distinguish between quartz and clay minerals component within X-ray CT imagery as the attenuation coefficients of kaolinite, illite and dickite lie within the same range of quartz. In the study of Long et al (2009), kaolinite and dickite are often having similar dark grey levels as quartz (Figure 6.7).

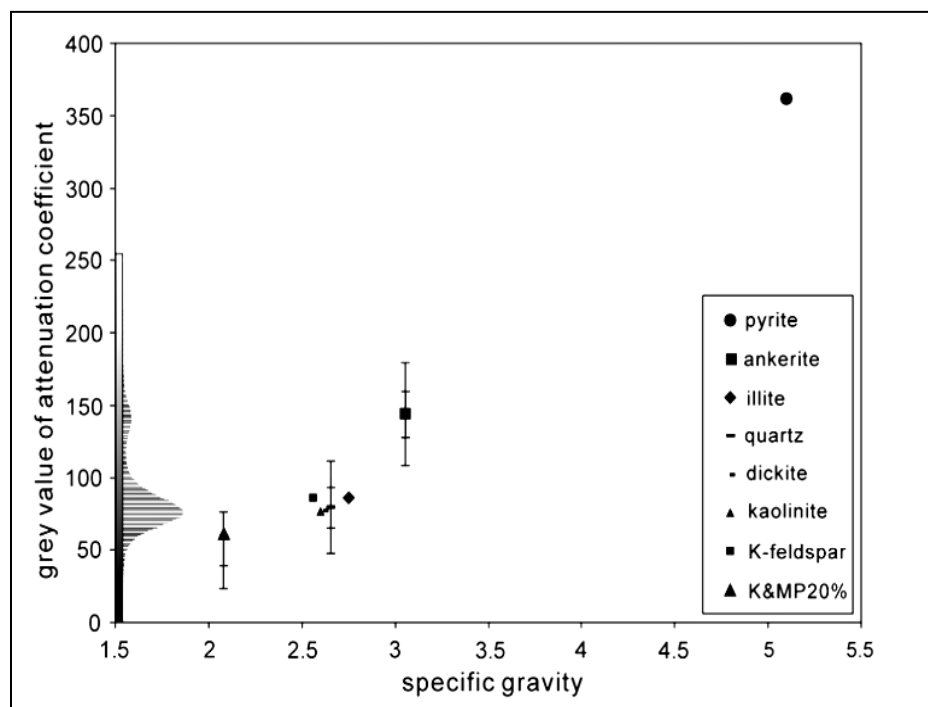


Figure 6.7: Grey level values of components studied by (Long et al., 2009). Recalculated grey values of illite, dickite, kaolinite, pyrite, and k-feldspar.

## **6.7. Image Segmentation**

Each value of attenuation of coefficient within the sample coincides to a 3D pixel (voxel). As the X-ray CT images represent a reconstruction of linear x-ray attenuation coefficient values. Each one of these attenuation values is distinctive for each phase within the 3D dataset. Linear attenuation coefficient is used for assigning radiation energy. Hence it will make a distinctive contrast between two or more materials in a radiograph, and making the phase identification easier. Low attenuation coefficient value will be found in pores and voids. Pyrite, rutile and other heavy minerals will have considerably high attenuation coefficient values. Image segmentation is aimed to phase segmentation of micro-CT data, i.e. partitioning of an image into regions such as pore space, mineralization, and other rock component. The operation at the threshold between low-level image processing and image analysis is called segmentation (Jähne, 2006). Every pixel in an image is allocated to one of the segmented partitions. Image segmentation tool in Avizo Fire was used to partition pore spaces phase from mineral phase. A threshold was assigned for each phase within the X-ray CT dataset, and each voxel range was given a label e.g. pores were assigned a range of value within the voxel that correspond pore phase only. The Same thresholding technique was applied to segment quartz and mineralization (Figure 6.8). Once a segregation of the pore spaces is made, an extraction of the pore network-porosity can be done by using auto-skeleton module in Avizo Fire (Figure 6.9). This purpose of using this module is to create a spatial graph from data of interconnected regions extracted from CT image data.

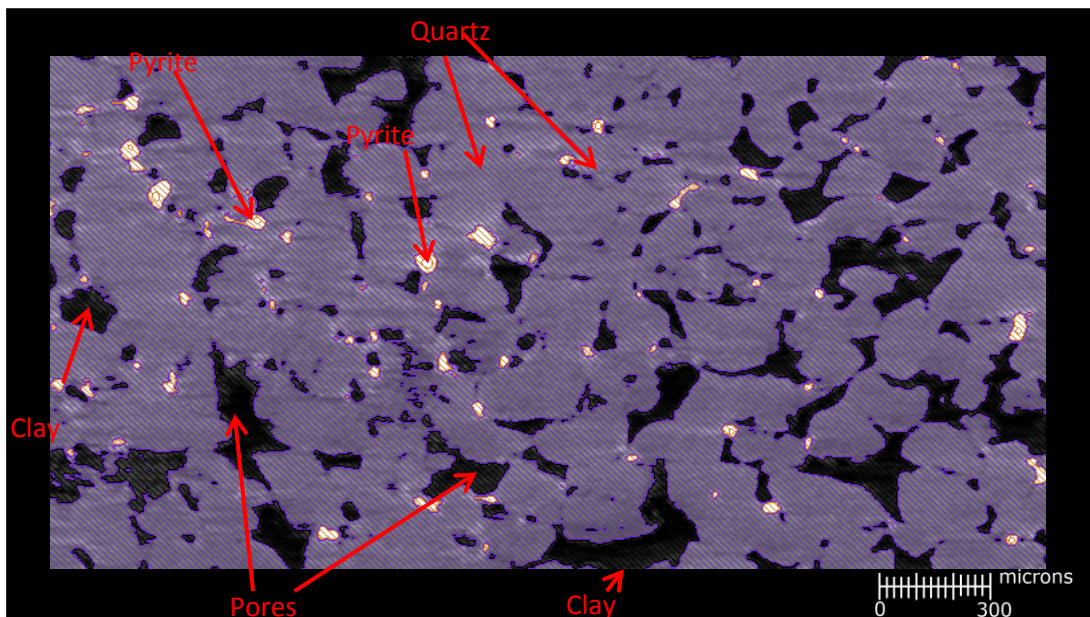


Figure 6.8: An orthoslice of micro-CT image Orthoslice shows segmented phases within Micro-CT dataset. Each one of these phases is assigned to a label. Segmented component shows possible pore lining clay mineral assemblages.

### 6.7.1. Micro-CT Image Segmentation Results

As previously discussed, 8 samples taken from the Zubair Formation were scanned using X-ray CT. I used the core of biggest diameter (8 cm) to assess the distribution of dendritic pyrite (Figure 6.10). Pyrite mineralisation within the big core is interestingly high as shown in (Figure 6.11). The small core samples were also segmented by using Avizo segmentation module. In order to skeletonise pore network, I copped a cubic volume from each volume render of these samples (Figure 6.12).

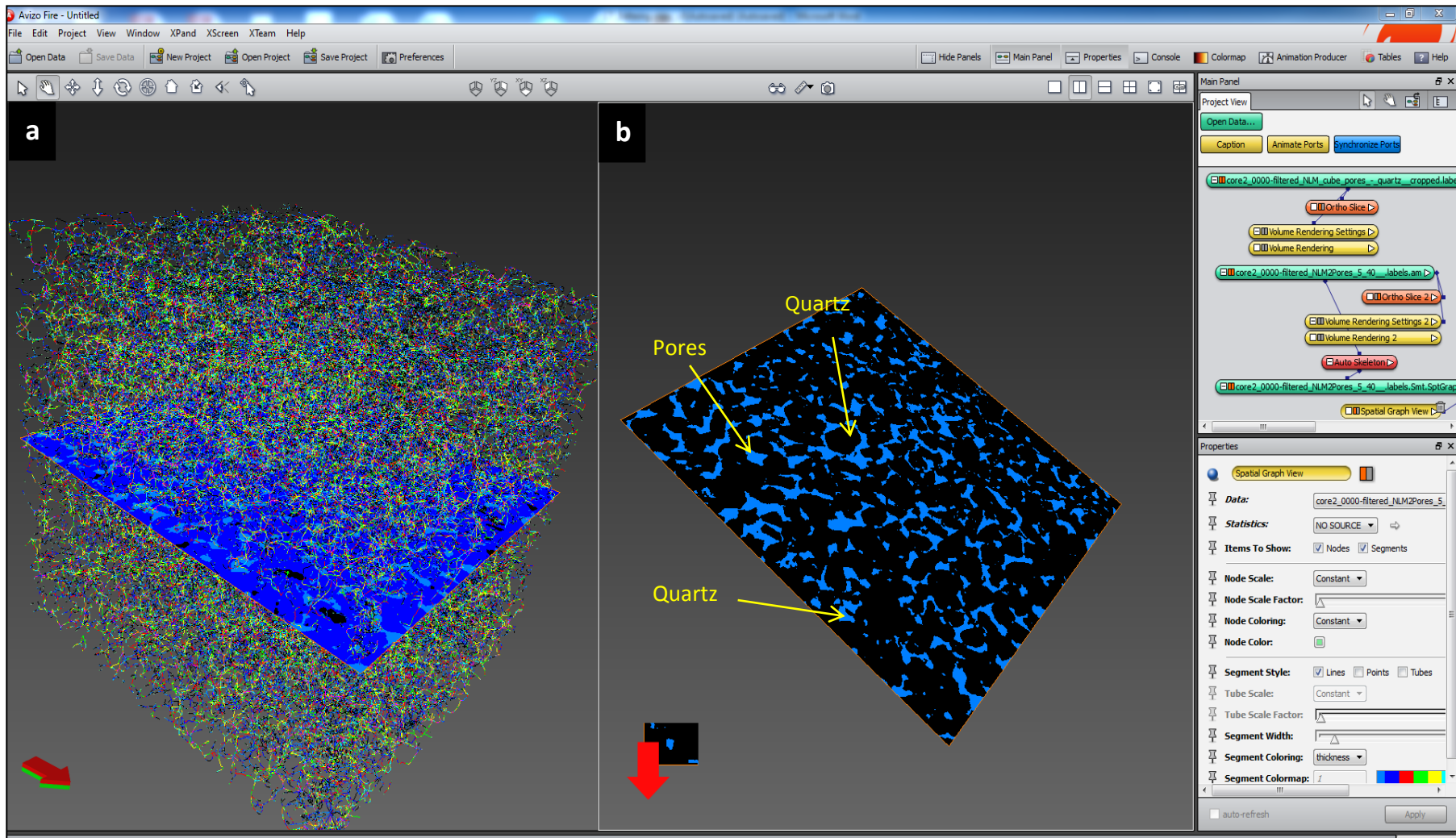


Figure 6.9: (a) skeletonised volume images of a cropped cubic volume of the sample, which was generated from segmented pore space. (b) orthoslice of the segmented pore spaces and quartz only (please note that this orthoslice contains pore and quartz labels only).



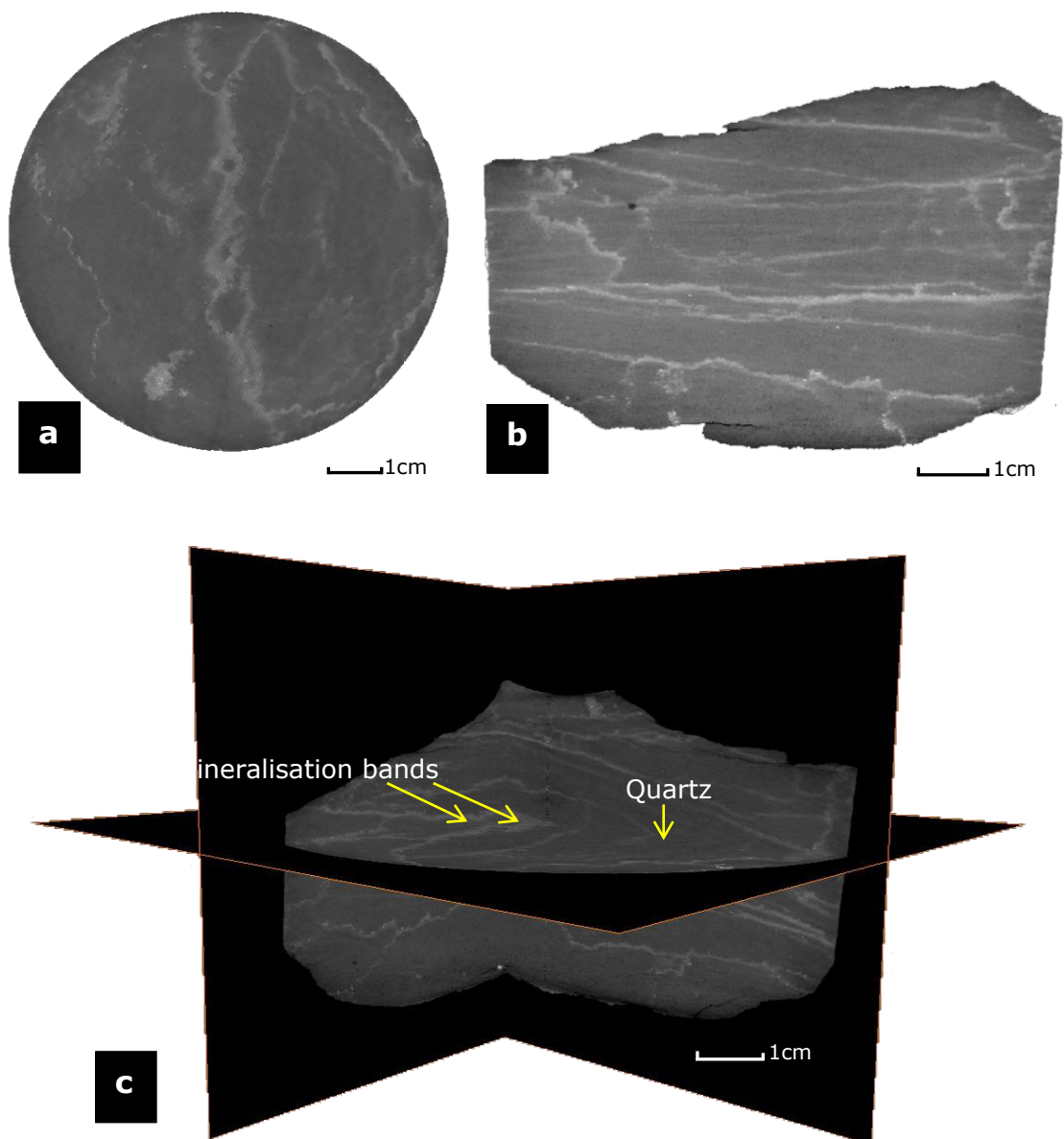


Figure 6.10: (a) Ortho slice from Tiff stack collected from the big core sample. We can clearly see mineralisation in light colour. (b) Ortho slice of the reconstructed big core volume render show the dendritic distribution of pyrite within this sample. (c) Ortho slices of reconstruction volume render of this same sample that show mineralisation bands and (light colour) quartz (grey level) colour.

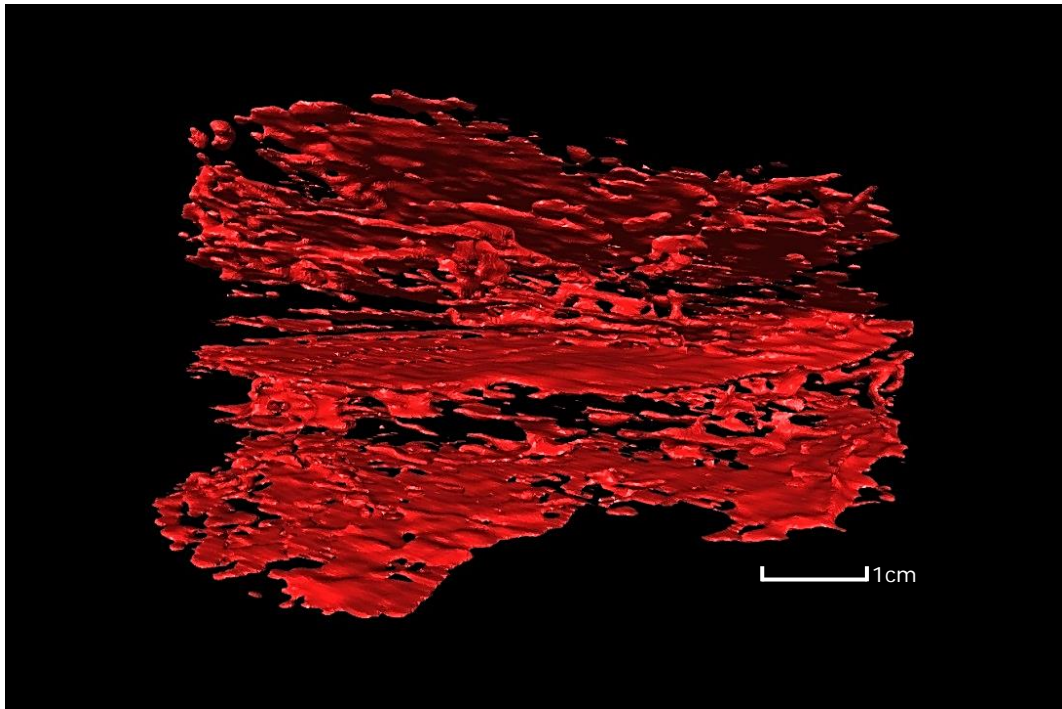


Figure 6.11: pyrite mesh volume segregated from the big core. This dendritic distribution of pyrite looks very clear in this image.

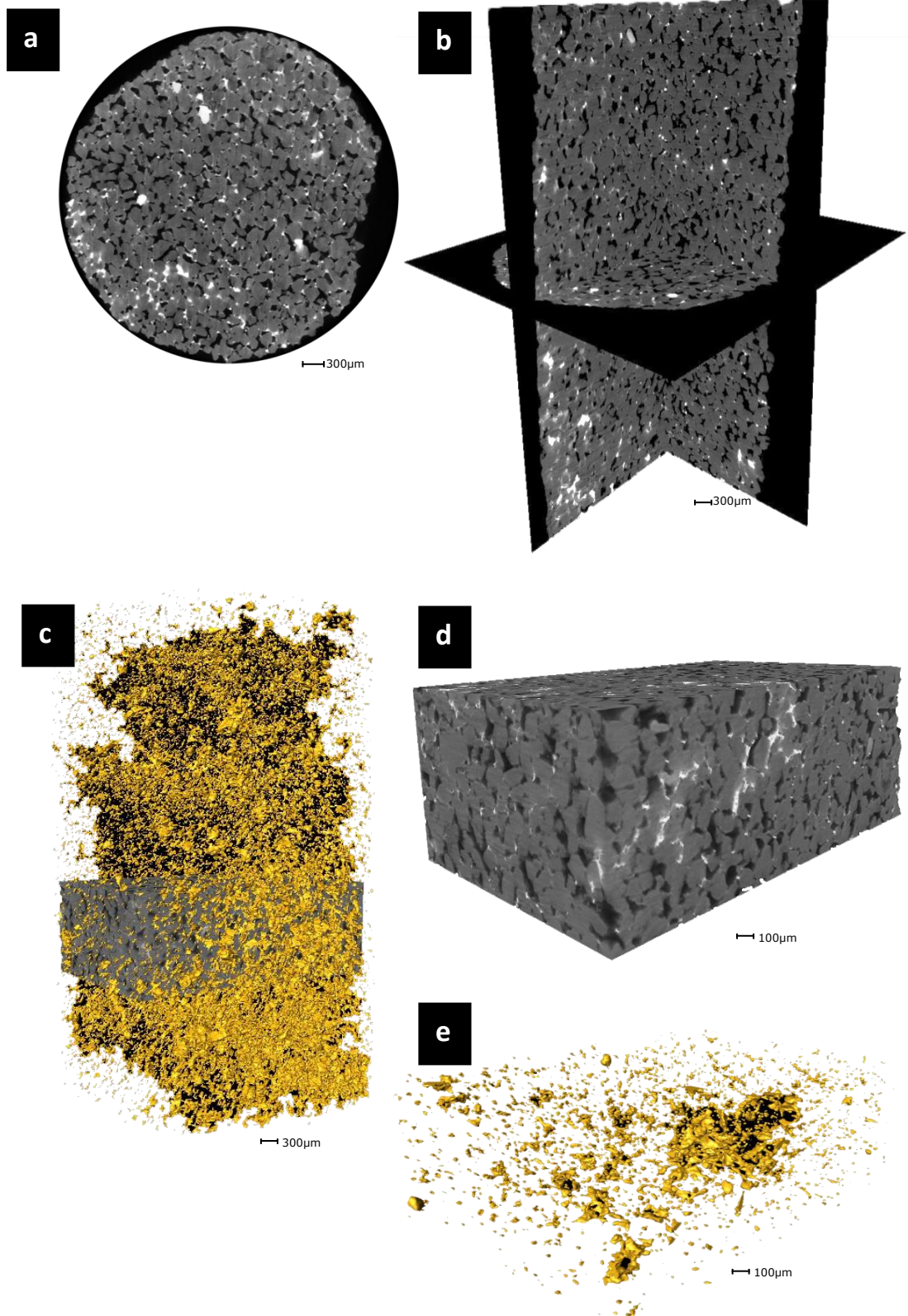


Figure 6.12: (a) orthoslice shows medium size quartz grains, with well-defined pores. The light spot represent mineralisation within this sample. (b) orthoslices in X-Y , X-Z and Y-Z orientations show the distribution of mineralisation. (c) Segmented pyrite mesh found in this sample (gold colour) from which we cropped a cube volume render for further processing. (d) Cubic volume render cropped from the total volume in which we can see pores space (black colour), quartz grains (grey level colour) and mineralisation (light colour). (e) Segmented pyrite mesh found in this cubic volume.



## 6.9. Results of Core Material Characterisation

Otholsices of sample D\* reveals clean (quartz arenite) sandstone, of sub-rounded-sub angular medium size grains (Figure 6.12). Pyrite mineralisation can be seen in this sample in large quantities as well as in samples D, D\*, and G (Figure 6.12). It has very bright appearance, which makes it very easy to distinguish in this sample (Figure 6.12). Another phase was observed in sample D, could be a clay mineral. These clays are pore lining quartz grains and they exist in very small quantities (Figure 6.8).

Phase segmentation of sample taken from well A reveals band like pyrite mineralisation. The diameter of core sample is 6mm. Grain size is fine-very fine and quartz grains are angular to sub-angular. I cropped a cube volume out of the whole volume render of it. In order to apply further processing smoothly. Pore skeleton network has also been generated for this sample (Figure 6.15f).

Overall observation from phase segmentation of core material suggest potential diagenetic pyrite impact on reservoir characteristics. Hence pyrite is found as dendritic and lattice shape in the big core sample as well as framboidal pyrite was identified in ESEM (Figure 6.14 )

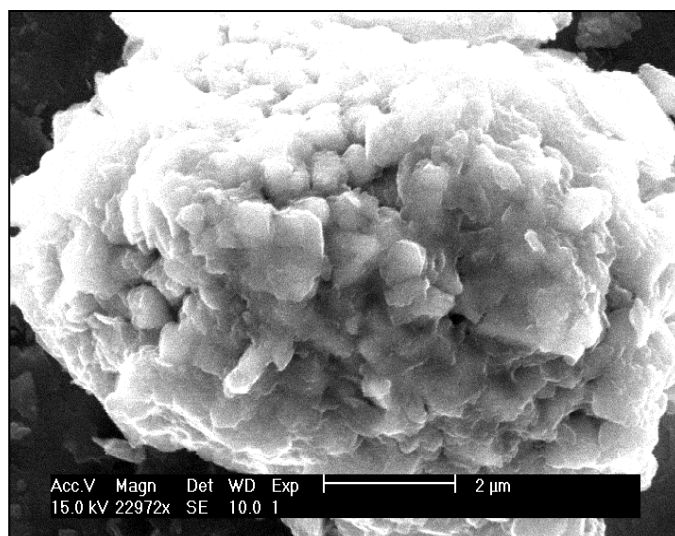
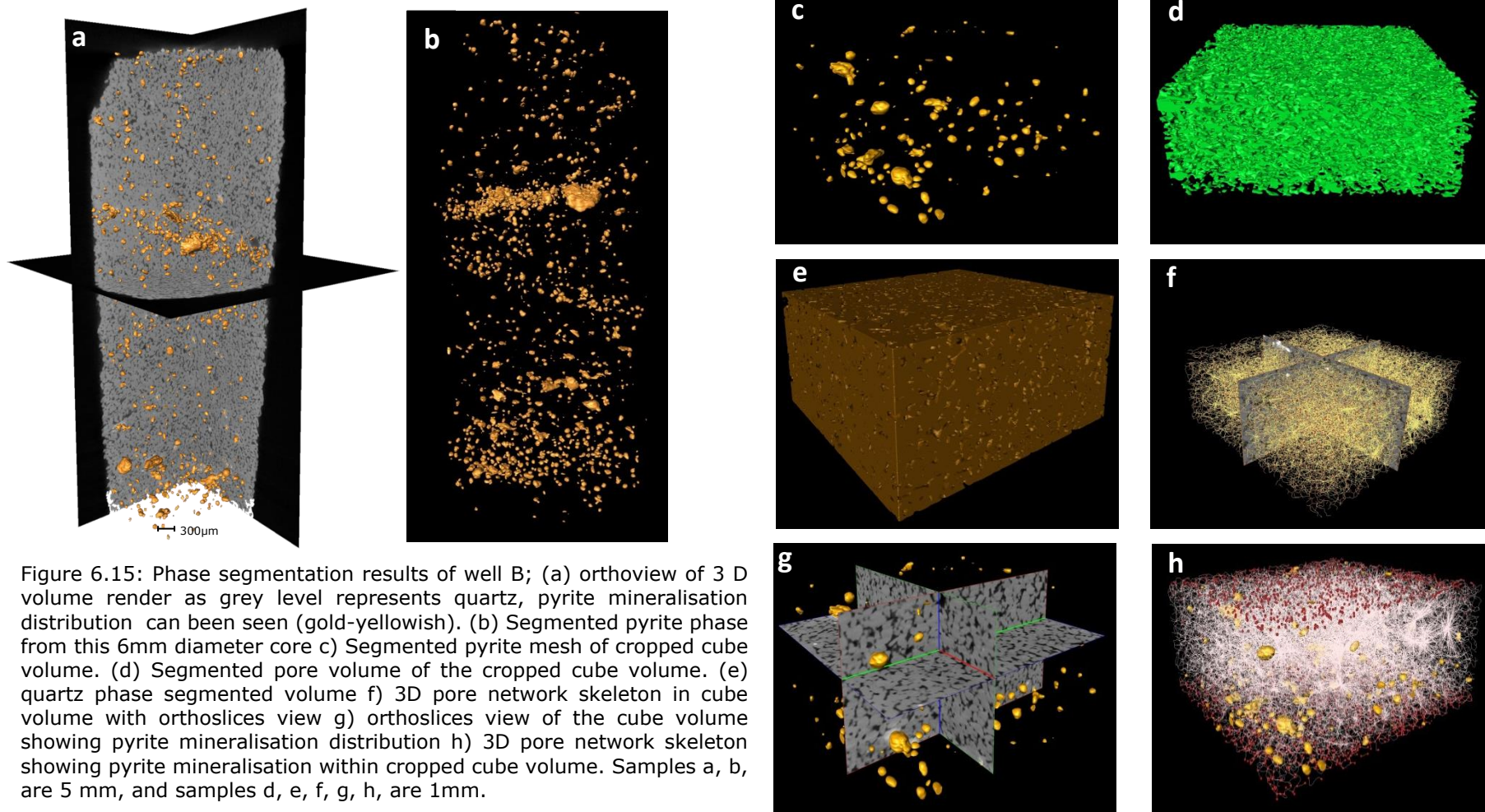


Figure 6.14: ESEM photo shows pyrite framboid identified in sample D which was collected from well D.



## 6.10. Pore network Extraction

Pore volume has been segmented from the total volume render of the rocks under study.

The separated phases were stacked binary images (black and blue). These two colours represent pores and quartz grains. By converting voxel based 3D structure into 3D structure graph of pore skeleton, porosity distribution can be estimated. Prior to the application of volumetric operations of pore skeletonisation module in Avizo, binary images dataset needed to be cut down because this type of mathematical operation can only be applied to a fixed volume.

Porosity can be calculated as pore volume out of the total volume (bulk volume) of the rock by using the following formula:

$$\phi = \frac{\text{pore volume (Pv)}}{\text{total volume}} \times 100 \quad (3)$$

Pore network extraction in Avizo is based on maximal ball algorithm (MB), in which the clustered pore and throats represent the maximal balls. Pore network extraction based on (Oren et al., 1998, Øren and Bakke, 2003) mathematical calculations of the pores and throats volumetric size, length and shape factors.

Pore Network Model is used to capture the properties of real rock system as PNM, it describes the porous medium space. X-ray micro CT images enable a 3D description for the pore space. However, it is mainly reliant upon the resolution of X-ray micro CT machine. Three- dimensional pore space was extracted from the micro-CT data loaded to Avizo and PerGeos by applying autoskeleton module. The extracted pore network models comprise the interconnected pores within these samples. Some of these X-ray

CT data reveal poor or low pore connectivity. They comprise truncated pore, while the poor connectivity in samples D\* and F is good (Figure 6.16).

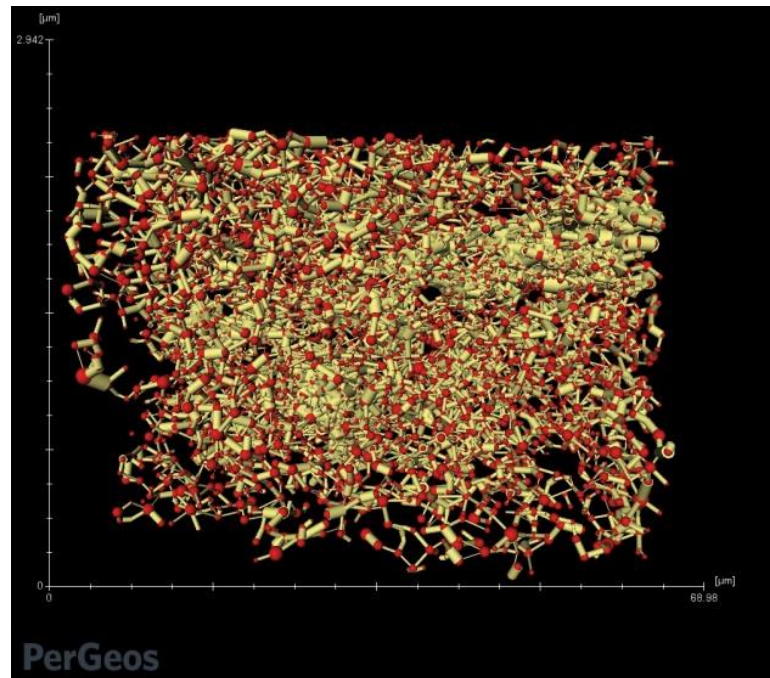


Figure 6.16: Extracted pore network from sample D. Yellow conduits represent pore throats and the red balls represent pores.

### 6.11. Permeability Test

An attempt was made on a single representative sample (D\*) to compare between mineralised and unmineralised meshes. Numerical simulation was performed by using XLab extension in PerGeos (and valuation copy). Despite challenges of working with rotated cube cropped X-ray CT data, which might have affected fluid flow simulation using Avizo XLab extensions due to the lack of XY primary orientation. An attempt was made to simulate fluid flow within the study samples. Permeability (K) estimates by using Avizo XLab were applied on two phases; the first attempt was administered to the mineralised pore mesh (Figure 6.17a.b). A binary image consists of two colours (black and white). Mathematically, pixels have only two values; black =0 and white =1.



Three channels binary image dataset was used. Quartz and pyrite were combined in one colour (blue) and black was assigned to segmented pore space.

#### **6.11.1. Permeability Estimate for Mineralised Mesh**

Permeability estimate computation using PerGeos XLab was performed on mineralised pore mesh. However, precautions are to be taken in account prior to run simulation. This type of computation is very sensitive to small pore sizes and the pore throats. The minimum pore size can be defined arbitrarily according to the image resolution and the desired complexity (level) of detail (Dong, 2008). Permeability computation was failed in poor voxel size of 5nm.resoluti (level the computation will not converge if the minimum pore size is too small, and the pore size i. Additionally, permeability estimate are affected by small voxel sizes. A set of parameters and options need to be checked prior to run simulation. Details of XLab setting can be seen on downloadable PerGeos manual. K simulation's computations are reliant upon the computer (workstation) processor's CPU speed and graphic processing unit GPU speed. As this type of computation consumes a huge amount of computer's memory, at least 64GB of RAM is required to run simulation smoothly and efficiently. At this phase of K estimate, I used a segmented pore mesh after inverting the originally segmented mesh. Inverted binary image, which was used in this phase of permeability simulation has two voxels values; pore space = blue colour = 1 and (quartz + pyrite) = black colour = 0 (Figure 6.17 b). Calculated K using PerGeos Absolute Permeability Experiment Simulation (APES)  $K_z = 123\text{md}$ .

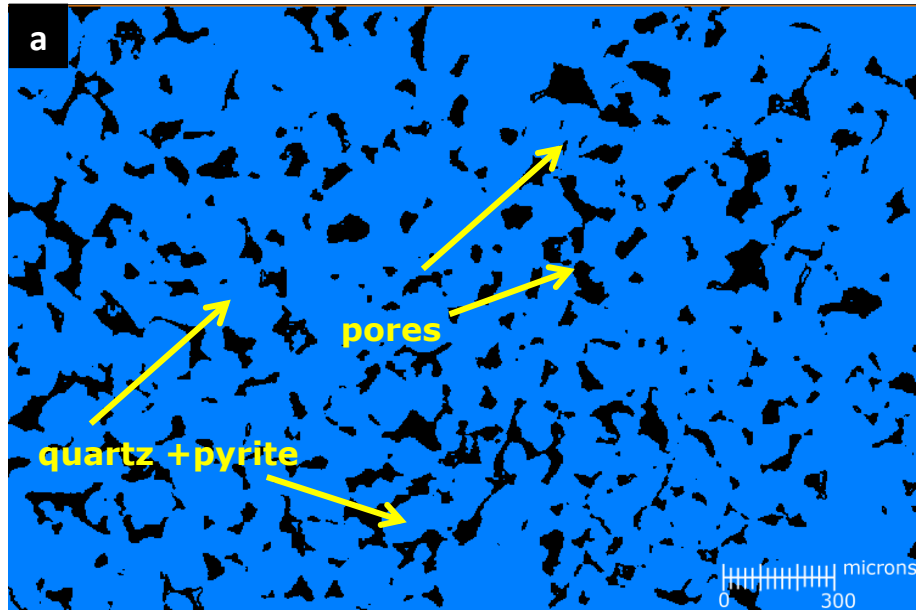


Figure 6.17.a: two channels (labels) binary image. The blue colour represents combined (quartz grains and pyrite). Segmented pore space represents black spaces in this binary image.

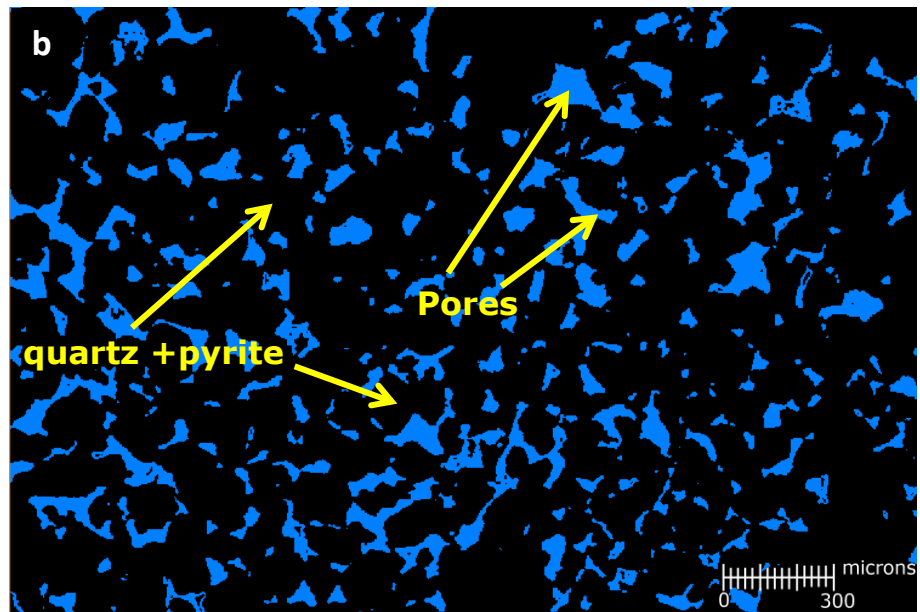


Figure 6.17.b: inverted two channels (labels) binary images. The black colour represents combined (quartz grains and pyrite). Segmented pore space represents blue space in this binary image.

### 6.11.2. Permeability Estimate for Unmineralised Mesh

The second phase of permeability computation using PerGeos XLab module was administered on binary image dataset of the unmineralised pore mesh, in which pyrite mesh was eliminated by combining it with pore space (Figure 6.18a.b).

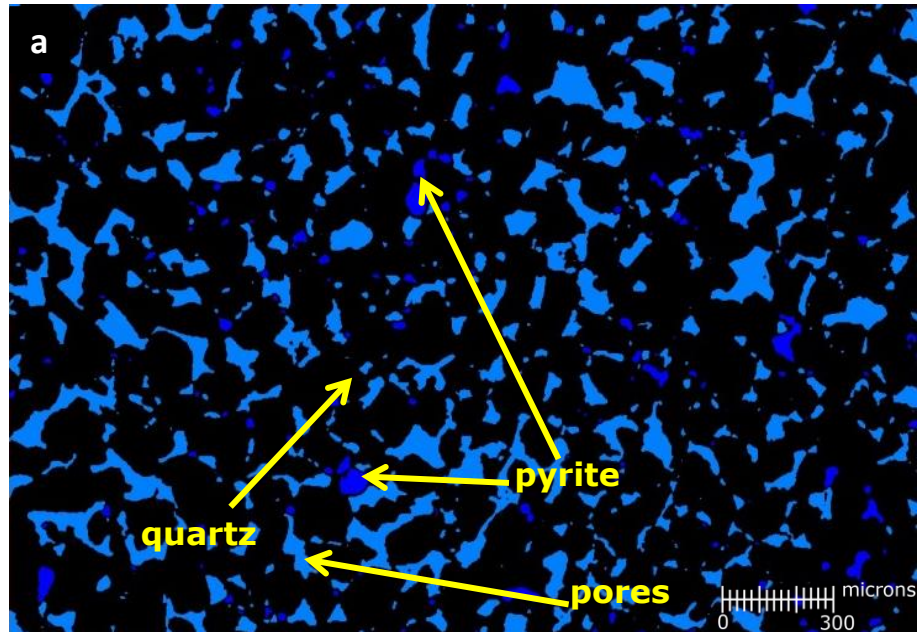


Figure 6.18.a: Three channels binary image of pores, pyrite and quartz. Their colours are; sky blue, royal blue and black respectively. This mesh still represents mineralised mesh

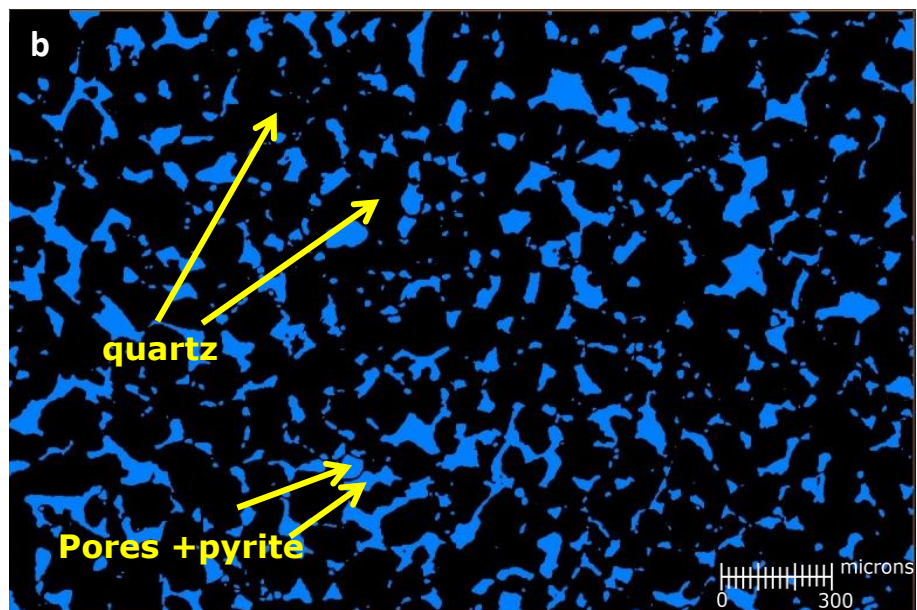


Figure 6.18.b: Inverted binary image of unmineralised mesh, in which pyrite label has been added to the pore space to eliminate its effect (sky blue). Quartz represented by black colour.

Based on Absolute Permeability Experiment Simulation (APES) applied to unmineralised mesh, the estimated  $K_z= 227\text{md}$ , which is considerably higher than it for the mineralised mesh.

### **6.12. Discussion of Permeability Estimates**

Despite the application of PerGeos XLab extensions to 8 samples from 6 wells, I was unable to obtain realistic prediction of permeability due to a number of factors that might have affected the validity of permeability realisations. One of these factors was the voxel size, which should not be in nm. Additionally small pore sizes and pore throat radii lead to negative or very low permeability values. Kaczmarczyk et al. (2001) draws our attention to the impact of segmentation on porosity as he stated that all of techniques used in thresholding are followed by the following equation to calculate porosity:

$$\epsilon = \frac{n_p}{\sum_i n_i} \cdot 100\% \quad (4)$$

Where

$n_p$  = is voxels number allocated to a pore layer

$n_i$  = is voxels number allocated to i- layer

Hence, implication of porosity estimated by using X-ray CT porosity module is often lower than porosity measured by using density measurement (Kaczmarczyk et al., 2010). Morphological operations such as dilation and closing were applied to binary images of the study samples in order to remove bright pixel out of the edges of foreground pixels. However, I couldn't get realistic or close to the reality K estimate.

The sample with high pyrite mineralisation manifested variation in permeability values (Figure 6.17a.b), comparing the two permeability values;  $k_z= 123\text{md}$ ,  $K_z= 227\text{md}$  for both mineralised and unmineralised pore meshes respectively (Figure 6.18.a.b), a possible explanation may be related to the distribution of dendritic pyrite mineralisation in this sample. Therefore, it potentially controls fluid flow within the Zubair. Nevertheless, this raises questions about the extent of influence of pyrite mineralisation on reservoir characteristic of the Zubair Formation. Hence, I tested the impact of mineralisation on micro scale.

By comparing the two results of streamlines generated from velocity vector Z from both mineralised and unmineralised pore meshes, distinctive impact of mineralisation on streamlines was revealed (Figure 6.19.a.b). Overall, these results suggest potential influence of pyrite mineralisation on reservoir characteristics, which in turn may control fluid flow within this sample. Animation video of streamlines can be seen in attached CD.

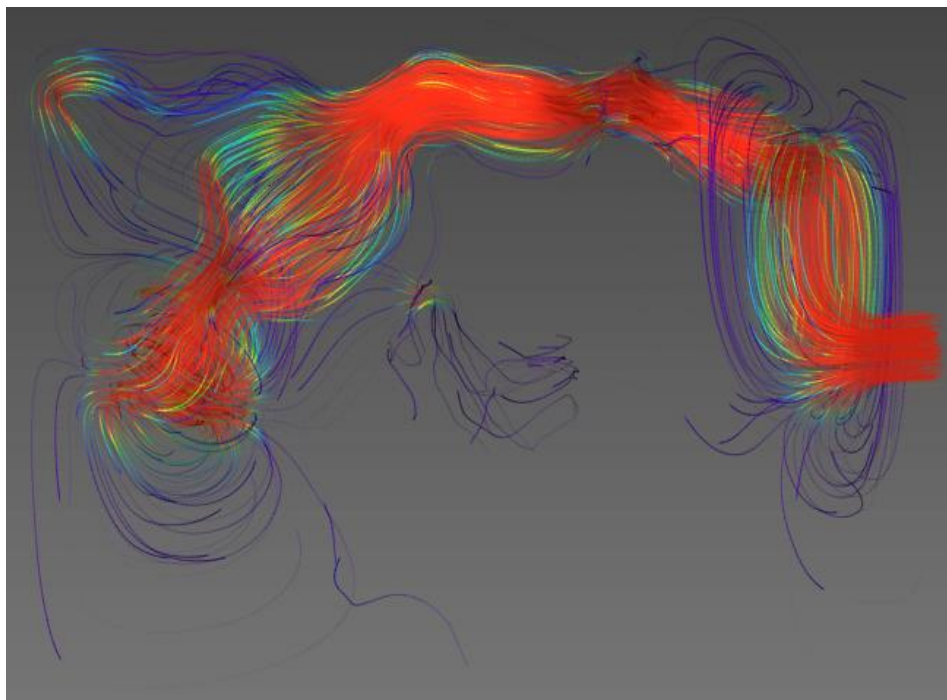


Figure 6.19.a: Streamlines generated from velocity vector of the mineralised pore mesh.  $K_z= 123\text{ md}$ .

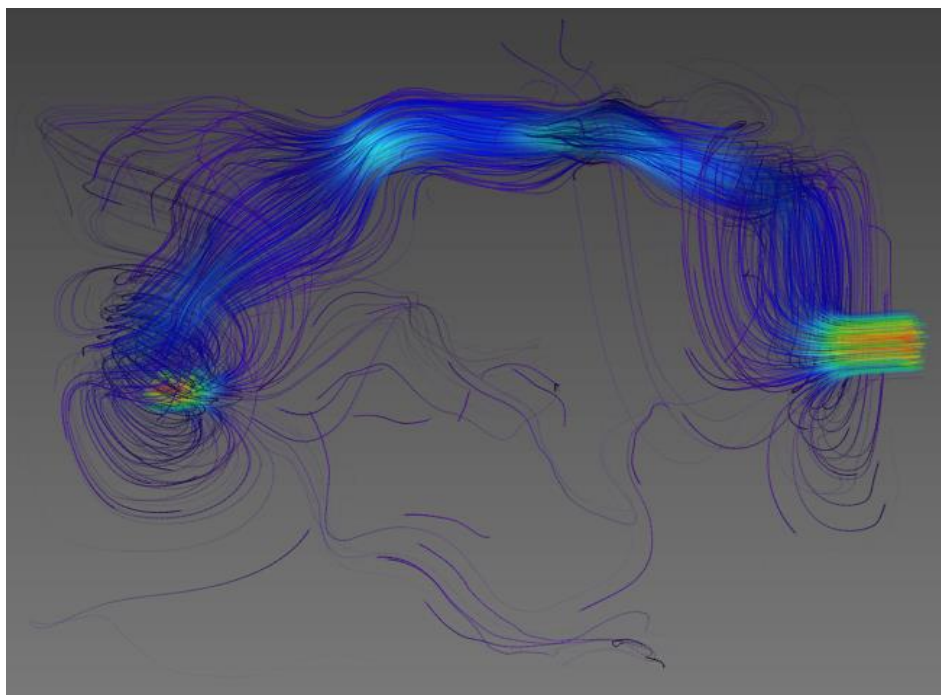


Figure 6.19.b: Streamlines generated from velocity vector of the unmineralised pore mesh.  $K_z = 227$  m

### 6.13. Well Log Analysis

In this section we will present results of petrophysical analysis, which was done on the study wells, in order to examine the impact of mineralisation of porosity and permeability. As was discussed in Chapter three Techlog software was used to perform this analysis we have used. Prior to start work on these dataset, it is important to do data calibration and quality check for any missing information related to digital well log datasets. This step is crucial to reduce the amount of error. Petrophysical analysis was performed on the Zubair's Main Pay reservoir units, which are subdivided into 9 units.

#### 6.13.1. Results of Well log analysis

Effective porosity was calculated by using neutron-density well log data. This type of porosity represents the volume of interconnected pores. However, clay mineral impact on these interconnected pores cannot be assessed directly. Unless using NGS log. Petrophysical analysis shows fair reservoir quality reveals an average porosity of 13%-

15%, which reflects good reservoir quality (Figure 6.20) and (Figure 6.21). Please see Appendix 1 for more details of effective porosity and permeability estimates of selected wells.

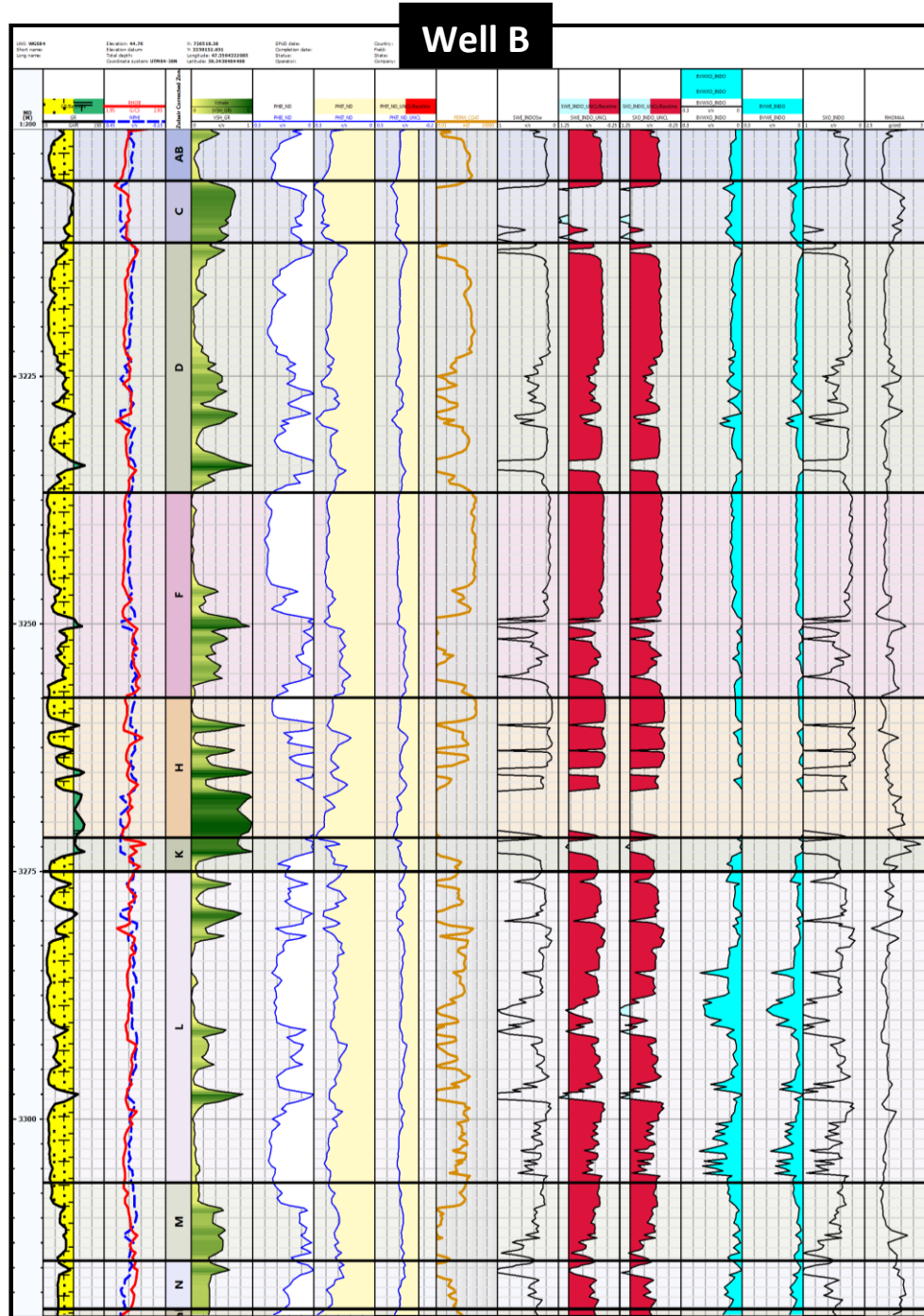


Figure 6.20: Petrophysical analysis by using well log data of well B. effective porosity displays average porosity of about 20%, which is fair .Permeability estimates are of good quality is also fair with an average of 10 md. Highest K is at distributary channel fill and also at unit Ab of coarsening upward.

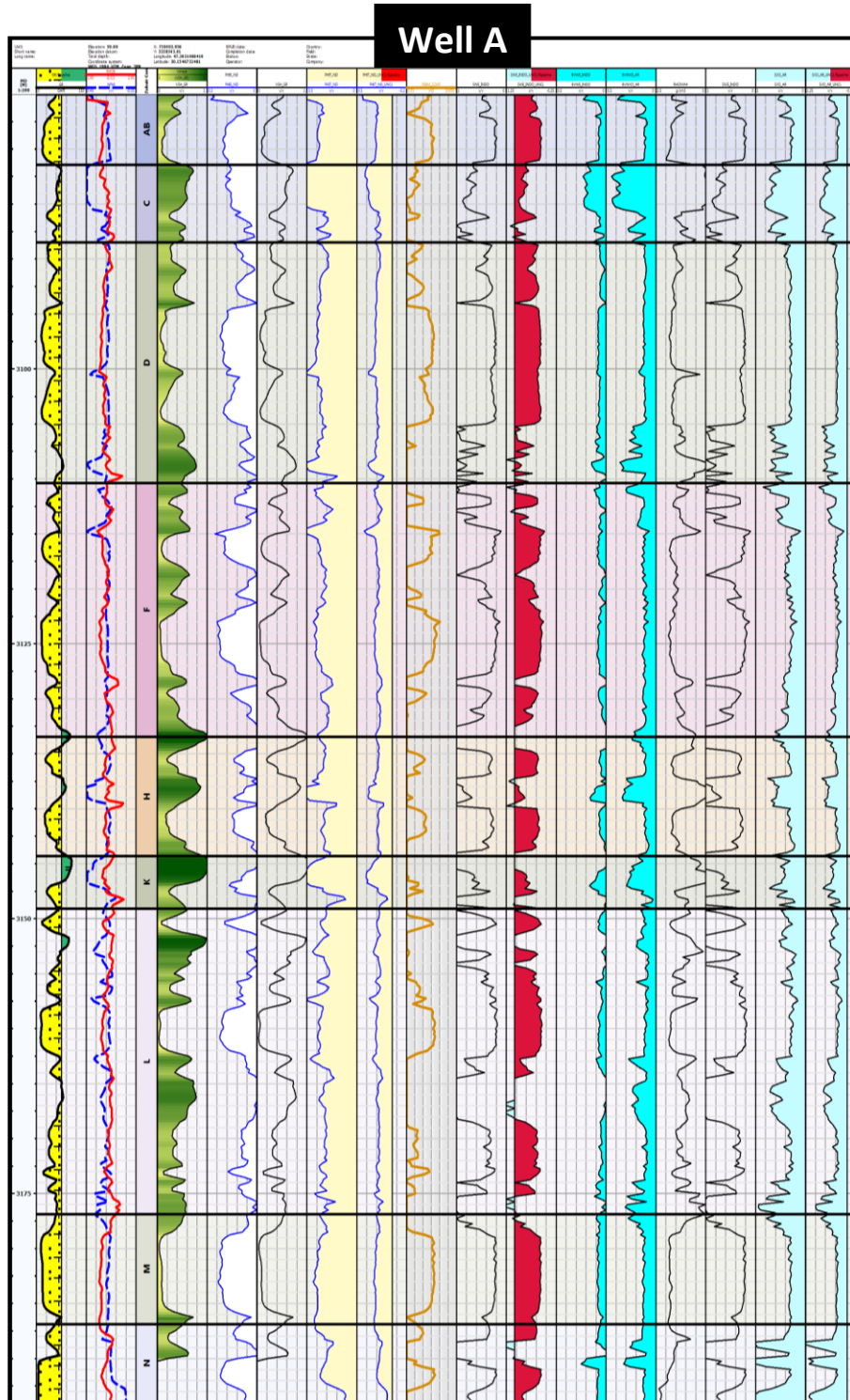


Figure 6.21: Petrophysical analysis by using well log data of well A. effective porosity displays average porosity of about 15%, which is fair .Permeability estimates are of good quality is also fair with an average of 4 md. Highest K is at distributary channel fill.



## **6.14. Discussion and Conclusions**

Pyrite is one of authigenic diagenetic minerals that can be found as local distributions. As the formation of pyrite occurs during the very beginning stage of diagenesis (Deschamps et al., 2012). The identification of framboidal pyrite in many samples was confirmed by ESEM and XRD analyses. As well as three dimensional visualisation of X-ray CT dataset collected from the big demonstrated dendritic distributions of pyrite (Figure 6.11).

X-ray CT micro-imaging undertaken here, has extended our knowledge of potential controls on pressure distribution within the Zubair Formation by reporting pyrite mineralisation in 8 representative samples selected from the Zubair facies. Although the current study is based on a few numbers of samples, the findings could have important implication of the impact of dendritic pyrite on fluid flow and pressure distribution.

Petrophysical analysis of Well B reveals good reservoir properties in some part of unit AB which is mainly massive sandstone. Whilst this unit shows poor permeability values in well D due to pyrite mineralisation. Therefore applying comparative studies on segmented images collected by X-ray computed tomography of both mineralised and unmineralised samples will greatly improve the understanding of the fluid flow physics upon sandstone reservoirs using a novel set of modern computational approaches. Due to the poor information management of historical core data from the Zubair, a non-destructive technique such as X-ray computed tomography is valuable for petrophysical and petrographic studies. As we were able to generate pore network model PNM by using binary image dataset.

# Chapter 7

---

## Synthesis and Conclusions



## **Chapter 7**

### **Introduction**

This chapter highlights a synopsis of the outcomes of the study and conclusions made in the light of study aim. It also brings attention to any further recommendations for potential future work to be done on the Zubair Formation.

### **7.1. Synopsis of key findings and suggestions**

This research project concentrates on using integrated studies, which rely on subsurface datasets to improve the quality of spatial and temporal distributions of subsurface reservoirs. Nevertheless, a significant source of uncertainty within subsurface reservoir is the controls upon hydrodynamic pressure distributions it not well understood. The key objectives of the study were to: (a) examine the impact of clay mineralogy on the Zubair Formation, by providing more detailed knowledge of the distributions and diagenetic evolution of clay minerals (b) to petrophysically characterise the reservoir units (c) to characterise mineralisation within the Zubair by applying X-ray CT imaging technique. The main aim of the study was to reduce uncertainty related to pressure distribution within the Zubair Formation by providing more detailed knowledge of the influence of mineralisation-related flow heterogeneity using integrated studies, which utilize X-ray diffractometry, Scanning Electron Microscope and X-ray Computed Tomography. The level of analysis used in this study encompassed a variety of scales (Figure 7.1).

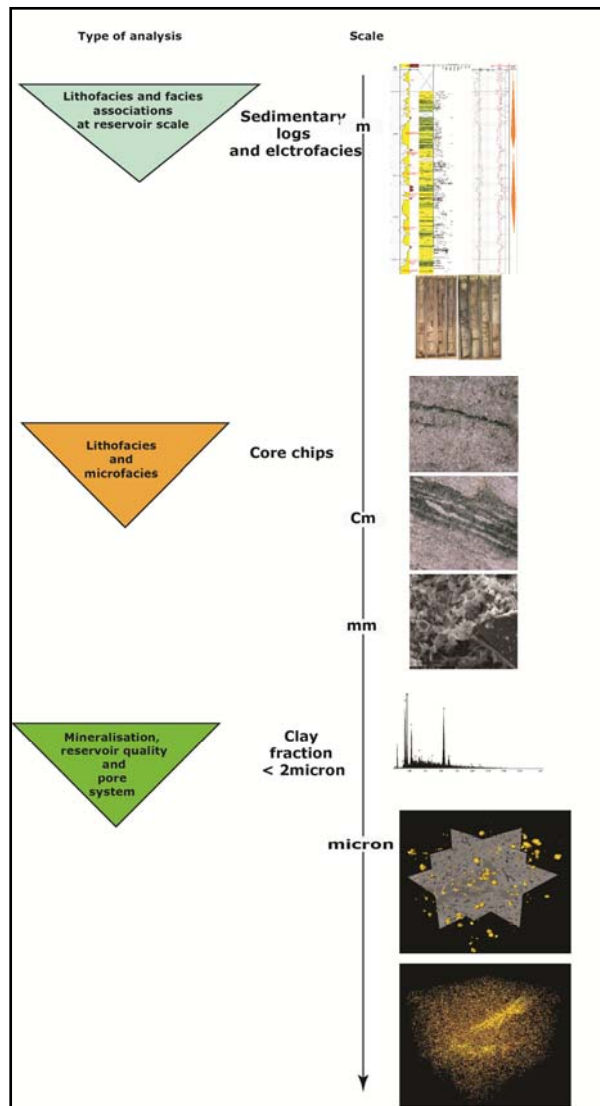


Figure 7.1: Schematic of the scales of analysis performed throughout this project.

### 7.1.1. Problem statement

Previous studies done on the lower Cretaceous Zubair Formation were mainly focused on petrographic, stratigraphic and sedimentological relationships on a large scale. A significant source of uncertainty within the Zubair is the controls upon hydrodynamic pressure distributions (Liu et al., 2013). Directional trend of reservoir pressure is linked to tilted oil water contact while observation related to directional trend of the pressure in the Zubair Formation is not associated with titled oil water contact (Liu et al., 2013) shows that no titled oil contact.

### **7.1.2. Facies associations of the Zubair Formation.**

One the main aims of this research project aims was to improve understanding of depositional processes and environments and their amplifications on reservoir quality. Therefore, lithofacies and electrofacies characterisation was conducted to the Zubair Formation which led to the interpretation of the depositional environment and facies association classification see (Table 4.1, page ).

A total of thirteen lithotypes representative for the facies associations have been identified within the Zubair Formation core data. Lithofacies interpretation was incorporated with electrofacies interpretation. Four electrofacies have been rationalised according to Gamma-ray log motifs which are: Bell shaped-finning upward, Prograding and retrograding oval shaped, Funnel shaped-coarsening upward, and blocky shaped- aggradational.

### **7.1.3. Depositional Setting**

In this PhD study the Zubair Formation deposits have been categorised into thirteen lithotypes, The Zubair Formation is subdivided into nine units. The absence of core data of the Upper Shale Member has limited the analysis and which was only done on the Main Pay of the Zubair Formation. Unit AB comprises the onset of the Zubair Formation–Main Pay which is also called Upper Sandstone Member. This unit comprises the heterogeneous upper part of the Main Pay. Facies analysis indicates sandbodies of heterolithic nature prograding-deltaic conditions in unit N and L. While units D and H indicate the depositional conditions of distributary channel-fill deposits which overlie deposits of prodelta (mud-prone) / interdistributary channel fill deposits. Depositional environment of the Zubair Formation-Main Pay reflects river- dominated, wave-influenced delta.

#### **7.1.4. Depositional Textures and Fabrics**

Textural and fabrics studies of the Zubair Formation reveal that it has grain size range from clean, fine to medium (Hmood, 2002; Al-Muhalhal, 2004). Coarse grain size is associated with channel-fill deposit and mouthbar. Variations in reservoir quality within the Main pay are mainly reliant upon variations in grain size on bed /set scale. The Zubair Formation sandstones are mature, comprising quartz arenite-sub-lithic arenite (Hmood, 2002).

#### **7.1.5. Mineral Characterisation**

One of the key objectives of this research is to examine the impact of mineralisation on the Zubair Formation. Integrated studies using XRD, ESEM, and X-ray CT micro-imaging were applied to a group of samples collected from the Zubair Formation. The identified clay minerals in the study wells encompass kaolinite, illite, and clinochlore. Kaolinite is predominant clay mineral in the study wells. It exists as blocky and booklets for dickite. Poly-type kaolinite suggests diagenetic reactions in sandstones reservoirs. It was identified in Facies D which lies within prodelta deposits. Crystallisation of dickite can be related to two mechanisms; the first growth of this new substance due to dissolution of instable kaolinite or other detrital mineralogical component such as feldspars, and the second mechanism is neoformation of dickite through contiguous or progressive accretion of it due dissolution and crystallization (Beaufort et al., 1998). Modes of occurrence and distribution of kaolinite suggest moderate impact on reservoir quality of the Zubair sandstones. The weight percentage of Illite identified in the study wells increases with depth due to illitization. Relative abundance of chlorite is commonly found at coarser grain size. Mineralogical analysis of samples collected from sandstone/shale contacts reveals concentrations of chlorite in sandstone adjacent to shale. Petrophysical analysis reveals low permeability at some sand/shale contacts which can be linked to local heterogeneity due to fluid and ion

exchange within the vicinity of sandstone /shale contacts significant amounts of pyrite were observed in core representative core samples collected from the study wells. This pyrite mineralisation was 3D characterised using X-ray CT datasets of 8 samples taken from the Zubair Formation. Permeability experimental studies were applied to both of mineralised and unmineralised meshes in order to examine the impact of mineralisation on fluid flow. Predicted absolute permeability in mineralised mesh was 123md (Figure 6.17a, b). While it was 227 md in unmineralised (Figures 6.18a, b). The implication of pyrite mineralisation on reservoir quality may comprise a control on fluid flow within mineralised sandstones (see permeability test results in video clips in the attached DVD. The identification of pyrite was confirmed first by ESEM and XRD analyses. The heavy minerals assemblage shown in the Zubair Formation sandstones comprises pyrite and probably anatase or rutile. As revealed by quantitative analysis done on XRD data collected from clay fraction and bulk powder samples. Pyrite was identified in powdered samples of the Zubair Formation. As well as nodes of pyrite were identified in cored intervals. Pore filling framboidal pyrite was also observed in SEM samples. Pyrite is an authigenic diagenetic mineral that can be found as local distributions. Applying comparative studies on segmented images collected by X-ray computed tomography will greatly improve the understanding of the fluid flow physics upon sandstone reservoirs (Sullivan and McBride, 1991).

#### **7.1.6. Reservoir Quality**

The internal reservoir quality of the Zubair Formation is more likely controlled by mud content and grain size. As good–moderate revoir quality is related to coarse grain size. However, mineralisation heterogeneity at local scale can influence reservoir quality. Such mineralisation comprises potential control on reservoir quality.



Therefore, more detailed diagenetic studies that are based on digital image analysis of the X-ray CT data is strongly required to fill this gap o knowledge.

## **7.2. Recommendations for Future Work**

1-Mineralogical studies on larger scale can greatly help to improve understanding of their impact on flow heterogeneity. For example, isotopic analyses such as carbon and oxygen isotopes would help to assess the conditions of cement forming through knowing the composition of pore water and temperature.

2-Due to the poor information management of historical core data from the Zubair, an non-destructive technique such as X-ray computed tomography is valuable for improving understanding of mineralisation upon the trapping and transfer of mobile geofluids.

3-Volume images collected using X-ray computed tomography are to be used in the future research on the Zubair Formation by applying Computational Fluid Dynamics (CFD) modelling.

## References

- ABBO, A. S. & SAFAR, V. M. 1967. Sand and Shale Correlation in the Zubair and Rumaila Oil Fields, Iraq Petroleum Company.
- ABEED, Q., LEYTHAEUSER, D. & LITTKE, R. 2012. Geochemistry, origin and correlation of crude oils in Lower Cretaceous sedimentary sequences of the southern Mesopotamian Basin, southern Iraq. *Organic Geochemistry*, 46, 113-126.
- AL-AMERI, T. & BATTEN, D. 1997. Palynomorph and palynofacies indications of age, depositional environments and source potential for hydrocarbons: Lower Cretaceous Zubair Formation, southern Iraq. *Cretaceous Research*, 18, 789-797.
- AL-AMERI, T. K., AL-KHAFAJI, A. J. & ZUMBERGE, J. 2009. Petroleum system analysis of the Mishrif reservoir in the Ratawi, Zubair, North and South Rumaila oil fields, southern Iraq. *GeoArabia*, 14, 91-108.
- AL-AMERI, T. K., PITMAN, J., NASER, M. E., ZUMBERGE, J. & AL-HAYDARI, H. A. 2011. Programed oil generation of the Zubair Formation, Southern Iraq oil fields: results from Petromod software modeling and geochemical analysis. *Arabian Journal of Geosciences*, 4, 1239-1259.
- AL-AZZAWI, R. M. 2012. The Petroleum System of Zubair Formation in Selected Oil Fields Southern Iraq Unpublished Thesis.

- AL-FADEL , K. & AL-ANSARI , F. 1992. The Petroleum Geology of The Upper Sandstone Member of the Zubair Formation in North Rumaila Oilfield.
- AL-FARES, A. A., BOUMAN, M. & JEANS, P. 1998. A new look at the Middle to Lower Cretaceous stratigraphy, offshore Kuwait. *GeoArabia*, 3, 543-560.
- AL-MUHALHAL, A., A 2004. Geological and Petrophysical Evaluation of the Zubair Formation in Selected Well, Southern Iraq. . 118.
- ALI, A. & NASSER, M. 1989. Facies analysis of the Lower Cretaceous oil-bearing Zubair Formation in southern Iraq. *Modern Geology*, 13, 225-242.
- ALI , F. A. 1989. Bitumen Distribution in The Upper Sandstone Member in Unit DJ -North Rumaila and West Qurna Fields Unpublished Report - South Oil Company - Basrah - Department of Geology., 13.
- ALMUTURY , W. G. & AL-ASADI , M. M. 2008. Tectonostratigraphic History of Mesopotamian Passive Margin During Mesozoic and Cenozoic , Southern Iraq. . *Journal of Kirkuk University , Scientific Studies.*, 3, 20.
- ALSHARHAN, A. S. & NAIRN, A. E. M. 1997. Sedimentary basins and petroleum geology of the Middle East, Elsevier Science.
- AMBROSE, J. 1973. Computerized transverse axial scanning (tomography): Part 2. Clinical application. *The British Journal of Radiology*, 46, 1023-1047.

- AQRAWI, A. A., GOFF, J., HORBURY, A. & SADOONI, F. 2010. The petroleum geology of Iraq, Scientific Press UK.
- ASHMAWY, A. K., EL-HAJJI, D., SOTELO, N. & MUHAMMAD, N. 2002. Hydraulic performance of untreated and polymer-treated bentonite in inorganic landfill leachates. *Clays and Clay Minerals*, 50, 546-552.
- ASHOOR , S. M. 1990. Clay Mineralogy of Upper Shale Member Zubair Formatin in South Rumaila Field. South Oil Company - Iraqi Ministry of Oil
- BARAKA-LOKMANE, S., MAIN, I., NGWENYA, B. & ELPHICK, S. 2009. Application of complementary methods for more robust characterization of sandstone cores. *Marine and Petroleum Geology*, 26, 39-56.
- BEAUFORT, D., CASSAGNABERE, A., PETIT, S., LANSON, B., BERGER, G., LACHARPAGNE, J. & JOHANSEN, H. 1998. Kaolinite-to-dickite reaction in sandstone reservoirs. *Clay minerals*, 33, 297-316.
- BISCAYE, P. 1964. DISTINCTION BETWEEN KAOLINITE+ CHLORITE IN RECENT SEDIMENTS BY X-RAY DIFFRACTION. *American Mineralogist*, 49, 1281-&.

- BJØLYKKE, K. 1998. Clay mineral diagenesis in sedimentary basins—a key to the prediction of rock properties. Examples from the North Sea Basin. *Clay minerals*, 33, 15-34.
- BLATT, H. 1979. Diagenetic processes in sandstones.
- BRADLEY, W. 1945. Diagnostic criteria for clay minerals. *Am. Miner.*, 30, 704-713.
- BUDAY, T. 1980. The regional geology of Iraq: stratigraphy and paleogeography, State Organization.
- BUDAY, T. 1987. Tectonism, Magmatism and Metamorphism, State Establishment of Geol. Survey and Mineral Investigations, Ministry of Heavy Industries.
- BUDAY, T. & JASSIM, S. Z. 1987. The Regional Geology of Iraq. Vol.2. Tectonism, Magmatism and Metamorphism. In: M.J., Abbas and I.I., Kassab (Eds.) GEOSURV, Baghdad, , 352pp.
- CARLSON, W. D., DENISON, C. & KETCHAM, R. A. 2000. High-resolution X-ray computed tomography as a tool for visualization and quantitative analysis of igneous textures in three dimensions. *Visual Geosciences*, 4, 1-14.
- CNUUDE, V. & BOONE, M. N. 2013. High-resolution X-ray computed tomography in geosciences: A review of the current technology and applications. *Earth-Science Reviews*, 123, 1-17.
- COLES, M., HAZLETT, R., SPANNE, P., SOLL, W., MUEGGE, E. & JONES, K. 1998. Pore level imaging of fluid transport using

synchrotron X-ray microtomography. *Journal of Petroleum Science and Engineering*, 19, 55-63.

DESCHAMPS, R., KOHLER, E., GASPARRINI, M., DURAND, O., EUZEN, T. & NADER, F. 2012. Impact of mineralogy and diagenesis on reservoir quality of the Lower Cretaceous Upper Mannville Formation (Alberta, Canada). *Oil & Gas Science and Technology–Revue d'IFP Energies nouvelles*, 67, 31-58.

DEWERS, T. & ORTOLEVA, P. 1991. Influences of clay minerals on sandstone cementation and pressure solution. *Geology*, 19, 1045-1048.

DOLSON, J. 2016. *Quantifying Seals and Saturations: Capillary Pressure, Pseudo-capillary Pressure and Quantitative Show Assessment. Understanding Oil and Gas Shows and Seals in the Search for Hydrocarbons*. Cham: Springer International Publishing.

DONG, H. 2008. *Micro-CT imaging and pore network extraction*. Department of Earth Science and Engineering, Imperial College London.

ESLINGER, E. & PEVEAR, D. R. 1988. *Clay minerals for petroleum geologists and engineers*, Society of Economic Paleontologists and Mineralogists.

FARRELL, K. M., HARRIS, W. B., MALLINSON, D. J., CULVER, S. J., RIGGS, S. R., PIERSON, J. & LAUTIER, J. C. 2012. *Standardizing texture and facies codes for a process-based*

- classification of clastic sediment and rock. *Journal of Sedimentary Research*, 82, 364-378.
- FISHER, W. L. 1969. Facies characterization of Gulf Coast Basin delta systems, with some Holocene analogues.
- FLANNERY, B. P., DECKMAN, H. W., ROBERGE, W. G. & D'AMICO, K. L. 1990. Three-dimensional X-ray microtomography. *NDT International*, 23, 291.
- FLOHR, T. G., RAUPACH, R. & BRUDER, H. 2009. Cardiac CT: how much can temporal resolution, spatial resolution, and volume coverage be improved? *Journal of cardiovascular computed tomography*, 3, 143-152.
- FOLK, R. L. 1974. *Petrology of Sedimentary Rocks*. : Austin, Hemphill Publishing Company, 182 p.
- FOUAD, S. 2010. Tectonic and structural evolution of the Mesopotamia Foredeep, Iraq. *Iraqi bull. Geol. and Min*, 6, 41-53.
- GAWLER, J., SANDERS, M., BULL, J., DU BOULAY, G. & MARSHALL, J. 1974. Computer assisted tomography in orbital disease. *The British journal of ophthalmology*, 58, 571.
- GILBOY, W., FOSTER, J. & FOLKARD, M. 1982. A tomographic gamma-ray scanner for industrial applications. *Nuclear Instruments and Methods in Physics Research*, 193, 209-214.
- GODEL, B. 2013. High-Resolution X-Ray Computed Tomography and Its Application to Ore Deposits: From Data Acquisition to Quantitative

- Three-Dimensional Measurements with Case Studies from Ni-Cu-PGE Deposits. *Economic Geology*, 108, 2005-2019, <http://doi.org/10.2113/econgeo.108.8.2005>.
- GRODZINS, L. 1983. Optimum energies for x-ray transmission tomography of small samples. *Nuclear Instruments and Methods in Physics Research*, 206, 541-545.
- HAKIM, N. A. & HASAN, S. A. 1980. Geological Study of The Upper Shale Member Rumaila North & West Qurna Fileds.
- HASAN, S. A. 1988. Updating Geological Study of the Upper Shale Member -Zubair Formation ,South Rumaila Field.
- HENSON, R. Observations on the geology and petroleum occurrences in the Middle East. 3rd World Petroleum Congress, 1951. World Petroleum Congress.
- HMOOD, H. G. 2002. Geological correlation of the Upper Shale Member Zubair Formation , Ratga Area , South Rumaila Oilfield to Evaluate The Extensions and Properties of The Reservoir Units Thesis.
- HOUNSFIELD, G. N. 1973. Computerized transverse axial scanning (tomography): Part 1. Description of system. *The British Journal of Radiology*, 46, 1016-1022.
- HUNT, J. M. 1990. Generation and Migration of Petroleum from Abnormally Pressured Fluid Compartments (1). *AAPG bulletin*, 74, 1-12.



- HURST, A., SCOTT, A. & VIGORITO, M. 2011. Physical characteristics of sand injectites. *Earth-Science Reviews*, 106, 215-246.
- IDAN, R. M., FAISAL, R. F., NASSER, M. E., AL-AMERI, T. K. & AL-RAWI, D. 2015. Hydrocarbon potential of Zubair Formation in the south of Iraq. *Arabian Journal of Geosciences*, 8, 4805-4817.
- JÄHNE, B. 2006. *Digital Image Processing*.
- JASSIM, S. & AL-GAILANI, M. 2006. Hydrocarbons. *Geology of Iraq*. Dolin, Prague and Moravian Museum, Brno, 232-250.
- JASSIM, S. Z. & GOFF, J. J. C. 2006. *The Geology of Iraq*, Geological Society Publishing House.
- JIN, L., RAVELLA, R., KETCHUM, B., BIERMAN, P. R., HEANEY, P., WHITE, T. & BRANTLEY, S. L. 2010. Mineral weathering and elemental transport during hillslope evolution at the Susquehanna/Shale Hills Critical Zone Observatory. *Geochimica et Cosmochimica Acta*, 74, 3669-3691.
- JOLLEY, S., FISHER, Q. & AINSWORTH, R. 2010. Reservoir compartmentalization: an introduction. Geological Society, London, Special Publications, 347, 1-8.
- JONAS, E. C., MCBRIDE, E. F., JONAS, E. C., UNIVERSITY OF TEXAS AT, A. & DEPARTMENT OF GEOLOGICAL, S. 1977. Diagenesis of sandstone and shale : application to exploration for hydrocarbons, Austin, Dept. of Geological Sciences, the University of Texas at Austin.

- JOZANIKOHAN, G., SAHABI, F., NOROUZI, G. H., MEMARIAN, H. & MOSHIRI, B. 2016. Quantitative analysis of the clay minerals in the Shurijeh Reservoir Formation using combined X-ray analytical techniques. *Russian Geology and Geophysics*, 57, 1048-1063.
- KACZMARCZYK, J., DOHNALIK, M., ZALEWSKA, J. & CNUUDE, V. 2010. The interpretation of X-ray Computed Microtomography images of rocks as an application of volume image processing and analysis.
- KETCHAM, R. A. & CARLSON, W. D. 2001. Acquisition, optimization and interpretation of X-ray computed tomographic imagery: applications to the geosciences. *Computers & Geosciences*, 27, 381-400.
- LIU, Z., C. TIAN, et al. (2013). "Causes of hydrodynamic pressure distribution: A case of the 4 th Pay in Zubair Formation, Rumaila Oilfield, Iraq." *Petroleum Exploration and Development* 40(6): 774-779.
- LONG, H., Swennen, R., Foubert, A., Dierick, M. & Jacobs, P. 2009. 3D quantification of mineral components and porosity distribution in Westphalian C sandstone by microfocus X-ray computed tomography. *Sedimentary Geology*, 220, 116-125.
- MACEWAN, D. M. C. 1944. Identification of the Montmorillonite Group of Minerals by X-Rays. *Nature*, 154, 577.

- MOORE, D. M. & REYNOLDS, R. C. 1989. X-ray Diffraction and the Identification and Analysis of Clay Minerals, Oxford university press Oxford.
- MOORE, D. M. & REYNOLDS, R. C. 1997. X-Ray Diffraction and the Identification and Analysis of Clay Minerals (2nd ed.), Oxford University Press.
- NADEAU, P. H. 1998a. AN EXPERIMENTAL STUDY (OF THE EFFECTS OR DIAGENETIC CLAY MIN HRALS ( ) N RESERVOIR SANDS.
- NADEAU, P. H. 1998b. An experimental study of the effects of diagenetic clay minerals on reservoir sands. *Clays and Clay Minerals*, 46, 18-26.
- NAZEER, A., ABBASI, S. A. & SOLANGI, S. H. 2016. Sedimentary facies interpretation of Gamma Ray (GR) log as basic well logs in Central and Lower Indus Basin of Pakistan. *Geodesy and Geodynamics*, 7, 432-443.
- ØREN, P.-E. & BAKKE, S. 2003. Reconstruction of Berea sandstone and pore-scale modelling of wettability effects. *Journal of Petroleum Science and Engineering*, 39, 177-199.
- ORSI, T. H., EDWARDS, C. M. & ANDERSON, A. L. 1994. X-Ray Computed Tomography: A Nondestructive Method for Quantitative Analysis of Sediment Cores: RESEARCH METHOD PAPER. *Journal of Sedimentary Research*, 64.

- ORTOLEVA, P. J. 1994a. Basin compartmentation: definitions and mechanisms. MEMOIRS-AMERICAN ASSOCIATION OF PETROLEUM GEOLOGISTS, 39-39.
- ORTOLEVA, P. J. 1994b. Basin compartments and seals, AAPG.
- OWEN, R. M. S. & NASR, S. N. 1958. The stratigraphy of the Kuwait-Basrah area. Weeks G. L. (editor) Habitat of Oil a Symposium. Am. Assoc. Petr. Geol., Tulsa.
- PÁPAY, J. 2003. Development of petroleum reservoirs: theory and practice, Akadémiai Kiadó.
- POPPE, L., PASKEVICH, V., HATHAWAY, J. & BLACKWOOD, D. 2001. A laboratory manual for X-ray powder diffraction. US Geological Survey Open-File Report, 1, 1-88.
- PRIMAK, A. N., FLETCHER, J. G., VRTISKA, T. J., DZYUBAK, O. P., LIESKE, J. C., JACKSON, M. E., WILLIAMS, J. C. & MCCOLLOUGH, C. H. 2007. Noninvasive differentiation of uric acid versus non-uric acid kidney stones using dual-energy CT. Academic radiology, 14, 1441-1447.
- RAMÓN, J. C. & CROSS, T. 1997. CHARACTERIZATION AND PREDICTION OF RESERVOIR ARCHITECTURE AND PETROPHYSICAL PROPERTIES IN FLUVIAL CHANNEL SANDSTONES, MIDDLE MAGDALENA BASIN, COLOMBIA. CT&F - Ciencia, Tecnología y Futuro, 1, 19-46.
- RICHARD, S. 1998. Elements of petroleum geology.

- RIVERS, M. L., WANG, Y. & UCHIDA, T. Microtomography at GeoSoilEnviroCARS. 2004. 783-791.
- ROHAN , A. B. 1975. Subsurface Investigation of the Upper Two Members of Zubair Formation N and S Rumaila Oilfields 115.
- ROSENBERG, E., FERREIRA DE PAIVA, R., GUÉROULT, P. & LYNCH, J. 1999. Microtomography applications in rock analysis and related fields. Proceedings of the Deutsche Gesellschaft für Zerstörungsfreie Prüfung-DGZfP, 9-18.
- SELLEY, R. C. & SONNENBERG, S. A. 2014. Elements of petroleum geology, Academic Press.
- SHARLAND, P. R., ARCHER, R., CASEY, D. M., DAVIES, R. B., HALL, S. H., HEWARD, A. P., HORBURY, A. D. & SIMMONS, M. D. 2001. Arabian Plate Sequence Stratigraphy. GeoArabia Special Publication 2, Gulf Petrolink, Bahrain, 371p.
- SMALLEY, P. & MUGGERIDGE, A. 2010. Reservoir compartmentalization: get it before it gets you. Geological Society, London, Special Publications, 347, 25-41.
- SMALLEY, P. C., DODD, T. A., STOCKDEN, I. L., RAHEIM, A. & MEARNS, E. W. 1995. Compositional heterogeneities in oilfield formation waters: identifying them, using them. The geochemistry of reservoirs, 59-69.
- HMOOD, H. G. 2002. Geological correlation of the Upper Shale Member Zubair Formation , Ratga Area , South Rumaila

Oilfield to Evaluate The Extensions and Properties of The Reservoir Units Thesis.

- LIU, Z., TIAN, C., ZHANG, W., MA, J. & LUO, H. 2013. Causes of hydrodynamic pressure distribution: A case of the 4<sup>th</sup> Pay in Zubair Formation, Rumaila Oilfield, Iraq. *Petroleum Exploration and Development*, 40, 774-779.
- SULLIVAN, K. B. & MCBRIDE, E. F. 1991. Diagenesis of Sandstones at Shale Contacts and Diagenetic Heterogeneity, Frio Formation, Texas (1). *AAPG bulletin*, 75, 121-138.
- TONKIN, N. S. 2012. Chapter 17 - Deltas. In: KNAUST, D. & BROMLEY, R. G. (eds.) *Developments in Sedimentology*. Elsevier.
- VAN BELLEN, R., DUNNINGTON, H., WETZEL, R. & MORTON, D. 1959. Iraq: *Lexique Stratigraphique International*. Centre National de la Recherche Scientifique, III, Asie, Fasc. 10a, Paris.
- VAN GEET, M., SWENNEN, R. & WEVERS, M. 2001. Towards 3-D petrography: application of microfocus computer tomography in geological science. *Computers & Geosciences*, 27, 1091-1099.
- VERMA, M., AHLBRANDT, T. & AL-GAILANI, M. 2004. Petroleum reserves and undiscovered resources in the total petroleum systems of Iraq: reserve growth and production implications. *GeoArabia*, 9, 51-74.
- WELLINGTON, S. & VINEGAR, H. 1987. X-ray computerized tomography. *Journal of Petroleum Technology*, 39, 885-898.

WELTON, J. E. 1984. SEM petrology atlas, American Association of Petroleum Geologists Tulsa, OK.

WILKINSON, M., MILLIKEN, K. L. & HASZELDINE, R. S. 2001. Systematic destruction of K-feldspar in deeply buried rift and passive margin sandstones. *Journal of the Geological Society*, 158, 675-683.

#### Online Sources

-AL-KADHIMI, J.M.A., SISSAKIAN, V.K., FATTAH, A.S. and DEIKRAN, D.B., 1996. Tectonic Map of Iraq, scale 1:1000000, 2<sup>nd</sup> edit., GEOSURV, Baghdad, Iraq.

(13) TECTONIC AND STRUCTURAL EVOLUTION OF THE MESOPOTAMIA PLAIN. Available from:

[https://www.researchgate.net/publication/274637252\\_TECTONIC\\_AND\\_STRUCTURAL\\_EVOLUTION\\_OF\\_THE\\_MESOPOTAMIA\\_PLAIN](https://www.researchgate.net/publication/274637252_TECTONIC_AND_STRUCTURAL_EVOLUTION_OF_THE_MESOPOTAMIA_PLAIN)

[accessed Jun 25 2018].

-UPDATE 2-Iraq aims to up Rumaila oilfield output to 1.5 mln bpd in 2018, 2017. Reuters [viewed 30 November 2017]. Available from: <https://af.reuters.com/article/energyOilNews/idAFL8N1NZ2QH>.

## Appendices



## Appendix 1

### Effective porosity and Permeability estimates of well B.

Depth (m)	Permeability Estimates	Effective porosity _ND
3200	0.0000213	0.03092404
3200.25	0.492677	0.1022877
3200.5	0.01274522	0.06035064
3200.75	0.03489143	0.07092614
3201	2.519597	0.1192477
3201.25	4.966714	0.1482637
3201.5	5.293878	0.1662087
3201.75	5.836583	0.168839
3202	7.142787	0.1719084
3202.25	9.456553	0.178574
3202.5	18.22704	0.1965772
3202.75	21.31791	0.2077601
3203	19.02143	0.2109655
3203.25	16.42426	0.2020046
3203.5	11.07439	0.1874044
3203.75	12.6134	0.1933826
3204	14.79682	0.1893726
3204.25	14.59318	0.1908896
3204.5	23.38246	0.1998687
3204.75	35.21698	0.2073411
3205	21.06642	0.2083988
3205.25	20.83194	0.1918974
3205.5	17.08929	0.1814154
3205.75	6.958555	0.1633579
3206	0.01778914	0.1092893
3206.25	0.00035993	44 0.06955229
3206.5	0.0000189	0.06126381
3206.75	0.0000191	0.03530237
3207	0.0000199	0.0291132
3207.25	0	0.04927868
3207.5	0.000004	0.04310864
3207.75	0.0000026	0.05109614
3208	0.000002	0.0469719
3208.25	0.0000019	0.0497625
3208.5	0.0000005	0.05340512
3208.75	0.00024657	98 0.06574173
3209	0.00461172	7 0.09092067
3209.25	0.00837277	8 0.08344072
3209.5	0.00432806	9 0.08285104

3209.75	0.00076821	3 0.05701748
3210	0.1030654	0.1094964
3210.25	0.3848925	0.1216449
3210.5	0.05118295	0.1103636
3210.75	0.02421594	0.0905408
3211	0.00376639	6 0.07103616
3211.25	0.00367631	7 0.05795798
3211.5	0.04886068	0.08106834
3211.75	0.1236075	0.08698724
3212	0.00130056	4 0.03223277
3212.25	0	0
3212.5	0	0
3212.75	0.0000772	0.01563901
3213	0.0362643	0.05332302
3213.25	0.5425782	0.08915517
3213.5	1.422166	0.1068946
3213.75	0.9823304	0.110977
3214	4.6715	0.1412081
3214.25	11.27637	0.1651375
3214.5	10.53628	0.1665179
3214.75	9.159511	0.1650537
3215	12.14986	0.1770776
3215.25	22.37529	0.1999375
3215.5	25.89066	0.202687
3215.75	30.07554	0.199152
3216	16.23631	0.1861417
3216.25	13.52793	0.1878682
3216.5	5.965884	0.1610221
3216.75	5.393776	0.1366008
3217	6.985194	0.1431303
3217.25	11.14508	0.1733618
3217.5	10.54281	0.1769131
3217.75	17.07931	0.1878996
3218	23.34459	0.1992627
3218.25	23.61588	0.2029145
3218.5	27.12698	0.2090486
3218.75	34.25843	0.2045134
3219	25.58249	0.2060665
3219.25	28.09187	0.2047933
3219.5	29.98586	0.2008505
3219.75	26.51361	0.2108492
3220	35.07553	0.2149989
3220.25	44.42829	0.2253433
3220.5	73.65043	0.2268166

3220.75	42.03625	0.2248736
3221	29.30764	0.2135394
3221.25	25.74011	0.2099848
3221.5	37.49204	0.2046934
3221.75	29.14602	0.19758
3222	25.48347	0.1781847
3222.25	16.81652	0.185647
3222.5	40.19401	0.1861673
3222.75	12.04526	0.1723414
3223	3.093237	0.1327869
3223.25	0.4208055	0.1271252
3223.5	1.069435	0.1168874
3223.75	0.3712165	0.08901928
3224	0.1918261	0.1130678
3224.25	0.5172022	0.1330362
3224.5	1.24109	0.1408909
3224.75	0.1582114	0.09010178
3225	0.01428483	0.07766247
3225.25	0.09247512	0.09391284
3225.5	0.07983232	0.1116259
3225.75	0.4514909	0.1311114
3226	1.655113	0.1407359
3226.25	0.04700156	0.07093489
3226.5	0.00016207	89 0.0191662
3226.75	0	0
3227	0.01382413	0.05537452
3227.25	0.07882192	0.07467006
3227.5	0.05480577	0.101211
3227.75	1.382534	0.1274238
3228	1.434322	0.1138819
3228.25	0.256573	0.07349715
3228.5	0.1229099	0.06463853
3228.75	0.000065	0.01488522
3229	0.00032157	26 0.05709159
3229.25	0.02002866	0.111582
3229.5	2.132278	0.155104
3229.75	0.02719144	0.1222736
3230	0.9552889	0.1620147
3230.25	7.799506	0.1522556
3230.5	3.595267	0.1368908
3230.75	6.235581	0.1565571
3231	12.5781	0.1789061
3231.25	14.49875	0.1853393
3231.5	20.73053	0.1933703

3231.75	15.19858	0.1876446
3232	11.60172	0.1799471
3232.25	9.655911	0.1717027
3232.5	7.004793	0.1589358
3232.75	1.369504	0.1133712
3233	0.3257849	0.08334237
3233.25	0.1483705	0.07367143
3233.5	0	0.00226365
3234.75	0.0049886	1 0.03515998
3235	0.6676412	0.09808067
3235.25	0.6087335	0.09857981
3235.5	0.1796923	0.07901188
3235.75	0.0709209	0.06512158
3236	2.762911	0.1351748
3236.25	5.937842	0.1549856
3236.5	16.90862	0.1865394
3236.75	35.78658	0.2043567
3237	36.72071	0.2167581
3237.25	75.90878	0.2246489
3237.5	82.49689	0.2356485
3237.75	69.06384	0.2358305
3238	46.28702	0.2281607
3238.25	56.5502	0.219633
3238.5	34.15304	0.2057373
3238.75	27.81817	0.2029314
3239	26.7534	0.2067821
3239.25	75.84956	0.2169895
3239.5	54.19518	0.2162903
3239.75	44.52121	0.2188348
3240	45.48065	0.2220757
3240.25	36.1586	0.2122263
3240.5	31.09515	0.215184
3240.75	36.55289	0.2152785
3241	67.67487	0.2231685
3241.25	70.68478	0.2347889
3241.5	70.21996	0.2421646
3241.75	46.98664	0.2327697
3242	76.60271	0.2309313
3242.25	76.21718	0.2300004
3242.5	48.11051	0.2206349
3242.75	50.70168	0.2263411
3243	49.92061	0.2259745
3243.25	34.53133	0.2217927
3243.5	42.16004	0.2261417

3243.75	57.45561	0.2325247
3244	75.21594	0.2262629
3244.25	61.16779	0.2277493
3244.5	55.43274	0.2296087
3244.75	59.62931	0.2360948
3245	43.28968	0.2309885
3245.25	69.49342	0.2236092
3245.5	55.48705	0.2201013
3245.75	38.8993	0.2161255
3246	24.61552	0.206673
3246.25	9.138908	0.1669066
3246.5	1.150769	0.1097016
3246.75	0.1617622	0.0782644
3247	2.917197	0.1189744
3247.25	7.391105	0.1505729
3247.5	5.127119	0.1342913
3247.75	1.161616	0.1242035
3248	5.178164	0.1565801
3248.25	17.99022	0.1920847
3248.5	26.12651	0.2061848
3248.75	20.57649	0.1742646
3249	3.365225	0.1383131
3249.25	0.1139833	0.06911533
3249.5	0	0.003125742
3249.75	0.00718911	3 0.02787739
3250.5	0.0000306	0.01620796
3250.75	0.00791136	9 0.05052759
3251	0.03153037	0.05310314
3251.25	0.0000405	0.0145334
3251.75	0.000004	0.008167192
3252	0.00690199	3 0.04578943
3252.25	0.00588362	1 0.05102071
3252.5	0.02631241	0.05713966
3252.75	0.1056998	0.06887666
3253	0.03865554	0.04904389
3253.25	1.079306	0.08726145
3253.5	0.14515	0.09381236
3253.75	0.1069039	0.06996367
3254	0.06515913	0.05619547
3254.25	0.00148641	8 0.03031166
3254.5	0.0000205	0.01294971
3254.75	0.000085	0.01834035
3255	0.00043899	22 0.02675937
3255.75	0.04637526	0.06628122

3256	1.286746	0.1147479
3256.25	8.896246	0.1553822
3256.5	6.397192	0.1388462
3256.75	2.757348	0.1259556
3257	4.711156	0.1329738
3257.25	31.72204	0.1813878
3257.5	43.78905	0.1904585
3257.75	67.40611	0.202032
3258	86.54635	0.2080747
3258.25	79.06131	0.2039225
3258.5	63.56704	0.1963483
3258.75	81.58272	0.2038867
3259	94.41274	0.207122
3259.25	61.45879	0.1955362
3259.5	29.40843	0.1734641
3259.75	0.6761486	0.0819204
3260	0	0.000067
3260.75	0.00390201	4 0.02944066
3261	4.703635	0.1462257
3261.25	3.828896	0.1284608
3261.5	2.664727	0.105649
3261.75	4.578964	0.1156856
3262	11.97853	0.1285386
3262.25	7.261658	0.1188196
3263.25	1.262952	0.08626837
3263.5	6.384486	0.1192384
3263.75	4.882768	0.1170049
3264	0.4969137	0.09023125
3264.25	0.1219525	0.0607864
3265.5	0.0000164	0.009984761
3265.75	0.1065691	0.0854014
3266	0.03656925	0.06346118
3266.25	0.01058589	0.04248943
3266.5	0.00019483	24 0.01885964
3271.75	0.00159928	9 0.03952511
3273.5	0.07119473	0.09018183
3273.75	0.3621204	0.1156879
3274	2.6467	0.1508051
3274.25	3.419608	0.1749856
3274.5	0.704197	0.1153952
3274.75	1.148849	0.1266629
3275	2.037405	0.1373988
3275.25	0.8551364	0.1324447
3275.5	0.9587715	0.1392759

3275.75	0.2229155	0.1101846
3276	0.00107419	1 0.07828558
3276.25	0.00112052	9 0.03006996
3276.5	0.05397063	0.07714975
3276.75	2.08717	0.1260218
3277	1.246992	0.1117791
3277.25	1.698822	0.125285
3277.5	1.888176	0.1206597
3277.75	1.445999	0.1157849
3278	4.121538	0.1416523
3278.25	5.432294	0.1525717
3278.5	0.4804032	0.1074511
3278.75	0.1257486	0.07891049
3279	0.02536611	0.04453577
3279.25	0.000005	0.007235751
3279.5	0.00022834	66 0.0155201
3279.75	0.00227	8 0.04966858
3280	0.0000151	0.04097024
3280.25	0.03190993	0.05235673
3280.5	0.3149181	0.1043982
3280.75	44.0824	0.1866672
3281	25.7161	0.1764261
3281.25	9.49279	0.1340788
3281.5	0.01717047	0.03759553
3281.75	0.1915892	0.06773666
3282	14.4157	0.1343832
3282.25	9.348904	0.1447553
3282.5	21.58379	0.1510831
3282.75	2.04518	0.1526354
3283	1.15115	0.1461665
3283.25	1.765062	0.1433473
3283.5	6.625951	0.1801351
3283.75	8.924995	0.1901737
3284	6.073035	0.1825006
3284.25	5.725856	0.1806808
3284.5	5.637442	0.1797084
3284.75	7.803192	0.1915725
3285	6.697948	0.1927263
3285.25	0.115745	0.2055661
3285.5	1.431076	0.1892668
3285.75	3.561129	0.1692998
3286	2.090581	0.1564776
3286.25	2.079733	0.1575021
3286.5	4.185946	0.1748623

3286.75	7.493403	0.1918089
3287	3.979468	0.1847944
3287.25	7.981075	0.1845113
3287.5	3.306175	0.1804962
3287.75	0.7225892	0.1820665
3288	0.1491607	0.1892149
3288.25	0.7859253	0.1951806
3288.5	0.08076823	0.1911853
3288.75	0.08121083	0.1815888
3289	0.00362041	4 0.1813019
3289.25	0.001287	4 0.1907069
3289.5	0.03705911	0.1828293
3289.75	0.3165456	0.1832704
3290	1.729853	0.1812993
3290.25	1.42221	0.1818466
3290.5	0.01026162	0.153893
3290.75	0.07282383	0.1120584
3291	0.0000154	0.03857963
3291.25	0.000062	0.04023609
3291.5	0.00589545	7 0.08411382
3291.75	0.7391361	0.1318106
3292	1.186003	0.11295
3292.25	0.3872337	0.0972193
3292.5	0.00673014	1 0.05106655
3292.75	0.01475251	0.05520391
3293	0.03502629	0.06329228
3293.25	0.09228157	0.07905371
3293.5	0.1637026	0.09356982
3293.75	1.299363	0.1138066
3294	1.405897	0.1167559
3294.25	0.3334648	0.08843382
3294.5	0.02741298	0.05514611
3294.75	0.00592614	4 0.04597871
3295	2.132568	0.1369091
3295.25	2.503249	0.150287
3295.5	6.340602	0.1679124
3295.75	24.61905	0.182682
3296	9.389083	0.1887365
3296.25	2.058818	0.1746129
3296.5	0.2338719	0.1732776
3296.75	2.495048	0.1693735
3297	0.00875856	7 0.1381041
3297.25	0.00718372	0.07168122
3297.5	0	0



3297.75	0.0000017	0.01354018
3298	0.00021854	92 0.04226771
3298.25	0.2819309	0.08278604
3298.5	11.82653	0.1333013
3298.75	6.762877	0.1447384
3299	33.21892	0.1572766
3299.25	4.092535	0.1343724
3299.5	4.863012	0.1527333
3299.75	9.896914	0.1783036
3300	15.45423	0.2027529
3300.25	12.26173	0.1806893
3300.5	0.3878919	0.1663076
3300.75	3.369418	0.1675789
3301	4.116464	0.1908469
3301.25	1.892219	0.2044701
3301.5	6.935391	0.2031942
3301.75	1.997754	0.2072969
3302	1.799526	0.2139817
3302.25	8.810261	0.2181887
3302.5	17.2077	0.2171174
3302.75	3.279141	0.2068992
3303	2.974969	0.199887
3303.25	0.1214624	0.2104848
3303.5	10.81964	0.2177025
3303.75	8.038369	0.2152088
3304	14.46449	0.2156621
3304.25	0.8234761	0.2218602
3304.5	8.957217	0.2218721
3304.75	0.3342921	0.207328
3305	0.895645	0.1879195
3305.25	1.859021	0.1781764
3305.5	0.1094581	0.1900479
3305.75	20.82202	0.1964325
3306	10.02272	0.2011856
3306.25	12.52453	0.2004231
3306.5	8.078619	0.1984854
3306.75	7.523627	0.1891313
3307	5.819122	0.1783369
3307.25	4.185463	0.1747144
3307.5	1.577541	0.1549818
3307.75	3.873336	0.1609537
3308	7.329644	0.1803089
3308.25	6.492487	0.1789749
3308.5	4.733503	0.1601987

3308.75	1.574559	0.1167309
3309	0.00819842	9 0.04802307
3309.25	0.0011767	3 0.03099787
3309.5	0.07117745	0.07053502
3309.75	0.02497711	0.0644573
3310	0.04151927	0.06775065
3310.25	0.03415604	0.07323262
3310.5	0.02129895	0.06957911
3310.75	0.03471449	0.05762899
3311	0.00272304	9 0.03433914
3311.25	0.00093903	32 0.02609183
3311.5	0.01149376	0.04329777
3311.75	0.00467252	1 0.06284545
3312	0.04856244	0.06030108
3312.25	0.00014182	85 0.02991094
3312.5	0.0000008	0.01064956
3312.75	0.00108205	6 0.04145411
3313	0.00623105	4 0.0619406
3313.25	0.00017966	79 0.03326267
3313.5	0	0.0126503
3313.75	0.00216631	6 0.06404848
3314	0.1135043	0.1102388
3314.25	0.3204663	0.1130913
3314.5	0.06210874	0.0764842
3314.75	0.0000971	0.02911022
3315	0.0000019	0.01476771
3315.25	0	0
3315.5	0.0000018	0.02453089
3315.75	0.00111736	1 0.06511822
3316	0.00536282	7 0.05528097
3316.25	0.3275652	0.100287
3316.5	0.2224579	0.1092245
3316.75	0.1630377	0.1165413
3317	0.1484746	0.1262124
3317.25	0.75757	0.1492176
3317.5	0.7420147	0.1384897
3317.75	0.1734677	0.1279208
3318	0.1234453	0.1162097
3318.25	0.9988822	0.1193948
3318.5	1.092844	0.1291949
3318.75	0.5519471	0.1208267
3319	0.4718262	0.1258724
3319.25	1.136165	0.1544899
3319.5	1.367146	0.168435

3319.75	3.359705	0.1950583
---------	----------	-----------

**Effective porosity and Permeability estimates of well A.**

Depth	Permeability (md)	PHIT_ND
3075	12.52299	0.4358963
3075.25	3.305411	0.414594
3075.5	4.215742	0.4153615
3075.75	0.6371701	0.2389278
3076	0.4856299	0.2088949
3076.25	0.3671006	0.203758
3076.5	0.09082381	0.2125826
3076.75	0.004183718	0.1958586
3077	0.1019836	0.2306081
3077.25	1.640533	0.2193429
3077.5	4.755092	0.2188587
3077.75	11.90951	0.2262969
3078	8.580468	0.2297405
3078.25	9.26197	0.2340071
3078.5	8.602084	0.2370868
3078.75	8.593219	0.2370868
3079	20.16275	0.237611
3079.25	14.54468	0.2324489
3079.5	10.32604	0.2241063
3079.75	12.71037	0.2236516
3080	12.68389	0.2268334
3080.25	15.14227	0.2338165
3080.5	12.49952	0.2358772
3080.75	9.280225	0.2408158
3081	4.592742	0.2440699
3081.25	0.1471148	0.2956239
3081.5	0.1304455	0.3435065
3081.75	0.1074698	0.3641686
3082	0.2199325	0.3763784
3082.25	0.09308826	0.3823486
3082.5	0.1038527	0.3825207
3082.75	0.02528686	0.3517921
3083	0.1471427	0.3551714
3083.25	0.3662659	0.3616126
3083.5	0.162955	0.3554157

3083.75	0.07768311	0.3359315
3084	0.06766293	0.3259525
3084.25	0.04207195	0.3361645
3084.5	0.01078044	0.3362423
3084.75	0.006759207	0.3221566
3085	0.01370728	0.3151346
3085.25	0.0175013	0.3011393
3085.5	0.02646251	0.2649408
3085.75	0.02217447	0.1848231
3086	0.3590512	0.2034811
3086.25	0.2265036	0.173811
3086.5	0.004613547	0.17193
3086.75	0.0000121	0.1858371
3087	0.0000082	0.1993409
3087.25	0.000226302	9 0.2430562
3087.5	0.000188526	1 0.2131507
3087.75	0.0000301	0.154963
3088	0.0000001	0.1691836
3088.25	0.000885219	8 0.2257053
3088.5	0.1527295	0.2510801
3088.75	0.9033878	0.2066082
3089	0.6440789	0.1996648
3089.25	0.2732937	0.1874363
3089.5	0.08552618	0.1727266
3089.75	0.0417455	0.1692493
3090	0.1576663	0.1781882
3090.25	0.04643918	0.1718366
3090.5	0.004135745	0.1711096
3090.75	0.0000522	0.1697325
3091	0.0000085	0.1859287
3091.25	0.001489231	0.2019338
3091.5	0.04202696	0.2105739
3091.75	0.09970727	0.2173645
3092	0.2445199	0.2205448
3092.25	0.6188359	0.2217209
3092.5	1.139046	0.2248269
3092.75	1.041443	0.2219462
3093	0.6321045	0.2190839
3093.25	0.2942195	0.2164281
3093.5	0.04326518	0.2186334
3093.75	0.000737283	2 0.2160154
3094	0	0.2233463
3094.25	0.01261541	0.2328033
3094.5	1.980714	0.2352777

3094.75	5.17678	0.2275005
3095	4.366297	0.2218887
3095.25	4.883858	0.2286256
3095.5	6.25939	0.2344537
3095.75	9.097982	0.2393919
3096	12.2232	0.2402796
3096.25	14.23752	0.2360467
3096.5	14.46712	0.2308675
3096.75	17.80584	0.2335766
3097	19.38771	0.2401713
3097.25	19.76582	0.2356261
3097.5	11.77523	0.2288367
3097.75	16.59083	0.2358227
3098	10.64277	0.2423429
3098.25	15.57324	0.2474893
3098.5	10.64895	0.2466044
3098.75	12.61927	0.2453107
3099	9.975349	0.2412308
3099.25	12.98389	0.2432306
3099.5	11.98691	0.251669
3099.75	5.491026	0.2676823
3100	1.977521	0.2819251
3100.25	3.380049	0.333974
3100.5	4.892685	0.334803
3100.75	0.3578075	0.2298202
3101	0.665763	0.2274949
3101.25	1.271683	0.2332424
3101.5	1.727831	0.2334833
3101.75	1.386537	0.214278
3102	1.39298	0.2097996
3102.25	2.366543	0.2147837
3102.5	3.181245	0.2138725
3102.75	3.234916	0.2070657
3103	4.873385	0.2156928
3103.25	8.152904	0.2221155
3103.5	13.42303	0.2214348
3103.75	14.80395	0.2183274
3104	13.91074	0.2223422
3104.25	7.104157	0.2098884
3104.5	8.336848	0.2024684
3104.75	2.920296	0.2059592
3105	0.2400982	0.2050028
3105.25	0.0000031	0.183216
3105.5	0.000483405	5 0.2070122

3105.75	0.0000003	0.2093707
3106	0.0000131	0.2076817
3106.25	0.0000085	0.2016377
3106.5	0.000209316	5 0.2301885
3106.75	0.02533976	0.23532
3107	0.1238244	0.2224104
3107.25	0.003428371	0.2383859
3107.5	0.0000333	0.2447191
3107.75	0.001263292	0.237902
3108	0.0000024	0.2255067
3108.25	0.0000252	0.2562108
3108.5	0.000553967	8 0.3258009
3108.75	0.006409267	0.34293
3109	0.001054486	0.3209171
3109.25	0.0000736	0.2866992
3109.5	0.000871016	4 0.2234531
3109.75	0	0.1158517
3110	0	0.1447297
3110.25	0.002782302	0.2039741
3110.5	0.00086613	6 0.2028053
3110.75	0.0000718	0.2012632
3111	0.000100797	7 0.2568839
3111.25	0.0000016	0.240758
3111.5	0.07326996	0.2483551
3111.75	0.9586338	0.2278846
3112	0.9882615	0.2111596
3112.25	0.9679717	0.1994335
3112.5	0.01206298	0.1698498
3112.75	0	0.1432213
3113	0	0.1606869
3113.25	0.000266415	2 0.1861385
3113.5	0.007043702	0.2009431
3113.75	0.0000447	0.1786258
3114	0.0000985	0.2045089
3114.25	0.01004031	0.2565206
3114.5	0.8529589	0.3256265
3114.75	74.36983	0.394051
3115	93.34983	0.3619544
3115.25	8.094682	0.2602619
3115.5	10.94167	0.2332817
3115.75	9.435285	0.2319167
3116	11.8016	0.2238411
3116.25	6.537325	0.2196885
3116.5	7.3567	0.2168049

3116.75	12.51663	0.2315423
3117	4.330146	0.2209122
3117.25	3.459553	0.215134
3117.5	1.207905	0.211448
3117.75	0.1102888	0.2132661
3118	0.003861248	0.1991095
3118.25	0.0000048	0.180741
3118.5	0.0000002	0.1923066
3118.75	0	0.1869085
3119	0.0000238	0.1886657
3119.25	0.003609747	0.1989587
3119.5	0.01020648	0.1950295
3119.75	0.01070047	0.1801564
3120	0.02985371	0.1878117
3120.25	0.2021594	0.2016317
3120.5	0.5956815	0.2089959
3120.75	0.4845676	0.2152385
3121	0.000614622	1 0.1948159
3121.25	0.0000004	0.1867643
3121.5	0.004342876	0.2032505
3121.75	0.1906444	0.2321571
3122	2.421912	0.244472
3122.25	1.556288	0.2303442
3122.5	3.929579	0.2338878
3122.75	13.2157	0.2478617
3123	103.8585	0.2613223
3123.25	34.12582	0.2504732
3123.5	20.575	0.2414164
3123.75	25.44488	0.2401158
3124	38.13605	0.2471829
3124.25	38.04524	0.2551981
3124.5	26.44511	0.2478504
3124.75	19.36351	0.2418984
3125	21.544	0.2421207
3125.25	24.29194	0.2446438
3125.5	19.17036	0.2410081
3125.75	18.87944	0.2496253
3126	14.92729	0.2485168
3126.25	14.243	0.2432306
3126.5	10.30128	0.2331125
3126.75	2.887172	0.2236993
3127	1.702853	0.2123959
3127.25	0.9761949	0.2102157
3127.5	1.006287	0.2120637

3127.75	0.1615815	0.1966577
3128	0.0000244	0.1689061
3128.25	0	0.1498306
3128.5	0	0.1511065
3128.75	0	0.1430988
3129	0.009248543	0.1665661
3129.25	0.3770383	0.187302
3129.5	2.459989	0.21714
3129.75	1.158731	0.2147269
3130	0.3620961	0.214603
3130.25	0.112941	0.2046243
3130.5	0.008565486	0.1799164
3130.75	0.001449644	0.1687058
3131	0.000144385	6 0.1679798
3131.25	0.000499034	1 0.1668546
3131.5	0.01479538	0.1815871
3131.75	0.003085746	0.1705871
3132	0.0000868	0.171536
3132.25	0.0000002	0.1742278
3134.75	0.01354837	0.1984106
3135	0.1635786	0.1870429
3135.25	0.7003232	0.1908349
3135.5	1.62356	0.1978487
3135.75	1.041658	0.1994852
3136	0.2723505	0.2004345
3136.25	0.07665115	0.1990089
3136.5	0.0893835	0.2054622
3136.75	0.39604	0.2272968
3137	0.01439239	0.2367819
3137.5	0.0000125	0.2674677
3138	0.000217459	2 0.3241625
3138.25	0.000399953	8 0.3330183
3138.5	0.000899548	1 0.3230401
3138.75	0.01256853	0.3382163
3139	0.05251135	0.3420371
3139.25	0.005246148	0.2839188
3139.75	0.0000001	0.1237587
3140	0.1225467	0.1793906
3140.25	0.6292266	0.1918454
3140.5	1.598963	0.1996648
3140.75	2.260875	0.1997183
3141	1.825899	0.1934059
3141.25	1.291937	0.190392
3141.5	1.132535	0.1973836



3141.75	2.0558	0.2098884
3142	2.278011	0.2167339
3142.25	0.9953594	0.2077041
3142.5	0.2996476	0.1984986
3142.75	0.02048789	0.1916542
3143	0.00011521	9 0.1891671
3143.25	0.000357024	5 0.1937912
3143.5	0.003938915	0.1986022
3143.75	0.0000427	0.199174
3145.75	0.000966379	7 0.3609834
3146	0.006456848	0.3650418
3146.25	0.01759174	0.368098
3146.5	0.009002804	0.3456307
3146.75	0.2704932	0.352919
3147	0.2229592	0.2785285
3147.25	0.02638149	0.2025923
3147.5	0.9692994	0.2053659
3147.75	0.06072296	0.173048
3149	0.0000699	0.1859021
3149.5	0.000185789	7 0.1821237
3149.75	0.02075521	0.1840897
3150	0.9211348	0.191934
3150.25	7.974988	0.2191575
3150.5	15.1163	0.2191135
3150.75	1.422647	0.2124142
3151	0.1188409	0.201894
3151.25	0.000174556	4 0.1901271
3152.75	0.0000007	0.2522849
3153	0.02062415	0.2655229
3153.25	0.01735168	0.2527813
3153.5	0.0000367	0.1973229
3153.75	0.0000192	0.1957649
3154.5	0.0000603	0.1706339
3154.75	0.00258192	0.1632558
3155	0.03463049	0.1636693
3155.25	0.001119458	0.1714458
3155.5	0.01527483	0.2166079
3155.75	0.1394505	0.2381825
3156	0.190603	0.1907296
3156.25	0.3864945	0.1673039
3156.5	0.3796448	0.1780132
3156.75	0.3146141	0.1997183
3157	0.1370506	0.2363091
3157.25	2.023275	0.3220188

3157.5	0.603142	0.2930453
3157.75	0.06288046	0.2401588
3158	0.528581	0.2038863
3158.25	10.17143	0.2026206
3158.5	14.89856	0.2099762
3158.75	12.54249	0.2117216
3159	11.84734	0.2164071
3159.25	20.36158	0.227704
3159.5	26.14387	0.2308675
3159.75	22.23796	0.2222843
3160	14.26462	0.2190433
3160.25	24.26322	0.2288744
3160.5	19.54392	0.2324866
3160.75	26.6848	0.2349485
3161	20.77057	0.2324539
3161.25	16.8629	0.2227197
3161.5	16.59004	0.2177301
3161.75	6.882425	0.2203737
3162	3.352647	0.2303825
3162.25	0.2332361	0.2235877
3162.5	0.04744549	0.2601052
3162.75	0.000619281	8 0.2807203
3163	0.000643895	6 0.2611569
3163.25	0.000882379	8 0.2285007
3163.5	0.003860623	0.2054398
3163.75	0.001087617	0.1636501
3164	0.007604987	0.1576412
3164.25	0.0000128	0.1537921
3167.5	0.0000001	0.1871116
3167.75	0.0000004	0.1900892
3168	0.0000004	0.1940365
3168.25	0.0000002	0.1917036
3168.5	0.000984693	3 0.1880697
3168.75	0.00561739	0.1842606
3169	0.02206369	0.1796536
3169.25	0.2131546	0.1891271
3169.5	0.1831693	0.1831905
3169.75	0.143296	0.1811572
3170	0.2226447	0.1895248
3170.25	0.1371358	0.1934893
3170.5	0.066307	0.1930822
3170.75	0.07476424	0.19611
3171	0.1206611	0.1834351
3171.25	0.2050605	0.1811572

3171.5	0.2284914	0.1842403
3171.75	0.2019462	0.1938877
3172	0.01381113	0.1797798
3172.25	0.03103416	0.2066604
3172.5	0.04150684	0.22632
3172.75	3.382102	0.2213657
3173	6.17061	0.2125018
3173.25	1.468801	0.1863286
3173.5	0.04624989	0.1796874
3173.75	0.000622781	2 0.2021683
3174	0.0000002	0.206094
3174.25	0.04337528	0.2217352
3174.5	0.09034022	0.2003376
3174.75	0.09134694	0.1790219
3175	0.1132237	0.2526208
3175.25	0.0000285	0.2354032
3175.5	0.0000285	0.1846555
3176	0.0000004	0.1824437
3176.25	0.0000424	0.1958405
3176.75	0.0000006	0.2065801
3177	0.000309821	0.2233643
3177.25	0.0000321	0.2128702
3177.5	0.000022	0.2035844
3177.75	0.000918724	9 0.1923705
3178	0.000270452	1 0.1806833
3178.25	0.01431273	0.1847226
3178.5	0.05690074	0.1740275
3178.75	1.484251	0.2059814
3179	10.85565	0.2163415
3179.25	13.87994	0.2265719
3179.5	20.73899	0.2288192
3179.75	12.04318	0.220033
3180	11.30201	0.2226645
3180.25	17.17039	0.2369782
3180.5	24.22824	0.2364529
3180.75	15.40869	0.2338165
3181	10.76349	0.2301842
3181.25	20.99855	0.2369782
3181.5	16.08917	0.2356261
3181.75	16.00961	0.2421898
3182	16.94595	0.2496253
3182.25	21.56193	0.2522375
3182.5	19.39679	0.2474055
3182.75	18.39175	0.2517389

3183	21.122	0.2611036
3183.25	20.72525	0.2553087
3183.5	17.4733	0.2417919
3183.75	15.75151	0.2340071
3184	14.70023	0.2383257
3184.25	10.62497	0.2351745
3184.5	11.54891	0.2349485
3184.75	11.10317	0.2335766
3185	8.595076	0.2353744
3185.25	6.511765	0.2353744
3185.5	3.646445	0.2347012
3185.75	1.318556	0.2385499
3186	0.1186554	0.243307
3186.25	0.001113061	0.2526252
3186.5	0.03463262	0.2551981
3186.75	0.1164733	0.2536445
3187	0.1997425	0.247628
3187.25	0.5853107	0.2511724
3187.5	0.8631974	0.2417919
3187.75	1.016145	0.2154347
3188	0.5356752	0.195708
3188.25	0.4157865	0.1931196
3188.5	0.001447123	0.1417757
3188.75	0.000191407	7 0.1424403
3189	0.0000242	0.1632558
3190	0.000242684	5 0.1802994
3190.25	0.1517287	0.1841924
3190.5	0.07752494	0.1943457
3190.75	0.7877602	0.2006689
3191	20.1587	0.211118
3191.25	15.77766	0.2137821
3191.5	26.42054	0.2200988
3191.75	15.9317	0.2187508
3192	9.750885	0.2042868
3192.25	5.393516	0.1867231
3192.5	1.055784	0.1507635
3192.75	0.1322272	0.1112253
3193	0.009239403	0.08078949
3193.25	0.001403272	0.06787051
3193.5	0.001072083	0.06749865
3193.75	0.003007267	0.07465319
3194	0.004775777	0.0779148
	<b>4.886377271</b>	<b>0.154042628</b>

**Quantitative analysis summary done by using XRD data of representative samples from Well C**

Sample no.	Phase Name	Weight %	Error %
Well C _Blk4	Illite 2M1	9.03	2.116
	Kaolinite (BISH)	23.522	3.797
	Quartz	66.382	4.367
	Pyrite	1.066	0.538
Well CBlk6	Kaolinite (BISH)	2.035	0.337
	Quartz	97.824	0.345
	Pyrite	0.142	0.075
Well C Blk7	Clinochlore Iib-2	11.667	1.573
	Illite 2M1	11.471	1.975
	Kaolinite (BISH)	28.109	2.602
	Quartz	48.264	2.904
	Pyrite	0.49	0.217
Well C Blk15	Clinochlore Iib-2	1.41	0.848
	Illite 2M1	8.973	1.609
	Kaolinite (BISH)	9.392	1.508
	Quartz	64.2	3.388
	Pyrite	0.184	0.337
	Augite Px	7.692	1.132
	Albite	8.149	1.245
Well C_ 15 3-54	Clinochlore Iib-2	5.515	5.104
	Illite 2M1	56.979	7.426
	Kaolinite (BISH)	33.671	7.446
	Calcite	3.835	2.146
Well C_ 15 3-54h	Illite 2M1	58.705	7.585
	Kaolinite (BISH)	36.109	7.176
	Quartz	3.115	0.796
	Pyrite	0.718	4.296
	Anatase	1.354	0.433

Well C_ 4 3-54	Illite 2M1	68.969	11.09
	Kaolinite (BISH)	29.058	11.012
	Quartz	1.911	1.696
	Calcite	0.063	2.814
Well C_ 4 3-54h	Illite 2M1	50.55	4.802
	Kaolinite (BISH)	37.835	4.502
	Quartz	7.65	1.263
	Pyrite	1.11	0.34
	Anatase	2.856	0.453
Well C_ 4 4-06	Clinochlore Iib-2	2.679	2.833
	Illite 2M1	73.346	8.804
	Kaolinite (BISH)	12.43	7.907
	Quartz	6.413	2.124
	Pyrite	3.254	1.477
	Calcite	1.878	1.455
Well C_ 4 4-06h	Clinochlore Iib-2	0.098	1.006
	Illite 2M1	67.583	3.248
	Kaolinite (BISH)	16.064	2.336
	Quartz	12.707	1.501
	Pyrite	1.017	0.346
	Anatase	2.531	0.344
Well C_ 6 4-06	Kaolinite (BISH)	23.315	1.574
	Quartz	76.685	1.574
Well C_ 6 4-06h	Clinochlore Iib-2	0.661	1.798
	Illite 2M1	8.769	2.872
	Kaolinite (BISH)	7.33	1.842
	Quartz	81.356	3.671
	Pyrite	1.04	0.664
	Calcite	0.845	0.909
Well C_ 7 2-58	Clinochlore Iib-2	5.107	2.354

	Illite 2M1	63.138	7.122
	Kaolinite (BISH)	25.042	7.441
	Quartz	6.713	1.385
Well C_ 7 2-58h	Clinochlore Iib-2	0	1.053
	Illite 2M1	83.777	3.403
	Kaolinite (BISH)	1.902	1.192
	Quartz	12.41	2.738
	Anatase	1.911	0.458

Blk= Bulk powder sample

h= treated –heated sample

### Quantitative analysis summary done by using XRD data of representative samples from Well D

Sample no.	Phase Name	Weight %	Error %
6 4-06h	Illite 2M1	36.255	8.136
	Kaolinite (BISH)	59.701	8.23
	Quartz	4.045	1.252
6 4-06	Illite 2M1	26.507	11.368
	Kaolinite (BISH)	65.772	10.617
	Quartz	7.722	2.276
6	Kaolinite (BISH)	36.303	0.966
	Pyrite	0.114	0.084
	Quartz	63.583	0.967
30 2-58	Clinochlore Iib-2	6.68	2.357
	Illite 2M1	37.554	4.67
	Kaolinite (BISH)	51.512	4.94
	Pyrite	3.348	1.023
	Calcite	0.906	1.56

30 2-58h	Illite 2M1	79.149	5.404
	Kaolinite (BISH)	18.952	5.213
	Pyrite	0.41	0.531
	Anatase	1.49	0.655
30 3-54	Clinochlore Iib-2	4.047	6.284
	Illite 2M1	34.428	5.639
	Kaolinite (BISH)	52.628	6.804
	Quartz	2.125	1.056
	Calcite	6.773	1.49
30 3-54h	Clinochlore Iib-2	0.663	1.917
	Illite 2M1	71.667	7.559
	Kaolinite (BISH)	22.413	4.304
	Pyrite	0.215	8.547
	Quartz	5.042	1.156
30 4-06	Clinochlore Iib-2	6.787	3.711
	Illite 2M1	22.343	3.996
	Kaolinite (BISH)	70.871	4.845
30 4-06h	Clinochlore Iib-2	1.924	1.263
	Illite 2M1	51.115	4.989
	Kaolinite (BISH)	39.145	4.618
	Pyrite	0.386	1.605
	Quartz	7.431	1.265
30	Illite 2M1	2.466	0.417
	Kaolinite (BISH)	18.817	0.549
	Pyrite	0.738	0.076
	Quartz	77.978	0.642
5 2-58h	I've only identified kaolinite, so it's 100% by default.		



**Representative lithofacies description of the Zubair cored interval of Well D. Please note that description sequence from bottom to top.**

Depth	Facies number	Facies description	Thickness m
3198-3193.70	Shale A	Shale , dark Grey, fissile with some intercalations of sand shales in 3196	4.70
3193- 3193.35	A	Shale intercalated with very fine sandstone( thin lamination )	0.35
3193-3190.30	c	Massive sandstone ,fine -medium grains , with carbonaceous material , band like structure, and argillaceous laminations	2.70
3190-3190.30	B	Shale , dark grey fissile	0.30
3190-3189.10	c	Shale , dark grey, fissile with some intercalations of sand shales in 3196	0.90
3189.10- 3189	A	Shale – dark Grey, fissile	0.10

3189- 3188.95	C	Massive sandstone ,fine -medium grains , with carbonaceous material , band like structure, and argillaceous laminations	0.05
3189- 3188.95	C	Massive sandstone ,fine -medium grains , with carbonaceous material , band like structure, and argillaceous laminations	0.05
3188.95- 3188	D	Silty sandstone with high argillaceous material , bioturbation	0.95
3188- 3180.90	c	Massive sandstone ,fine -medium grains , with carbonaceous material , band like structure, and argillaceous laminations	7.1
3180.90-3180.50	missing	----	-----
3180.50-3178.50	c	Massive sandstone ,fine -medium grains , with carbonaceous material , band like structure, and argillaceous laminations	2
3178.50- 3177.90	D	Silty sandstone with high argillaceous material , bioturbation , with lenticular sand stones (very fine sandstones)	0.6
3177.90- 3177.50	C	Massive sandstone ,fine -medium grains , with carbonaceous material , band like structure, and argillaceous laminations	0.40
3177.5- 3174.30	D	Silty sandstone with high argillaceous material, bioturbation, with some intercalation (about 15 cm	3.20

		thick o) on massive sandstone of fine grains. At 3175.30 , with lenticular sand stones (very fine sandstones)	
3174.30 – 3172.90	C	Massive sandstone ,fine -medium grains , with carbonaceous material , band like structure, and argillaceous laminations	1.40
3172.90-3172.50	D	Silty sandstone with high argillaceous material , bioturbation , with some intercalation , with lenticular sand stones (very fine sandstones)	0.40
3172.53164.75	E	Massive sandstone intercalated with clay (shale), parallel lamination – Oil show, fine grained sandstone, shale dark Grey, fissile with organic matter and some coals.	7.75
3164.75- 3164.65	C	Massive sandstone ,fine -medium grains , with carbonaceous material , band like structure, and argillaceous laminations	0.10
3164.65-3163.75	A	Shale intercalated with very fine sandstone ( thin lamination )	0.90
3163.75- 3159.75	C	Massive sandstone ,fine -medium grains , with carbonaceous material , band like structure, and argillaceous laminations	4
3159.75-3159.00	A	Shale intercalated with very fine sandstone ( thin lamination )	0.75
3159.00—3158.00	C	Massive sandstone, fine -medium grains, with carbonaceous material, band like structure, and argillaceous laminations, burrows.	1.00

3158.00 -3157.60	A	Shale intercalated with very fine sandstone ( thin lamination )	0.40
3157.60-3156.75	C	Massive sandstone ,fine -medium grains , with carbonaceous material , band like structure, and argillaceous laminations , burrows	0.85
3156.75-3156.45	E	Massive sandstone intercalated with clay (shale), parallel lamination – Oil show, fine grained sandstone, shale dark grey, fissile with organic matter and some coals.	0.30
3156.45-3155.75	C	Massive sandstone ,fine -medium grains , with carbonaceous material , band like structure, and argillaceous laminations , burrows	0.7
3155.75-3152.75	E	Massive sandstone intercalated with clay (shale), parallel lamination – Oil show, fine grained sandstone, shale dark grey, fissile with organic matter and some coals. (bottom of this facies has about 45 cm dense oil saturation with obvious dark colour )	3
3152.75-3152	C	Massive sandstone ,fine -medium grains , with carbonaceous material , band like structure, and argillaceous laminations , burrows	0.75
3152-3151	E	Massive sandstone intercalated with clay (shale) , parallel lamination – Oil show, fine grained sandstone , shale dark grey , fissile with organic matter and some coals.	1

3151- 3150.75	C	Massive sandstone ,fine -medium grains , with carbonaceous material , band like structure, and argillaceous laminations , burrows	0.25
3150.75- 3148.75	E	Massive sandstone intercalated with clay (shale), parallel lamination – Oil show, fine grained sandstone, shale dark grey, fissile with organic matter and some coals.	2
3146.26-3145.33	A	Shale intercalated with very fine sandstone ( thin lamination )	0.93
3145.55- 3143.75	E	Massive sandstone intercalated with clay (shale), parallel lamination – Oil show, fine grained sandstone, shale dark grey, fissile with organic matter and some coals.	1.60
3143.75-3142.00	C	Massive sandstone ,fine -medium grains , with carbonaceous material , band like structure, and argillaceous laminations , burrows With oil show.	1.75
3142.00 – 3141.95	F	Massive sandstone of fine grain size with very thin parallel lamination of clay, burrows ,	0.05
3141.95- 3140.33	C	Massive sandstone ,fine -medium grains , with carbonaceous material , band like structure, and argillaceous laminations , burrows With oil show.	1.62
3140.33- 3139.83	A	Shale, dark grey, fissile with some intercalations of sandy shales.	0.50
3139.83-3139-18	G	Sandstone, medium grains with bioclasts.	0.65
3139.18- 3138.33	A	Shale, dark grey, fissile with some intercalations of sandy shales.	0.85

3138.33—3137.83	C	Massive sandstone ,fine -medium grains , with carbonaceous material , band like structure, and argillaceous laminations , burrows	0.50
3137.83- 3137.33	A	Shale, dark grey, fissile with some intercalations of sandy shales.	0.50
3137.33-3135.33	Missing		
3135.33-3135.00	C	Massive sandstone ,fine -medium grains , with carbonaceous material , band like structure, and argillaceous laminations	0.30
3135.00- 3134.33	H	Very fine sandstone + Siltstone , with thin lamination of clay (argillaceous ) +coal deposits	0.67
3134.33- 3134.13	E	Massive sandstone intercalated with clay (shale), parallel lamination – Oil show, fine grained sandstone, shale dark grey, fissile with organic matter and some coals.	0.20
3134.13- 3133.33	C	Massive sandstone ,fine -medium grains , with carbonaceous material , band like structure, and argillaceous laminations , burrows With oil show.	0.80
3133.33-3130.48	I	Massive fine sandstone/ mud, High shale content, with lamination (rippy and wavy), dark Grey f shale, coal, and bioturbation can be seen in some parts of it.	2.85
3130.48- 3130.33	C	Massive sandstone ,fine -medium grains , with carbonaceous material , band like structure, and argillaceous laminations	0.15
3130.33-3129.33	I	Massive fine sandstone/ mud, High shale content, with lamination (rippy and wavy), dark Grey.	1

3129.33-3128.13	H	Very fine sandstone + Siltstone , with thin lamination of clay (argillaceous ) +coal deposits	1.20
3128.13- 3127.03	J	Siltstone, green colour, with some ferrous content	1.1
3127.03- 3126.33	E	Massive sandstone intercalated with clay (shale), parallel lamination – Oil show, fine grained sandstone, shale dark grey, fissile with organic matter and some coals.	0.7
3126.33-3125.68	c	Massive sandstone ,fine -medium grains , with carbonaceous material , band like structure, and argillaceous laminations	0.65
3125.68- 3125.33	J	Siltstone, green colour, with some ferrous content a	0.20
3125.33- 3123.33	c	Massive sandstone ,fine -medium grains , with carbonaceous material , band like structure, and argillaceous laminations	2
3123.33- 3123.13	K	Massive sandstone, very fine grained, silty, with high clay content, ripple, wave lamination, greenish colour. Heterolithic	0.20
3123.13- 3122.23	C	Massive sandstone ,fine -medium grains , with carbonaceous material , band like structure, and argillaceous laminations	0.9
3122.23- 3121.83	K	Massive sandstone, very fine grained, silty, with high clay content, ripple, wave lamination, greenish colour.	0.45
3121.83-3121.48	C	Massive sandstone ,fine -medium grains , with carbonaceous material , band like structure, and argillaceous laminations	0.35

3121.48-3121.43	k	Massive sandstone, very fine grained , silty , with high clay content , ripple , wave lamination , greenish colour( Heterlolithic)	0.05
3121.43-3121.33	missing		
3121.33- 3121.13	c	Massive sandstone ,fine -medium grains , with carbonaceous material , band like structure, and argillaceous laminations	0.20
3121.13-3121. 05	k	Massive sandstone,(Heterlolithic ) very fine grained , silty , with high clay content , ripple , wave lamination , greenish colour	0.05
3121.05- 3120.33	c	Massive sandstone, very fine grained , silty , with high clay content , ripple , wave lamination , greenish colour	
3120.00 -3119.55	H	Very fine sandstone + Siltstone , with thin lamination of clay (argillaceous ) +coal deposits	0.45
3119.55- 3118.80	C	Massive sandstone , thin parallel lamination of sandstone and clay, oil shows	0.55
3118.80- 3118	J	Siltstone, green colour, with some ferrous content	0.80
3118-3116	C	Massive sandstone, thin parallel lamination of sandstone and clay, oil shows, burrows.	
3116- 3115.50	E	Massive sandstone intercalated with clay (shale), parallel lamination – Oil show, fine grained sandstone, shale dark grey, fissile with organic matter and some coals.	0.50
3115.50-3115.20	C	Massive sandstone, fine grain size, thin parallel lamination of sandstone and clay, oil shows, burrows.	0.30
3115.20-3115	missing		

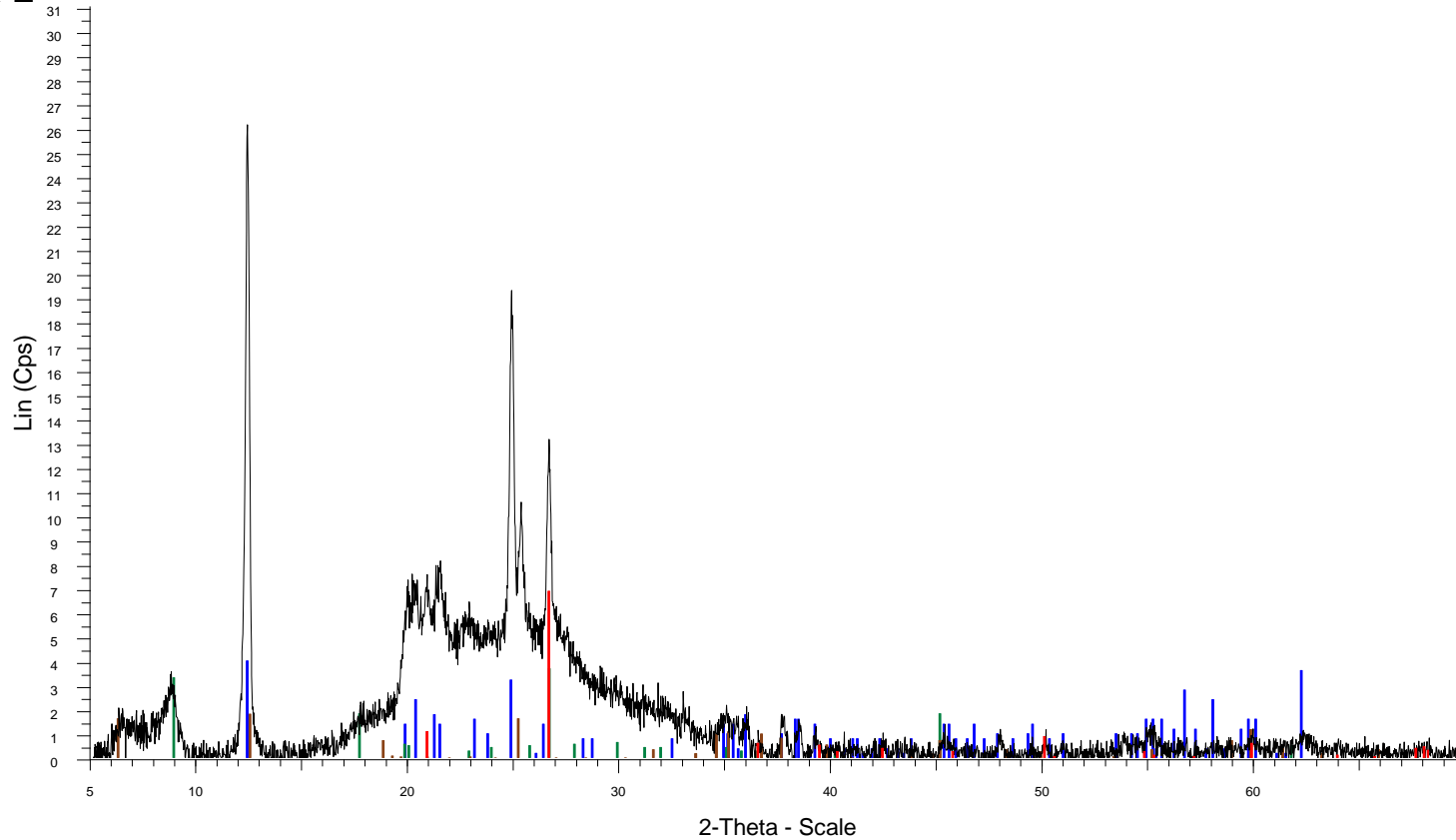


3115- 3112.50	J	Siltstone, green colour, with some ferrous content and coals.	2
3112.50-3112	C	Massive sandstone, thin parallel lamination of sandstone and clay, oil shows, burrows. Fine grain size.	0.50
3112- 3106.00	k	Massive sandstone,(Heterlolithic ) very fine grained , silty , with high clay content , ripple , wave lamination , greenish colour (there is shale , dark grey interval in between at 3110 -3109)	6
3106-3105.45	C	Massive sandstone, thin parallel lamination of sandstone and clay, oil shows, burrows. Fine grain size.	0.55
3105.45-3105	E	Massive sandstone,(Heterlolithic ) very fine grained , silty , with high clay content , ripple , wave lamination , greenish colour (there is shale , dark grey interval in	0.45
3105-3104	C	Massive sandstone, thin parallel lamination of sandstone and clay, oil shows, burrows. Fine grain size, carbonaceous material.	1
3104- 3101.29	E	Massive sandstone,(Heterlolithic ) very fine grained , silty , with high clay content , ripple , wave lamination , greenish colour (there is shale , dark grey interval in	2.71
3101.29- 3100.79	C	Massive sandstone, thin parallel lamination of sandstone and clay, oil shows, burrows. Fine grain size, carbonaceous material.	0.50
3100.79- 3100.39	H	Very fine sandstone + Siltstone , with thin lamination of clay (argillaceous ) +coal deposits	0.4

3099.63-3090	C	Massive sandstone, thin parallel lamination of sandstone and clay, oil shows, burrows. Fine grain size, carbonaceous material.	9.63
3090-3085.30	E	Massive sandstone,(Heterolithic ) very fine grained , silty , with high clay content , ripple , wave lamination , greenish colour (there is shale , dark grey interval in	4.70
3085.30- 3084.40	A	Shale, dark grey, fissile.	

## Appendix 2

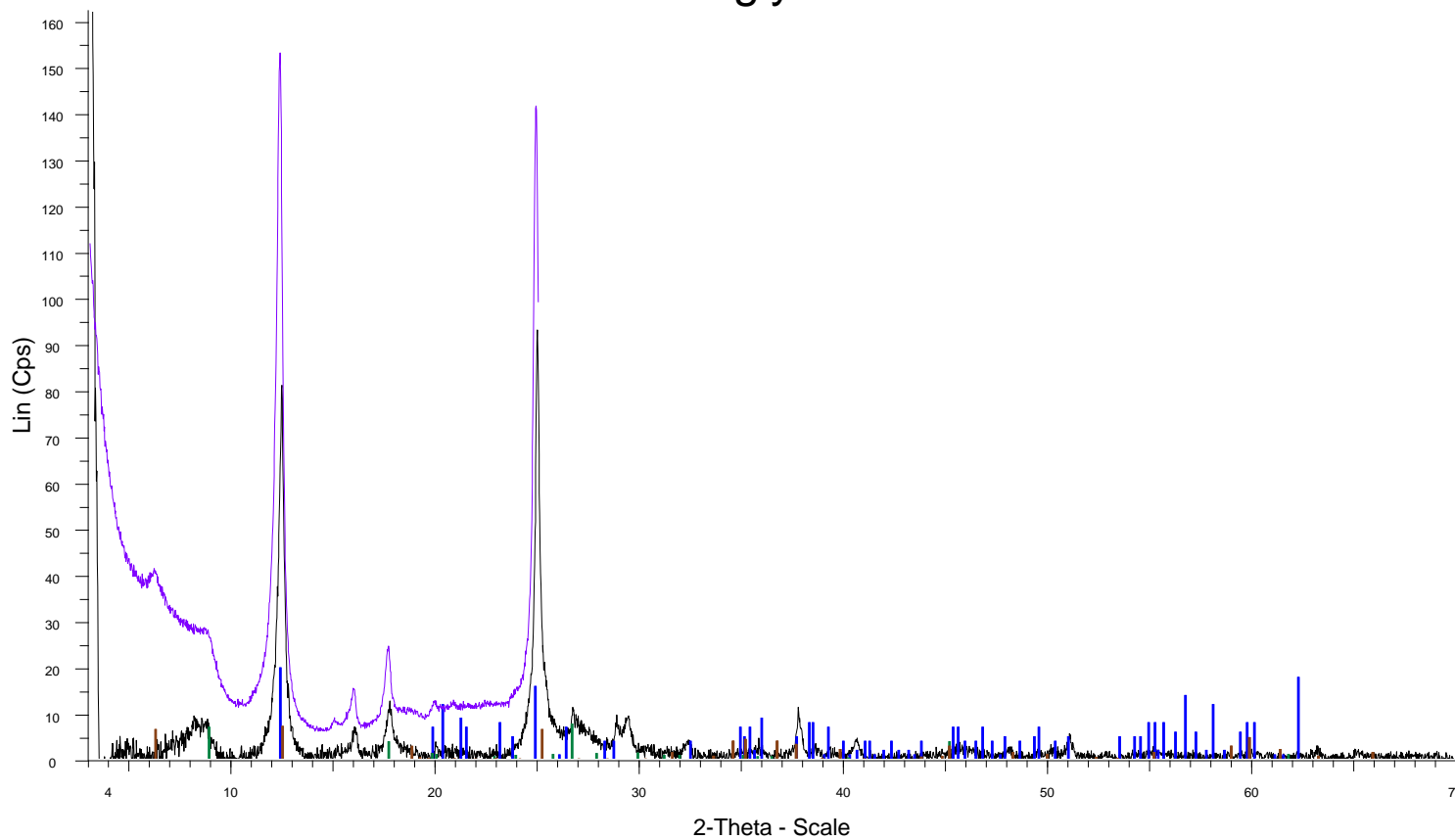
23 4:06 heat treated



File: 23 4-06h.raw - Type: 2Th/Th locked - Start: 5.000 ° - End: 70.013 ° - Step: 0.020 ° - Step time: 76.5 s - Temp.: 25 °C (Room) - Time Started: 27 s - 2-Theta: 5.000 ° - Theta: 2.500  
Operations: Background 0.257,1.000 | Import

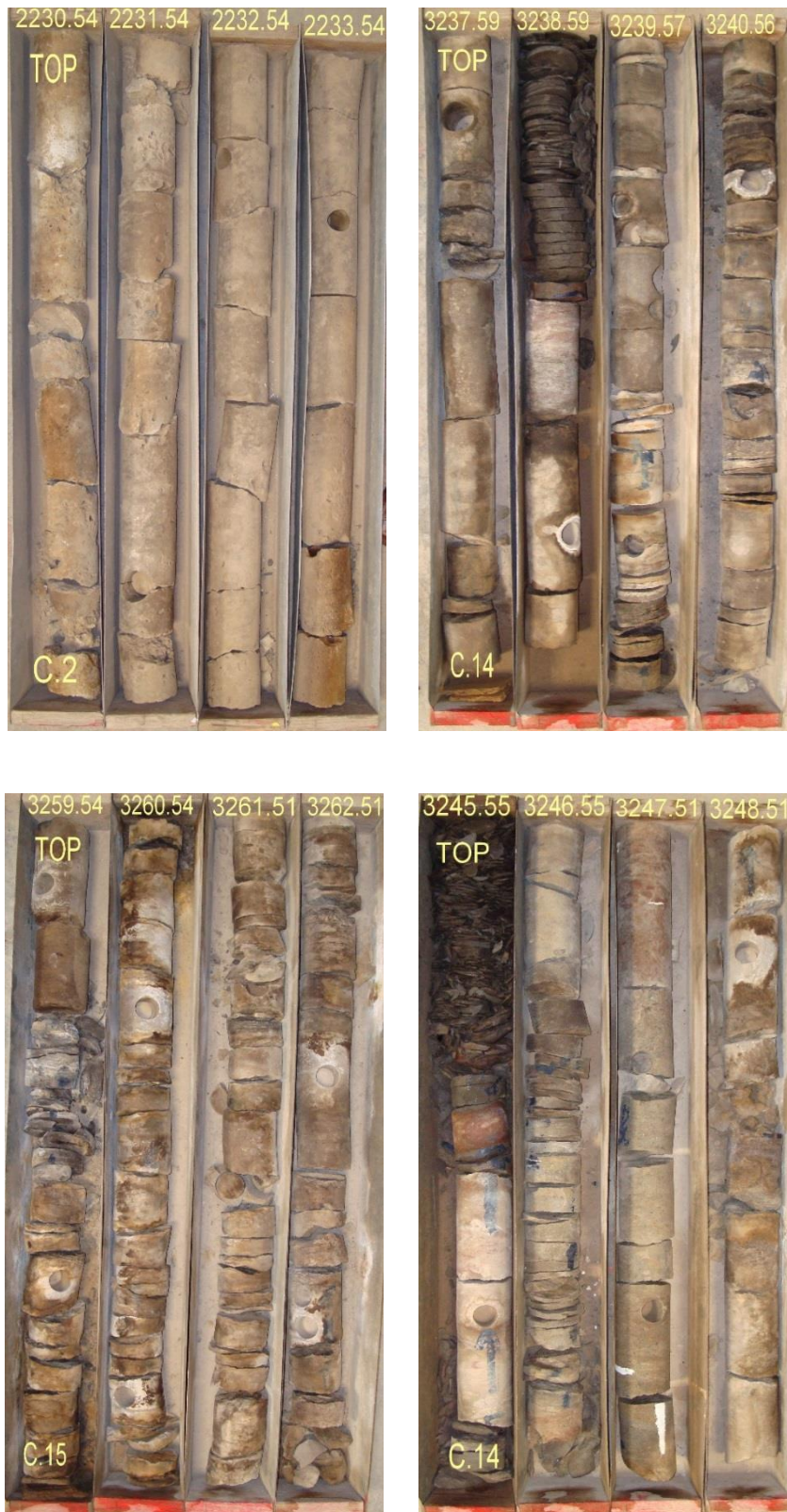
- 00-046-1045 (\*) - Quartz, syn - SiO<sub>2</sub> - Y: 22.28 % - d x by: 1. - WL: 1.5406 - Hexagonal - a 4.91344 - b 4.91344 - c 5.40524 - alpha 90.000 - beta 90.000 - gamma 120.000 - Primitive -
- 00-014-0164 (I) - Kaolinite-1A - Al<sub>2</sub>Si<sub>2</sub>O<sub>5</sub>(OH)<sub>4</sub> - Y: 13.01 % - d x by: 1. - WL: 1.5406 - Triclinic - a 5.15500 - b 8.95900 - c 7.40700 - alpha 91.680 - beta 104.900 - gamma 89.940 - Ba
- 00-026-0911 (I) - Illite-2M1 - (K,H<sub>3</sub>O)Al<sub>2</sub>Si<sub>3</sub>AlO<sub>10</sub>(OH)<sub>2</sub> - Y: 11.94 % - d x by: 1. - WL: 1.5406 - Monoclinic - a 5.19000 - b 9.00000 - c 20.16000 - alpha 90.000 - beta 95.180 - gamma
- 00-046-1323 (I) - Clinocllore-1M1lb-2 - (Mg,Al,Fe)<sub>6</sub>(Si,Al)<sub>4</sub>O<sub>10</sub>(OH)<sub>8</sub> - Y: 5.89 % - d x by: 1. - WL: 1.5406 - Monoclinic - a 5.34700 - b 9.26300 - c 14.25000 - alpha 90.000 - beta 97.20

## 24 2:56 & glycolated



File: 24 2-56.raw - Type: 2Th/Th locked - Start: 2.000 ° - End: 69.996 ° - Step: 0.020 ° - Step time: 31. s - Temp.: 25 °C (Room) - Time Started: 14 s - 2-Theta: 2.000 ° - Theta: 1.000 ° - Operations: Background 0.012,1.000 | Import  
 File: 24 2-58 gly.raw - Type: 2Th/Th locked - Start: 3.000 ° - End: 25.007 ° - Step: 0.020 ° - Step time: 76.5 s - Temp.: 25 °C (Room) - Time Started: 36 s - 2-Theta: 3.000 ° - Theta: 1.5 ° - Operations: Import  
 00-014-0164 (I) - Kaolinite-1A - Al<sub>2</sub>Si<sub>2</sub>O<sub>5</sub>(OH)<sub>4</sub> - Y: 0.39 % - d x by: 1. - WL: 1.5406 - Triclinic - a 5.15500 - b 8.95900 - c 7.40700 - alpha 91.680 - beta 104.900 - gamma 89.940 - Bas  
 00-026-0911 (I) - Illite-2M1 - (K,H<sub>3</sub>O)Al<sub>2</sub>Si<sub>3</sub>AlO<sub>10</sub>(OH)<sub>2</sub> - Y: 0.15 % - d x by: 1. - WL: 1.5406 - Monoclinic - a 5.19000 - b 9.00000 - c 20.16000 - alpha 90.000 - beta 95.180 - gamma 90.000  
 00-046-1323 (I) - Clinocllore-1Mllb-2 - (Mg,Al,Fe)<sub>6</sub>(Si,Al)<sub>4</sub>O<sub>10</sub>(OH)<sub>8</sub> - Y: 0.14 % - d x by: 1. - WL: 1.5406 - Monoclinic - a 5.34700 - b 9.26300 - c 14.25000 - alpha 90.000 - beta 97.20

### Appendix 3



Representative core photos pf Well C  
North Rumaila Oilfield -Iraq



Representative core photos pf Well B  
 North Rumaila Oilfield -Iraq